3D PRINTING SHAPE-CHANGING DOUBLE-NETWORK HYDROGELS

KATE LOUISE OLIVER

A DISSERTATION SUBMITTED TO THE UNIVERSITY OF BRISTOL IN ACCORDANCE WITH THE REQUIREMENTS FOR AWARD OF THE DEGREE OF DOCTOR OF PHILOSOPHY IN THE FACULTY OF SCIENCE, MARCH 2019.

WORD COUNT: 65, 659

ABSTRACT

The technique of 3D printing enables the creation of a vast range of shapes with no setup beyond design. Printing materials which change shape once printed, so-called 4D printing, opens up still more possibilities. However, much prior work in 4D printing uses proprietary equipment and hard polymers. This work presents an alternative route using thermoresponsive hydrogels processed using accessible, low-cost techniques. The working material is a tough double network hydrogel comprised of the thermoresponsive polymer poly-N-isopropyl acrylamide (PNIPAM) and the polysaccharide alginate, formed by UV-initiated and ionic crosslinking respectively.

An open-source, low-cost printer suitable for processing this hydrogel material is presented, which is at least a factor of 4 cheaper than alternatives and licensed such that others may replicate or modify it. This machine has been used to explore a new method for generating shape change in printed hydrogel pieces. PNIPAM-alginate hydrogels, initially printed flat, adopt a curved configuration when equilibrated in both ambient, and thermally contracted, conditions. The degree of curvature in these states differs in magnitude and direction depending on the dimensions of the printed piece and the angle of curing. This is demonstrated with 1D beams and gripper shapes. Potential origins for this effect including crosslink density and porosity variation are explored. While no conclusive evidence is found a theory based on solvent flow towards the first areas crosslinked is proposed. These findings form a complete package of technology and material to reproduce the results seen.

An alternative approach to changing the properties of PNIPAM-alginate gels was trialled with the addition of 1-6µg/ml concentration of gold nanorods. Despite the low concentration, significant effects on swelling ratio, elastic moduli, and thermoresponse were seen. This indicates that even at low concentrations nanoparticles can affect the hydrogel matrix containing them, relevant for workers on soft matter systems.

An expert is a person who has found out, by [their] own painful experience, all the mistakes that one can make in a very narrow field..

- Niels Bohr

It takes a village to raise a child; it takes a university to raise a thesis. These pages come from me and at least a hundred other people, from technicians who helped me learn the techniques to the people who gave me work that paid my rent. A few individual thank-yous:

To the occupants of G.39, for the camaraderie, the irony, the relentless dark humour, coding advice, coffee, sweets, and pep talks. In particular Max, Ioatzin, James, Peter, Josh and Chris, all of whom provided scientific advice, solutions and shoulders to cry on, sometimes simultaneously.

To my BCFN cohort and extended network, for answering strange queries from how to mix xanthan gum to statistical processing of small sample sizes and who has a spare laser cutter, and for easing me back into student life with a healthy dose of Mexican-flavoured fun. Particularly Jen, Maddy and Beth, for reality checks about how bloody hard all of this is and commiseration.

The staff of the School of Physics, particularly Gemma Winter and Tom Kennedy for help with people and electronics, respectively.

To my supervisors: Annela Seddon, for always going above and beyond the requirements of not only being a good scientist, but also a good person. And Steve Eichhorn, for much-needed feedback and critical assessment, coupled with humanity.

To the Science Showoff Talent Factory, who convinced me it's the same all over and gave me the artistic outlet to hit small, achievable, showbiz goals in the middle of a long trudge.

To my family. My grandparents Ray and Beryl Oliver left this planet while I was working on this; I hope I'd have been able to convince them of its utility. My grandmother and grandfather Eileen and Jinks Newman dedicatedly sent supplies for treats and provided relentless complimenting – but then they've done that since I was born. I wish my father Ken Oliver could have seen this; he'd probably have a million thoughts on how to improve the machinery. My brother Tom Oliver (not the scientist mentioned in here, a different one) answered questions about stats.

My mother, Kim Newman, remains the rock on which all this is built: from scraping me up when I was having anxiety attacks or staring numbly at the ceiling, to proofreading more technical terms than anyone deserves, or helping me move out of my house while in the middle of thesis writing. She is objectively the best mother.

And ultimately, my partner Rikard Anglerud. Just four months after we moved in together, I won a place to study for four years a hundred miles away. Since then we circumnavigated the globe once each in coaches to see each other for precious weekends. He remains my biggest fan (and biggest help with debugging Python). Not leaving him again.

I declare that the work in this dissertation was carried out in accordance with the requirements of the University's REGULATIONS AND CODE OF PRACTICE FOR RESEARCH DEGREE PROGRAMMES and that it has not been submitted for any other academic award. Except where indicated by specific reference in the text, the work is the candidate's own work. Work done in collaboration with, or with the assistance of, others, is indicated as such. Any views expressed in the dissertation are those of the author.

SIGNED: ..... DATE:.....

CONTENTS

TABLE OF FIGURES

LIST OF TABLES

LIST OF ABBREVIATIONS

3D	Three-Dimensional
4D	Four-Dimensional
AM	Additive Manufacture
ANOVA	ANalysis Of VAriance
AuNR	Gold Nanorod
CAD	Computer-Aided Design
CNC	Computer Numerical Control
DEAP	Diethoxyacteophenone
DI	De-ionized (water)
DLS	Dynamic Light Scattering
DMPA	2,2-Dimethoxy-2-phenylacetophenone
DNG	Double Network Gel
DSC	Differential Scanning Calorimetry
FFF	Fused Filament Fabrication
FTIR	Fourier Transform Infra-Red
G	Guluronate unit
GIMP	GNU Image Manipulation Program
GPL	Gnu Public Licence
IPAM	Isopropyl acrylamide
IPN	Inter-penetrating networks
IR	Infra-red
LCST	Lowest Critical Solution Temperature

M	Mannuronate unit
MBA	Methylene Bis-acrylamide
NIPAM-alginate	A blend of the monomer isopropyl acrylamide and alginate
NP	Nanoparticle
NR	Nanorod
PLA	Poly Lactic Acid
PNIPAM	Poly-N-isopropyl acrylamide
PNIPAM(O)	Opaque gel of PNIPAM
PNIPAM(T)	Transparent gel of PNIPAM
PNIPAM-alginate ...	Interpenetrated cured gel of a polymerised and crosslinked isopropyl acrylamide network and crosslinked alginate networks
RPM	Revolutions Per Minute
SAED	Selected Area Electron Diffraction
SAXS	Small Angle X-ray Scattering
SEM	Scanning Electron Microscope/Microscopy/Micrograph
SLA	Stereo-lithographic Assembly
SMP	Shape Memory Polymer
TEM	Transmission Electron Microscope/Microscopy/Micrograph
Tg	Glass Transition Temperature
UV	Ultra-violet
UV-Vis	Ultraviolet-Visible
YM	Young's Modulus

PUBLICATIONS

Publications relating to the work published in this thesis:

- **Oliver, K.,** Seddon, A. & Trask, R.S., *"Morphing in nature and beyond: a review of natural and synthetic shape-changing materials and mechanisms",* J. Mater. Sci. (2016) **51: 10663**. https://doi.org/10.1007/s10853-016-0295-8

0. MOTIVATION

The developing technology of 3D printing enables a single machine to create thousands of different shapes, with no set up beyond the digital design required. This has clear potential in fields requiring customisability, such as prosthetic design, and also in extreme environments where it is impossible to anticipate, or carry tools to meet, every need. We already see 3D printers revolutionising the lives of amputees[1,2] and astronauts[3,4] - it is inevitable that future applications will emerge as the technology develops and greater functionality is possible.

The utility of prints could be increased further by the use of smart materials which respond to the environment around them by changing their physical properties, creating prints capable of changing in shape even after removal from the printer. These multifunctional objects open up entirely new design possibilities, of a versatile world of forms which can diversify still further over time as needed. These could have applications in responsive architecture, soft robotics, biomedical implants, and much more, enabling concepts which human designers can currently only dream of – although many examples are on view every day in the natural world.[5]

The concept of time-evolution post-print was named '4D printing' by Skylar Tibbits when launched in 2013.[6] The prototypical example utilized two custom-designed plastics, one of which expands in contact with water, which are printed together as one part using a Stratasys Connex multi-material printer.[7] Subsequent work using the same technology, this time blending between two plastics with differing responses, has been able to show curvature in two dimensions,[8] and materials which deploy in sequence. [9] While work using these techniques is impressive and the closest to market of any 4D prints so far, the Stratasys Polyjet™ technology[10,11] has a high capital cost (upwards of $0.25 million dollars) and the raw materials are proprietary and expensive. It is therefore desirable to increase the selection of printable smart materials available, methods by which they can be printed, and understanding of how the behaviour may evolve once printed.

An alternative approach uses hydrogels, cross-linked polymers swollen with water into low-density materials capable of large deformations. The raw materials for some responsive hydrogels include the most prolific polymers on earth, which can be easily and sustainably harvested, then biologically degraded. Such soft materials are currently of interest to the medical community as substrates for cell growth, due to their similarity to biological extracellular matrices.[12,13] Other potential applications are in engineering of microfluidics[14] and soft

robots.[15–17] Prior work has produced beautiful complexly curved surfaces using hydrogel nanocomposites and directional printing,[18] and working self-regulating valves composed of two materials.[14,19]

Within this thesis steps are taken towards replicating the achievements of hard polymer-based 4D printing for hydrogels printed using accessible, low-cost printing technology and simple, one-step techniques. While the additional dimension in 4D printing may be used to refer to any change of properties, such as conductivity, opacity, or malleability, the focus in this thesis will be on shape change – that is, using materials which change their original dimensions in response to stimuli. In order to move beyond the trivial case where a print shrinks uniformly as the environment changes, it will be necessary to develop materials with a range of responses, and combine them within a single print.

Accessibility is important for verification and speed of development. Hobbyist 3D printing has shown the strides that can be made using open development methods[20] and it seems plausible that this would also aid the development of 4D printing. Therefore, the equipment developed for this work derives from open-source projects and the modifications made for this project are publicly documented according to the requirements of open-source practice. The material used, a hydrogel composed of alginate blended with isopropyl acrylamide, developed from a formulation used by Bakarich et al.,[21] is low cost and low-toxicity, and requires no specialised equipment to create.

This thesis documents the process of developing 3D printing equipment, followed by the creation and characterisation of heat-sensitive hydrogels with variable properties. Two routes are investigated for modifying PNIPAM-alginate; firstly, the effects of a UV-curing direction and print dimensions, and secondly the effects of the addition of gold nanorods.

The contributions of this thesis to the field are therefore:

- One enabling technology: the combination of existing open-source 3D printing technology with illumination into an open-source, UV-curing printer capable of shaping and curing isopropyl acrylamide-alginate gels. Control over UV-curing as a variable that can be specified during print adds an additional dimension of control.

- A previously-undocumented phenomenon by which initially flat isopropyl acrylamide-alginate (PNIPAM-alginate) hydrogels display bending behaviour at both extremes of their thermal behaviour as a result of curing conditions. The direction and magnitude of curvature can be sensitively varied as a function of illumination direction and sample dimensions using the equipment developed, providing a simple, effective route to shape-change. The relationship between curvature and dimension is explored, as are potential mechanisms behind the effect, and a hypothesis based on osmotic gradients proposed.

- A parallel investigation extending the prior technology of adding gold nanorods to isopropyl acrylamide to incorporation within PNIPAM-alginate double network gels. Complex, non-monotonic effects on mechanical strength and thermoresponse are seen. Implications for future use of nanoparticles as additives in gels are concluded.

The remainder of this introductory chapter will set the work in context, reviewing shape-changing materials, 3D printing, and their combination. Since many shape changing materials exist – indeed in the most limited case, that of thermal expansion or contraction, all materials could be said to change shape – this background must necessarily be selective. Within the brief of achieving a 3D printed shape change, the potential for modification of the material, and the limitations of processing using additive manufacture, suggest suitable criteria for narrowing down the field – while considering there is of course interplay between the choice of material and the mechanism for shaping it.

The introduction will first briefly discuss additive manufacturing methods and shape changing materials compatible with additive manufacture – the latter drawing strongly on a review paper authored during the course of doctoral studies.[22] The choice of hydrogels as a working material will be justified, and the options for varying their behaviour explored, focusing particularly on the use of nanocomposites. Finally, theory relevant to the behaviour of hydrogels, and its limitations, will be outlined, along with the measurements required.

1 APPROACHES TO ADDITIVE MANUFACTURE OF SHAPE CHANGING MATERIALS

1.1 ADDITIVE MANUFACTURE

Additive manufacture (AM), commonly known as '3D printing', was initially developed in the 1980s for rapid prototyping.[23] Rapid prototyping is a general term covering a range of techniques whereby one piece of equipment can construct a vast range of geometries, rapidly progressing from computer-aided design to physical object, as required in the early stage of a design project.

Within this field, 'additive manufacture' refers to the use of computer control to construct objects by building up the structure required layer by layer. This contrasts with the subtractive method it descends from, CNC (Computer Numerical Control) milling, where a precisely controlled bit removes material from an initial block. 3D printing is isomorphic in its meaning to additive manufacture, but due to its wider use in informal settings tends to be used outside engineering and technologies. As of 2018, the technology is currently coming of age, encompassing a strong hobbyist, open-source community, in addition to a broad academic spectrum of users and industrial applications.[24]

Within the academic sphere, interest in researching the techniques crosses many disciplines, including the biomedical, engineering, materials science and fine art communities. Multiple methods exist for producing structures additively, including extrusion of filaments, selective photoreaction using masks, or joining of particulate matter. The review by Lewis covers the current variety of methods, materials, architectures and applications of small-scale printing,[25] while the work of Gross et al. covers the evolution of the process. [26] Given the many variants of 3D printing currently available, this section will focus on only the two lowest-cost AM techniques.[27] These are Fused Filament Fabrication and Stereo-lithographic Assembly.

1.1.1 FUSED FILAMENT FABRICATION

Fused Filament Fabrication (FFF) traces out each layer by extruding working material from a nozzle. This requires rheological properties that permit initial flow at accessible yield stresses, but upon reaching the target position exhibit minimum spreading or shearing, while retaining enough strength to support the weight of additional layers. This switch in properties is commonly achieved by heating during extrusion, followed by rapid cooling and therefore solidification, ready for subsequent deposition. This is seen in the majority of 'hobby' level printers

which use thermoplastic materials, such as acrylonitrile butadiene styrene (ABS) and polylactic acid (PLA), with accessible glass transition temperatures between 180 and 210°C. Alternative methods include triggering photo-polymerisation in situ, [28] drying,[29] use of epoxies with an appropriate curing time[30], or printing into a solution which triggers curing.[31] However, if the material is selected to have appropriate shear-thinning rheological properties the need for a time-dependent or triggered material state change is avoided.[32–34] This richness of processing methods means that hydrogels, shape memory polymers, foodstuffs and many other materials are amenable to FFF.

Due to the nature of FFF construction, certain structures, such as overhangs or totally enclosed ball joints, require the use of supports; either lightweight supports that are intended to be broken off, or sections rendered in a sacrificial material which is subsequently removed. Multiple material prints are also possible; these may be produced using separate nozzles for each material, use of the same nozzle but replacing the feed material, or even through dynamic mixing, as demonstrated by Lewis *et al.*[35] Resolution varies dramatically depending on the material, but would typically be around 100 µm. For comparison, inkjet printing may attain 20 µm resolution in the xy plane dimensions and 100nm vertically.[36] As observed by Lewis, this is sufficiently detailed resolution to manufacture structures such as auxetic cells and bioprint lines of single cells. [25]

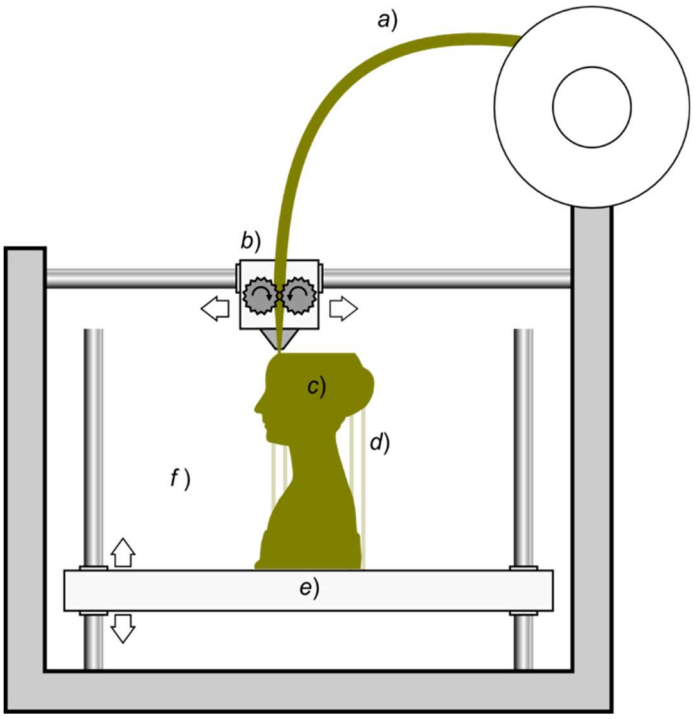

Figure 1.1. Fused Filament fabrication requires filament (a) to be pushed through a (rather self-explanatory) 'hot end' by a motor (b). Here, it melts, and is extruded through the nozzle along a 2D path on the print bed. The bed then moves down to allow the next layer to be placed on top. From Scopigno et al. [47]

1.1.2 STEREOLITHOGRAPHIC ASSEMBLY

From the well-developed technology of lithography the three-dimensional technique of stereolithographic assembly (SLA) has evolved. The first version used a reservoir of photoreactive materials, which are illuminated through a mask or digital screen, solidifying exposed regions. The solid area is then lowered and covered with a fresh layer of liquid. This is again exposed, and solid areas in contact with the layers below are joined to it. Typical feature sizes for SLA are around 25 µm, [26] restricted by laser size; use of an array of digitally controlled micro-mirrors for focusing brings the resolution down to around 1µm. [37] The related light-based technique of two-photon polymerisation has a diffraction-limited maximum resolution of below a micron.[38] Benefits of SLA include smooth surface finish, rapid production rates, non-contact processes, and the highest current resolution.

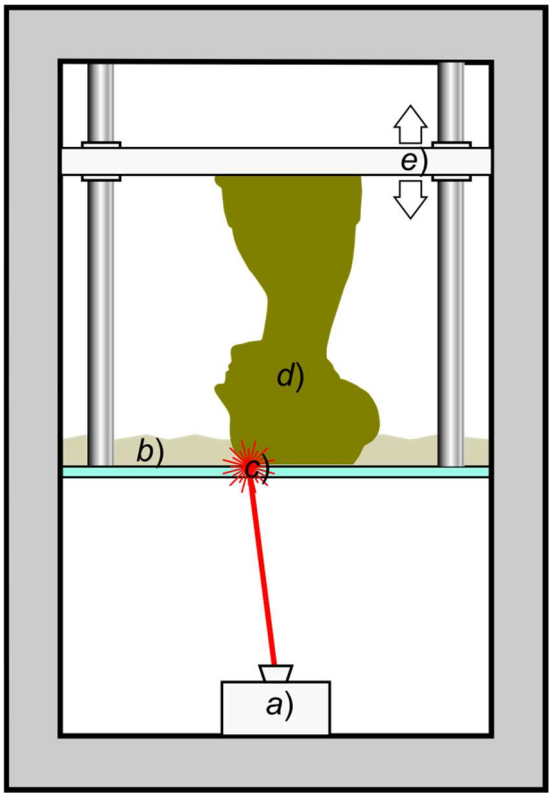

Figure 1.2. Diagram of Stereolithographic Assembly (SLA). This requires a vat of photocuring resin (b), upon which is projected or traced by laser an image of one layer (c). When solidified, the material is moved up to expose another liquid resin surface (e). This is repeated to form subsequent layers.

Downsides to this technique include the amount of material required, although alterative configurations aim to reduce this issue. Importantly for a 4D printing application which potentially exploits multiple materials, the method is restricted to one material unless the operation is stopped, all resin removed and replaced, and a second process restarted. This causes a large amount of waste and requiring additional stages.[39] The majority of SLA printing utilises highly crosslinked resins, although some novel formulations which can, for example, be fired and become porous ceramic are available.[40]

An exciting actuating example comes from the Hebrew University of Jerusalem, where UV curable elastomers have been developed which are highly suitable for pneumatically actuated prints.[41] However, their requirement for external pumps and pressure systems mean that an actuating device cannot be created exclusively using a printer, and thus are beyond the remit of this project. Shape memory polymers (SMPs) are the work-horse of shape-changing prints and will be covered more thoroughly in section 1.2.1.

At micron-scale SLA, hydrogels are the principal responsive materials processed via two photon polymerisation. This method has been used for the fabrication of small scale hydrogel devices such as reversible ion-responsive hydrogel microcantilevers [42] and micropumps(shown in Figure 1.3).[43] High spatial resolution manufacture is particularly relevant for hydrogels, as their material shortcomings decreases as the size of the device reduces – see section 1.2.2. However, these production methods are high-cost, and also proprietary, limiting experimentation with techniques.

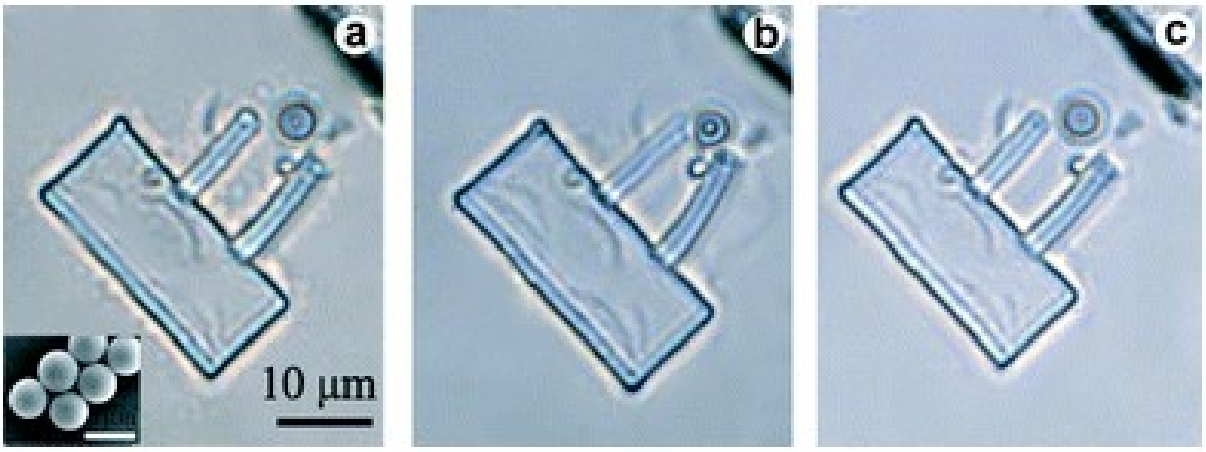

Figure 1.3. Ion-responsive hydrogel microcantilever showing bending induced by exposure to 1M NaCl (a), then water – inducing 'gripping'(b), and back to 1M NaCl for (c), release. This was fabricated with a photo-responsive polymer solution, cured using a laser capable of scanning in XY and movement in Z relative to the pre-cured substance. The printer system was developed by the paper authors.[42]

Both SLA and FFF share common downsides of AM; components are structurally weak compared to, for example, casting or vacuum forming, no economies of scale are possible, and as a result production time is slow. Work is ongoing to address the issue of weakness through reinforcement [44], use of print direction[45] and, in the case of SLA, maintaining a continuous liquid interface between layers [46]. The other issues are inherent to the process and are best addressed by making an intelligent choice of fabrication technique for the application.

Of the two methods, FFF is vastly more affordable[26,47] and better documented in the open-source community. It also offers the potential to switch between and combine multiple materials with increased ease, a key requirement for non-trivial shape change, and has already been successfully used to print materials with similar rheological properties to the polymer blends from which crosslinked hydrogels are formed. Therefore, FFF is the technique which will be used in this thesis.

For the purposes of reproducibility, accessibility and affordability as highlighted earlier, the FFF system used will be developed from off-the-shelf and open source components; the performance and construction of the system is documented in Chapter 3.

1.2 SHAPE CHANGING MATERIALS COMPATIBLE WITH ADDITIVE MANUFACTURE

Much work in 4D printing has hitherto focused on the use of shape memory polymers (SMPs). However, these materials are often proprietary, require complex or toxic syntheses, or are only compatible with proprietary, costly systems. Here a case is made for an alternative approach using hydrogels; greener, more accessible shape-changing materials.

1.2.1 SHAPE MEMORY POLYMERS

Shape memory polymers (SMPs) can undergo deformation into an intermediary shape, be 'set' in that intermediary shape, and then upon input of additional energy return to their original condition. At a microscale, the behaviour arises from a system of netpoints, which may be physical or chemical bonds, and chains between them. These change their flexibility under different conditions, the most common of which is a change in heat.

In a typical application (shown in Figure 1.4), the system is heated above the glass transition temperature (T_g) of the chain sections, when they become flexible, and is then deformed by an external force while cooling occurs to below T_g, 'locking' the chains in place in a high energy state. When the temperature is raised above T_g, the chains regain mobility and release strain to gain entropy, and return to their original maximum entropy state, corresponding to the relaxed macroscopic shape. The family of SMPs, their composites and properties is large and more exhaustively listed in many recent reviews of SMPs. [48–50]

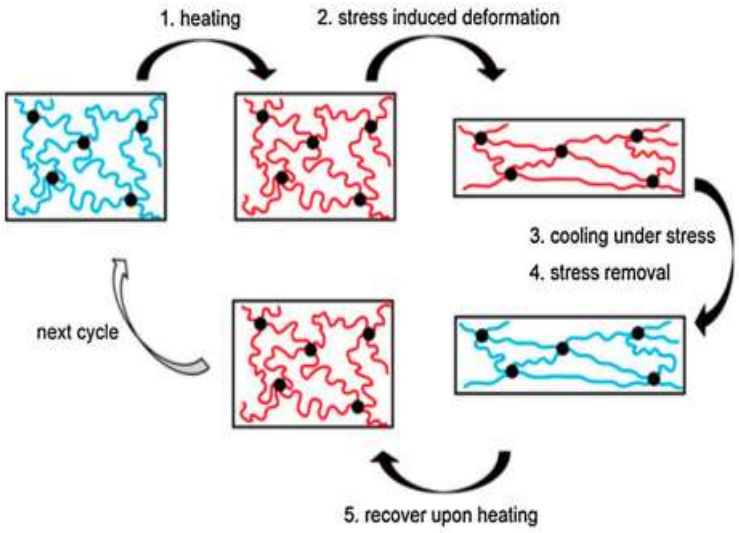

Figure 1.4 The molecular mechanism of a dual shape memory polymer throughout a thermal cycle. Black dots are netpoints; blue lines molecular chains of low mobility below transition temperature; red lines molecular chains of high mobility above transition temperature. Reproduced from Zhao et al.[49]

SMPs are attractive for lower cost, lower density (and therefore improved energy to weight ratio, a key element if the actuator is required to move its own mass) easier processing and larger attainable strains compared to shape memory alloys or piezoelectric actuators.[50] A major advantage of SMPs over other shape changing materials is their programmability, which opens up multiple applications after the manufacturing stage depending on the secondary shape imprinted. However, the materials do require intervention to achieve this - picking up and curling a strip, or stretching a material while it cools – this expands their potential, but does add another manufacturing stage.

Significant amounts of work in 4D printing has already been dedicated to shape memory polymers, and multiple shape memory polymers have been used for demonstrations of 4d printing. These include approaches based on block copolymers with different glass transition temperatures,[51] as well as polymers in different phases, such as semicrystalline methacrylated polymer.[52] 3D printing of shape memory polymers has been achieved with SLA (shown in Figure 1.5.) and FFF, including multimaterial SLA printing. [8,53,54]

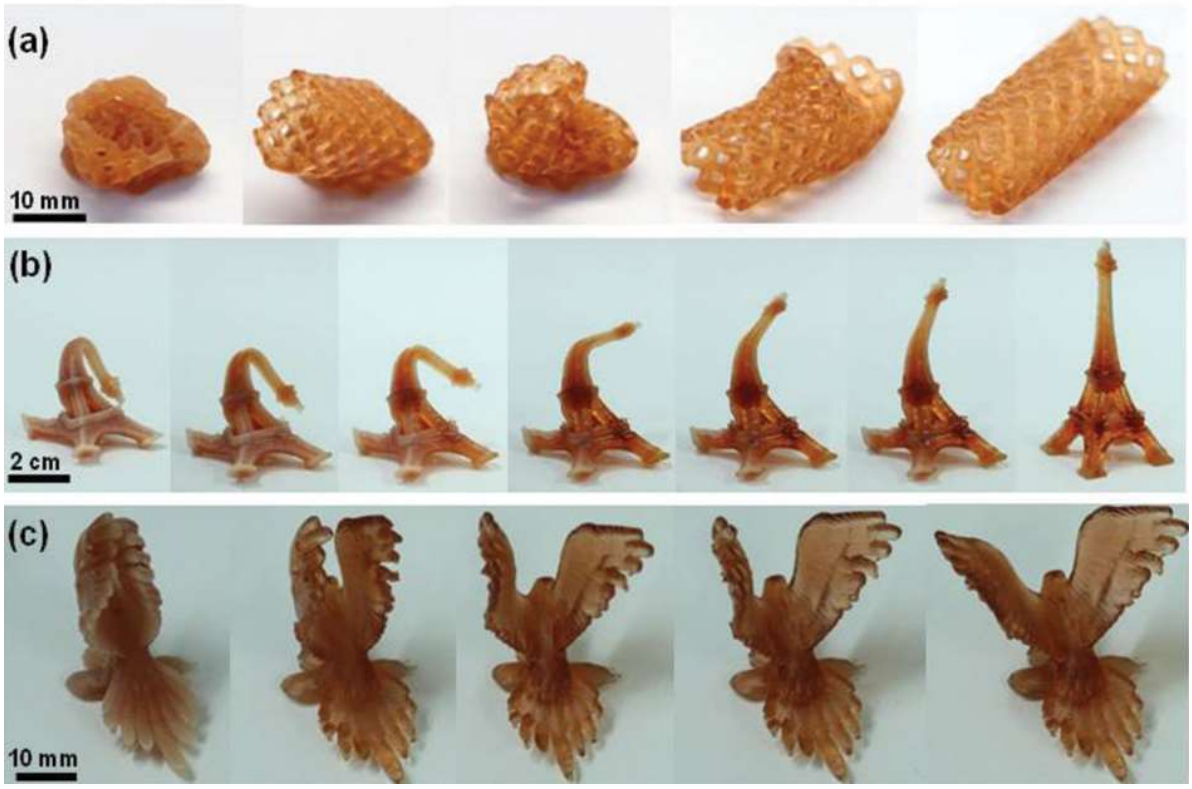

Figure 1.5. Shape memory polymer based on crystallites, printed using SLA technology, shows deployment over time. Such devices could be used as stents for medical purposes (top), or as self-closing circuits, self-repairing structures, or toys. From Zarek et al.[54]

However, the most elaborate examples of printing using shape memory polymers have used the Stratasys Connex Polyjet™ technology to combine SMPs with different functional temperatures and contraction rates. This patented technology (US 6,259,962 B1) uses an inkjet-like head to extrude polymer inks and then cure them with UV light in place, meaning the variation of material can be achieved throughout the print. [10,11] This was utilised for both the initial 4D prints of Tibbits and further development to complex curved surfaces – another desirable feature of a 4D printed technology.[55] Examples are shown in Figure 1.6. The technology also allows blending between SMPs with different transition temperatures, resulting in blends with transition temperatures linearly interpolated between the components. However, while this technique shows good results, it is expensive (machines begin at around $20,000 USD[26]) and proprietary.

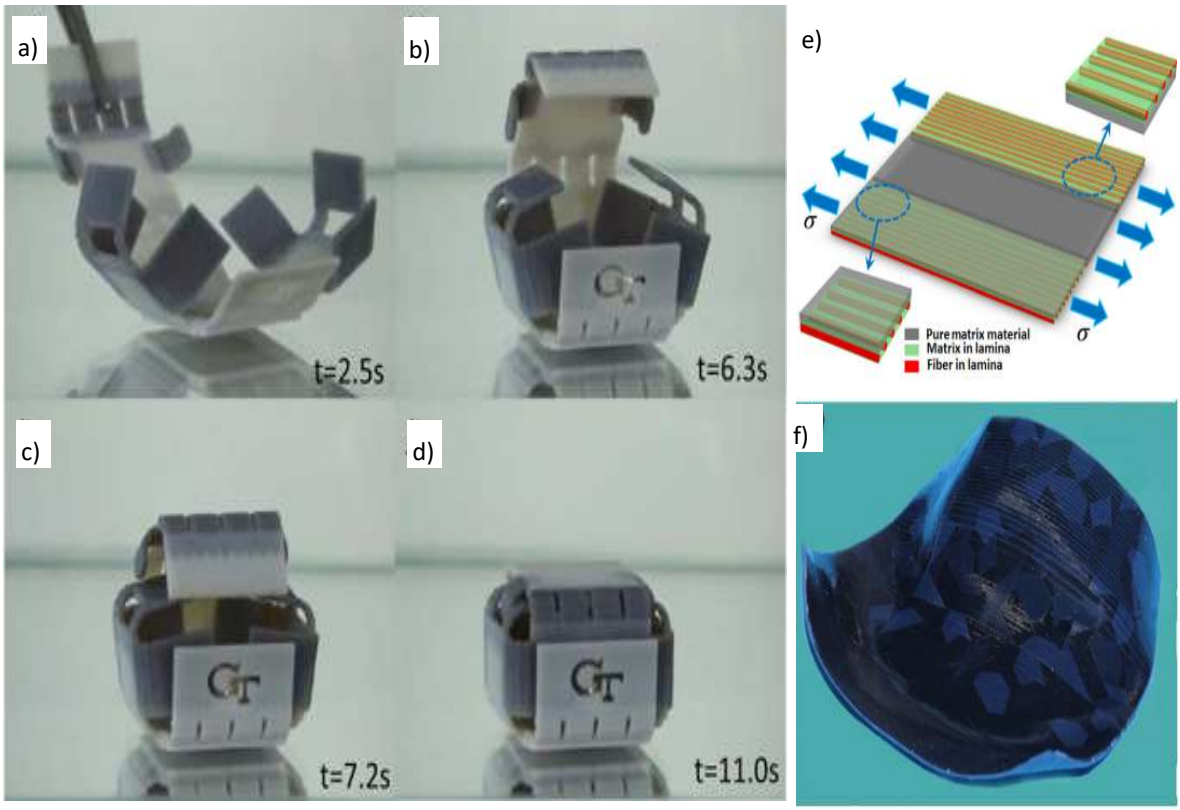

Figure 1.6. Shape-changing objects rendered with the Stratasys Polyjet™ process. A-d: A 3D printed box, made of blended shape memory polymers with differing transition temperatures such that, as the temperature is increased, they are triggered sequentially to return to their unstressed configuration, causing folding.. By Mao et al, 2015. Right: a combination of fibres and lamina with different thermal responses is printed (e). Once it heated, stretched, cooled and released, it takes a complex temporary shape (f). From Ge et al., 2013.

1.2.2 HYDROGELS AS A MATERIAL

Within this thesis hydrogels will be defined following Finch, as "polymeric materials which are able to swell in water and retain a significant fraction of water within their structure, but do not completely dissolve in water". This lack of dissolution is caused by crosslinks between the polymer chains, which may be permanent covalent bonds or molecular associations, ie. hydrogen or ionic bonds. [56].

While many synthetic hydrogels are weak, scientific interest in them as responsive materials remains strong, largely bolstered by their similarity to some extremely impressive and successful biological systems. Responsive hydrogels made of pectin are found in the vasculature tissue of plants, which react to increasing ion concentration with corresponding changes in volume that modify the uptake of liquids[57]. Hydrogels are also similar to the extra-cellular matrix, the organic frame which holds cells in place within multicellular animals, and

so are an exciting prospect in biomedical fields to shape cultured cells into synthetic organs, for fundamental biological studies, and even as vehicles for living cells as devices.[58–61] Their soft nature and viscoelastic properties are also a good match to a wide variety of animal tissues, suggesting applications in robotics, internal and external medical devices, and human computer interfaces. [15,62,63]

Hydrogels may contain a tiny proportion - as little as 0.1% by mass[64] - of polymer, and still hold their shape; they are capable of responding to biological,[65] chemical,[66] hygroscopic, heat,[67] or light[68] triggers, and may also exhibit shape memory characteristics[69] – some relevant examples will be given here, but a wider picture is given in Oliver et al.[22] and also in the reviews of Ionov and Tokarev.[70,71] For the scientist, their ease of modification recommends them as model materials. One can vary the choice of polymer, copolymer or blend, polymer/solvent ratio, the solvent used, the crosslink density or the nature of crosslinks [72]. Still further variation may be introduced by reinforcement elements of various shapes or chemistries, with surface modifications or without, with or without orientation, at different concentrations.[22]

Hydrogels, of course, have downsides: they are typically slow to reach maximum deformation, brittle and exert a limited force. While they are easy to work with, and similar to some biological materials, they hold two major drawbacks; their slow response time and their lack of mechanical strength. Their need for hydration also presents challenges.[73]

The problems of small force and slow response have a common origin: the intrinsic requirement for hydrogels to transport water. This makes their responses fundamentally diffusion-based and shows a power-law relationship between time and length scale.[74] Delayed response also arises from the time-dependent viscoelastic behaviour of the sample.[75] The relevant contributions of different phenomena depend fundamentally on the size of the sample and the dominant diffusion mechanism.[7677]

Response rate can be increased with the addition of micro-channels[76], mimicking the operation of vasculature and allowing integration into microfluidic devices. On a molecular level, the addition of graft chains, creating a comb-type hydrogel, has been demonstrated to improve the response speed of photothermally sensitized PNIPAM/magnetite nanocomposites by around a factor of three,[67] while the presence of a non-crosslinked polymer is thought to introduce hydration channels.[78]

With regard to strength, hope for hydrogel-based devices is inspired by the properties of gels seen in nature. Synthetic hydrogels typically have fracture energies of about $10Jm^{-2}$; cartilage, meanwhile, withstands an additional two orders of magnitude, fracturing at around 1,000 Jm^{-2}.[79] Many strategies are currently being employed to strengthen hydrogels, of which some of the most promising are nanoreinforcement and the use of double network structures, but it is commonly accepted there is a long way to go.[73]

Possible solutions are improvements in gel nanostructure or microstructure. For example, the 20% of 20nm collagen fibres found in the cornea are theorised to be the source of its 4MPa tensile strength[79] , while analogously fibre reinforcement of an epoxy-based hydrogel has been shown to increase its breaking stress by a factor of 20.[80]. The remarkable performance of cartilage is due to its anisotropic response, which has been mimicked by the inclusion of 1.5% wt of flakes of graphene oxide within a hydrogel.[81] Other promising nanocomposites have been demonstrated, with the addition of silicates and metal oxides found to promote cross linking, increase strength, and modulate shear response. [82] For responsive hydrogels specifically, cellulosic polymers have been used to sensitize hydrogels to temperature, pH, and redox potential.[83]. Metal oxide NPs can improve conductivity, add an orthogonal degree of responsiveness,[84] and give additional properties such as antimicrobial activity.[82]

Modification of gel nanostructure has also produced hydrogels with a large swelling ratio, rapid response rate and elastic properties that permit tying the sample in a knot, using a two-step synthesis where functionalised nanogels of less than 100nm in diameter are created, then joined together in a second stage.[85] This approach generates heterogenous mesh-like structures relatively easily.

Heterogeneity can also improve strength through the synergistic combination of two gels into interpenetrating network gels (IPNs). Here one gel network is formed around a second in such a way that the molecules are interlaced and inseparable without bond breaking.[86] Double network gels (DNGs) are a special case of this, defined by their creator Gong as having a first network formed of a rigid, highly crosslinked polyelectrolyte, with a second network of loosely crosslinked ductile neutral polymers around them.[87]

1.2.2.1 PRIOR USE OF HYDROGELS IN 3D PRINTING

3d printing of hydrogels has been a topic of great interest to the bioengineering community, as they have similar properties to the extracellular matrix which encases many mammalian cells in vivo.[88] This has led to the use of many different materials for 3d printing cells, including Pluronic™, peptides, PEGDA, alginates, and celluloses.[13,89–91]

Focusing exclusively on 3d printed responsive materials, the field is smaller. Muscle cells contained in poly(ethylene glycol) diacrylate gels have been used to create 'biobots', although these require more carefully controlled environments than non-living smart materials.[61]. Prints combining hydrogels with different expansion rates upon hydration have been shown by the Woolongong group of Panhuis to create folding gel cubes.[92] (Figure 1.7, left) The same group have also used thermally responsive gels to create a working valve that self-regulates to inhibit influx of hot liquids once a set temperature is reached.

Work by the Lewis group at Harvard's Wyss Institute elegantly uses the shear-alignment of cellulose within the hydrogel while printing to cause directional restriction of printed gel lattices, determined by the path of an extrusion based 3d printer. Examples of shapes produced are shown in Figure 1.7 (right). Notably, this is

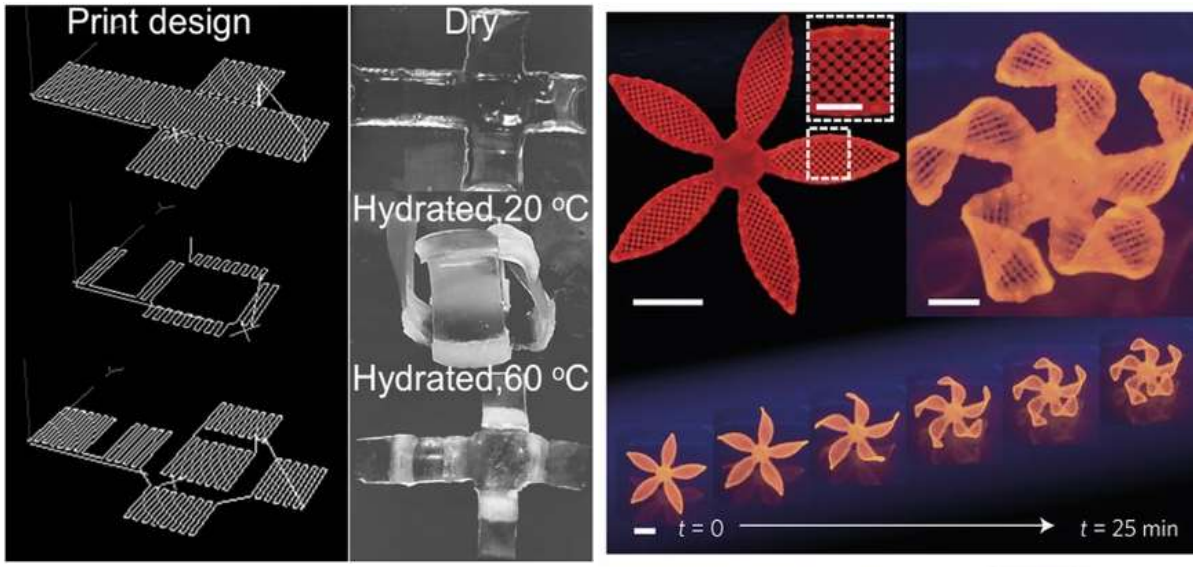

Figure 1.7. Examples of responsive, shape changing hydrogels so far created with 3D printing. Left, two different hydrogels are printed by the group of in het Panhuis. When hydrated the outer layers swell, causing the shape to bend up into a box, and when heated their contraction opens the shape again.[139] Right, the work of Gladman et al., Harvard. The print path of the head defines the alignment of cellulose fibres which resist expansion in one direction as the hydrogel swells. [18]

accompanied by a mathematical model that allows the construction of the print patterns required to create arbitrarily curved shapes.[18]

1.3 SELECTED HYDROGEL AND MANUFACTURING ROUTES

Following this review of the current environment, we can conclude that the manipulation of shape memory polymers is an established 4D printing technique at a research level, with materials, methods and predictive models.[8,9,93,94] These can be used for printing programmable shapes with both curved surfaces and sequential deployment, and the examples produced are resilient and robust. The potential of this route is, however, constrained by the nature of the proprietary nature and high cost of both the materials and the machines used, specifically the proprietary Polyjet™ technology and its polymer formulations.[11] Producing alternative approaches with a similar capacity would require a method for blending polymers with complementary properties using thermoplastic FFF, which is a challenging problem for a university lab operating at a low technological readiness level. Even without blending capabilities, the production of separate filaments with different properties presents a problem as the consistent diameter of the filament is key to achieving an optimal, repeatable outcome.

Complex 4D hydrogel printing has also been achieved using proprietary systems such as the BioPlotter[95] and custom installations at the Wyss institute.[18,19,92] This is a more accessible option, as numerous open-source projects for the processing of paste-like materials exist, aimed at processing of food, ceramics, and solder paste.[96–98] The high water percentage polymer blends which form hydrogel precursors are amenable to many of the techniques developed for dispensing other pastes and liquids, such as accessible syringe pumps are also directly translatable to this application. Further, fabrication of hydrogels is straightforward, requiring little specific equipment or complex syntheses. With a wide variety of properties to tailor, the mechanical properties of hydrogels may be readily adapted.

It is true that hydrogels depart from the traditional materials of engineering, and can be expected to be less robust and long-lasting. They do, however, offer novel advantages, as detailed by Quake and Scherer.[99] Soft elements are necessary for fluidic mechanical devices; they are efficient to manufacture at small scale; and they can be easily integrated with hard elements as required. In addition, soft devices have increased compatibility with human and animal users, the ability to operate in unpredictable, extreme environments, and greater adaptability.

While these characteristics make them suitable for certain specialist applications, such as synthetic extracellular matrices for tissue characterisation, contact lenses or soft robots, the author recognises that hydrogels are not going to find applications in consumer technology without both improvement in their toughness and resilience, and a dramatic change in the properties required of the materials of the built world. However, the understanding of what is possible is an essential first step towards defining what is pragmatically required in future materials, and any models or techniques developed to understand this laboratory test material would hopefully be transferrable into developing future work. Having said this, some prototype example devices have been made of hydrogels – such as a self-regulating microfluidic device[14] and a device for selective trapping of cells in a laboratory context[100] – and so there may be applications for this technology more immediately in niche areas.

1.3.1 PNIPAM-ALGINATE, A STRONG, THERMORESPONSIVE GEL

As mentioned above, the toughest known hydrogels are those comprised of interpenetrating networks, which have dramatically improved properties compare to single networks. The double network gel (DNG), first presented by Gong et al in 2003,[101] exhibits highly non-linear improvements in yield stress and mechanical

strength – for example, a poly (2-acrylamido-2-methylpropane sulfonic acid): poly acrylamide DNG yields at 17 MPa, while the components individually yield at 0.68MPa and 0.05MPa respectively. The origin of this phenomenon is complex, but benefits are thought to derive from the denser network providing dissipative effects which prevent cracks from growing.[102] Xin et al. consider that the properties of first gel formed are directly causative of the equilibrium swelling, modulus, strength and toughness of the composite gel, while demonstrating increases of up to 150 times in toughness in the final double system compared to the first lone network.[103]

Double network gels where the two components have crosslinks of a different nature – one physical and one chemical – have been shown to push the performance still further, adding repeatable, self-healing effects arising from the ionic crosslinks to the benefits of covalent linking.[104] An established responsive double-network hydrogel is poly-N-isopropyl acrylamide (PNIPAM)-alginate. This blends the well-characterised synthetic PNIPAM, a polymer which undergoes contraction at around 32°C, is non-toxic and easily processed,[58,105,106] with the tough, abundant biopolymer alginate, upon which much bioprinting work has focused.[88,107,108]

PNIPAM-alginate blends have already been used for responsive 3d printing applications, notably by researchers at the Woolongong.[21,92,109] The high molecular weight, inter-chain hydrogen bonding and tailorable degree of crosslinking from alginate confer the high viscosity and shear thinning properties which are desirable for extrusion 3d-printing.[109] Meanwhile, the PNIPAM network makes the resulting hydrogels thermoresponsive.[110]

More details are given in Chapter 4, but in summary, the process involves a polymer solution of the IPAM monomer, blended with alginate chains to increase the viscosity further, extruded through a print head. When in the desired shape, UV illumination polymerises and crosslinks the PNIPAM network. Further layers may be printed on top until the desired shape is attained. When finished, the gel shape is coherent but weak; it may then be removed from the printer and immersed in a bed of $CaCl_2$ so that the cations may penetrate the weak gel and finally crosslink the alginate network to its maximum strength, interlocking around the chemically bonded network to create a strong, flexible interpenetrating network gel.

However, the work above used a proprietary Bioplotter (~$200,000); given that the materials used are accessible and affordable, it would be desirable to render these achievements on an open-source platform as a first step to developing a responsive hydrogel printing system accessible to all.[111]

The combination of PNIPAM and alginate has already been studied as a responsive hydrogel. The materials have been used as a blend,[19] with the alginate not crosslinked,[112] as a grafted copolymer,[113,114] with crosslinking only in the PNIPAM and the sodium alginate acting as a filler[78], and with the PNIPAM and alginate both joined into a single, heterogenous network.[115,116]

1.3.2 OUTSTANDING QUESTIONS IN 3D PRINTING SHAPE-CHANGING PNIPAM-ALGINATE

Previously published work has demonstrated that combining alginate and PNIPAM as interpenetrated networks created strong, tough, thermoresponsive gels that were suitably robust to undergo mechanical testing.[19,110,114,117] However, few works have assessed this behaviour in the context of 3D printing, examining how shapes made from this material would deform, or how their behaviour is modified with the addition of a further composite element. These points are addressed in the present work.

Firstly: can PNIPAM-alginate be readily processed using a fully open-source printer, with both extrusion and curing? Secondly, for more complex print behaviour, one requires variation in the mechanical and thermoresponsive properties in different regions of the print. Could this be achieved by modifications to the PNIPAM-alginate hydrogels, either through processing or through the addition of varying percentages of a composite?

A difference in shape-changing properties requires two or more formulations which differ in equilibrium volume both below and above the transition temperature of PNIPAM, or in mechanical properties which lead to one deforming the other out of equilibrium.

The volume adopted is governed by the equilibrium configuration of the polymer-solvent network(s) – the relevant parameters governing this are covered in section 1.4 following. In practical terms, volume change often arises from a difference in average distance between crosslinks, polymer volume fraction, or chemical potential. Mechanical properties can be described in bulk by visco-elastic behaviour, covered in 1.5. The next sections review available models, relevant variables and testing methods.

1.4 HYDROGEL BEHAVIOUR AND THEORETICAL UNDERPINNINGS

1.4.1 A THEORETICAL HYDROGEL MODEL

Following the original work of Flory and Rehner on the swelling of a crosslinked polymer network, the Gibbs free energy of a gel can be expressed as the sum of the mixing and elastic contributions.[118] This considers the increase in entropy caused by mixing polymer and solvent – favouring swelling –, the decrease in entropy as the number of possible chain conformations of each polymer is reduced by stretching – opposing swelling –, and the enthalpic contribution from the interaction of polymers and solvent. Enthalpy changes are material dependent, may be positive or negative, and are parametrized by χ, the Flory solvent-polymer interaction term. This describes the difference in energy between polymer-polymer, polymer-solvent, and solvent-solvent interactions. This has been extended by Brannon and Peppas to include ionic contributions.[119]

For a double network gel composed of an ionic alginate network (1) and a covalent IPAM network (2), and using the independent network assumption from Zhang as a starting point[120] (limitations to this will be discussed later), the energy could therefore be expressed as the sum of the two gels independently, as given by Koetting:[121]

$$\Delta G_{tot} = \Delta G_{mix,1} + \Delta G_{mix,2} + \Delta G_{el,1} + \Delta G_{el,2} + \Delta G_{ionic,1}$$

Equation 1.1

The terms correspond to the total Gibbs free energy of the entire system, (ΔG_{tot}), the mixing energy of gel 1 ($\Delta G_{mix,1}$ - here the alginate), the mixing energy of gel 2 (($\Delta G_{mix,2}$ – here PNIPAM), the elastic energy of gel 1 ($\Delta G_{el,1}$), the mixing energy of gel 2 ($\Delta G_{el,2}$), and the ionic energy of gel 1, ($\Delta G_{ionic,1}$) assuming gel 2 to be uncharged (again, an assumption to be addressed later).

Applying Flory-Huggins theory to a three-component system (labelled in subscript respectively as: 0, solvent; 1, alginate; and 2, isopropyl acrylamide) the mixing term can be approximated as:

$$\left(\frac{\partial \Delta G}{\partial n_1}\right)_{T,P} = RT[\ln[1-(\phi_1+\phi_2)] + (\phi_1+\phi_2) + \bar{\chi}(\phi_1+\phi_2)^2]$$

Equation 1.2

Here R is the ideal gas constant, T is temperature, ϕ the volume fraction of the polymer, and χ is the interaction parameter. Here, the establishment of an individual interaction parameter is challenging and so it is replaced with an average χ value.

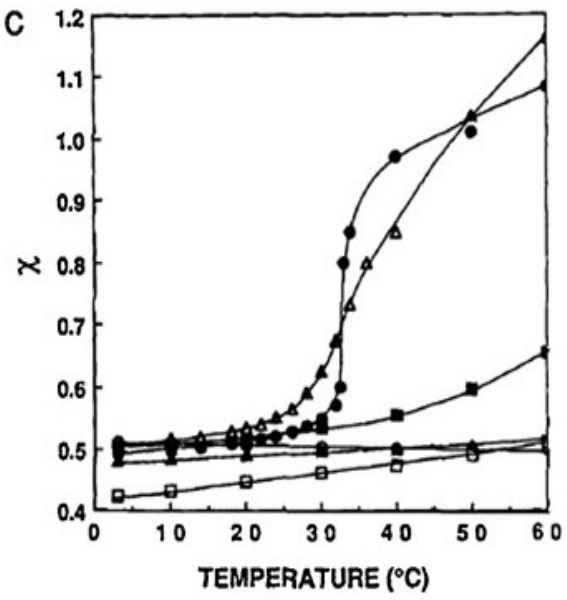

Figure 1.8. Dependence of the Flory interaction parameter, χ, on temperature, for a selection of acrylamides. Isopropyl acrylamide represented by filled circles and showing a clear transition at approximately 32°C. From Bae et al.[158]

While the Gibbs free energy must be evaluated under conditions of constant temperature, the value of the temperature strongly affects the value of χ for PNIPAM, as shown in Figure 1.8. Dependence of the Flory interaction parameter, χ, on temperature, for a selection of acrylamides. Isopropyl acrylamide represented by filled circles and showing a clear transition at approximately 32°C. From Bae et al.[158] For a shape changing application, one would therefore expect to evaluate the swelling behaviour twice: once below the LCST where χ is approximately 0.5, and once well above the transition, at approximately 1. A detailed calculation of χ for PNIPAM is a function of both polymer concentration and temperature, and has been achieved through experimental fitting by Afroze et al.[122]

Alginates do not fulfil the assumptions underlying the Flory model, most notably the assumption of a Gaussian polymer distribution, due to the nature of their rodlike junctions,[123] so it should be understood that this is an idealised model as a starting point. More detail on the deviation of alginates from this simple model is provided in Chapter 4.

The rubbery elasticity energy contribution can be expressed for network 1 as:

$$\Delta G_{el} = \frac{kTv_{e,2}}{2}(3{\alpha_1}^2 - 3 - \ln {\alpha_1}^3)$$

Equation 1.3

Where k is the Boltzmann constant, T temperature, v_e the effective number of chains in the network, and ${\alpha_1}^3$ equals the final volume of the whole IPN divided by the volume of the unswollen primary polymer network.

The entropic contribution to swelling for network 2 can be expressed as:

$$\Delta S_{el,2} = k v_e \left(\frac{1}{2} \ln \left(\frac{\alpha_2^3}{\alpha_2^{0^3}} \right) - \frac{3}{2} \left[\left(\frac{\alpha_2}{\alpha_2^0} \right)^2 - 1 \right] \right)$$

Equation 1.4

Here, k is the Boltzmann constant, v_e the effective number of chains of network 2 within the network structure. The α parameters denote the change in extension as the polymers of the second network swell to equilibrium. With the superscript 0, α_2^0 gives the linear deformation factor for the joint network – the state of the polymers when both networks have been formed but not allowed to swell to equilibrium volume. This can be found as the inverse cube root of the volume fraction of the second network at this time, φ_2, if known. If not directly measurable, this can be found as the cube root of the volume of both networks combined and not swollen (V^0), divided by the difference between this volume and the volume of the primary network alone, V_0 (thus, the contribution provided by the second), as shown in Equation 1.5.

$$\alpha_2^0 = \left(\frac{1}{{\varphi_2}^0} \right)^{\frac{1}{3}} = \left(\frac{V^0}{V^0 - V_0} \right)^{\frac{1}{3}}$$

Equation 1.5

The second alpha parameter analogously describes the extent of the polymers of the double network when swollen:

$$\alpha_2 = \left(\frac{1}{\varphi_2} \right)^{\frac{1}{3}} = \left(\frac{V}{V^0 - V_0} \right)^{\frac{1}{3}}$$

Terms are defined as in Equation 5, with the addition of V, the total final volume of the combined swollen IPN.

The final piece necessary to describe the behaviour is the ionic contribution, which has been expressed by Brannon-Peppas and Peppas[119] as:

$$(\Delta\mu_1^*)_{ion} - (\Delta\mu_1)_{ion} = \frac{\bar{V}_s RT}{4IM_r}\left(\frac{\varphi_1+\varphi_2}{\bar{v}}\right)^2\left(\frac{K_a}{10^{-pH}+K_a}\right)^2$$

Equation 1.6

This expresses the difference in chemical potentials between ions outside (indicated with an asterisk) and inside the gel. M_r is the molecular weight of the repeat units of the charged polymer, I the ionic strength of the solvent, V_s the molar volume of the solvent, $\bar{v}$ the specific volume of the charged polymer, and K_a the equilibrium constant of the anionic network, in this case alginate. $\Phi_{1,2}$ indicate the polymer volume fractions of both network 1 and 2.

By differentiating Equation 1.1, Equation 1.2 and Equation 1.3 with respect to the number of solvent molecules in the system, chemical potential may be related to the Gibbs free energy, yielding an overall expression for chemical potential difference in an IPN with contributions from all the relevant factors (where the elastic terms have been re-expressed as a function of the volume fractions and molecular weight between crosslinks):

$$\mu_1 - \mu_1^0 = RT[\ln[1-(\phi_1+\phi_2)] + (\phi_1+\phi_2) + \bar{\chi}(\phi_1+\phi_2)^2] + \left(\frac{\bar{v}_0}{\bar{v}_1 M_{c,1}}\right)\left(1-\frac{2M_{c,1}}{2M_{n,1}}\right)\left(v_1^{\frac{1}{3}}\frac{v_2}{2}\right)$$

$$+\frac{\overline{v_0}}{v_1 M_{C,2}}\left(v_2^{0^2 3} v_2^{1/3} - \frac{v_2}{2}\right) + \frac{VsRT}{4IM_r}\left(\frac{v_1+v_2}{\bar{v}}\right)^2\left(\frac{K_a}{10^{-pH}+K_a}\right)^2$$

Equation 1.7

Here, terms are as above, with the addition of $M_{c,1}$, the molecular weight between crosslinks of component 1, in this case alginate, $M_{n,2}$, the molecular mass of the alginate network, and $M_{c,2}$, the molecular weight between crosslinks of IPAM.

Since this difference is by definition zero in equilibrium, Equation 1.7 can theoretically be solved in order to describe the swelling behaviour of an IPN – or, more realistically, to derive more esoteric measurements such as the molecular weight between crosslinks from easily measured characteristics such as the final swelling volume.

1.4.2 DOUBLE-NETWORK COMPLEXITIES

However, these theories derive from the idealised environment of polymer physics, which assumes, among other things, a Gaussian distribution for polymers in the network and point-like tetrafunctional crosslinks, two assumptions which are definitively not the case for alginates, as shown by the size and functionality of the junction zones.[124]

Further complexities are introduced by the double network structure required for a resilient, thermoresponsive gel suitable for robust testing. The independent network assumption is of limited validity in many experimental conditions. It is certainly evident that some interplay between the networks occurs in double network hydrogels, as the magnitude of synergistic improvement in resilience is far greater than expected from non-interacting physically interpenetrated networks.[125] The mechanism of this phenomenon is not well understood, but is thought to depend sensitively on the relative crosslinking densities of each network as well as the initial structure of the first network. [102,103]

In this case some electrostatic interaction could be expected. One network, alginate, is anionic; the second network, poly-n-isopropyl acrylamide, while theoretically neutral, can be expected to carry a small net charge due to its preparation method. Physical entanglement and the forming of unintended covalent bonds through the interaction of byproducts may also play a role in forming connections between the networks.

Recently, more complex models have been developed which aim to capture the synergistic behaviour of double network gels, including facets such as the rate-dependence of stress-strain behaviour during loading and rate independence during unloading. Mao et al. match their experimental work on large deformations of an alginate/polyacrylamide double network gel with a viscoelastic mathematical description which successfully captures these complex aspects.[126] While this work seems promising, it is not clear what this would imply for a thermoresponsive system.

Lu et al. also develop a phenomenologically double network stress-strain relationship which reproduces the strain-softening behaviour and hysteresis typified by such gels.[127] However, due to the phenomenological nature of the work, the variables used are not directly related to any physical observables in the gel. This limits the ability of these equations to be combined with other observations and link microscale gel phenomena with macroscale properties.

Due to the recent nature of these work, the hydrogel community has yet to reach a consensus on which models are appropriate for use, and research is still ongoing.

Having said all this, and recognising the immense complexity represented by this system, it should at least be possible to compare results to the theoretical predications of Equation 1.7 or identify general trends suitable for treatment with a phenomenological model. For example, the simple correlation of E, the Young's Modulus, with increasing crosslink density to an experimentally determined power has yielded reasonable results when predicting the deformation of 3d printed hydrogels previously.[92] [128] In practical terms, changes in the polymer volume fraction, the average molecular mass between crosslinks, the Flory interaction parameter as a function of temperature, or the chemical potential are all likely to affect the behaviour. Methods of investigating these parameters are given in section 1.6, while prior work on modifying volume and mechanical properties of hydrogels is described in the next section.

1.5 MECHANICAL BEHAVIOUR

Anisotropic response across a hydrogel object can be achieved by varying chemistry or physical properties. Many examples exist where hydrogels have been used as a bilayer, either in combination with a material that does not substantially change volume, or with a material which still exhibits a relative difference. A subtler option is to grade the different materials, blending them together – this has the advantage of avoiding a discontinuity which could initialise cracks. Finally, the most subtle option, and that often employed by nature, is to introduce anisotropic distribution of material properties with localised directional constriction or restraint, as in the cellulose of the pine cone,[129,130] or localised volume expansion in certain areas.

1.5.1 MODULATING RESPONSE ACROSS THE MATERIAL

The simplest case to generate a bending response is to join two materials with differing responses to the same stimulus. This motif is seen in the classic bimetallic strip,[131] the pinecone,[129] and from the very beginning of work in hydrogel actuators.[132] Lithographically patterning a bilayer structure introduces a second dimension to bilayer fabrication, as shown by Bassik et al.[133] Only those areas exposed to polymerizing UV remain attached to the bottom layer, thus creating a surface with some bilayer bending regions and some flat monolayers. This is used to create an all-hydrogel version of a Venus flytrap. In another example of two dimensional patterning, Andres

et al. localise inkjet deposition of carbon nanotube composites within a polymer, creating folding regions with reduced hygroscopic swelling which act as hinges.[134]

More complicated curvature from a two-material system was demonstrated by Wu in 2013,[135] where hydrogels with thin, directed stripes of alternating chemical composition which varied in degree of expansion were used to create complex deforming surfaces. The relatively small lateral modulation involved is directly reminiscent of plant motion, where, as in nature, small effects add up to create an overall larger movement.

These changes in composition can be achieved in many ways, but an appealing approach is the addition of nanoparticles in specific regions or with varying orientations. Due to the high surface to volume ratio of nanoparticles, a small amount of composite can be expected to have a large effect, creating material cost savings, and many working examples of shape-changing nanocomposites may be seen in nature.[130] Plant behaviour has been synthetically mimicked by the orientation of high aspect ratio particles in a magnetic field[136] and the shear alignment of cellulose by print direction.[18] However, surprisingly, 3d printing has not been used, to the author's knowledge, to localise regions of nanoparticles. This would seem to be a simple and appealing

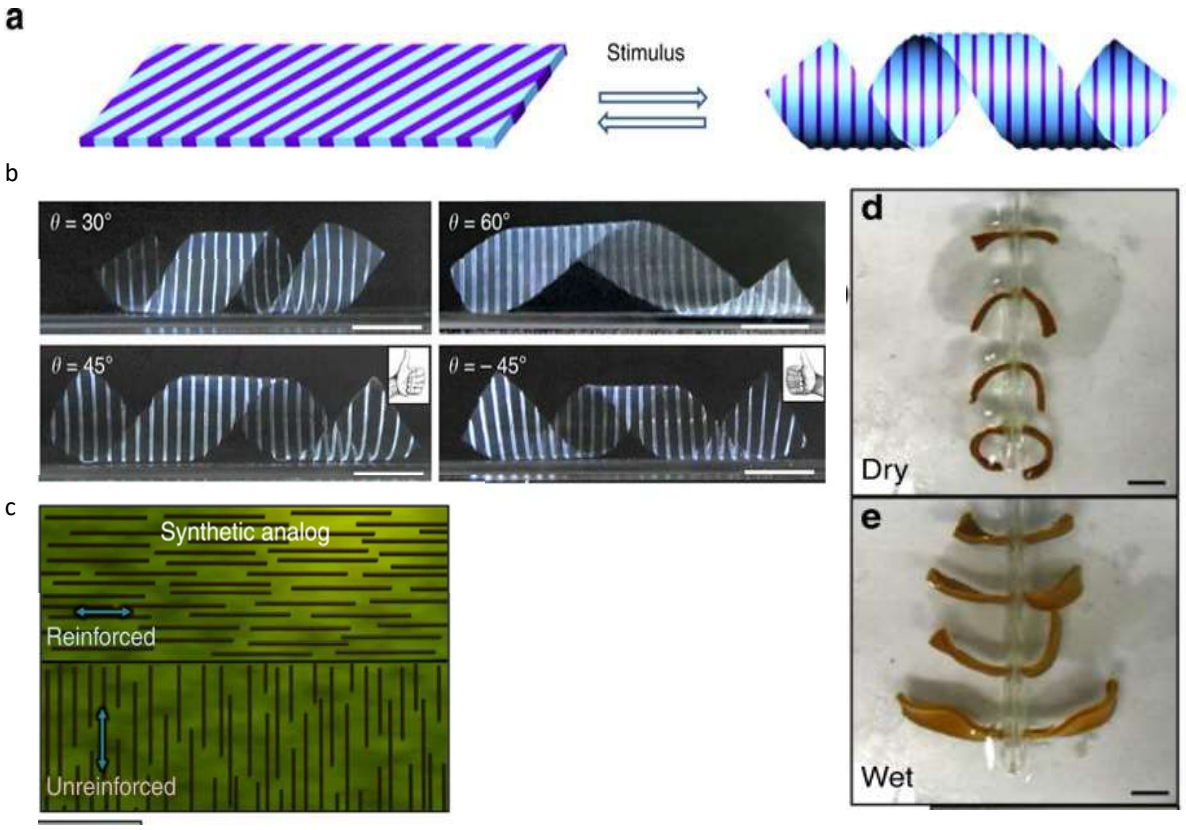

Figure 1.9. Examples of prior work combining just two different material properties to create responsive curvature upon hydration. A) a sketch of the combination of stripes of different hydrogels used by Wu et al. Due to their different swelling ratios, the flat sheet becomes helical. B) Experimental images showing angle and chirality can be controlled. C), the concept used by Erb et al. of magnetic orientation of microplatelets. When placed within a gelatin matrix, swelling becomes directional (d and e).

route for achieving shape change, allowing the flexibility of 3d printing to create myriad shape-changing designs and the efficiency of nanoparticles to use minimal material to do so.

Therefore, blending PNIPAM-alginate with small amounts of gold nanoparticles was selected as an approach. These particles are inert, non-toxic, may be triggered remotely by laser light, and have shown good performance in other shape changing composites based on PNIPAM.[137,138]

An alternative route, following a similar principle, would be to modify the processing conditions within certain regions of the print, creating, for example, a higher density of crosslinks within a certain region. This would be analogous to the lithographic patterning used elsewhere, but able to operate in 3D as part of one continuous process, creating gradients in X, Y and Z.

We see that just two different material configurations are sufficient to achieve multiple different shapes and responsive behaviour as desired. However, they should be characterised before combining them into more complex prints, and require a model to understand how material properties and shaping translate into form.

1.5.2 A ONE-DIMENSIONAL BENDING MODEL

We begin with the simplest relevant model, derived by Timoshenko, which treats the system as a one-dimensional beam. While of course the behaviour of the polymers and solvent within thermoresponsive gel is complex, with contributions at the molecular scale from entropic considerations, ionic interactions and elastic behaviour of the network,[118,121] simplified assumptions arising from scaling laws have previously been successfully applied,[139] and should at least provide a starting point.

To programme the transition to a desired 3D shape, the actuation deformation of the materials involved must be related to the final shape parameters. The radius of curvature for a bilayer system with differing rates of expansion was found by Timoshenko to be governed by the equation:[131]

$$\kappa = \frac{1}{R} = \frac{6\Delta\lambda(1+m)^2}{h\left[3(1+m)^2 + (1+mn)\left(m^2 + \frac{1}{mn}\right)\right]}$$

Equation 1.8

where R is the radius of curvature, α_1 and α_2 are the linear expansion ratios of each layer when separate, $\Delta\lambda = \alpha_1 - \alpha_2$, the difference between their expansion ratios, a_1 and a_2 are the heights of the first and second layers respectively, h is the total height (ie., $h = a_1 + a_2$), m is the ratio of a_1 and a_2, and n is the ratio of the Young's moduli of the layers 1 and 2, E_1/E_2.

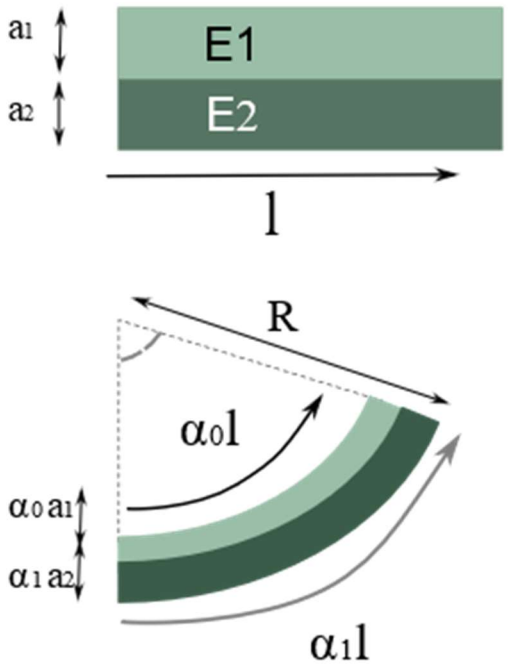

Figure 1.10. Top: initial configuration of bilayer composed of two gels with different youngs moduli and coefficients of thermal contraction. Bottom, the curved configuration adopted upon heating this bilayer.

As thermoresponsive gels undergo their transition above the Lowest Critical Solution Temperature (LCST), they contract from an initial volume v_i to a final volume v_f, here notated $v_{f(1,2)}$ to indicate that these volumes are not necessarily the same for each layer. In this simple model, we assume the contraction to be isotropic, so defining $\alpha_{(1,2)}$ as the linear expansion factor and maintaining the subscript notation:

$$\left(\frac{v_i}{v_f}\right)^{1/3} = \frac{\alpha_1}{\alpha_2} = \Delta\lambda$$

Equation 1.9

Thus the swelling ratio and change in volume for a two-material hydrogel bilayer can be related to the bend it will form. This equation holds under linear elastic deformations only, and relies on certain assumptions about ideal hydrogels. However, a full treatment of this complex phenomenon is beyond the scope of this primarily experimental work.

Existing material models include the work of Cai and Suo, describing the phase transition of PNIPAM gels, and the recent work on double networks mentioned in section 1.4.2. These would require significant modification to be applied to PNIPAM-alginate.[140]

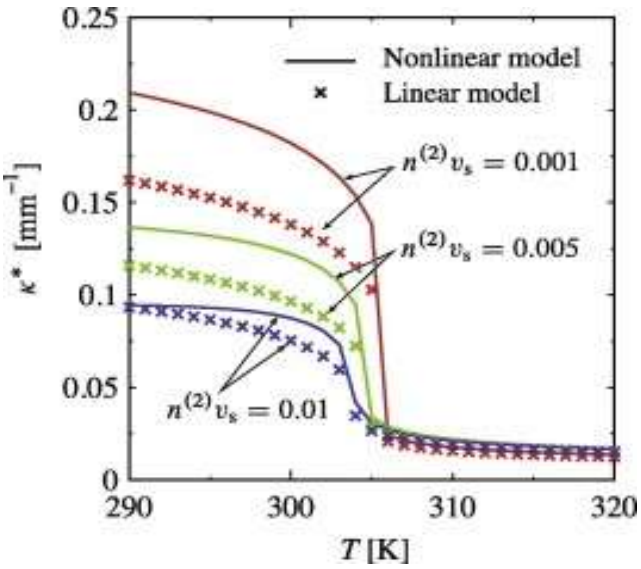

Figure 1.11 How the curvature predicted by a linear (Timoshenko) model differs fromtheir non-linear model for different crosslink densities. Differences are most significant for low crosslinker densities.

Bilayer hydrogels have been treated by Lucatonio et al, who developed a treatment which split each the bilayer system into a contribution from swelling as if the beam were free, and an elastic contribution arising from constraint.[141] Morimoto and Ashida consider a bilayer composed of gel on an incompressible elastomer, using an approach which separates swelling and bending components. The first is treated with a virtual one-dimensional homogenous swelling, and then, imposing the condition of balanced forces on the homogenous bending component, the final configuration is found. Results compared with a standard Timoshenko model show a significant difference. (Figure 1.11)

1.5.3 TESTING REQUIREMENTS AND MODALITIES

For the simplest model of deformation, the bimetallic strip of Timoshenko, we can see we require the swelling ratios for various gel compositions (i.e. the ratio of their volumes before and after transition) and their Young's moduli in the final state. This simple requirement defines much of the relevant testing techniques that will be used within this thesis.

Hydrogels are challenging to test by mechanical means due to their high deformability, low yield stresses, and low friction. Their high water content also introduces difficulties due to the change in properties as the piece dehydrates, potentially affecting the measurements.[142]

As yet, no body of standards for hydrogel testing exists that is comparable to the large body of work on testing, for example, rubbers. The approach taken in this thesis is therefore to start from standards for testing soft materials, such as synthetic tissues, where they exist; to benchmark against well-cited papers in the field; and finally to adapt according to the availability of equipment locally. It should be noted that since hydrogels are the subject of investigation by mechanical engineering, bioengineering, chemical engineering, soft matter

chemistry, biology and polymer physics communities, and this is far from an exhaustive list, one often sees discipline-specific assessment methods; these will be noted as they become relevant.

1.6 HYDROGEL ANALYSIS TECHNIQUES

1.6.1 SWELLING RATIO

For measurements comparing the volume of the dry gel to that of it swollen in equilibrium, as required by Equation 1.7, simple drying and weighing is sufficient. While Flory-Rehner analysis suggests that the Young's modulus of a gel should scale with the segment concentration of the polymer, or the number of monomers per unit volume,[128] and therefore be directly correlated to the swelling ratio, this result rests on a number of simplifying assumptions which are not necessarily expected to hold true in this experimental situation. These include the requirement for a simple network structure, with no dangling ends or loops, the requirement that the polymer chains within the gel exhibit a Gaussian distribution, and the requirement that the affine assumption holds true.[77,143] For this reason, Young's modulus should also be measured via additional methods.

1.6.2 ELASTICITY: RESPONSE TO DEFORMATION

The response to deformation of a hydrogel is obviously crucial to the performance of a printed hydrogel object. Less obvious is that if hydrogels are to be used as artificial extracellular matrixes, for example in bioprinting or drug delivery, the stiffness of the gel influences the life cycle of cells and the differentiation of pluripotent cells.[144,145] Thus, characterising the resistance of the material to bending is important not only for this application, but for future work that may incorporate it within the life sciences.

The elastic modulus (E) relates the stress (σ) – the force per unit area - to the strain (ε) – displacement relative to original length - within the elastic limit for an isotropical material subject to uniaxial stress.

Simple models of elasticity are only appropriate in the small-strain region, where the relationships are linear - ie. where the material returns to its original shape when the force applied is removed and energy is conserved. In this regime the measure relating the stress and the strain is referred to as the Young's modulus. The elastic

modulus is one of three moduli which describe the elastic properties of a material in response to different deformations, shown below.

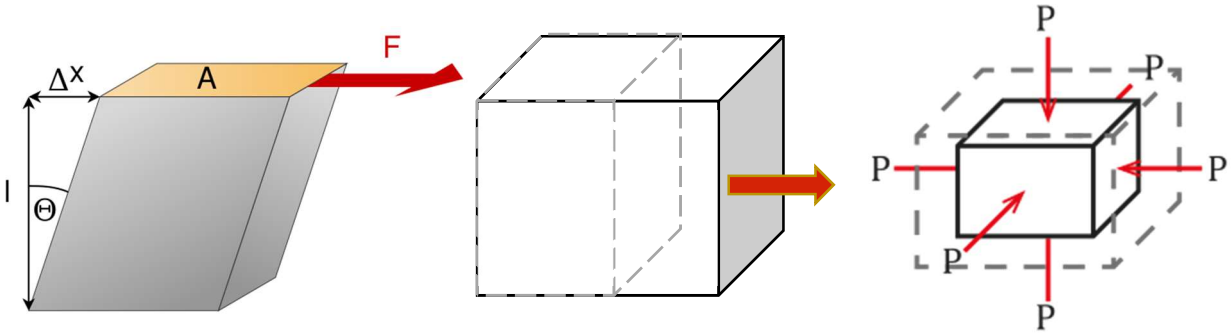

Figure 1.12. Sketches of the deformation modes of a cube of material. Left, shear modulus, characterised by G, centre, Young's modulus, E, and right, bulk modulus deformation, K.

In reality, few materials exhibit true linear deformation. Biological materials in particular typically exhibit a J-shaped stress-strain curve, where at higher strains more force is required for a given extension.[146] This is advantageous in an evolutionary context, limiting damage.[147] A fuller description of this behaviour requires a tensor treatment – relating the stress or strain for each face of a volumetric element.[148] This will be described in more detail when considering the behaviour of specific prints in Chapter 4.

Evaluating the elastic response introduces some difficulties when working with hydrogels due to their high extensibility and fragile nature; most testing protocols currently available were developed for materials thousands, if not millions, of times stiffer. However, as the field of hydrogels material science has developed, a selection of methods have evolved, with significant crossover with the testing of biological materials. Some commonly used methods for characterising the materials include nanoindentation,[149] Atomic Force Microscopy (AFM), tensile testing and compression testing, which all have strengths and weaknesses.

1.6.2.1 NANOINDENTATION AND AFM PROBES

Nanoindentation involves approaching a small (μm-radius) probe towards the sample and measuring the load and displacement it experiences. From this the mechanical properties of the system may be determined. AFM may be used in many different modes, but the simplest uses a nano-scale probe to take the same measurements at a much smaller lengthscale. These methods provide good resolution and information on the microscale variations of the surface, but require an appropriate model to derive macroscopic mechanical properties from the result. For new materials without established models or calibration standards this can present a challenge, and for samples where the bulk behaviour is the object of study it is hard to quantify how many samples should be taken to achieve a measurement representative of the whole. The values found are also sensitive to surface roughness and particularly adhesion, which can cause errors.[150]

1.6.2.2 TENSILE TESTING

Tensile testing requires mounting a bar of the material to be tested between two sets of jaws, which are moved apart at a steady rate while the load on them is measured. From this force-displacement data information about sample behaviour is derived. Yield stress and strain, the Young's modulus, and the shape of the stress-strain curve for fitting are some parameters commonly extracted.

For delicate materials such as hydrogels, however, it can be difficult to manufacturing a sample capable of enduring testing, and mounting the typically slippery, soft items. As hydrogels are highly extensible they will often show strong 'necking' phenomena, decreasing in area dramatically before yielding. This require measurement of the changing area in addition to the separation and load of clamps. Possibly the most challenging aspect of tensile testing of hydrogels is the suggestion that to prevent drying effects, they should be tested while immersed in water: this is difficult to combine with existing systems without the use of costly additional components which were not obtainable for this project.

1.6.2.3 COMPRESSION TESTING

Uniaxial compression testing is a macroscopic case of nanoindentation, whereby a sample is contained between two parallel plates as these are approached together at a set rate, compressing the material and recording load and displacement. This may be continued until the point of yield, or oscillated to elucidate the process of

material recovery through defining hysteresis curves. Again, load and displacement are measured, and characteristic variables extracted, such as the Young's modulus in the linear region of the graph, and the compressive strength – found as the ratio between the maximum load at failure and the original cross-sectional area.

If unconfined, the materials will expand in cross-sectional area, yielding the Poisson's ratio, ν. This is the ratio of transverse contraction strain to longitudinal extension strain in the direction of stretching force, and therefore defines how a sample changes volume in response to stress. Together with E, K and G (see Figure 1.12),the Poisson's ratio satisfies a set of equations from which, if any three are known, the fourth variable can be established.

For many hydrogels stress-strain behaviour is rate dependent, as the time taken for dynamic rearrangement of the molecules is of the same order as typical compression rates (~1mm/s to 60mm/s). Compression testing has been used to test many hydrogels and will be used within this thesis to determine the elastic response regime, the Young's modulus for use in the Timoshenko model, and hysteresis behaviour.[151–153]

1.6.2.4 VISCOELASTICITY: RESPONSE TO SHEAR AND TIME-DEPENDENT BEHAVIOUR

The Timoshenko model additionally requires the beams it describes to show purely elastic behaviours. Hydrogels are complex materials which can exhibit a large spectrum of viscoelastic behaviour, as a function of frequency, ageing, magnitude of stress and strain, and history.[77,142] It is therefore required that the viscoelastic behaviour of the gels are assessed to determine in what situations, and within what limits, the elastic response dominates. Such experiments on gels typically use rheometry or dynamic mechanical analysis (DMA), with rheometry being used for more 'liquid-like' viscoelastic samples and DMA for more 'solid-like' polymer blends. Resilient gels such as PNIPAM-Alginate are amenable to both treatments; in this thesis, rheology is used as it is suitable for assessing both the crosslinked (post-printing) and uncrosslinked (before printing) materials. Crosslinked materials are evaluated in terms of their shear elasticity, to find their response to perpendicular strains. Uncrosslinked materials are evaluated for their yield shear and viscosity which inform their suitability and requirements for extrusion printing.[33]

1.6.2.5 RHEOLOGY

Rheology is the study of the behaviour of materials which exhibit viscoelastic behaviour - that is, solids that are not perfectly elastic and non-Newtonian fluids - as they respond to applied force. A rheometer consists of a finely-controlled arm which can be oscillated at a range of rates and strains. This is vertically approached towards the sample, and rotated about the direction of approach, shearing the sample. Similar to the previously mentioned mechanical testing, load and displacement are monitored as the sample experiences various oscillation amplitudes and frequencies and the amount of energy returned and dissipated is used to infer the relationship between viscous and elastic behaviours within the sample. The principles and use of rheology within this work are described further in Chapter 2, Materials and methods.

1.6.2.6 POROELASTIC CONSIDERATIONS

An additional complexity is introduced since the gel is a two-phase system consisting of 'solid' (at timescales shorter than the viscous relaxation time) polymers, enclosing pores filled with liquid. An external force will change the pressure within the pores, stretching the walls and thus contributing to the strain within the system. Consideration of the interplay between pressure and strain in a mixed material requires the theory of poroelasticity. However, as demonstrated by Wang et al., since viscoelastic stress relaxation is independent of sample size and poroelastic effects require time for diffusion (dependent on the diffusivity and the sample size), one can choose a sample size for which viscoelasticity dominates.[154]

Helpfully, the simulation considered in the paper referenced above is directly applicable to this case. Taking an alginate diffusivity of approximately 6×10^{-9},[155] we can see that with a sample size much greater than 100μm viscoelastic effects dominate until a time period of 10^{10} s, and I intend my experiments to be shorter than that. This also indicates that nano-indentation measurements and AFM measurements would explore the poroelastic regime, directing attention towards macroscopic compression measurements as a more appropriate way to access the relevant properties.

1.6.2.7 THERMORESPONSE: RESPONSE TO TEMPERATURE

Information about the rate of contraction would also be desirable, for the possibility of sequential activation as shown in Figure 1.6. Differential Scanning Calorimetry (DSC), measures the change in temperature as a sample

is heating and can be used to infer phase changes. For PNIPAM, the thermal switching behaviour can be seen as an endothermic peak on heating and an exothermic peak on cooling, as the amide groups fold inwards and form bonds with each other, or unfold and achieve a lower energy state, respectively. DSC has been used successfully to characterise the response rate and transition temperature of PNIPAM-NP composites and will be used in this thesis.[156,157]

1.7 CONCLUSION

In this chapter, the applications for 3D-printed responsive materials and the availability and potential of existing printing systems were reviewed. It was noted that printing of responsive materials with shape memory polymers is well established, but limited by high material and equipment cost. Hydrogels and open source 3D printers were offered as an alternative, accessible route. Double network hydrogels were identified as working materials for their exceptional toughness, tailorability and high levels of deformation, and a focus on extrusion-printed PNIPAM-alginate hydrogels was justified based on their low toxicity, affordability, abundance, and proven performance.

Methods for modifying hydrogels spatially within a print was considered, and some areas requiring further research were identified. One key point was that much published work uses custom or proprietary printing systems, limiting reproducibility: there is a gap for an open-source, well-documented enabling technology. This had first to be built and then to be used to print an established 3D printable material, PNIPAM-alginate. Secondly, noting the success of combining nanoparticles with PNIPAM, there is a natural extension in testing the performance of nanoparticles in a 3D-printable PNIPAM composite, namely PNIPAM-alginate.

In order to interpret the results of hydrogel shape change, the relevant theory was reviewed and its limitations with regard to double network systems noted. A simple model for one-dimensional deformation, the Timoshenko bilayer, was introduced. From this, methods of determining the relevant material properties required to apply the Timoshenko model were discussed, and compression testing, rheology, and thermoresponse analysis focused on as the most relevant in this situation. The next chapter will detail the building of an appropriate open-source extrusion-based 3D printer, in keeping with the stated focus on accessibility and reproducibility. Subsequent chapters will detail the properties of PNIPAM-alginate bulk samples and printed samples, and PNIPAM-alginate with the addition of gold nanorods.

1.8 REFERENCES

(1) Open Bionics. Hero Arm - an affordable, advanced and intuitive bionic arm https://openbionics.com/hero-arm/ (accessed Sep 4, 2018).

(2) Zuniga, J. M.; Carson, A. M.; Peck, J. M.; Kalina, T.; Srivastava, R. M.; Peck, K. The Development of a Low-Cost Three-Dimensional Printed Shoulder, Arm, and Hand Prostheses for Children. *Prosthet. Orthot. Int.* **2017**, *41* (2), 205–209. https://doi.org/10.1177/0309364616640947.

(3) Wong, J. Y.; Pfahnl, A. C. 3D Printing of Surgical Instruments for Long-Duration Space Missions. *Aviat. Space. Environ. Med.* **2014**, *85* (7), 758–763. https://doi.org/10.3357/ASEM.3898.2014.

(4) Prater, T. J.; Werkheiser, N. J. *Summary Report on Phase I and Phase II Results From the 3D Printing in Zero-G Technology Demonstration Mission, Volume II*; 2018.

(5) Oliver, K.; Seddon, A.; Trask, R. S. Morphing in Nature and beyond: A Review of Natural and Synthetic Shape-Changing Materials and Mechanisms. *J. Mater. Sci.* **2016**, *51* (24), 10663–10689. https://doi.org/10.1007/s10853-016-0295-8.

(6) Tibbits, S. Skylar Tibbits: The Emergence of "4D Printing" | TED Talk. TED 2013, p NA.

(7) Tibbits, S. 4D PRINTING. *Archit. Des.* **2014**, *84* (1), 116–121. https://doi.org/https://doi.org/10.1002/ad.1710.

(8) Ge, Q.; Sakhaei, A. H.; Lee, H.; Dunn, C. K.; Fang, N. X.; Dunn, M. L.; Bartlett, N. W.; Ge, Q.; Dunn, C. K.; Qi, H. J.; et al. Multimaterial 4D Printing with Tailorable Shape Memory Polymers. *Sci. Rep.* **2016**, *6*, 31110. https://doi.org/10.1038/srep31110.

(9) Mao, Y.; Yu, K.; Isakov, M. S.; Wu, J.; Dunn, M. L.; Jerry Qi, H. Sequential Self-Folding Structures by 3D Printed Digital Shape Memory Polymers. *Sci. Rep.* **2015**, *5* (1), 13616. https://doi.org/10.1038/srep13616.

(10) Stratasys Ltd. Apparatus and Method for Three Dimensional Model Printing. US6259962, March 1, 1999.

(11) Stratasys Ltd. PolyJet Technology | Stratasys http://www.stratasys.com/3d-

printers/technologies/polyjet-technology (accessed Dec 23, 2015).

(12) Klouda, L. Thermoresponsive Hydrogels in Biomedical Applications A Seven-Year Update. *European Journal of Pharmaceutics and Biopharmaceutics*. 2015. https://doi.org/10.1016/j.ejpb.2015.05.017.

(13) Malda, J.; Visser, J.; Melchels, F. P.; Jüngst, T.; Hennink, W. E.; Dhert, W. J. A.; Groll, J.; Hutmacher, D. W. 25th Anniversary Article: Engineering Hydrogels for Biofabrication. *Adv. Mater.* **2013**, *25* (36), 5011–5028. https://doi.org/10.1002/adma.201302042.

(14) Eddington, D. T.; Liu, R. H.; Moore, J. S.; Beebe, D. J. An Organic Self-Regulating Microfluidic System. *Lab Chip* **2001**, *1* (2), 96–99. https://doi.org/10.1039/b108078d.

(15) Kim, S.; Laschi, C.; Trimmer, B. Soft Robotics: A Bioinspired Evolution in Robotics. *Trends Biotechnol.* **2013**, *31* (5), 287–294. https://doi.org/10.1016/j.tibtech.2013.03.002.

(16) Rus, D.; Tolley, M. T. Design, Fabrication and Control of Soft Robots. *Nature* **2015**, *521* (7553), 467–475. https://doi.org/10.1038/nature14543.

(17) Satarkar, N. S.; Biswal, D.; Hilt, J. Z. Hydrogel Nanocomposites: A Review of Applications as Remote Controlled Biomaterials. *Soft Matter* **2010**, *6* (11), 2364. https://doi.org/10.1039/b925218p.

(18) Sydney Gladman, A.; Matsumoto, E. A.; Nuzzo, R. G.; Mahadevan, L.; Lewis, J. A. Biomimetic 4D Printing. *Nat. Mater.* **2016**, *15* (4), 413–418. https://doi.org/10.1038/nmat4544.

(19) Bakarich, S. E.; Gorkin, R.; Naficy, S.; Gately, R.; in het Panhuis, M.; Spinks, G. M. 3D/4D Printing Hydrogel Composites: A Pathway to Functional Devices. *MRS Adv.* **2015**, 1–6. https://doi.org/10.1557/adv.2015.9.

(20) Pearce, J. M. The Future of Open-Source Hardware and Science. In *Open-Source Lab*; 2014; pp 255–263. https://doi.org/10.1016/B978-0-12-410462-4.00007-X.

(21) Bakarich, S. E.; Gorkin, R.; in het Panhuis, M.; Spinks, G. M. 4D Printing with Mechanically Robust, Thermally Actuating Hydrogels. *Macromol. Rapid Commun.* **2015**, *36* (12), 1211–1217. https://doi.org/10.1002/marc.201500079.

(22) Oliver, K.; Seddon, A.; Trask, R. S. Morphing in Nature and beyond: A Review of Natural and Synthetic

Shape-Changing Materials and Mechanisms. *J. Mater. Sci.* **2016**, *51* (24). https://doi.org/10.1007/s10853-016-0295-8.

(23) Wong, K. V.; Hernandez, A. A Review of Additive Manufacturing. *ISRN Mech. Eng.* **2012**, *2012*, 1–10. https://doi.org/10.5402/2012/208760.

(24) Sherman, L. M. Additive Manufacturing: Materials for 'Real-World' Parts : *Plastics Technology*. 2014.

(25) Raney, J. R.; Lewis, J. A. Printing Mesoscale Architectures. *MRS Bull.* **2015**, *40* (11), 943–950. https://doi.org/10.1557/mrs.2015.235.

(26) Gross, B. C.; Erkal, J. L.; Lockwood, S. Y.; Chen, C.; Spence, D. M. Evaluation of 3D Printing and Its Potential Impact on Biotechnology and the Chemical Sciences. *Anal. Chem.* **2014**, *86* (7), 3240–3253. https://doi.org/10.1021/ac403397r.

(27) Scopigno, R.; Cignoni, P.; Pietroni, N.; Callieri, M.; Dellepiane, M. Digital Fabrication Techniques for Cultural Heritage: A Survey. *Comput. Graph. Forum* **2017**, *36* (1), 6–21. https://doi.org/10.1111/cgf.12781.

(28) Bakarich, S. E.; in het Panhuis, M.; Beirne, S.; Wallace, G. G.; Spinks, G. M. Extrusion Printing of Ionic–covalent Entanglement Hydrogels with High Toughness. *J. Mater. Chem. B* **2013**, *1* (38), 4939. https://doi.org/10.1039/c3tb21159b.

(29) Lam, C. X. .; Mo, X. .; Teoh, S. .; Hutmacher, D. . Scaffold Development Using 3D Printing with a Starch-Based Polymer. *Mater. Sci. Eng. C* **2002**, *20* (1–2), 49–56. https://doi.org/10.1016/S0928-4931(02)00012-7.

(30) Compton, B. G.; Lewis, J. A. 3D-Printing of Lightweight Cellular Composites. *Adv. Mater.* **2014**, *26* (34), 6043–6043. https://doi.org/10.1002/adma.201470235.

(31) Gratson, G. M.; Xu, M.; Lewis, J. A. Microperiodic Structures: Direct Writing of Three-Dimensional Webs. *Nature* **2004**, *428* (6981), 386. https://doi.org/10.1038/428386a.

(32) Avery, M. P.; Klein, S.; Richardson, R.; Bartlett, P.; Adams, G.; Dickin, F.; Simske, S. The Rheology of Dense

Colloidal Pastes Used in 3D-Printing. **2014**.

(33) Kirchmajer, D. M.; Gorkin III, R.; in het Panhuis, M. An Overview of the Suitability of Hydrogel-Forming Polymers for Extrusion-Based 3D-Printing. *J. Mater. Chem. B* **2015**, *3* (20), 4105–4117. https://doi.org/10.1039/C5TB00393H.

(34) Li, Q.; Lewis, J. A. Nanoparticle Inks for Directed Assembly of Three-Dimensional Periodic Structures. *Adv. Mater.* **2003**, *15* (19), 1639–1643. https://doi.org/10.1002/adma.200305413.

(35) Ober, T. J.; Foresti, D.; Lewis, J. A. Active Mixing of Complex Fluids at the Microscale. *Proc. Natl. Acad. Sci. U. S. A.* **2015**, *112* (40), 12293–12298. https://doi.org/10.1073/pnas.1509224112.

(36) Lewis, J. A.; Gratson, G. M. Direct Writing in Three Dimensions. *Mater. Today* **2004**, *7* (7–8), 32–39. https://doi.org/10.1016/S1369-7021(04)00344-X.

(37) Zhu, W.; Li, J.; Leong, Y. J.; Rozen, I.; Qu, X.; Dong, R.; Wu, Z.; Gao, W.; Chung, P. H.; Wang, J.; et al. 3D-Printed Artificial Microfish. *Adv. Mater.* **2015**, *27* (30), 4411–4417. https://doi.org/10.1002/adma.201501372.

(38) Maruo, S.; Ikuta, K. Submicron Stereolithography for the Production of Freely Movable Mechanisms by Using Single-Photon Polymerization. *Sensors Actuators A Phys.* **2002**, *100* (1), 70–76. https://doi.org/10.1016/S0924-4247(02)00043-2.

(39) Melchels, F. P. W.; Feijen, J.; Grijpma, D. W. A Review on Stereolithography and Its Applications in Biomedical Engineering. *Biomaterials* **2010**, *31* (24), 6121–6130. https://doi.org/10.1016/j.biomaterials.2010.04.050.

(40) Varghese, G.; Moral, M.; Castro-García, M.; López-López, J. J.; Marín-Rueda, J. R.; Yagüe-Alcaraz, V.; Hernández-Afonso, L.; Ruiz-Morales, J. C.; Canales-Vázquez, J. Fabrication and Characterisation of Ceramics via Low-Cost DLP 3D Printing. *Boletín la Soc. Española Cerámica y Vidr.* **2018**, *57* (1), 9–18. https://doi.org/10.1016/J.BSECV.2017.09.004.

(41) Patel, D. K.; Sakhaei, A. H.; Layani, M.; Zhang, B.; Ge, Q.; Magdassi, S. Highly Stretchable and UV Curable Elastomers for Digital Light Processing Based 3D Printing. *Adv. Mater.* **2017**, *29* (15), 1606000.

https://doi.org/10.1002/adma.201606000.

(42) Xiong, Z.; Zheng, M.-L.; Dong, X.-Z.; Chen, W.-Q.; Jin, F.; Zhao, Z.-S.; Duan, X.-M. Asymmetric Microstructure of Hydrogel: Two-Photon Microfabrication and Stimuli-Responsive Behavior. *Soft Matter* **2011**, *7* (21), 10353. https://doi.org/10.1039/c1sm06137b.

(43) Xiong, Z.; Dong, X.-Z.; Chen, W.-Q.; Duan, X.-M. Fast Solvent-Driven Micropump Fabricated by Two-Photon Microfabrication. *Appl. Phys. A* **2008**, *93* (2), 447–452. https://doi.org/10.1007/s00339-008-4735-4.

(44) Llewellyn-Jones, T. M.; Drinkwater, B. W.; Trask, R. S. 3D Printed Components with Ultrasonically Arranged Microscale Structure. *Smart Mater. Struct.* **2016**, *25* (2), 02LT01. https://doi.org/10.1088/0964-1726/25/2/02LT01.

(45) Llewellyn-Jones, T.; Allen, R.; Trask, R. Curved Layer Fused Filament Fabrication Using Automated Toolpath Generation. *3D Print. Addit. Manuf.* **2016**, *3* (4), 236–243. https://doi.org/10.1089/3dp.2016.0033.

(46) Tumbleston, J. R.; Shirvanyants, D.; Ermoshkin, N.; Janusziewicz, R.; Johnson, A. R.; Kelly, D.; Chen, K.; Pinschmidt, R.; Rolland, J. P.; Ermoshkin, A.; et al. Continuous Liquid Interface Production of 3D Objects. *Science (80-.).* **2015**, *347* (6228), 1349–1352. https://doi.org/10.1126/science.aaa2397.

(47) Scopigno, R.; Cignoni, P.; Pietroni, N.; Callieri, M.; Dellepiane, M. Digital Fabrication Techniques for Cultural Heritage: A Survey. *Comput. Graph. Forum* **2017**, *36* (1), 6–21. https://doi.org/10.1111/cgf.12781.

(48) Meng, H.; Li, G. A Review of Stimuli-Responsive Shape Memory Polymer Composites. *Polymer (Guildf).* **2013**, *54* (9), 2199–2221. https://doi.org/10.1016/j.polymer.2013.02.023.

(49) Zhao, Q.; Qi, H. J.; Xie, T. Recent Progress in Shape Memory Polymer: New Behavior, Enabling Materials, and Mechanistic Understanding. *Prog. Polym. Sci.* **2015**, *49–50*, 79–120. https://doi.org/10.1016/j.progpolymsci.2015.04.001.

(50) Leng, J.; Lan, X.; Liu, Y.; Du, S. Shape-Memory Polymers and Their Composites: Stimulus Methods and

Applications. *Prog. Mater. Sci.* **2011**, *56* (7), 1077–1135. https://doi.org/10.1016/j.pmatsci.2011.03.001.

(51) Choong, Y. Y. C.; Maleksaeedi, S.; Eng, H.; Wei, J.; Su, P.-C. 4D Printing of High Performance Shape Memory Polymer Using Stereolithography. *Mater. Des.* **2017**, *126*, 219–225. https://doi.org/10.1016/J.MATDES.2017.04.049.

(52) Zarek, M.; Layani, M.; Cooperstein, I.; Sachyani, E.; Cohn, D.; Magdassi, S. 3D Printing of Shape Memory Polymers for Flexible Electronic Devices. *Adv. Mater.* **2015**, n/a-n/a. https://doi.org/10.1002/adma.201503132.

(53) Zhang, Q.; Yan, D.; Zhang, K.; Hu, G. Pattern Transformation of Heat-Shrinkable Polymer by Three-Dimensional (3D) Printing Technique. *Sci. Rep.* **2015**, *5*, 8936. https://doi.org/10.1038/srep08936.

(54) Zarek, M.; Layani, M.; Cooperstein, I.; Sachyani, E.; Cohn, D.; Magdassi, S. 3D Printing of Shape Memory Polymers for Flexible Electronic Devices. *Adv. Mater.* **2016**, *28* (22), 4449–4454. https://doi.org/10.1002/adma.201503132.

(55) Ge, Q.; Qi, H. J.; Dunn, M. L. Active Materials by Four-Dimension Printing. *Appl. Phys. Lett.* **2013**, *103* (13), 131901. https://doi.org/10.1063/1.4819837.

(56) Finch, C. A. Hydrophilic Polymers. In *Speciality Polymers*; Dyson, R. W., Ed.; Blackie Academic and Professional, 1998; p 78.

(57) Zwieniecki, M. A.; Melcher, P. J.; Michele Holbrook, N. M. Hydrogel Control of Xylem Hydraulic Resistance in Plants. *Science* **2001**, *291* (5506), 1059–1062. https://doi.org/10.1126/science.1057175.

(58) Guan, Y.; Zhang, Y. PNIPAM Microgels for Biomedical Applications: From Dispersed Particles to 3D Assemblies. *Soft Matter* **2011**, *7* (14), 6375. https://doi.org/10.1039/c0sm01541e.

(59) Guvendiren, M.; Lu, H. D.; Burdick, J. A. Shear-Thinning Hydrogels for Biomedical Applications. *Soft Matter* **2012**, *8* (2), 260–272. https://doi.org/10.1039/C1SM06513K.

(60) Deligkaris, K.; Tadele, T. S.; Olthuis, W.; van den Berg, A. Hydrogel-Based Devices for Biomedical Applications. *Sensors Actuators B Chem.* **2010**, *147* (2), 765–774.

https://doi.org/10.1016/j.snb.2010.03.083.

(61) Cvetkovic, C.; Raman, R.; Chan, V.; Williams, B. J.; Tolish, M.; Bajaj, P.; Sakar, M. S.; Asada, H. H.; Saif, M. T. A.; Bashir, R. Three-Dimensionally Printed Biological Machines Powered by Skeletal Muscle. *Proc. Natl. Acad. Sci. U. S. A.* **2014**, *111* (28), 10125–10130. https://doi.org/10.1073/pnas.1401577111.

(62) McEvoy, M. A.; Correll, N. Materials That Couple Sensing, Actuation, Computation, and Communication. *Science (80-.).* **2015**, *347* (6228), 1261689–1261689. https://doi.org/10.1126/science.1261689.

(63) Sareh, S.; Rossiter, J.; Conn, A.; Drescher, K.; Goldstein, R. E. Swimming like Algae: Biomimetic Soft Artificial Cilia. *J. R. Soc. Interface* **2012**, *10* (78), 20120666-. https://doi.org/10.1098/rsif.2012.0666.

(64) Martin, B. D.; Linhardt, R. J.; Dordick, J. S. Highly Swelling Hydrogels from Ordered Galactose-Based Polyacrylates. *Biomaterials* **1998**, *19* (1–3), 69–76. https://doi.org/10.1016/S0142-9612(97)00184-1.

(65) King, P. J. S.; Saiani, A.; Bichenkova, E. V.; Miller, A. F. A de Novo Self-Assembling Peptide Hydrogel Biosensor with Covalently Immobilised DNA-Recognising Motifs. *Chem. Commun.* **2016**, *52* (40), 6697–6700. https://doi.org/10.1039/C6CC01433J.

(66) Xiang, Y.; Chen, D. Preparation of a Novel PH-Responsive Silver Nanoparticle/Poly(HEMA–PEGMA–MAA) Composite Hydrogel. *Eur. Polym. J.* **2007**, *43* (10), 4178–4187. https://doi.org/10.1016/j.eurpolymj.2007.08.005.

(67) Lee, E.; Kim, D.; Kim, H.; Yoon, J. Photothermally Driven Fast Responding Photo-Actuators Fabricated with Comb-Type Hydrogels and Magnetite Nanoparticles. *Sci. Rep.* **2015**, *5*, 15124. https://doi.org/10.1038/srep15124.

(68) Dicker, M. P. M.; Rossiter, J. M.; Bond, I. P.; Weaver, P. M. Biomimetic Photo-Actuation: Sensing, Control and Actuation in Sun-Tracking Plants. *Bioinspir. Biomim.* **2014**, *9* (3), 036015. https://doi.org/10.1088/1748-3182/9/3/036015.

(69) Hu, Y.; Lu, C.-H.; Guo, W.; Aleman-Garcia, M. A.; Ren, J.; Willner, I. A Shape Memory Acrylamide/DNA Hydrogel Exhibiting Switchable Dual PH-Responsiveness. *Adv. Funct. Mater.* **2015**, *25* (44), 6867–6874. https://doi.org/10.1002/adfm.201503134.

(70) Ionov, L. Biomimetic Hydrogel-Based Actuating Systems. *Adv. Funct. Mater.* **2013**, *23* (36), 4555–4570. https://doi.org/10.1002/adfm.201203692.

(71) Tokarev, I.; Minko, S. Stimuli-Responsive Hydrogel Thin Films. *Soft Matter* **2009**, *5* (3), 511–524. https://doi.org/10.1039/B813827C.

(72) Hennink, W. E.; van Nostrum, C. F. Novel Crosslinking Methods to Design Hydrogels. *Adv. Drug Deliv. Rev.* **2012**, *64*, 223–236. https://doi.org/10.1016/j.addr.2012.09.009.

(73) Ionov, L. Hydrogel-Based Actuators: Possibilities and Limitations. *Mater. Today* **2014**, *17* (10), 494–503. https://doi.org/10.1016/j.mattod.2014.07.002.

(74) Sato Matsuo, E.; Tanaka, T. Kinetics of Discontinuous Volume–phase Transition of Gels. *J. Chem. Phys.* **1988**, *89* (3), 1695. https://doi.org/10.1063/1.455115.

(75) Shapiro, J. M.; Oyen, M. L. Hydrogel Composite Materials for Tissue Engineering Scaffolds. *JOM* **2013**, *65* (4), 505–516. https://doi.org/10.1007/s11837-013-0575-6.

(76) Beebe, D.; Moore, J.; Bauer, J.; Yu, Q.; Liu, R.; Devadoss, C.; Jo, B. Functional Hydrogel Structures for Autonomous Flow Control inside Microfluidic Channels. *Nature* **2000**, *404* (6778), 588–590. https://doi.org/10.1038/35007047.

(77) Peppas, N. A.; Huang, Y.; Torres-Lugo, M.; Ward, J. H.; Zhang, J. Physicochemical Foundations and Structural Design of Hydrogels in Medicine and Biology. *Annu. Rev. Biomed. Eng.* **2000**, *2* (1), 9–29. https://doi.org/10.1146/annurev.bioeng.2.1.9.

(78) Zhang, G.-Q.; Zha, L.-S.; Zhou, M.-H.; Ma, J.-H.; Liang, B.-R. Rapid Deswelling of Sodium Alginate/Poly(N-Isopropylacrylamide) Semi-Interpenetrating Polymer Network Hydrogels in Response to Temperature and PH Changes. *Colloid Polym. Sci.* **2005**, *283* (4), 431–438. https://doi.org/10.1007/s00396-004-1172-6.

(79) Calvert, P. Hydrogels for Soft Machines. *Adv. Mater.* **2009**, *21* (7), 743–756. https://doi.org/10.1002/adma.200800534.

(80) Agrawal, A.; Rahbar, N.; Calvert, P. D. Strong Fiber-Reinforced Hydrogel. *Acta Biomater.* **2013**, *9* (2), 5313–5318. https://doi.org/10.1016/j.actbio.2012.10.011.

(81) Meng, Y.; Ye, L.; Coates, P.; Twigg, P. In Situ Cross-Linking of Poly(Vinyl Alcohol)/Graphene Oxide–Polyethylene Glycol Nanocomposite Hydrogels as Artificial Cartilage Replacement: Intercalation Structure, Unconfined Compressive Behavior, and Biotribological Behaviors. *J. Phys. Chem. C* **2018**, *122* (5), 3157–3167. https://doi.org/10.1021/acs.jpcc.7b12465.

(82) Schexnailder, P.; Schmidt, G. Nanocomposite Polymer Hydrogels. *Colloid Polym. Sci.* **2008**, *287* (1), 1–11. https://doi.org/10.1007/s00396-008-1949-0.

(83) Hebeish, A.; Farag, S.; Sharaf, S.; Shaheen, T. I. Thermal Responsive Hydrogels Based on Semi Interpenetrating Network of Poly(NIPAm) and Cellulose Nanowhiskers. *Carbohydr. Polym.* **2014**, *102* (1), 159–166. https://doi.org/10.1016/j.carbpol.2013.10.054.

(84) Mohr, R.; Kratz, K.; Weigel, T.; Lucka-Gabor, M.; Moneke, M.; Lendlein, A. Initiation of Shape-Memory Effect by Inductive Heating of Magnetic Nanoparticles in Thermoplastic Polymers. *Proc. Natl. Acad. Sci. U. S. A.* **2006**, *103* (10), 3540–3545. https://doi.org/10.1073/pnas.0600079103.

(85) Xia, L.-W.; Xie, R.; Ju, X.-J.; Wang, W.; Chen, Q.; Chu, L.-Y. Nano-Structured Smart Hydrogels with Rapid Response and High Elasticity. *Nat. Commun.* **2013**, *4*, 2226. https://doi.org/10.1038/ncomms3226.

(86) IUPAC. Interpenetrating Polymer Network. In *IUPAC Compendium of Chemical Terminology*; IUPAC: Research Triangle Park, NC. https://doi.org/10.1351/goldbook.I03117.

(87) Gong, J. P. Why Are Double Network Hydrogels so Tough? *Soft Matter* **2010**, *6* (12), 2583. https://doi.org/10.1039/b924290b.

(88) Drury, J. L.; Mooney, D. J. Hydrogels for Tissue Engineering: Scaffold Design Variables and Applications. *Biomaterials* **2003**, *24* (24), 4337–4351. https://doi.org/10.1016/S0142-9612(03)00340-5.

(89) Pereira, R. F.; Bártolo, P. J. 3D Bioprinting of Photocrosslinkable Hydrogel Constructs. *J. Appl. Polym. Sci.* **2015**, *132* (48), n/a-n/a. https://doi.org/10.1002/app.42458.

(90) Chinga-Carrasco, G. Potential and Limitations of Nanocelluloses as Components in Biocomposite Inks for Three-Dimensional Bioprinting and for Biomedical Devices. *Biomacromolecules* **2018**, *19* (3), 701–711. https://doi.org/10.1021/acs.biomac.8b00053.

(91) Raphael, B.; Khalil, T.; Workman, V. L.; Smith, A.; Brown, C. P.; Streuli, C.; Saiani, A.; Domingos, M. 3D Cell Bioprinting of Self-Assembling Peptide-Based Hydrogels. *Mater. Lett.* **2017**, *190*, 103–106. https://doi.org/10.1016/J.MATLET.2016.12.127.

(92) Naficy, S.; Gately, R.; Gorkin, R.; Xin, H.; Spinks, G. M. 4D Printing of Reversible Shape Morphing Hydrogel Structures. *Macromol. Mater. Eng.* **2017**, *302* (1), 1600212. https://doi.org/10.1002/mame.201600212.

(93) Raviv, D.; Zhao, W.; McKnelly, C.; Papadopoulou, A.; Kadambi, A.; Shi, B.; Hirsch, S.; Dikovsky, D.; Zyracki, M.; Olguin, C.; et al. Active Printed Materials for Complex Self-Evolving Deformations. *Sci. Rep.* **2014**, *4*, 7422. https://doi.org/10.1038/srep07422.

(94) Yu, K.; Ritchie, A.; Mao, Y.; Dunn, M. L.; Qi, H. J. Controlled Sequential Shape Changing Components by 3D Printing of Shape Memory Polymer Multimaterials. *Procedia IUTAM* **2015**, *12*, 193–203. https://doi.org/10.1016/j.piutam.2014.12.021.

(95) Envisiontec. 3D-Bioplotter® Developer Series | EnvisionTEC https://envisiontec.com/3d-printers/3d-bioplotter/developer-series/ (accessed Jul 18, 2018).

(96) Horne, R. Reprap development and further adventures in DIY 3D printing: Universal Paste extruder - Ceramic, Food and Real Chocolate 3D Printing... https://richrap.blogspot.com/2012/04/universal-paste-extruder-ceramic-food.html (accessed Jul 18, 2018).

(97) Unfold. Ceramic 3d printing http://unfold.be/pages/ceramic-3d-printing (accessed Jul 18, 2018).

(98) Benchoff, B. Dispensing Solder Paste With A 3D Printer | Hackaday https://hackaday.com/2014/04/02/dispensing-solder-paste-with-a-3d-printer/ (accessed Jul 18, 2018).

(99) Quake, S. R. From Micro- to Nanofabrication with Soft Materials. *Science (80-.).* **2000**, *290* (5496), 1536–1540. https://doi.org/10.1126/science.290.5496.1536.

(100) Kaehr, B.; Shear, J. B. Multiphoton Fabrication of Chemically Responsive Protein Hydrogels for Microactuation. *Proc. Natl. Acad. Sci. U. S. A.* **2008**, *105* (26), 8850–8854. https://doi.org/10.1073/pnas.0709571105.

(101) Gong, J. P.; Katsuyama, Y.; Kurokawa, T.; Osada, Y. Double-Network Hydrogels with Extremely High Mechanical Strength. *Adv. Mater.* **2003**, *15* (14), 1155–1158. https://doi.org/10.1002/adma.200304907.

(102) Tanaka, Y.; Kuwabara, R.; Na, Y. H.; Kurokawa, T.; Gong, J. P.; Osada, Y.; Yoshimi Tanaka, †; Rikimaru Kuwabara, ‡; Yang-Ho Na, ‡; Takayuki Kurokawa, ‡; et al. Determination of Fracture Energy of High Strength Double Network Hydrogels. *J. Phys. Chem. B* **2005**. https://doi.org/10.1021/jp0500790.

(103) Xin, H.; Saricilar, S. Z.; Brown, H. R.; Whitten, P. G.; Spinks, G. M. Effect of First Network Topology on the Toughness of Double Network Hydrogels. *Macromolecules* **2013**, *46* (16), 6613–6620. https://doi.org/10.1021/ma400892g.

(104) Sun, J.-Y.; Zhao, X.; Illeperuma, W. R. K.; Chaudhuri, O.; Oh, K. H.; Mooney, D. J.; Vlassak, J. J.; Suo, Z. Highly Stretchable and Tough Hydrogels. *Nature* **2012**, *489* (7414), 133–136. https://doi.org/10.1038/nature11409.

(105) Schild, H. G. Poly(N-Isopropylacrylamide): Experiment, Theory and Application. *Prog. Polym. Sci.* **1992**, *17* (2), 163–249. https://doi.org/10.1016/0079-6700(92)90023-R.

(106) Haq, M. A.; Su, Y.; Wang, D. Mechanical Properties of PNIPAM Based Hydrogels: A Review. *Mater. Sci. Eng. C* **2017**, *70*, 842–855. https://doi.org/10.1016/j.msec.2016.09.081.

(107) Darnell, M. C.; Sun, J.-Y.; Mehta, M.; Johnson, C.; Arany, P. R.; Suo, Z.; Mooney, D. J. Performance and Biocompatibility of Extremely Tough Alginate/Polyacrylamide Hydrogels. *Biomaterials* **2013**, *34* (33), 8042–8048. https://doi.org/10.1016/j.biomaterials.2013.06.061.

(108) Bjørnøy, S. H.; Mandaric, S.; Bassett, D. C.; Åslund, A. K. O.; Ucar, S.; Andreassen, J. P.; Strand, B. L.; Sikorski, P. Gelling Kinetics and in Situ Mineralization of Alginate Hydrogels: A Correlative Spatiotemporal Characterization Toolbox. *Acta Biomater.* **2016**, *44*, 243–253. https://doi.org/10.1016/j.actbio.2016.07.046.

(109) Panhuis, M. in het; Bakarich, S.; Beirne, S. T.; Wallace, G. G.; Spinks, G. M. Extrusion Printing of Ionic-Covalent Entanglement Hydrogels with High Toughness.

(110) de Moura, M. R.; Guilherme, M. R.; Campese, G. M.; Radovanovic, E.; Rubira, A. F.; Muniz, E. C. Porous Alginate-Ca2+ Hydrogels Interpenetrated with PNIPAAm Networks: Interrelationship between Compressive Stress and Pore Morphology. *Eur. Polym. J.* **2005**, *41* (12), 2845–2852. https://doi.org/10.1016/j.eurpolymj.2005.06.007.

(111) Ozbolat, I. T.; Moncal, K. K.; Gudapati, H. Evaluation of Bioprinter Technologies. *Addit. Manuf.* **2017**, *13*, 179–200. https://doi.org/10.1016/J.ADDMA.2016.10.003.

(112) Zheng, W. J.; An, N.; Yang, J. H.; Zhou, J.; Chen, Y. M. Tough Al-Alginate/Poly(N -Isopropylacrylamide) Hydrogel with Tunable LCST for Soft Robotics. *ACS Appl. Mater. Interfaces* **2015**, *7* (3), 1758–1764. https://doi.org/10.1021/am507339r.

(113) Soledad Lencina, M. M.; Iatridi, Z.; Villar, M. A.; Tsitsilianis, C. Thermoresponsive Hydrogels from Alginate-Based Graft Copolymers. *Eur. Polym. J.* **2014**, *61*, 33–44. https://doi.org/10.1016/j.eurpolymj.2014.09.011.

(114) Vasile, C.; Nita, L. E. Novel Multi-Stimuli Responsive Sodium Alginate-Grafted-Poly(N-Isopropylacrylamide) Copolymers: II. Dilute Solution Properties. *Carbohydr. Polym.* **2011**, *86* (1), 77–84. https://doi.org/10.1016/j.carbpol.2011.04.012.

(115) Dumitriu, R. P.; Mitchell, G. R.; Vasile, C. Multi-Responsive Hydrogels Based on N-Isopropylacrylamide and Sodium Alginate. *Polym. Int.* **2011**, *60* (2), 222–233. https://doi.org/10.1002/pi.2929.

(116) Dong, L.; Agarwal, A. K.; Beebe, D. J.; Jiang, H. Adaptive Liquid Microlenses Activated by Stimuli-Responsive Hydrogels. *Nature* **2006**, *442* (7102), 551–554. https://doi.org/10.1038/nature05024.

(117) Zadražil, A.; Štěpánek, F. Investigation of Thermo-Responsive Optical Properties of a Composite Hydrogel. *Colloids Surfaces A Physicochem. Eng. Asp.* **2010**, *372* (1–3), 115–119. https://doi.org/10.1016/j.colsurfa.2010.09.039.

(118) Flory, P. J.; Rehner, J. Statistical Mechanics of Cross-Linked Polymer Networks II. Swelling. *J. Chem. Phys.*

1943, *11* (11), 521–526. https://doi.org/10.1063/1.1723792.

(119) Brannon-Peppas, L.; Peppas, N. A. Equilibrium Swelling Behavior of PH-Sensitive Hydrogels. *Chem. Eng. Sci.* **1991**, *46* (3), 715–722. https://doi.org/10.1016/0009-2509(91)80177-Z.

(120) Zhang, J. Structure and Morphology of Poly(Methacrylic Acid) Poly(N -Isopropyl Acrylamide) Interpenetrating Polymeric Networks with PH and Temperature Sensitivity, 2000.

(121) Koetting, M. C.; Peters, J. T.; Steichen, S. D.; Peppas, N. A. Stimulus-Responsive Hydrogels: Theory, Modern Advances, and Applications. *Mater. Sci. Eng. R Reports* **2015**, *93*, 1–49. https://doi.org/10.1016/j.mser.2015.04.001.

(122) Afroze, F.; Nies, E.; Berghmans, H. Phase Transitions in the System Poly(N-Isopropylacrylamide)/Water and Swelling Behaviour of the Corresponding Networks. *J. Mol. Struct.* **2000**, *554* (1), 55–68. https://doi.org/10.1016/S0022-2860(00)00559-7.

(123) Chan, A. W.; Neufeld, R. J. Modeling the Controllable PH-Responsive Swelling and Pore Size of Networked Alginate Based Biomaterials. *Biomaterials* **2009**, *30* (30), 6119–6129. https://doi.org/10.1016/J.BIOMATERIALS.2009.07.034.

(124) Yapeng Fang, *,†; Saphwan Al-Assaf, †; Glyn O. Phillips, †,‡; Katsuyoshi Nishinari, †,§; Takahiro Funami, ‖; Peter A. Williams, ⊥ and; Li#, L. Multiple Steps and Critical Behaviors of the Binding of Calcium to Alginate. **2007**. https://doi.org/10.1021/JP0689870.

(125) Nakajima, T.; Furukawa, H.; Tanaka, Y.; Kurokawa, T.; Osada, Y.; Gong, J. P. True Chemical Structure of Double Network Hydrogels. *Macromolecules* **2009**, *42* (6), 2184–2189. https://doi.org/10.1021/ma802148p.

(126) Mao, Y.; Lin, S.; Zhao, X.; Anand, L. A Large Deformation Viscoelastic Model for Double-Network Hydrogels. *J. Mech. Phys. Solids* **2017**, *100*, 103–130. https://doi.org/10.1016/J.JMPS.2016.12.011.

(127) Lu, H.; Wang, X.; Shi, X.; Yu, K.; Fu, Y. Q. A Phenomenological Model for Dynamic Response of Double-Network Hydrogel Composite Undergoing Transient Transition. *Compos. Part B Eng.* **2018**, *151*, 148–153. https://doi.org/10.1016/J.COMPOSITESB.2018.06.011.

(128) de Gennes, P.-G. *Scaling Concepts in Polymer Physics*, 1st ed.; Cornell University Press: London, 1979.

(129) Reyssat, E.; Mahadevan, L. Hygromorphs: From Pine Cones to Biomimetic Bilayers. *J. R. Soc. Interface* **2009**, *6* (39), 951–957. https://doi.org/10.1098/rsif.2009.0184.

(130) Studart, A. R.; Erb, R. M. Bioinspired Materials That Self-Shape through Programmed Microstructures. *Soft Matter* **2014**, *10* (9), 1284–1294. https://doi.org/10.1039/c3sm51883c.

(131) Timoshenko, S. Analysis of Bi-Metal Thermostats. *J. Opt. Soc. Am.* **1925**, *11* (3), 233–255. https://doi.org/10.1364/JOSA.11.000233.

(132) Hu, Z.; Zhang, X.; Li, Y. Synthesis and Application of Modulated Polymer Gels. *Science* **1995**, *269* (5223), 525–527. https://doi.org/10.1126/science.269.5223.525.

(133) Bassik, N.; Abebe, B. T.; Laflin, K. E.; Gracias, D. H. Photolithographically Patterned Smart Hydrogel Based Bilayer Actuators. *Polymer (Guildf).* **2010**, *51*, 6093–6098. https://doi.org/10.1016/j.polymer.2010.10.035.

(134) Andres, C. M.; Zhu, J.; Shyu, T.; Flynn, C.; Kotov, N. A. Shape-Morphing Nanocomposite Origami. *Langmuir* **2014**, *30* (19), 5378–5385. https://doi.org/10.1021/la404955s.

(135) Wu, Z. L.; Moshe, M.; Greener, J.; Therien-Aubin, H.; Nie, Z.; Sharon, E.; Kumacheva, E. Three-Dimensional Shape Transformations of Hydrogel Sheets Induced by Small-Scale Modulation of Internal Stresses. *Nat. Commun.* **2013**, *4*, 1586. https://doi.org/10.1038/ncomms2549.

(136) Erb, R. M.; Sander, J. S.; Grisch, R.; Studart, A. R. Self-Shaping Composites with Programmable Bioinspired Microstructures. *Nat. Commun.* **2013**, *4*, 1712. https://doi.org/10.1038/ncomms2666.

(137) Hribar, K. C.; Metter, R. B.; Ifkovits, J. L.; Troxler, T.; Burdick, J. A. Light-Induced Temperature Transitions in Biodegradable Polymer and Nanorod Composites. *Small* **2009**, *5* (16), 1830–1834. https://doi.org/10.1002/smll.200900395.

(138) Hühn, D.; Govorov, A.; Gil, P. R.; Parak, W. J. Photostimulated Au Nanoheaters in Polymer and Biological Media: Characterization of Mechanical Destruction and Boiling. *Adv. Funct. Mater.* **2012**, *22* (2), 294–

303. https://doi.org/10.1002/adfm.201101134.

(139) Naficy, S.; Gately, R.; Gorkin, R.; Xin, H.; Spinks, G. M. 4D Printing of Reversible Shape Morphing Hydrogel Structures. *Macromol. Mater. Eng.* **2017**, *302* (1), 1600212. https://doi.org/10.1002/mame.201600212.

(140) Cai, S.; Suo, Z. Mechanics and Chemical Thermodynamics of Phase Transition in Temperature-Sensitive Hydrogels. **2011**. https://doi.org/10.1016/j.jmps.2011.08.008.

(141) Lucantonio, A.; Nardinocchi, P.; Pezzulla, M. Swelling-Induced and Controlled Curving in Layered Gel Beams. *Proc. R. Soc. A Math. Phys. Eng. Sci.* **2014**. https://doi.org/10.1098/rspa.2014.0467.

(142) Anseth, K. S.; Bowman, C. N.; Brannon-Peppas, L. Mechanical Properties of Hydrogels and Their Experimental Determination. *Biomaterials* **1996**, *17* (17), 1647–1657. https://doi.org/10.1016/0142-9612(96)87644-7.

(143) Oyen, M. L. Mechanical Characterisation of Hydrogel Materials. *Int. Mater. Rev.* **2014**, *59* (1), 44–59. https://doi.org/10.1179/1743280413Y.0000000022.

(144) Vogel, V.; Sheetz, M. Local Force and Geometry Sensing Regulate Cell Functions. *Nat. Rev. Mol. Cell Biol.* **2006**, *7* (4), 265–275. https://doi.org/10.1038/nrm1890.

(145) Even-Ram, S.; Artym, V.; Yamada, K. M. Matrix Control of Stem Cell Fate. *Cell*. 2006. https://doi.org/10.1016/j.cell.2006.08.008.

(146) Storm, C.; Pastore, J. J.; MacKintosh, F. C.; Lubensky, T. C.; Janmey, P. A. Nonlinear Elasticity in Biological Gels. *Nature* **2005**, *435* (7039), 191–194. https://doi.org/10.1038/nature03521.

(147) Vogel, S. A Matter of Materials. In *Comparative Biomechanics: Life's Physical World*; Princeton University Press: Princeton and Oxford, 2003; p 316.

(148) Young, R. J.; Lovell, P. A. *Introduction to Polymers*; 1992.

(149) Ebenstein, D. M.; Pruitt, L. A. Nanoindentation of Biological Materials. *Nano Today* **2006**, *1* (3), 26–33. https://doi.org/10.1016/S1748-0132(06)70077-9.

(150) Kaufman, J. D.; Klapperich, C. M. Surface Detection Errors Cause Overestimation of the Modulus in

Nanoindentation on Soft Materials. *J. Mech. Behav. Biomed. Mater.* **2009**, *2* (4), 312–317. https://doi.org/10.1016/J.JMBBM.2008.08.004.

(151) Zhao, X.; Huebsch, N.; Mooney, D. J.; Suo, Z. Stress-Relaxation Behavior in Gels with Ionic and Covalent Crosslinks. *J. Appl. Phys.* **2010**, *107* (6), 63509. https://doi.org/10.1063/1.3343265.

(152) Mancini, M.; Moresi, M.; Rancini, R. Mechanical Properties of Alginate Gels: Empirical Characterisation. *J. Food Eng.* **1999**, *39* (4), 369–378. https://doi.org/10.1016/S0260-8774(99)00022-9.

(153) Baker, A. B.; Wass, D. F.; Trask, R. S. Thermally Induced Reversible and Reprogrammable Actuation of Tough Hydrogels Utilising Ionoprinting and Iron Coordination Chemistry. *Sensors Actuators B Chem.* **2018**, *254*, 519–525. https://doi.org/10.1016/j.snb.2017.07.095.

(154) Zhao, Q.-M. W.; Mohan, A. C.; Oyen, M.; Zhao, X. Separating Viscoelasticity and Poroelasticity of Gels with Different Length and Time Scales. *Acta Mech. Sin.* **2014**, *30* (1), 20–27.

(155) Cai, S.; Hu, Y.; Zhao, X.; Suo, Z. Poroelasticity of a Covalently Crosslinked Alginate Hydrogel under Compression. *J. Appl. Phys.* **2010**, *108* (11), 113514. https://doi.org/10.1063/1.3517146.

(156) Ma, X.; Li, Y.; Wang, W.; Ji, Q.; Xia, Y. Temperature-Sensitive Poly(N-Isopropylacrylamide)/Graphene Oxide Nanocomposite Hydrogels by in Situ Polymerization with Improved Swelling Capability and Mechanical Behavior. *Eur. Polym. J.* **2013**, *49* (2), 389–396. https://doi.org/10.1016/j.eurpolymj.2012.10.034.

(157) Yang, B.; Huang, W. M.; Li, C.; Lee, C. M.; Li, L. On the Effects of Moisture in a Polyurethane Shape Memory Polymer. *Smart Mater. Struct.* **2004**, *13* (1), 191–195. https://doi.org/10.1088/0964-1726/13/1/022.

(158) Bae, Y. H.; Okano, T.; Kim, S. W. Temperature Dependence of Swelling of Crosslinked Poly(N,N'-Alkyl Substituted Acrylamides) in Water. *J. Polym. Sci. Part B Polym. Phys.* **1990**, *28* (6), 923–936. https://doi.org/10.1002/polb.1990.090280609.

2 MATERIALS AND METHODS

In this chapter, materials used throughout the subsequent work will be described. The principles behind methods and techniques which were used without development or refinement are outlined, and the relevant parameters and equipment used specified. In the case of methods designed explicitly for this body of work, these were considered to form part of the research, and are detailed in methods development sections in section 4.3.

2.1 MATERIALS

Alginate (medium viscosity) was sourced from Sigma Aldrich and stored in a sealed container at ambient temperature. Due to the high levels of variation within alginate properties, even from the same suppliers in different batches, the blended contents of a single batch from a single supplier was characterised for molecular weight, found to be 20.6 ± 0.6 kDa, and M:G ratio (see sections 2.2.4.4 and 4.2.2) and used throughout.[12]

Calcium chloride was sourced from Sigma Aldrich and stored in a sealed container at ambient temperature.

N-isopropyl acrylamide (IPAM) of 97% purity was sourced from Sigma Aldrich, and stored at below 5 °C in a laboratory fridge.

2,2-Dimethoxy phenyl acetophenone (DMPA) was obtained from Acros Organics, and stored below 5 °C in a laboratory fridge.

Methylene bisacrylamide (MBA) was sourced from Acros Organics and stored below 5 °C in a laboratory fridge.

The formulation of IPAM monomer, photoinitiator (DMPA), crosslinker (MBA), alginate, and calcium chloride devised by Bakarich et al.[3] was used throughout for PNIPAM-alginate gels. This comprises a molar concentration of 0.01M $CaCl_2$, 1.45 x10^{-3}M 20.6kDa alginic acid, 1.77M IPAM, 6.49 x10^{-3}M MBA, and 0.0104M DMPA.

Gold nanorods, synthesized using the cationic surfactant cetyl trimethylammonium bromide and citric acid, stabilized in aqueous solution at a concentration of >30 µg/ml, were purchased from Sigma Aldrich.[4] Their stated dimensions were 10 x 35 nm, corresponding to a primary plasmon resonance at 785 nm. These values were independently evaluated for the purposes of this thesis by means of transmission electron microscopy and dynamic light scattering (see section 5.4.1). The nanorod solution was stored at below 5 °C in a laboratory fridge.

2.2 METHODS

2.2.1 COMPRESSION TESTING

To determine the elastic behaviour of gel samples compressed uniaxially, mechanical compression testing using a small load cell was performed. This process sees a right cylindrical sample of material placed on a fixed plate while another flat plate is moved towards it. The position and force exerted on the mobile plate are recorded, from which the stress (σ) and strain (ε) experienced by the sample can be calculated.[5]

Strain is simply found as the force (F) per unit area (A).

$$\sigma = \frac{F}{A}$$

Equation 2.1

The nominal or engineering stress takes A to be constant and equal to the area of the undeformed sample, A_0 while the true stress (σ'), a closer representation of the actual force experienced by the sample, represents the reality that for most materials A will increase with compression and decrease with extension. Analogously, engineering or nominal strain is evaluated as the ratio of the change in length (Δl) to the original length L_0, while true strain (ε') is defined with respect to the length at the time of the additional extension. So while engineering strain is given by Equation 2.2:

$$\varepsilon = \frac{\Delta l}{L_0}$$

Equation 2.2

True strain is defined as the change in length with respect to the instantaneous length at that time, L:

$$\varepsilon' = \int_{L_0}^{L} \frac{dL}{L}$$

Equation 2.3

Combining Equation 2.2 and Equation 2.3, true and nominal strain can therefore be related by:

$$\varepsilon' = \ln(1 + \varepsilon)$$

Equation 2.4

Relating true and nominal stress requires knowledge of the volume change under stress, but for cases where volume can be assumed constant, this relationship between A_0 and L_0 may be used to express the true stress:

$$\sigma' = \sigma(1 + \varepsilon)$$

Equation 2.5

Compression tests were performed on a Starrett FMS-500-L2 with an approach rate of 1 mm/min and a 100 N load cell. Sample dimensions were measured before testing with a digital micrometer (Silverline, Model number 282378) and their diameter and height recorded for subsequent determination of stress and strain. Errors due to instrument precision were lower than variation due to changing levels of gel compression during measurement. An initial measurement error of ± 0.1 mm was assigned to represent this, which was propagated through further calculations according to standard error methods.

Reproducibility within mechanical testing of hydrogels is typically poor, with up to two orders of magnitude difference found in the moduli reported by different groups for the same composition.[6] This is likely to arise from the extreme sensitivity of the materials to processing conditions, the inherent heterogeneity of the gel structure, and details unintentionally omitted in the literature, as within a publication data are generally consistent. Therefore, the minimum number of required samples specified by comparable protocols[5] was increased from 3 to 5, and visually defective samples were discarded.

Data were recorded using the L2 software package, and processed using Python 3.0, with packages Numpy, Scipy and Matplotlib. Raw force-extension data were converted into engineering stress and strain using the dimensions recorded before testing, and into true stress and strain using the assumption of constant volume.

Linear fitting was performed on the stress-strain graphs produced using the curve_fit function in Scipy to implement the Levenberg-Marquardt least squares fitting algorithm in the region of interest.[7] Errors were assigned as the square root of the diagonalisation of the normalised covariance matrix.

2.2.2 RHEOLOGICAL TESTING

Rheology measures the balance between viscous (energy-dissipating) and elastic (energy storing) mechanical response within liquids, gels and other materials that exhibit behaviour which falls between these extremes. In this thesis rheological techniques are used to measure the response of both crosslinked gels and highly viscous liquids to shear strain, yielding information about their mechanical behaviour when printed and their suitability for printing.

For rheological testing the sample is placed between a geometry mounted on a finely controlled arm, whose displacement and load may be monitored and a fixed plate. As the top geometry rotates the sample thus experiences variable shear rate and amplitude, and either the resulting stress or strain may be measured. A simple parallel plate geometry is appropriate for elastic hydrogels and viscous liquids, sketched in Figure 2.1.

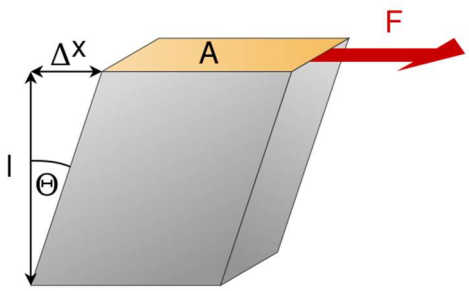

Figure 2.1. Sketch of a volume element of edge length l in shear, showing a force F acting on an area A to create a displacement Δx, forming an angle Θ to the vertical

Applying shear to a sample generates shear stress and shear strain, analogously to linear stress and strain. Shear stress is defined as:

$$\tau = \frac{f}{A}$$

Equation 2.2.6

Where τ is the shear stress, f the shear force and A the area over which it acts.

Correspondingly, the shear strain is:

$$\gamma = \tan\theta$$

Equation 2.2.7

With γ as shear strain and θ as the angle between the unsheared and sheared edge of the surface, as shown in Figure 2.1.

For an ideal elastic solid, shear stress is in phase with the shear strain: the response of the material keeps pace with the force applied to it as it oscillates. For liquids, the stress response lags behind the strain by a phase factor δ, which is 90° for an ideal liquid. A viscoelastic material (and, in reality, any material to some degree) has $0 \leq \delta \leq 90°$ and may be characterised by the response time between shear stress and strain. Physically this is measured as the change in force experienced by the top geometry depending on the motion of the sample with respect to the driving oscillation.

The change in amplitude of oscillations induced in the materials is the second factor uniquely identifying the materials' viscoelastic behaviour. As known from common experience, elastic materials store energy and return it, whereas in liquids the energy used shearing them is dissipated as friction. The combination of these behaviours is expressed in rheological notation as a complex shear modulus G. Here the real part is G', the elastic or storage shear modulus, and the imaginary represents G'', the viscous or loss shear modulus. The angle thus defined on the complex plane is δ and therefore the complex shear modulus vector is a complete description of the system – at a given frequency, strain and point in time. Tan δ measures the ratio of energy dissipated to energy stored during single cycle and quantifies the system damping.[8]

In this thesis, rheological testing was principally used in two modes. Firstly, on cured gels, to evaluate the elastic and viscous shear moduli as a function of the amplitude of oscillations, or of frequency. This predicts the behaviour a material will exhibit in a given regime. Secondly, on uncured gels, to assess their viscosity as a function of shear rate and therefore find the force necessary to initiate flow. Rheology was performed on a Malvern Kinexus Pro rheometer with a Peltier unit to provide thermal stability. Due to the high viscosity of the blend even when uncured, all measurements were taken with a 20 mm diameter parallel plate configuration, following Song *et al.,*[9] and at an isothermal 25° C.

2.2.2.1 SMALL-AMPLITUDE OSCILLATION SHEAR TESTING

For cured gels, a custom program was developed which would allow for variable sample heights, due to swelling to be compared. This loaded samples by compressing to a fixed force level of 0.1 N rather than a fixed height.

For each sample composition, a protocol based on Zuidema et al. was followed; a frequency sweep was conducted to determine the linear viscoelastic region (LVER) and ensure that testing was conducted in a consistent regime.[10] 1 Hz was found to be appropriate for all samples. The sample used for frequency sweep testing was then removed and allowed to rest for 1.5 h, which preliminary tests showed was sufficient to match virgin samples, while oscillation amplitude tests were conducted to determine the shear and loss moduli between 0.01 and 100 % strain. Finally, the frequency sweep sample was used for oscillation amplitude testing. Each composition was tested with at least three independent samples, the results averaged and errors assigned according to the standard error on the mean.

2.2.2.2 SHEAR-RAMP TESTING

For the polymer-monomer uncured blend, shear-viscosity ramps were taken at shear rates 0.01 to 500 s^{-1} to investigate the variation in viscosity with the imposed force. This range corresponds approximately to shear rates experienced by polymers during extrusion through a 3D printer and at rest on the printbed.[11]

2.2.2.3 THREE-STAGE THIXOTROPY TESTING

It was observed for uncured blends that the viscosities recorded in shear ramp tests depended sensitively on the age of the samples and their shear history. Therefore, it was desirable to determine the timescale of recovery and any variation of this with composition, and whether these could be considered constant throughout the extrusion, photocuring and ionocuring stages of print processing.

A protocol was developed to mimic the forces experienced by the materials while printing and monitor their time evolution on relevant scales. This is also used as a method to gain insight into the forces contributing to self-organisation of the liquid as a function of composition.

The process is based on three-stage thixotropy testing and, surprisingly, comprises three stages.

The first stage imposes small angle oscillatory shear at a frequency and strain determined by frequency and strain sweeps to be within the LVER. This establishes suitable parameters under which the viscoelastic response is stable: for materials used in this work, 1 Hz and 1 % strain. Oscillations are performed for 30 s until a stable complex viscosity is reached.

Then, a higher shear is imposed for 30 seconds. This rate was assigned as 50 s^{-1} to represent the shear forces experienced during mixing – shear during needle extrusion will be greater. However, the lower rate is sufficient to destroy order in the sample and significantly reduce the complex viscosity. Finally, small angle oscillatory shear with the same parameters as the initial stage is imposed to monitor the rebuilding of structure within the system, which manifests as an increase in viscosity, an increase in elastic shear modulus, and a decrease in viscous shear modulus. The values obtained here represent the behaviour of the polymer at rest in the cast or on the print bed, although they will be reduced by the disturbance caused by the oscillation used as measurement.

2.2.2.4 DIFFERENTIAL VISCOMETRY

The molecular weight of alginate was found using differential viscometry using an Ubbelohde viscometer. This equipment consists of a reservoir marked with two lines, which drains through a small capillary. Additional tubes allow the equalisation of pressure differences. The time taken for a polymer solution to drain through the capillary, relative to the time taken by the pure solution, is linearly related to the concentration. In the limit of zero concentration, this yields the intrinsic viscosity.

The intrinsic viscosity, in turn, depends on the molecular weight of the polymer and characteristic values derived from solvent-polymer interactions, typically found experimentally. This relationship is given by the Mark–Houwink equation,

$$[\eta] = KM^a$$

Equation 2.8

Where K and a are experimentally determined, $[\eta]$ is the intrinsic viscosity, and M is the viscosity average relative molecular mass. M lies between the number average molecular mass and the mass average molecular mass, but is usually closer to the latter due to the greater contribution of large molecules to the viscosity.[12]

Due to the thermal sensitivity of PNIPAM, the linear relationship between the normalised increase in draining time breaks down at temperatures over 20 °C.[13] For this reason viscometry on PNIPAM was performed on an Ostwald viscometer in a water bath held stable at 21 °C, kindly provided by the ChemLabs team in the School of Chemistry.

2.2.3 MICROSCOPY

Today's scientist has before her a vast selection of microscopic techniques. Those selected here for use were chosen based on availability of equipment, compatibility with sample characteristics and suitability for the resolution required. The relevant material features to this thesis have length scales from microns (the pores within gels) to nanometres (the dimensions of nanorods). Since the fundamental resolution of a microscope in far-field mode is limited by the wavelength of the radiation used for imaging, confocal laser microscopy and electron microscopy were appropriate to study these features.

2.2.3.1 TRANSMISSION ELECTRON MICROSCOPY

Transmission electron microscopy (TEM) uses the small de Broglie wavelength of a beam of electrons, accelerated at close to the speed of light, to image samples with atomic resolution. A sketch of the equipment is shown in

Figure 2.2. A high energy beam of electrons is generated by thermionic or field-effect emission, and accelerated towards the sample by a voltage on the order of kiloVolts. In the perpendicular plane, the beam is shaped by electromagnets to focus on a sample, which they pass through before arriving at a detector – typically a charge-coupled diode array. Electrons which must travel through the sample interact with its electronic structure, experiencing attenuation and interference effects in electron-dense regions. Thus, when the beam arrives at the detector it bears a greyscale image representative of the region of the sample it has intersected. The detector may be photographic film, a fluorescent screen, or a charge-coupled detector.

As the name suggests, this is a transmission technique and therefore limited to thin samples, which additionally must have adequate electron contrast. A further requirement is that to increase the mean free path taken by electrons between scattering interactions, the chamber must be kept at low pressure – samples therefore must be dried and vacuum-resistant.

TEM images for this work were taken on a JEOL 1400 in the Chemical Imaging Facility of the University of Bristol, by Dr Jean-Charles Eloi. Samples were evaporated on carbon coated copper grids which had been pre-plasma treated to overcome the hydrophobicity of the nanoparticles.

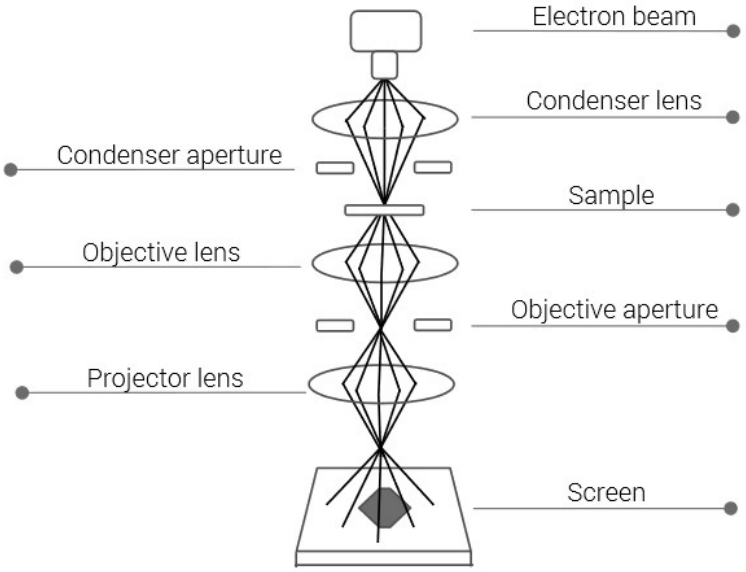

Figure 2.2. Key components of a Transmission Electron Microscope. A beam is generated by an electron gun, is focused and shaped, and passes through the sample before arriving at a screen.

2.2.3.2 SCANNING ELECTRON MICROSCOPY

Scanning electron microscopy (SEM) uses the de Broglie wavelength of a beam of electrons, much smaller than that of light, to image samples at nanometre, or even sub-nanometre, scales.[14] A sketch of the equipment is shown in Figure 2.3. The beam is raster scanned across the region of interest and an image is built up through recording the intensity of scattered electrons received at each point. Samples must be dry and conductive, which can be achieved if necessary through a surface deposition coating of metal. This, however, requires that hydrogels are processed before imaging and the sample post-preparation may not be representative of the native material.

Vacuum scanning electron microscopy images were taken on a JEOL IT300 in the Chemical Imaging Facility of the University of Bristol, assisted by Dr Jean-Charles Eloi. Different preparations were attempted in order to assess the effect of preparation on the gel, given in Chapter 4. All samples were sputter coated in silver and mounted on carbon pads.

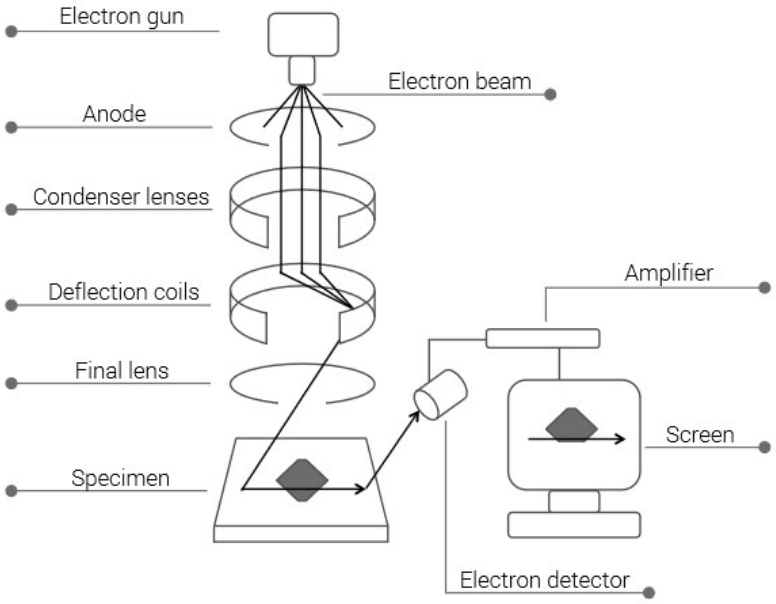

Figure 2.3. Schematic of scanning electron microscope. Electrons are generated by the electron gun. Their wavelength may be modulated by varying the kinetic energy imparted by the accelerating voltage of the anode. The beam diameter is reduced by the condenser lenses – formed by electromagnetic fields –, directed towards the region of interest by the deflection coils, and then brought into focus at the desired height by the final lens. An electron detector records the scattering from the sample and builds up a 2D grayscale image of the surface based on the intensity received at each location. Image by Dr Ioatzin Rios de Anda.[15]

2.2.3.3 ENVIRONMENTAL SCANNING ELECTRON MICROSCOPY

Environmental scanning electron microscopy (ESEM) is a modification to the technique of SEM which enables operation at lower vacuum and therefore with wet samples. Here, electrons are generated in vacuum as before, but a gradient of low pressure is maintained between the electron gun and the sample, which may therefore take a small partial pressure of around 10 Torr.[16] This enables a compromise between the high-vacuum conditions required for the electron beam and the lower vacuum required for testing hydrated samples, with image resolutions of down to 5 nm possible.[17]

ESEM measurements were performed on a Quanta 200 - FEI FEG (field emission gun)-SEM in the Wolfson Bioimaging Facility, with the kind assistance of Dr Judith Mantell.

2.2.3.4 CONFOCAL LASER SCANNING MICROSCOPY

An alternative approach to improving resolution, confocal laser scanning microscopy retains the use of optical wavelengths but changes the geometry to a confocal rather than wide-field configuration to yield sub-micron resolution. In this situation a screen with a narrow hole is used to exclude light originating from regions of the sample not currently under examination, and further specificity is given by imaging fluorescent light generated when a specific laser frequency stimulates dye molecules within the sample. This generates a small but specific signal which is enhanced by a photomultiplier tube. By rastering the sample and scanner a 2D image can be built up. If the material does not absorb too much of the signal, internal structures may also be imaged to create a stack of images along the vertical section.

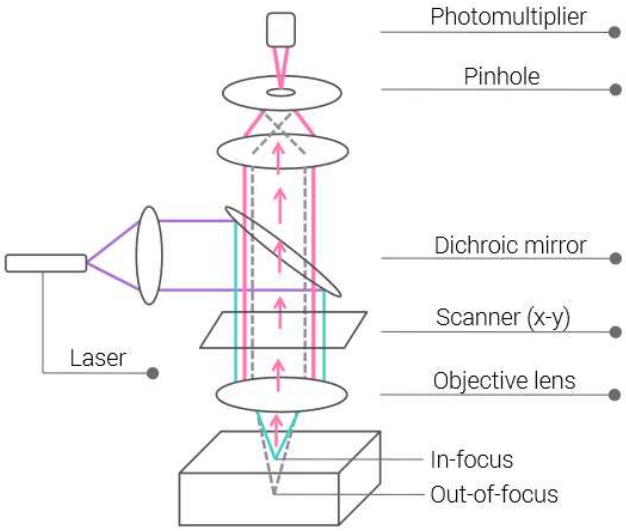

Figure 2.4. Sketch of layout for confocal laser microscopy. Laser light (purple) is sent to a dichroic mirror which selects the required wavelength (aqua). This is focused onto the sample where it excites fluorescence. This generates a small amount of In-focus light which is able to pass through the pinhole, and is enhanced by the photomultiplier into a stronger signal. Out-of-focus light not emanating from that location is not able to pass through the pinhole and reach the photomultiplier and detector, thus reducing interference. Image from Dr Ioatzin Rios de Anda.[15]

For this work a Leica SP5 CLSM with DM6000 stage was used to scan hydrogel samples immersed in aqueous rhodamine solution (0.5 mg/ml) at a wavelength of 543 nm. The gel samples were sectioned an hour before imaging and sealed into an imaging cell as shown in Figure 2.5, constructed from sections of 1 x 76 x 26 mm thick standard slides, joined with Norland 63 UV-curing adhesive. The cell was wholly filled with rhodamine solution and sealed with a 0.13 x 12 x 12 mm coverslip, again using Norland 63. A 63 x numerical aperture oil immersion

objective was used at a zoom of 7.09 to capture all images shown. These are 512 x 512 pixels, corresponding to a real space sample size 16.4µm to a side and a pixel size of 32.1nm. Images were taken with the help of Dr Ioatzin Rios de Anda.

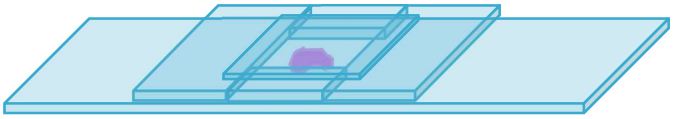

Figure 2.5. Schematic showing imaging cell containing rhodamine-soaked hydrogel sample for confocal microscopy

2.2.3.5 OPTICAL MICROSCOPY

A Leica optical microscope was used to capture visible light images of the print resolution obtained. Images were taken with the help of Abraham Mauleon Amieva.

2.2.4 SPECTROSCOPY

Spectroscopic techniques involve exposing a sample to a spectrum of radiation, either transmitted or reflected. Comparing the incident and returned spectra reveals distinct frequencies to have been absorbed, emitted or shifted. Since each frequency corresponds to a precise energy change within the material, and these are fundamentally quantised and characteristic, the difference between the spectra reveals details of the energetic structure encountered by the incident photons.

In the case of atomic spectroscopy, sharp lines emitted by a sample, or missing from a broad spectrum passed through the sample, correspond to electronic transitions between shells. Electrons moving to a lower energy lose energy and thus produce photons of a key frequency; electrons absorbing incident photons use that energy to move to a higher energy state and show their presence by dark lines missing from the spectrum.

The energy states of atoms in molecules are more complicated, with considerations such as the spacing of the atoms, their geometrical configuration, and the stiffness of the bonds between them. Geometric features of the environment, or externally applied electromagnetic fields, may also affect the separation of states.

2.2.4.1 UV-VISIBLE SPECTROSCOPY

Ultraviolet-visible (UV-Vis) spectroscopy records the interactions of the sample with photons in the ultraviolet to near infra-red region. The light absorbed yields information about electron transitions between discrete energy levels or band structures.

UV Vis spectroscopy was conducted on a Perkin Elmer Lambda 35 with a Peltier cooling system, at wavelengths 150 – 800 nm in a quartz cuvette with an optical path length of 10 mm.

2.2.4.2 FOURIER TRANSFORM INFRA-RED SPECTROSCOPY

Infra-red (IR) spectroscopy refers to spectroscopic interactions with electromagnetic radiation of wavelength between 0.8 – 1000 µm. To retain a linear relationship with energy, characteristic frequencies are usually given in terms of their wavenumber, the reciprocal of wavelength. In this unit the relevant region is 14,000 - 400 cm^{-1}. Interactions in this energy range correspond to couplings with rotational and vibrational modes in the molecule. Peaks in the spectrum indicate a resonant frequency in the system, characteristic of a given oscillation mode between chemical species.

An energy band will be IR-active if it corresponds to a change in the electric dipole of the molecule, *ie.* if the bond it interacts with is asymmetric. Observed IR bands can be used to characterise interactions within a material, and shifts in the position or pattern of frequencies yield information about orientation and bonding as well as composition.

Fourier Transform Infra-red Spectroscopy was performed on a Spectrum 100 FTIR spectrometer (Perkin Elmer) with an attenuated total internal reflection (ATR) configuration. In this measurement modality the incident and reflected spectra are compared via interferometry and a Fourier transform decomposition performed to translate the absorption into the wavenumber domain.

2.2.4.3 RAMAN SPECTROSCOPY

Raman scattering derives from the interactions of the electric field component of incident radiation with the sample polarisability. As in other forms of spectroscopy, incoming photons are absorbed, shifting the sample to

a higher virtual excited state. These energy states rapidly decay and re-emit the temporary energy boost as electromagnetic radiation.

However, it is possible that the energy after decay is not exactly the same as that before the interaction. If the energy afterwards is slightly higher, the energy difference is smaller upon relaxation than excitation, and the photon re-emitted has a lower energy than the one that was absorbed. This is known as Stokes mode Raman scattering. The opposite, where the excitation decays to a lower state than the one originally excited by the photon, is also possible. This causes more energy to be emitted than was delivered – seen as a higher energy photon. This is called the anti-Stokes mode of Raman scattering. Since this is less likely, Stokes mode scattering dominates. A sketch of the transitions involved is shown in Figure 2.6.

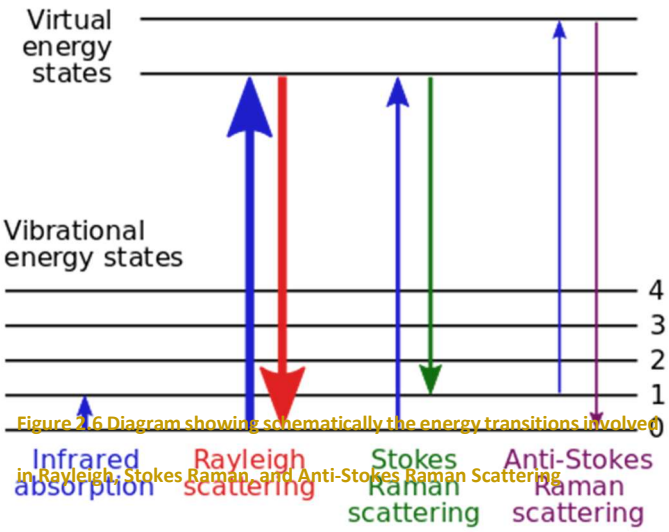

Figure 2.6 Diagram showing schematically the energy transitions involved in Rayleigh, Stokes Raman, and Anti-Stokes Raman Scattering

Only a small fraction – on the order of 10^{-6} - of the incident signal scatters inelastically through the Raman interaction, so the technique requires careful separation of the relevant signal from the reflected source. The vibrational modes which contribute to Raman shifts are those which change the electric dipole moment as a function of time, identified by those which are symmetric in space.

For this work, Raman spectroscopy was conducted on a Perkin Elmer Raman Micro 200 with a 350 mW 785 nm laser. This wavelength was selected to minimise the fluorescence generated by the polysaccharides. Samples were placed on an aluminium coated slide (Thermofisher Scientific) to enhance the Raman signal, and were focused using a 50 x magnification and 0.7 numerical aperture.

Exposure time and number of repeats varied depending on the samples and are given in subsequent chapters as the results are presented.

2.2.4.4 NUCLEAR MAGNETIC RESONANCE SPECTROSCOPY

Nuclear magnetic resonance spectroscopy (NMR) uses the sensitive shift in energy levels experienced by a particle with spin when an external magnetic field is imposed to extrapolate its molecular environment.

A nucleus with net spin and therefore a magnetic moment will be aligned in an external magnetic field. The energy of a particle with its magnetic moment aligned with an external field, compared to the same particle with an antiparallel alignment, will differ. This results in a splitting of the energy levels for the particle, creating a band gap which the particle may cross by absorbing energy of the correct radio frequency. The energy level split, ΔE, and thus the energy of the appropriate photon for transition is given by:

$$\Delta E = \frac{\mu B_z}{s}$$

Equation 2.9

Here B_z is the component of the magnetic field in the z direction, μ the magnetic moment of the particle (well quantified for known nuclei), and s the spin of the particle (1/2 for the nuclei used here).

Thus, for a known B_z the value of the energy gap can be found by probing with photons of different energies and monitoring for conditions where they are absorbed, indicating a match in energy values and resonance. The exact magnetic field and thus the magnitude of the energy gap is affected by the environment and bonding of the particle, and so the same nucleus (for example, ^1H) will resonate to a different frequency depending on its location. Thus, NMR results measure the resonant frequency for known standard and then calibrate the shift away from that standard for other nuclei, giving this value as a 'chemical shift' in parts per million (ppm). NMR for this thesis was kindly performed by Sarah Michel on a Varian VNMRS500 (500 MHz for the purposes of identifying the relative percentages of each monomer within alginate. A 1H proton NMR spectra was run at 80°C, following ASTM protocol F2259.[18] The reference solvent was D_2O, and the peaks were referenced to tetramethylsilane. Processing details are given in the section on characterisation of alginate in Chapter 4.

2.2.5 DENSITY AND VOLUME MEASUREMENTS

Density and volume measurements were performed using the buoyancy method. Three samples for each composition, of at least 1 cm^3 volume and thickness approximately 3 mm, were selected, patted dry and weighed

in air in a swollen state using a Sartorius balance. They were then weighed in 5 cSt silicone oil (Sigma Aldrich) of known density 0.913 g/cm^3, using a Specific Gravity Kit (Mineralab). The difference between the weights divided by the oil density yields the swollen volume.

Samples were then wrapped in tissue and placed in containers with dessicant, sealed against water and air. These beads were changed every two days until desiccation was achieved. Samples were then weighed in dry state, both in air and in silicone oil, and the volume calculated. Volume swelling ratio was simply the swollen divided by the dry volume, averaged across all samples for a given composition, with errors assigned as the standard error on the mean.

A similar method was used to verify whether unreacted monomer was being lost from the system. Three pairs of gels matched in volume were prepared. One of each pair was rinsed in 3 changes of DI water over 24 h to remove unreacted agents, while one was allowed to dry with no rinsing. Following drying their masses were compared to determine the ratio of reagents which were polymerized and fixed in the system.

2.2.6 DYNAMIC LIGHT SCATTERING

Light scattered from particles undergoing Brownian motion within a solution fluctuates due to the random density variations of solute molecules around them. Surrounding particles scatter the light imprinted with these fluctuations, and the patterns in the resulting superposition yield information about the size and distribution of the scattering particulates. Small particles move faster and their fluctuations evolve quicker; the time taken for correlations in signal intensity to die off is characteristic of the mean particle size and can be used to calculate the polydispersity.[19]

Dynamic light scattering measurements were taken on Malvern Instruments Zetasizer Nano S, taking the refractive index of gold nanoparticles to be 0.227.[20] Samples were filtered through a 0.8 µm filter before measurement, and thermally stabilised for 3 minutes prior to taking a measurement. Results are the average of three runs which are each made of 100 individual measurements.

2.2.7 ZETA POTENTIAL MEASUREMENTS

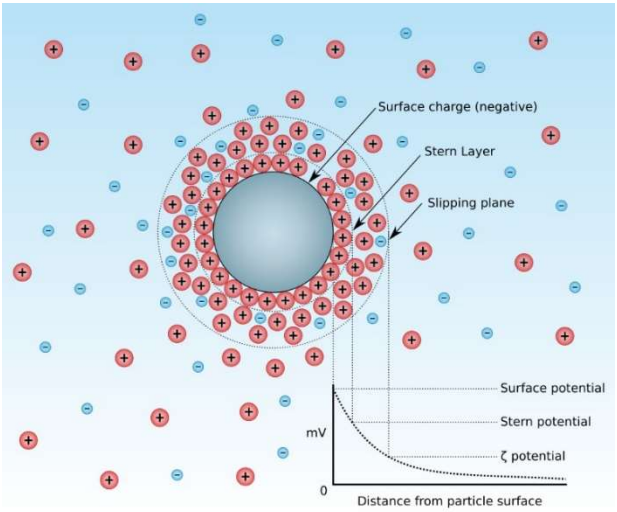

Figure 2.7. Diagram of zeta potential concept, released under CC-BY-SA 3.0 Modified and converted to SVG by Mjones1984. Original work by user Larryisgood.

The zeta potential quantifies the voltage at the interface between a surface and liquid. Any charge on the surface will accrue counter-ions, forming an electrical double layer. The zeta potential measures the potential difference generated by the charge bounded by the slipping plane. It is a function of the charge of the particle, any adsorbed layers, the solvent, and the temperature. For suspended particles, the electrophoretic mobility depends on the zeta potential. By using Doppler shift to record the velocity of the particles in response to a known imposed voltage, this can be calculated.

Zeta potential measurements were taken on a Malvern instruments Zetasizer with solutions diluted with deionized water by a factor of 30 from their experimental concentrations. Calculations used the Smoluchowski model.

2.2.8 SMALL ANGLE X-RAY SCATTERING (SAXS)

This technique records x-ray scattering from a sample to reveal its electronic density and structure at the nanometre to micrometre scale. To derive structure, the intensity of the scattered signal is recorded as a function of angle – typically in the range of 0.1 – 10 °. The angular dependency is usually parameterised in terms of q, the momentum transfer or scattering vector. This is defined by the equation following:

$$q = \frac{4\pi \sin(\theta)}{\lambda}$$

Equation 2.10

Here θ is half the scattering angle as shown in Figure 2.8 – where the factor of two derives from diffraction geometry - and λ the wavelength of the scattering radiation. The intensity of the x-rays arriving after scattering as a function of q is recorded by a sensor, typically a charge-coupled device (CCD). This 2D image may be processed in a variety of ways to extract information about the shape and spacing of scattering surfaces within the sample.

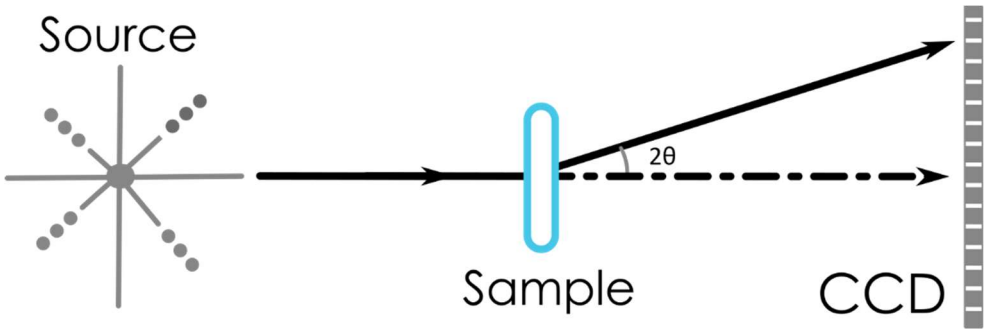

Figure 2.8. Schematic of small angle X-ray scattering. An x-ray soft (left) generated beams which scatter elastically as they interact with a target. The intensity as a function of angle 2θ is recorded on a CCD.

As in all scattering-based observations, the relationship between the scattering angle and characteristic length scale of scattering surface is reciprocal, with the larger angles relating to a small spacing and smaller angles to larger length scales. At low q, the intensity represents scattering from a large number of particles and thus reveals long-range system order such as spacing or alignment. At intermediate q, contributions derive from approximately one particle, and thus carries information about the size and shape of individual components. At higher q values, known as the Porod regime, only a section of each particle influences the scattering pattern and therefore this regime represents the characteristics of the interface between an individual particle and the medium it occupies. A sketch of the regions and the information they give about a system is shown in Figure 2.9.

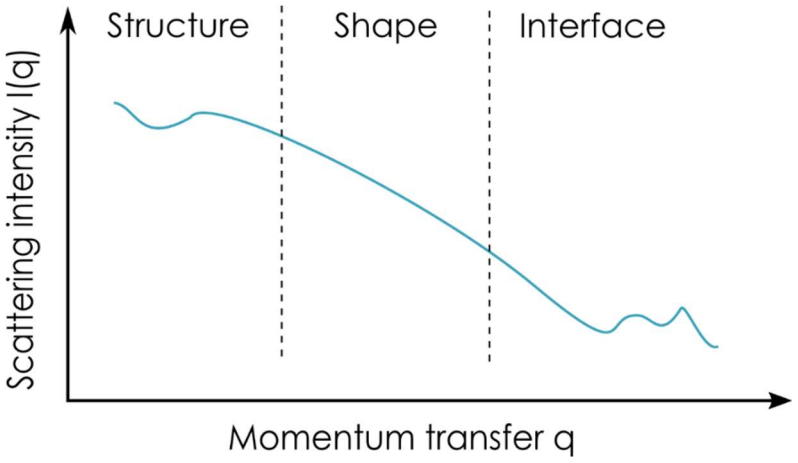

Figure 2.9. A sketch showing scattering intensity measured in SAXS as a function of momentum transfer q, and the regions of measurement which correspond to information about structure within the material (ordering and spacing of particles), the shape and size of individual particles, and the interface of the particles, respectively.

All X-ray scattering was performed on a SAXSLAB Ganesha 300XL instrument in a Q range of 0.007 - 0.25 $Å^{-1}$, with an exposure time of 7200 s per sample. Samples were sectioned into roughly rectangular sections of approximately 2 x 4 x 4 mm using a scalpel, and transferred directly to a flat mica cell for measurements. Remaining space in the cell was filled with deionised water to prevent dehydration effects. Background corrections were made using an empty cell, and sample thickness corrections were made using a cell half filled with water and comparing the beam intensities. All data presented in this work have already had thickness and background corrections subtracted. Fits were performed in SASview.[21]

2.2.9 DIFFERENTIAL SCANNING CALORIMETRY

This technique compares the energy required to maintain two sample pans at the same temperature. As the temperature is varied, changes in the molecular arrangement and bonding of the sample result in the intake or output of energy. Differential scanning calorimetry (DSC) samples are typically on the order of a few milligrams in mass, corresponding to a few millimetres in dimension and a short diffusion time. This makes their behaviour representative of the bulk performance of thermoresponsive gels. Samples are sealed in pans to eliminate effects of mass change due to evaporation.

Differential Scanning Calorimetry was conducted on TA Q200 (TA Instruments) with fully hydrated samples sealed in air within Tzero aluminium pans (TA instruments). A heat-cool-heat cycle was performed between 10 and 50 °C at a heating rate of 3 °C per minute against a reference sample of an air-filled empty pan.

2.3 REFERENCES

(1) Mancini, M.; Moresi, M.; Rancini, R. Mechanical Properties of Alginate Gels: Empirical Characterisation. *J. Food Eng.* **1999**, *39* (4), 369–378. https://doi.org/10.1016/S0260-8774(99)00022-9.

(2) Lee, K. Y.; Mooney, D. J. Alginate: Properties and Biomedical Applications. *Prog. Polym. Sci.* **2012**, *37* (1), 106–126. https://doi.org/10.1016/j.progpolymsci.2011.06.003.

(3) Bakarich, S. E.; Gorkin, R.; in het Panhuis, M.; Spinks, G. M. 4D Printing with Mechanically Robust, Thermally Actuating Hydrogels. *Macromol. Rapid Commun.* **2015**, *36* (12), 1211–1217. https://doi.org/10.1002/marc.201500079.

(4) Scarabelli, L.; Sánchez-Iglesias, A.; Pérez-Juste, J.; Liz-Marzán, L. M. A "Tips and Tricks" Practical Guide to the Synthesis of Gold Nanorods. *J. Phys. Chem. Lett.* **2015**, *6* (21), 4270–4279. https://doi.org/10.1021/acs.jpclett.5b02123.

(5) ASTM. D395-14: Standard Test Methods for Rubber Property — Compression Set. *ASTM Int.* **2003**. https://doi.org/10.1520/D0395-03R08.2.

(6) Oyen, M. L. Mechanical Characterisation of Hydrogel Materials. *Int. Mater. Rev.* **2014**, *59* (1), 44–59. https://doi.org/10.1179/1743280413Y.0000000022.

(7) The SciPy community. scipy.optimize.curve_fit — SciPy v1.1.0 Reference Guide https://docs.scipy.org/doc/scipy/reference/generated/scipy.optimize.curve_fit.html (accessed Oct 24, 2018).

(8) Rudin, A. 11.5 Polymer Viscoelasticity. In *The elements of Polymer Science and Engineering*; Academic Press, 1999.

(9) Song, K. W.; Kim, Y. S.; Chang, G. S. Rheology of Concentrated Xanthan Gum Solutions: Steady Shear Flow Behavior. *Fibers Polym.* **2006**, *7* (2), 129–138. https://doi.org/10.1007/BF02908257.

(10) Zuidema, J. M.; Rivet, C. J.; Gilbert, R. J.; Morrison, F. A. A Protocol for Rheological Characterization of Hydrogels for Tissue Engineering Strategies. *J. Biomed. Mater. Res. Part B Appl. Biomater.* **2014**, *102* (5),

1063–1073. https://doi.org/10.1002/jbm.b.33088.

(11) Malda, J.; Visser, J.; Melchels, F. P.; Jüngst, T.; Hennink, W. E.; Dhert, W. J. A.; Groll, J.; Hutmacher, D. W. 25th Anniversary Article: Engineering Hydrogels for Biofabrication. *Adv. Mater.* **2013**, *25* (36), 5011–5028. https://doi.org/10.1002/adma.201302042.

(12) Walton, D.; Lorimer, P. Polymer Properties and Characterisation. In *Polymers*; Oxford, 2000; p 30.

(13) Fujishige, S. Intrinsic Viscosity-Molecular Weight Relationships for Poly(N-Isopropylacrylamide) Solutions. *Polym. J.* **1987**, *19* (3), 297–300. https://doi.org/10.1295/polymj.19.297.

(14) Goldstein, J. I.; Newbury, D. E.; Michael, J. R.; Ritchie, N. W. M.; Scott, J. H. J.; Joy, D. C. 10.1 What Is "High Resolution SEM Imaging"? In *Scanning Electron Microscopy and X-Ray Microanalysis*; Springer, 2017; p 148.

(15) Rios de Anda, B. I. Self-Assembly of Multiple Soft Matter Systems, University of Bristol, 2018.

(16) Stokes, D. J. *Investigating Biological Ultrastructure Using Environmental Scanning Electron Microscopy (ESEM)*.

(17) Donald, A. M. The Use of Environmental Scanning Electron Microscopy for Imaging Wet and Insulating Materials. *Nat. Mater.* **2003**, *2* (8), 511–516. https://doi.org/10.1038/nmat898.

(18) ASTM. *Standard Test Method for Determining the Chemical Composition and Sequence in Alginate by Proton Nuclear Magnetic Resonance (1 H NMR)*; 2012. https://doi.org/10.1520/F2259-10R12E01.Copyright.

(19) Malvern Instruments. Dynamic Light Scattering: An Introduction in 30 Minutes. *MRK656-01*. 2012.

(20) Johnson, P. B.; Christy, R. W. Optical Constants of the Noble Metals. *Phys. Rev. B* **1972**, *6* (12), 4370–4379. https://doi.org/10.1103/PhysRevB.6.4370.

(21) Butler, P.; Doucet, M.; Jackson, A.; King, S. SasView. *http://www.sasview.org/*. 2012.

3 AN OPEN-SOURCE, UV-CURING, EXTRUSION-BASED 3D PRINTER

3.1 ABSTRACT

Preparation of complex PNIPAM-alginate gel geometries for shape-changing applications requires a cold-extrusion based 3D printer, with capability to print at 0-10 °C and cure with UV. Existing publications use high-performance, but proprietary and expensive solutions. To improve accessibility, reproducibility and customisation of the process, an open source solution has been developed as a platform for subsequent shaped-gel work in this thesis. This combines a delta-configuration 3D printer body, a syringe-based extruder connected to an extrusion needle, simple environmental control and UV-curing intensity-modulated LEDs. Together, this enables extrusion with a precision of ±0.25mm, with curing controllable by the same G-code file used for other print variables. All components of the printer, including hardware, firmware, electronics and design software are provided open source under the Gnu General Public License, and therefore freely reproducible. The total cost of the system is a factor of 4 less than comparable starter-level cold-extrusion based printers, while incorporating UV-curing abilities that exceed current off-the-shelf provision.

3.2 RATIONALE, REQUIREMENTS AND EXISTING SOLUTIONS

A requirement for accessibility in a 3D printer capable of shaping hydrogels places constraints upon the equipment to be used. Prior work, such as that conducted by the Wyss Institute team[1] and the Woolongong group[2], has made use of proprietary systems, built on a custom basis in-house, or high-end printers designed for tissue-printing applications. While still in their infancy as technologies, they already exhibit multiple functionalities, which may include UV exposure for curing and sterilization, temperature control, multimaterial blending, and more.[1–4] These machines would typically be constructed on a custom basis, or purchased at costs of tens of thousand pounds. This presents challenges for replication, as well as accessibility.[5]

The issue of accessibility is a particularly salient one in the field of 3D printing; one can readily see that following expiry of the patent on fused deposition modelling,[6] and the release of the first open source machine optimised for replicability, the RepRap series, the capabilities of the field increased dramatically.[7] In the world of science, CERN (the European Centre for Nuclear Research) has adopted open hardware protocols. This has enabled rapid

fixing of problems, bespoke designs, and independence from vendors, and also increased the impact of its work dramatically.[8,9]

In recognition of the increase in capabilities, independence, and speed of improvements seen in open source projects, as well as the need for replication, the technologies used in this work all fulfil open source licensing. This is a category of intellectual property licence which freely permits reproduction and reuse, if certain conditions (such as not generating profit, or attributing original creators) are respected.[10] Open source hardware is a growing research topic area within the scientific world and has potential for levelling the playing field between established and new groups, developed and developing countries, as well as democratising the practice of science and reducing the time taken to develop equipment of high quality.[11–13] Transparent access to all parts of the system is also advantageous to the working scientist, enabling them to fully understand, tailor and improve their instruments and processes.

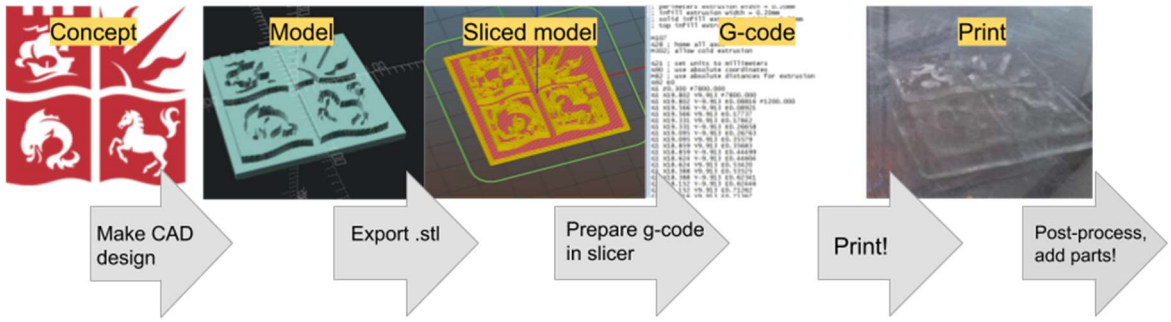

Figure 3-1. The 3D printing process. An idea must be rendered as a Computer Aided Design model (CAD) using CAD software. This is used to produce an .stl file, a 3D file format defining a hollow manifold. This is processed by a piece of slicing software into 2D slices in the XY plane capable of being produced by a printer. At this stage, the depth of each slice (z resolution), the resolution in x-y, whether pieces are hollow, solid or in-between, and the use of any supports will be defined. Slicing software translates these pieces into instructions for the movements of the print head and the amount of material to extrude, rendered as a text called G-code. Finally, the G-code instructions are sent to the printer which interprets the instructions using its firmware, executing the specified movements, creating the print piece. This may then be removed for further processing or assembly.

As sketched in Figure 3-1, the 3D printing process extends beyond the hardware. Designing, preparing and rendering prints all require access to software which may also place barriers to adoption. This aspect will also be considered. This chapter begins with a review of the requirements for processing the chosen hydrogel material, and available proprietary options, both as complete printers and bolt-on converting elements. The

composition and capabilities of the open source system developed are described, and processing choices justified. The performance of the setup developed for this purpose is evaluated and compared to commercial solutions. Finally, limitations are identified and future improvements are suggested.

3.2.1 PROCESS REQUIREMENTS

The process of preparing a shaped gel of the working thermoresponsive material, PNIPAM-alginate double network gel (described in more detail in Chapter 4.2), is illustrated in Figure 3-2. The initial polymer blend comprises monomer, photoinitiator and crosslinker, as well as alginate polymers and a 0.01M concentration of calcium ions to crosslink them. This solution is viscous, with a high zero shear viscosity. This enables it to hold its shape on the print bed but also increases the pressure required to extrude it.

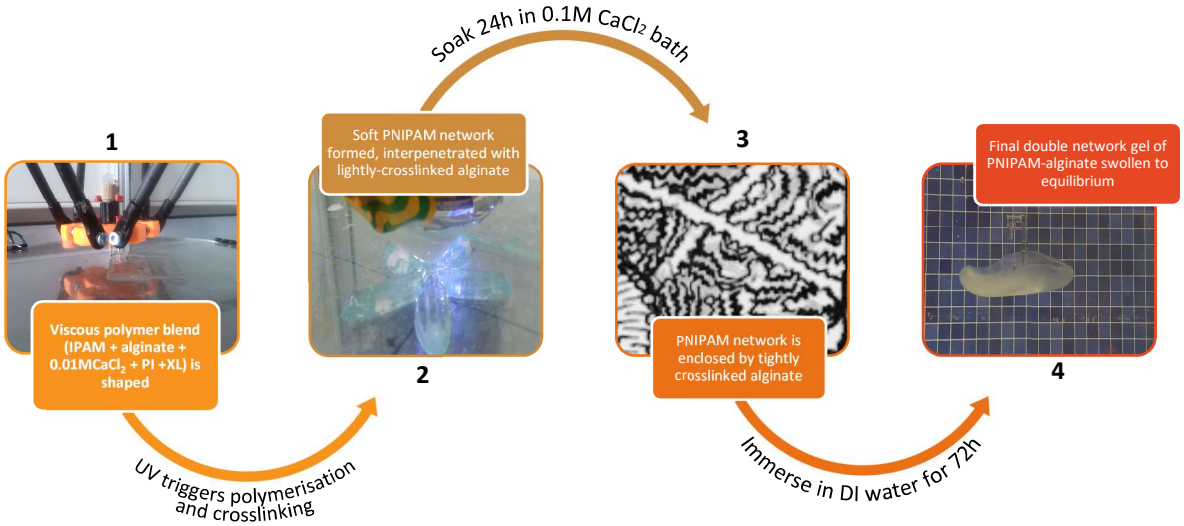

Figure 3-2. Stages in processing of PNIPAM-alginate double network gels. IPAM = Isopropyl acrylamide monomer, PI = photoinitiatior, XL = crosslinker. 1 shows the printing process, 2 UV curing of the PNIPAM network, 3 a sketch of molecular binding of alginate networks around the PNIPAM network, and 4 the relaxed, equilibrated gel.

Following shaping, UV light of the correct wavelength for a photoinitiator is directed on the printed shape, forming the covalently bonded PNIPAM network. Once this network is formed, the double gel is fixed in shape but fragile.

Immersion in a 0.1M $CaCl_2$ bath allows the uptake of further calcium ions to add more crosslinks to the second, alginate network. This increases the resilience and elasticity of the gel to its final level, making it easy to test. Finally, the fully formed gel is immersed in DI water to remove any unreacted monomer, photoinitiator and crosslinker, and allow the double network to take up water until it reaches an equilibrium state. Until the bath

immersion stages, the material should be kept at below 10 °C because the working material phase separates above this temperature, creating less stable and transparent gels (Bakarich *et al.*, supplementary information[2]).

The requirements of the printer thus emerge:

- It must be open source – therefore, this directs towards extrusion-based systems since these are much more established than the few stereolithographic approaches.
- Parts must be readily available or simple to manufacture.
- Viscous polymer blends must be extruded, suggesting a strong motor or other methods will be required to generate the pressure needed to extrude through a nozzle.
- Some method is required to connect the extrusion reservoir to the nozzle.
- A UV-emitting element is required to initiate crosslinking and set the gel in the final shape. Ideally this should be controllable during printing.
- There must be the ability to retain the print at a temperature below 10 °C for the duration of curing.
- Prints should then be able to be removed and immersed in a $CaCl_2$ bath for the final stage of printing.
- Printer parts must be suitable for cleaning and, at end of life, appropriate chemical waste disposal.

3.2.2 PRE-EXISTING OFF-THE-SHELF SOLUTIONS

There are two principal applications for paste extrusion-based printers: bioprinting and specialist food manufacture.[14,15] These serve two distinctly different markets. Specialist bioprinting machines have been around for approximately 10 years, mainly targeting academic or commercial R&D sectors, and offer printing with a variety of 'bioinks'. For this audience, 'plug and play' solutions are typically sought, with low degrees of process customisation and often a business model which relies on ongoing sales of custom consumables. Food printers are a smaller market sector, principally purchased as a novelty or with specialist event caterers in mind. Since food printing has not so far addressed issues of UV curing or chilled temperature control, commercial bioprinters are the more relevant comparison point.

Figure 3-3. Discov3ry paste extruder module (Structur3d printing)

The Biofactory™ and 3DDiscovery™ (both RegenHU, Switzerland) offer UV curing at three frequencies, as well as offering inkjet, paste printing, and heated polymers. Temperature can be controlled between 5-80 °C. This offers all the functionality needed to process PNIPAM-alginate blends to a high level of precision (±5 μm), although print volume is only 60 × 60 × 60 mm^3. Control systems are proprietary, and prints must be prepared with RegenHU software. Cost is subject to negotiation but articles place it at upwards of $200,000.[16]

The BioX from Cellink (Sweden) offers extrusion printing in the temperature range 4-65 °C and pressures of up to 700 kPa. UV crosslinking is offered at 270 nm wavelengths and a lightguide may be placed on the head for additional wavelengths. Maximum resolution is 1 μm and the total equipment cost was quoted in their press release as $39,000 USD.[17] The cheaper INKredible model has 365nm and 405nm curing build in, but no temperature control, and retails for $5,000USD. Cellink printers are compatible with Repetier software, which is open source.

The Discov3ry 3D printer (Structur3d printing, Waterloo, Canada) is an off-the-shelf solution which adds paste processing abilities to the popular Ultimaker range of 3D printers. This derives from the open-source RepRap stock, and the developers plan to open-source their paste dispenser in the future. It can be bought integrated with an Ultimaker (quoted as £4,794) or as an external unit to be incorporated into an existing printer. It is also available with dynamic mixing capabilities, which offer exciting potential in light of the observations in Chapter 1 of the requirements for blending materials. Layer resolution is strongly material dependent, but a nozzle of between 0.2-0.5 mm can be positioned with XYZ accuracy of 12.5 × 12.5 × 5 μm^3.

In summation, the combination of cooling and UV illumination is only found on more expensive printers for the bioprinting market. These cost from $5,000-$200,000 USD or more. For non-biological, macroscopic shape-changing applications many of the advanced features of a bioprinter are unnecessary – for example, the ability

to maintain sterility and a print precision of ~15 μm. To improve usability, these systems also commonly require proprietary file preparation methods, or other restrictions which limits the varying of parameters at will.

There are more cost-effective bio-printers available. These are summarised by Ozbolat *et al.*: "affordable dual-head bio-printers with thermal and photo-crosslinking capabilities range from $5000–10,000; however, the quality, resolution and operability of these cost effective bioprinters are inferior to higher priced instruments."[14] At time of writing none are fully open-source and few support processing of OS file formats to enable the desired flexibility. If this could be overcome, the cheaper models would be of interest for this application.

The Discov3ry 3D extrusion unit may be bought separately and mounted on an existing printer. It is functionally very similar to the MOST syringe pump described in Section 3.2.3.4, provided as a 'plug-and-play' solution. It has a volume of 60 ml, and costs $1299 CAD (~£770 GBP). This raises the alternative of purchasing a printer with some of the capabilities needed and adding functionality using some of the many open source options available.

3.2.3 COMPONENT SELECTION AND BUILD

In essence, a 3D printer is a frame, set of motors, and controlling electronics and integrated power supply which can move a print head (also known as an effector) and print bed with respect to each other. The same electronics typically power and control an additional motor to drive material extrusion through this head, and modulate the temperature of the print head and bed. In this section the selection of a printer body, extruder mechanism, and relevant connectors will be given and justified.

3.2.3.1 3D PRINTER BODY

Many inexpensive 3D printers are now available, most of which would be suitable for conversion to paste extrusion. Choices are often made on the basis of local available expertise and price. Selection for this project focused on the design decision of cartesian vs. delta printer, with outlines sketched in Figure 3-4.

Cartesian printers are those which move in three mutually orthogonal axes (Figure 3-4, left), and have formed the bulk of the 3D printers sold to date. The extrusion head moves in Z, and the base provides articulation in X and Y; or alternatively the head moves in X and Z and the base Y. They are robust, have a large extant body of work, and have convenient beams for mounting extra components. They also take up a large work area, due to

the need for the large base to move. The area that the head can access is limited, particularly with typical bulky extrusion heads.

Delta printers, the other design commonly seen, are equilateral triangular prisms with the triangular faces parallel to the ground. The print head is controlled via arms mounted on carriages which travel along the vertical edges of the prism. This design permits rapid movement of the head to all locations within a large hemispherical build volume, as the shortest path can be taken, and has a large amount of space for modifications and extra components.

However, the delta format limits the weight that can be borne on the effector without detriment to precision. Most designs place only a heating element here and feed solid polymer filament to the head through a Bowden tube from a motor mounted on the sides. A similar layout is necessary for paste extrusion, with a pipe joining the dispenser to the effector head. This introduces a certain lag into the system (determined by the viscoelastic properties of the print material) due to the time taken for pressure exerted by the syringe plunger to be transferred. Another significant downside is the need to fill the entire length of the pipe between the syringe and the print head before printing – for syntheses that yield only small amounts of material, the few millilitres required to bridge this gap may be a significant percentage of the material available. This was, however, not a problem with PNIPAM-alginate, selected due to its cheapness and abundance.

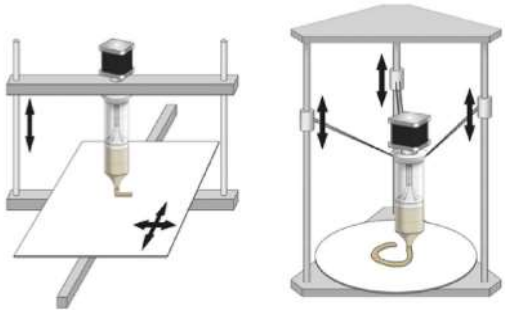

Figure 3-4. Cartesian (left) and delta (right) 3D printer. In Cartesian printers the extrusion head and bed both move, the head in the z dimension and bed in x-y. Delta printers access all x-y-z- space within them through adjusting the relative heights of three carriages connected to the extruder via rods. The base is static. Sketch from Sun et al.

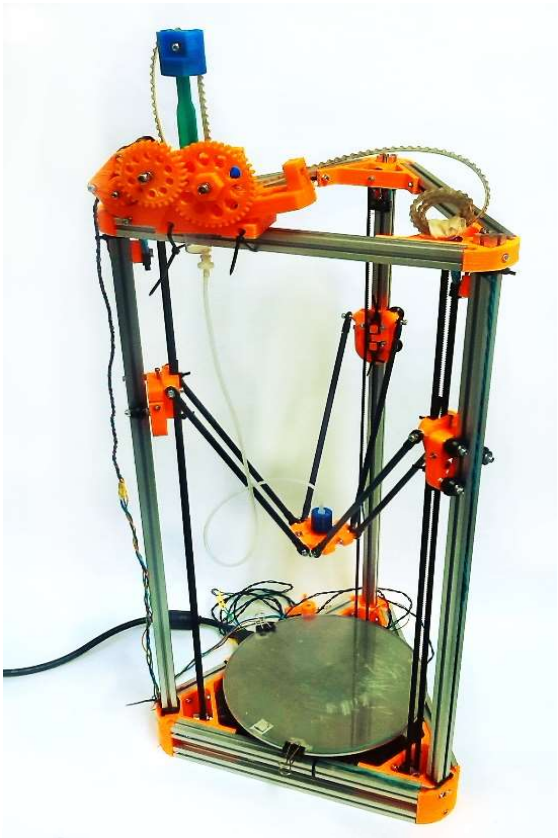

Figure 3-5. The Kossel Mini delta printer used in this project. At the time of taking this photo the original plastic filament extruder and hot end had been removed and replaced by the Universal Paste Extruder (top left) and a nozzle mount respectively.

The final major advantage of the delta is that since the base does not move, gel structures laid down on the base are not subject to lateral acceleration. This is helpful, as the polymer blend chosen is a polysaccharide that exhibits shear-thinning behaviour under stress. This is desirable when being extruded, but when in the final position the stresses experienced by the uncured gel could cause it to decrease in viscosity and exhibit undesirable flow behaviour. A static bed configuration prevents this happening.

The threefold symmetry of the design means that the build contains repeated elements, and it is therefore recommended, by some, for first time builders who are required to master fewer processes. Build is well documented, for example by Think3DPrint3D under CC-BY 4.0.[18] Finally, the small footprint and light weight design makes it easy to house in areas with limited space, and also to transport to different locations as required for testing.

The Kossel Mini, a smaller version of the Kossel printer, both designed by Johann Rocholl,[19] was selected following the recommendation of R. J. J. Allan (RIP). Part of the RepRap family, the printer (shown in aFigure 3-5 with a mounted extrusion pump described in 3.2.3.3) is of the delta type and licensed under the Gnu General Public Licence 2.0 + (GPL 2.0). This licence means that the design can be used for any purpose, including commercial, modification, or patented applications, on the condition the source is acknowledged, the licence remains the same and is stated, and changes are documented and republished. No warranty or liability is acknowledged. Use is therefore appropriate for a research project or publication, anywhere in the world, fulfilling criteria for customisability and accessibility.

The printer is provided open source on the code repository Github.[19] Parts are defined in openSCAD, an open-source piece of CAD software (described more fully in 3.2.3.10). This makes modification of parts easy (if one writes openSCAD). Electronic control is provided by an Arduino Mega 2560 with a Reprap Arduino Mega Polulu Stepper (RAMPS) board.[20] This will be discussed further in the electronics section.

A Kossel Mini kit was purchased from Think3DPrint3D (Nottingham, UK) for £500 and assembled following the documentation provided. The hot printhead was removed, as were the fans, as unnecessary for this purpose. Further, the bed levelling probe, used to adjust print instructions for any skews in the print bed or other misalignment, was removed to make more room for additional print head features.

3.2.3.2 EXTRUSION UNITS

As a computer-controlled device which changes the volume of a chamber to extrude a defined volume of liquid, this is essentially a syringe pump. Many DIY hydrogel printers (such as the one used by Naficy *et al.* in their 2016 work[21]) use syringe pumps intended for scientific purposes. These have the advantage of providing a precise and reproducible flow rate. However, if not interfaced with the printer, it is challenging to modulate the flow rate of the syringe pump in synchrony with the movement of the printer head. As an additional support for an open-source standardized approach, the difficulties tend to arise from the idiosyncratic nature of the syringe pump firmware.

In response to this, a number of open source extrusion pumps have been developed. These share the same operating principles as the original filament extruder, and thus can be incorporated into a standard 3D printing toolchain with only minimal adjustments to the printer firmware controlling them. Additionally, these solutions can be at least two orders of magnitude cheaper than an off-the-shelf pump.[22]

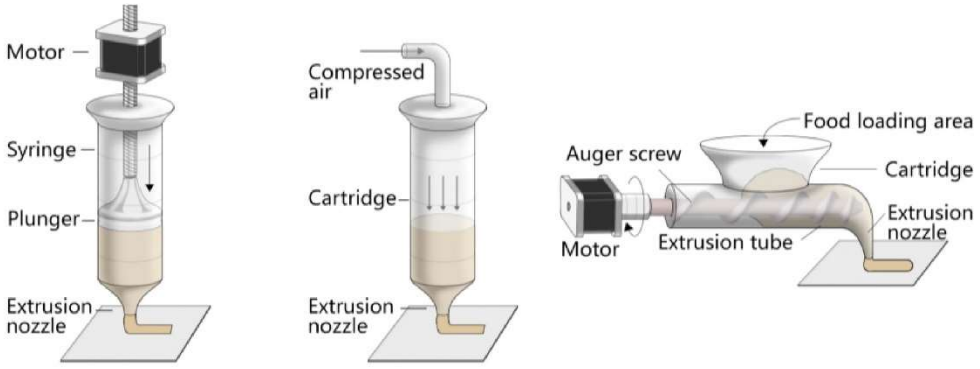

Figure 3-6. Varieties of liquid extrusion for 3D printing: a) Syringe-based extrusion, b) air-pressure driven extrusion, c) screw-based extrusion. From Sun et al.[15]

Three major approaches have been experimented with for this purpose, illustrated in Figure 3-6. The first uses straightforward displacement of a plunger on a syringe (shown in Figure 3-6, a), controlled by a stepper motor of similar nature to those used to move the print head on the 3D printer. This has numerous advantages. The most beneficial is that the extrusion may be controlled using the same stepper boards, motor and circuits as the rest of the printer, with only a few tweaks of constants in the firmware. The use of the syringe means it can be scaled for multiple volumes depending on the material required, while preparation of multiple disposable syringes may be used to speed up production, switch between materials, and provide appropriate chemical

disposal. Downsides include difficulty ensuring precision with strongly non-Newtonian fluids where a fixed displacement may not map to a well-defined volume extruded, a cumbersome form factor, and a limitation on the viscosity of liquids that can be processed.

Secondly, a pressure-based extrusion method (Figure 3-6, b), where air or hydraulics are used to modify the pressure behind the extrudate and force it from the needle. This has the advantage of immediacy and precise control, but again presents challenges with synchronising and often requires higher power as an external pump must generate the change.

Thirdly, progressive cavity pump or Moineau pump approaches (Figure 3-6, c). Here, a motor turns a screw in a tube stator, progressing a series of discrete cavities along the tube, which carry a fluid with them by the principle of positive displacement. Again, extrusion may be powered by a motor with the same control systems as others on the printer. This is a promising approach, commonly used in industries such as food processing, mining and drilling. It exerts very low shear on the fluid being transmitted which limits structural damage and allows processing of high viscosity materials.[15] Difficulties are presented by the manufacture and cleaning of the complex shapes required.

Syringe extrusion was the method selected for this project, principally due to its compatibility with disposable syringes designed for chemical handling and disposal, scaleability, and simplicity of assembly. Increasing numbers of open source plunger-based extrusion systems are available due to their many applications in science and engineering.[22] Below, two models trialled due to their clear instructions and ease of assembly are detailed.

3.2.3.3 UNIVERSAL PASTE EXTRUDER

This design, developed by Richard Horne and shown in Figure 3-7,[23] uses toothed gears to wind in a timing belt, depressing the plunger on a syringe. It was among the first paste-based extruders developed, is simple, and can easily handle a variety of viscoelastic substances. This extruder was used in early work with the printer (shown mounted in Figure 3-5). However, the high viscosity of the material used resulted in pressures at the limit of what could be exerted, which sometimes caused the gears to slip. This resulted in unreliable results and further damage to the gears. An additional downside was that, in the absence of some passive recovery system, no retraction was possible. Without this ability to pull back the plunger, extrusion-based systems suffer from

'drooling', where the nozzle continues to exude extrudate after active extrusion has stopped. This is a particular issue with low-viscosity and shear-thinning liquids, and severely limits the forms possible to those that can be achieved with a single continuous line per slice. The same limitation applies to extrusion heads which are not integrated with the printer.

Retraction is a desirable characteristic for a head used for both extrusion and UV curing, as the head may need to pass over pre-printed substances to cure them. Dropping extra uncured material on the piece at this stage would be undesirable. Additionally, resolution is already inherently limited by the viscosity of the material and lack of precision in placement decreases this further.

Figure 3-7. Universal paste extruder (Richard Horne). A motor turns a gear chain which pulls a toothed belt around a pulley. The belt contracts, bringing in a syringe holder, and with it depressing a syringe.

3.2.3.4 MOST SYRINGE PUMP

The symmetry between an extrusion drive and a syringe pump runs two ways; not only is a syringe pump an extruder, an extruder is a syringe pump. Open source syringe pump designs, produced for multiple applications including accessibility to medical technologies, are therefore a fruitful resource for 3D printer builders.

The Michigan Open Source Technology syringe pump (shown in Figure 3-8) was selected, as it benefits from a direct drive mechanism where the motor turns a screw-thread. A carriage mounted on the thread by a captured nut contains the syringe plunger. The body of the syringe is secured to a fixed point at the bottom of the thread, thus the rotation of the motor can be converted to an increased or decreased distance between syringe and plunger and thus extrusion. This configuration allows retraction, and the direct drive reduces the amount of moving parts and therefore slippage. The pump was assembled following instructions on the MOST page, with components printed on an Ultimaker 2 and on a Prusa i2s. The 3D printed parts holding the syringe were modified to accommodate the shape of the syringe plungers used, and to enable slip-on/slip-off of the retraction enabling section of the carriage. The motor originally provided with the Kossel Mini was repurposed as a driver for this system, and connected to the extrusion controller on the controlling circuit board (see 3.2.3.6).

Approximate firmware values for extrusion were calculated by multiplying the steps of the motor (minimum discrete angle turned through) by the pitch of the screw thread to calculate the distance moved by the plunger for each unit step. This was found to be approximately 4000 steps/mm. Multiplying the distance change by the internal cross-sectional area of the syringe gave the approximate conversion between motor steps and volume extruded. This was adjusted based on final printing results to allow for the volume of polymer blend extruded not correlating exactly to the displaced volume.

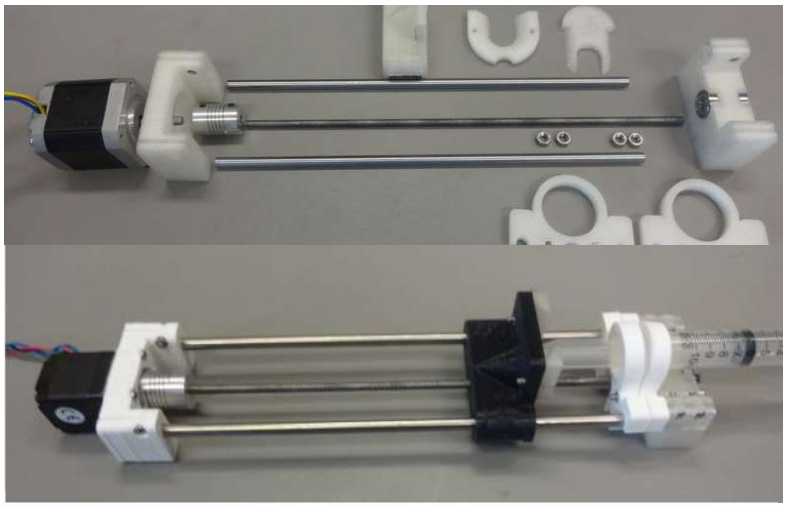

Figure 3-8. Top: Components required for the MOST syringe extruder. Bottom: assembled extruder. From Wijnen *et al.*[22]

While the limits small syringes place on print size is a concern for scientists working with established methods and materials,[24] small (10 mla) syringe sizes were appropriate for this project. Due to the iterative nature of materials research often only small volumes were available. A small volume had a more compact form factor and reduced potential waste due to unused material either becoming unreactive, or prematurely curing, in the syringe.

3.2.3.5 CONNECTING ELEMENTS

The extruder and the print head required connecting, and the fixtures developed for microfluidics were eminently suitable for this. Of the kinds of tubing tried (PTFE, HDPE, and silicone), silicone was found to be suitable due to its high flexibility – as the print head is highly mobile and the extruders are not, the material joining them must necessarily flex. To join the 3 mm tubing to the syringe, a standard Luer-lock to barb union

was used (male Luer lock-3/32" barb, Upchurch, UK)[1]; at the other end of the tubing a barb to threaded unit (3/32" barb/male 10-32 UNC, Upchurch, UK) enabled the connection to a final threaded unit holder with a female Luer lock for interchangeable needles (10/32 female UNC thread to female Luer-lock, Upchurch, UK). This final piece was secured between a 3D printed unit and a modified effector head. These were both custom designed in openSCAD in a parametric fashion (nozzle holder shown in Figure 3-9) meaning the design can be scaled by filling in the dimensions of different off-the-shelf union components and get a part designed to fit. The holder bolts onto the effector head through existing 3 mm holes in the piece, in a configuration shown in Figure 3-10.

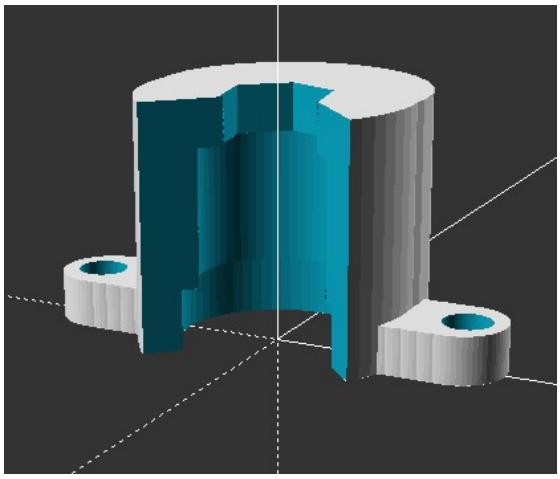

Figure 3-9 Nozzle holding component designed to fasten the end of the flexible pipe carrying polymer, and the dispensing needle, to the effector head. Designed in OpenSCAD and scaleable to the dimensions of the purchased component.

The head could then accept a variety of standard disposable Luer lock needles. 19 gauge (~1.1 mm) dispensing needles (provided cut off square at a length of 1") was found to be the most successful when printing large volume items where resolution was of low importance. Higher resolution was possible with smaller needles, but this reduced print speeds due to the limitations of the pressure possible through the syringe extruder, in accordance with Poiseille's law. As the methods of sample testing required a sample on the order of centimetres for reasonable precision, but were insensitive to fine print details, time to produce samples scaled inversely with needle diameter and a larger needle diameter was selected to enable the rapid (under 30 minutes) production of a 20 × 40 × 5 mm^3 sample. With the addition of this component, printing of viscous liquids could be achieved.

[1] Due, presumably, to the large influence of the US market, many components were only available in Imperial units. Therefore dimensions are stated in the units used by the manufacturers for clarity as to which were used successfully together, despite not being an exact match.

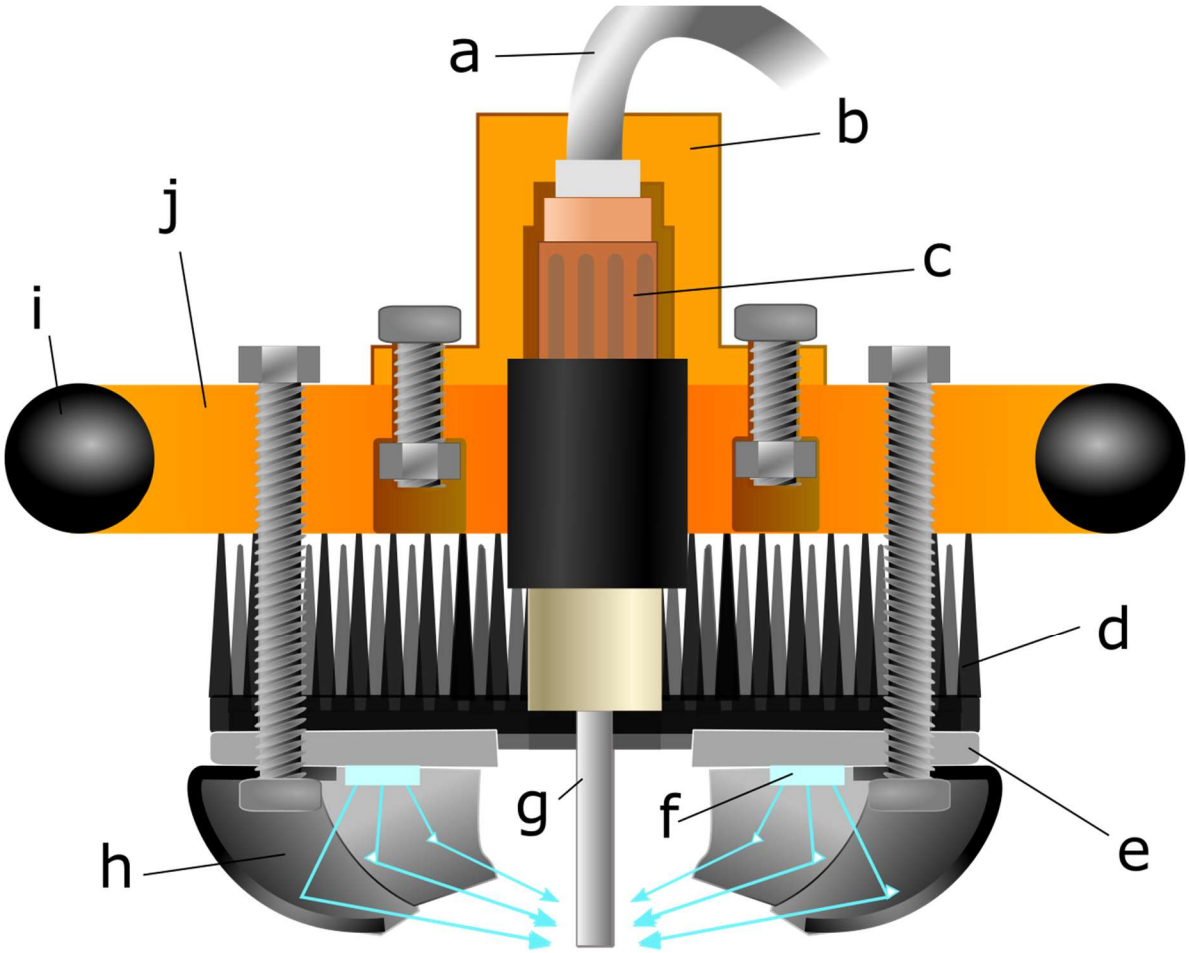

Figure 3-10. Cutaway drawing showing full print head. Labelled parts are a) tube carrying polymer from syringe, b) nozzle holder as shown in Fig 3.9, c) threaded union to needle holder, d) headsink, e) printed circuit board, f) UV LEDs, g) needle that extrusion comes from, h) focusing element, i) joints on the side which connect to rods that move the head, and j) effector mount which bears it all.

3.2.3.6 ELECTRONICS

Few changes were made to the Kossel Mini in terms of electronics. Heated components were disconnected and the firmware was overwritten to allow extrusion at low temperatures, eliminating a safety setting which prevents motors trying to push polymers through unheated extrusion nozzles and potentially causing damage. Motor wires were extended to allow the extruder to be located above the printer, and an additional simple circuit was added for LEDs, detailed in Section 3.2.3.5.

3.2.3.7 LIGHTING ELEMENTS

Much prior work has, where sources are specified, used a standalone UV lamp or one fitted with a waveguide, such as the Dymax BlueWave 75 Rev 2.0 UV Light Curing Spot Lamp System to cure 3D printed gels.[25,26] These retail for above £4,000 and are not designed to allow computer control. A cheaper, more streamlined and easier to integrate alternative is to use LEDs mounted in a printed circuit board. Compared to lamps, LEDs are more efficient, more compact, easily modulated to deliver precise intensities, and deliver a well-defined range of frequencies, thus avoiding unwanted photo-triggered reactions. LEDS have been used by Sears *et al.* to create a 'cure on dispense' system, where UV curing of emulsion inks enables the shaping of foams, with success.[27] This shows the potential of head-mounted LEDs on extrusion-based printers, even when restricted to binary operation; either continually illuminating the gels during the print process, or to cure a final product once assembled. In this work this is extended to integrate printer control of LEDs and modulate curing in the same manner as other print variables such as speed and temperature.

Surface-mounted deep UV LEDs of peak wavelength

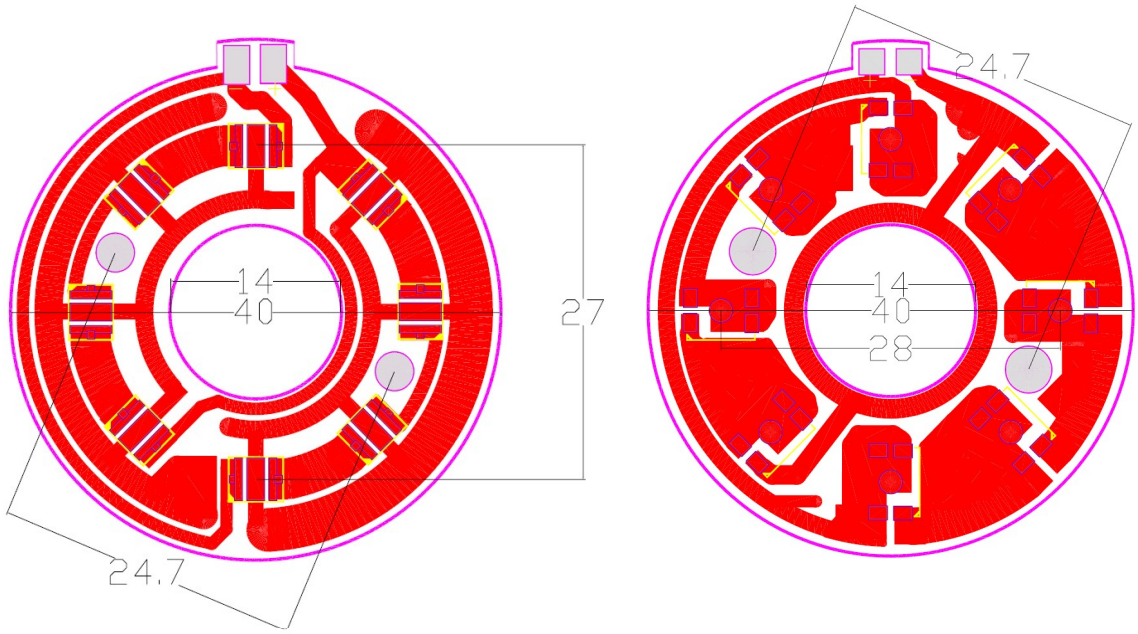

Figure 3-11. Printed circuitboard layouts for circular arrays of UV LEDs of wavelength 265nm (left) and 365nm (right). Distances are given in mm, red indicates tracks, magenta cut lines, and grey solder pads. Smaller holes are for screws to secure to effector and larger hole is for needle (see Figure 3-10 for diagram showing positioning in use)

265±14 nm (Zhuhai Tianhui Electronic Co Ltd, Shenzhen, part number TH-UV265A-3535) and 365±13 nm

(suppliers as before, part number TH-UV365t3WA-5045) were sourced from Zhuhai Tianhui Electronic Co, Shenzhen, China, and a circularly symmetric PCB bearing 8 LEDs was designed by the same company to specifications provided, to fit around the print needle as shown in Figure 3-10. The circuit boards are shown in Figure 3-11 and are provided freely online as industry-standard Gerber files at https://github.com/MxEntropic.

With a typical forward voltage of 6 V at 20 mA for 265nm, and 4.2 V at 500 mA for 365 nm, power losses could have been reduced by placing all LEDs in series, reducing the current. However, this would have required voltages of up to 48 V, which would be difficult to provide with off-the-shelf power supplies. As a compromise, the LEDs were connected in two parallel banks of 4, giving operating voltages and currents of 24 V, 40 mA for the 265 nm wavelength and 16.8 V, 1 A for 365 nm. This is beyond the capability of the Kossel Mini electronics to supply (12 V standard),[20] so a separate power supply (Voltcraft) was added to provide power.

The LEDs and printer were interfaced by a N-channel IRL540N MOSFET, connected as shown in Figure 3-12, allowing a spare pin on the Arduino Mega 2560 block to gate the power supply to the LEDs. Output pin D4 was selected as it supports pulse width modulation, allowing 256 levels of variation in intensity. UV LED brightness could then be set with the G-code sequence 'M42 P4 S{0-255}' where the number in brackets indicates the brightness level, 0 as off and 255 as brightest. This could be done during printing, as part of the G-code instructions sent to the printer, or while the machine was idle.

The 365 nm wavelength had a power of 16.8 W and so required heat dissipation elements in use. This was provided by a recycled aluminium heatsink, cut to shape. The LEDs have a wide field of illumination and so a simple focusing element was added. Made from thin aluminium, it was hand-crimped to form a rounded shape and direct the light into a central spot of approximately 10 mm diameter, as shown in Figure 3-10.

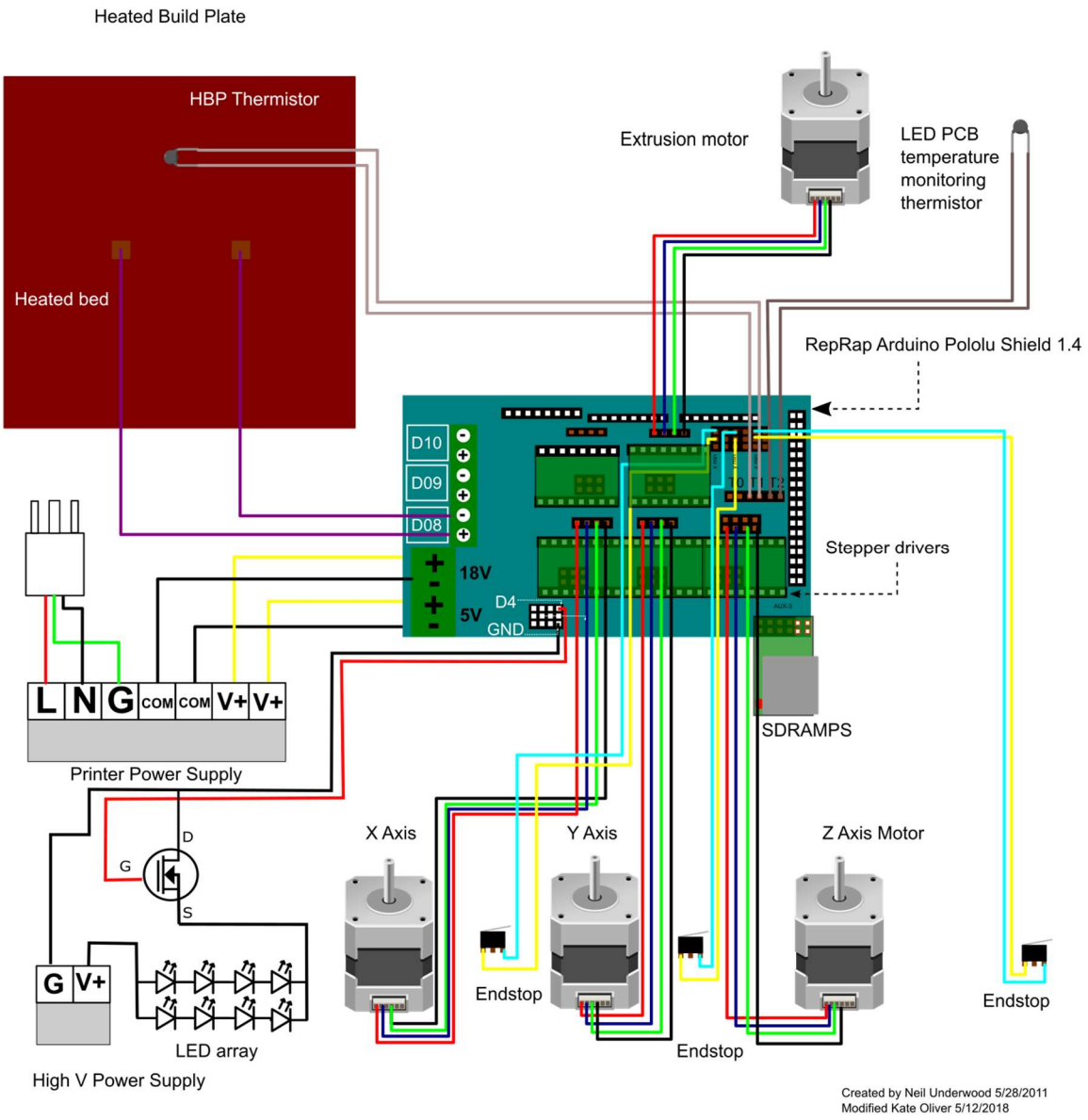

Figure 3-12. Wiring diagram showing RAMPS connections used for gel printer. Clockwise from bottom left: An additional, higher voltage supply powers the LEDs, switched by a transistor with output pin D4, from the servo block of output pins, acting as a gate. Motors and corresponding endstops (switches triggered when the carriages reach their limits of motion) are retained, and interfaced via stepper drivers which provide the appropriate signals to the motor coils. The thermistor originally used for regulating hot end temperature during melted plastic extrusion is repositioned on the LED mount and used to monitor circuit heating effects. The extrusion motor remains, only now the extrusion compresses a syringe rather than feeding a filament through cogs. Heated bed is retained for processing materials requiring drying (such as cellulose solution) and thermistor allows temperature control. 18V and 5V are supplied to the board, 18V to drive the motors and heating elements and 5V for the internal operations of the Arduino. Diagram created by Neil Underwood, CC-BY, and modified by the author

To relate the voltage supplied to the LEDs to a final intensity, a voltage-intensity curve was defined for 265nm LEDs using a 254 nm UV radiometer (UVP). This is shown in Figure 3-13.

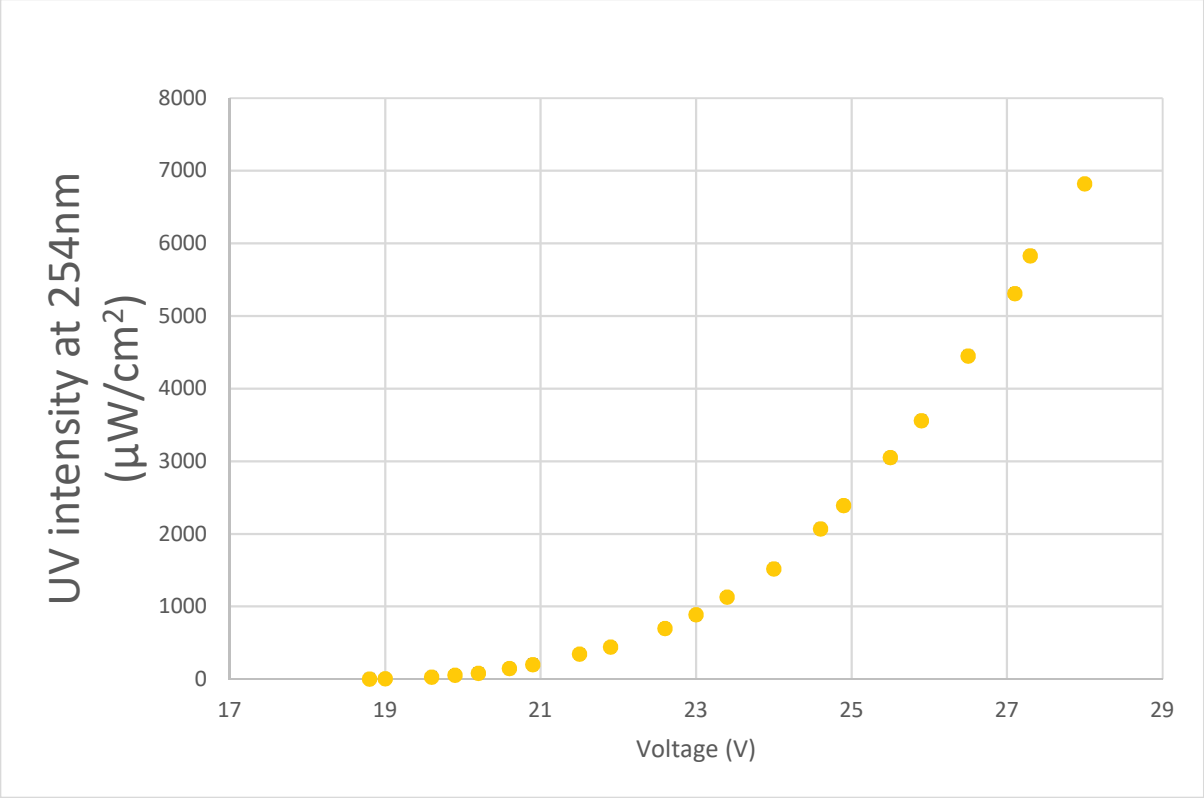

Figure 3-13. Intensity of 265nm sensitive LEDs, measured with 254nm light sensor, as a function of voltage supplied at constant current. Errors are derived from the equipment sensitivity.

The components tested exhibited a typical LED response curve with a turn-on voltage at around 20 V, increasing to an approximately linear relationship between 24 and 28 V. Measurements were discontinued at 28 V as this corresponded to the manufacturer's maximum advised voltage per component. When using this element for curing, an operating voltage of 27 V was used. This yielded an intensity of 5.5 mW/cm^2 without causing excessive damage to the LEDs that could shorten their lifetime.

3.2.3.8 COOLING CAPABILITY

Following the observations of Bakarich *et al.* a method to maintain the temperature below 15 °C until crosslinking was complete was required. The 3D printer incorporates some degree of thermal control by default, using the proportional-integral-derivative (PID) algorithm to adjust the amount of energy supplied to a heater in response to thermal measurements to approach a set value. This could theoretically be adapted to

accommodate a cooled stage or containing box by replacing the heating element with Peltier (thermo-electric) or water cooling. However, adding these elements into an already small form factor would reduce build space, and the heat moved from the system would need to be dissipated some distance away to avoid overheating the electronics.

No dynamic chilling control was required, only a fixed static temperature below 15°C. Further, the system was insensitive to thermal variation, as the largely water-based system has a high specific heat capacity. Therefore, there was no need for active interface between the printer and the cooling system. A simple, effective way to achieve the desired specifications was to place the printer in a domestic refrigerator, running wires out for power and control. A second-hand consumer fridge was purchased from Display Refrigeration for this purpose, selected for its dimensions and glass door. This latter permitted observation while providing an additional safety measure against harmful UV exposure.

The thermistor originally intended to monitor the temperature of the hot end in use was repurposed to monitor the temperature of the LED component, ensuring that temperatures did not exceed appropriate temperatures for the PLA effector head (below 120 °C). Bed temperature monitoring provided an indication of the temperature of the printed material in situ.

3.2.3.9 OPERATIONAL PRACTICE

In operation, standard print parameters used were an extrusion width of 0.8 mm, an extrusion height of 0.5 mm, and maximum print speed of 10 mm s^{-1}. Following the printing of the gel shape the extrusion head was removed to ensure no further drool and minimise the illumination-print distance. This step requires manual intervention, and it would be desirable to remove this in future iterations. The UV LEDs were illuminated, and curing was performed by rastering the head over the print at a speed of 0.6 mm s^{-1} at a height of 1mm over the final print surface. This speed was determined experimentally as ensuring total curing.

There are of course two ways to vary the exposure of the gel; the intensity of the LEDs and the speed of the head. This offers interesting modulation possibilities which are discussed further in Chapter 4; however, within this thesis maximum intensity was used at all times. This choice was made to minimize premature crystallisation (see Section 3.2.4).

To generate the instructions for curing, a Python script was written which takes an existing G-code script – a set of instructions of moves and extrusions the machine must make to print - and appends UV curing instructions. This can be a simple raster over a given area, or an exact copy of the print pattern used but with illumination. The latter was appropriate for shapes with a high concavity, such as the flower shown in Figure 3-2.

For speed of processing, prints were performed on glass slides (56 × 78 mm, 'Clarity' slides, Smith Scientific) which were then removed and placed in a 0.1 M calcium chloride bath in a petri dish for 24 h. Removable print surfaces allowed calcium chloride curing to occur simultaneously with printing, speeding up production. This also minimized contact between corrosive $CaCl_2$ solutions and metal printer parts. During curing, prints de-adhered from the slide, becoming suspended in solution and thus receiving even exposure to strengthening ions. Subsequently the ionised solution was replaced with deionized water for a further 48h to remove any unreacted monomers and allow the gel to swell to equilibrium volumes. When not being tested, samples were stored in vials of deionized water.

3.2.3.10 SOFTWARE AND FIRMWARE CHOICES

The hardware of the printer is only one part of the printing process, and all must be accessible to enable appropriate reproducibility.[5] While details of 3D printing vary according to the myriad of print materials and methods now available, the process can be broken down into well-defined stages illustrated in Figure 3-1. For this project, the following choices were made, ensuring that from concept to finished print all software and firmware was accessible.

3.2.3.10.1 DESIGN

All designs for printed hydrogel test samples were created in openSCAD. This was also used to generate all hard-polymer 3D-printed functional parts required. openSCAD is free software which generates 3D solids from text-based input: it can perform mathematical calculations, process recursion, and can take user-defined variables. Many existing works in paste extrusion and 3D printing are published in this language, which primarily drove adoption for this project. It is licensed as GPL 2.0.

3.2.3.10.2 SLICER

The software which translates between a design and the printer movements necessary is known as a slicer. For this work, Slic3r (Prusa Edition) was used. Slic3r is compatible with all printers, highly customisable, and licensed GPL 3.0. Setting profiles were created for different print nozzles and styles of printing - such as a simple back and forth print for test samples and a slow print with extra perimeters for edges. The Prusa version was used as it is the most stable at time of writing.

3.2.3.10.3 G-CODE SCRIPT MODIFICATION

Where G-code script modifications were necessary (such as to allow light exposure or integrate extra wait times for materials to dry between layers), this was easily performed in Python 3.0. The process simply required reading in a G-code file in text format, identifying move commands, removing extrusion commands and inserting commands to turn the lights on. Options included rastering over the bounding box of the shape, at a given speed and with a specified focus size, or following the print moves exactly.

3.2.3.10.4 PRINTER CONTROL

A graphical interface on a connected laptop enabled retraction of syringe holder for un-loading and re-loading, movement of head away from print surfaces to unimportant regions, and test extrusion of material through the nozzle before printing to check set up, without needing to open the fridge. For this Pronterface was used, as it has both a graphical user interface and command line, suiting a wide range of users. The interface can be customised but offers as standard a visualisation of the print path taken and graphs of bed and head extrusion temperature. As before, Pronterface is compatible with all sorts of printers and operating systems, licenced GPL 3.0.

3.2.3.10.5 PRINTER FIRMWARE

The firmware Marlin translates text instructions about locations and extrusion lengths into basic signals such as the voltages to be sent to motors. This runs on Arduino, a commonly-used open source electronics prototyping platform,[28] and is licensed GPL 2.0. This was used much as received from Think3DPrint3D, with the only variables modified being default motor distances, steps per millimetre, and extrusion temperatures, to account for the changes in range of motion, configuration, and cold extrusion.

3.2.4 PERFORMANCE EVALUATION

The purpose of this section of work was to enable PNIPAM-alginate gel processing in a manner similar to that of published papers on shape-changing hydrogels,[1,21] but using a fully open-source and reproducible solution. The system created can produce shaped PNIPAM-alginate gels which are elastic and transparent, suggesting no phase separation is taking place. This is supported by Raman spectroscopic observations shown in Chapter 4. The technologies used have been drawn from those provided by a GPL license, and innovations added have been documented and published under the same license at https://github.com/MxEntropic/protea-parts.

3.2.4.1 PRINT QUALITY

The printer can position a needle of the finest gauge available with a precision of 100 μm in X, Y and Z directions. However, for 3D print systems, this does not necessarily translate into an 100 μm resolution on finished prints, due to material flow, expansion during curing, uneven curing rate, and other variations between layers. With an extrusion-based system used for multiple materials the resolution achievable will vary depending on material. This system has successfully extruded and shaped 6 wt.% cellulose nanocrystal solution, 4 wt.% carboxymethyl cellulose solution, cellulose nanocrystals with ferrofluid, alginate at 3 wt.%, and silk dissolved in lithium bromide (into an ethanol bath).

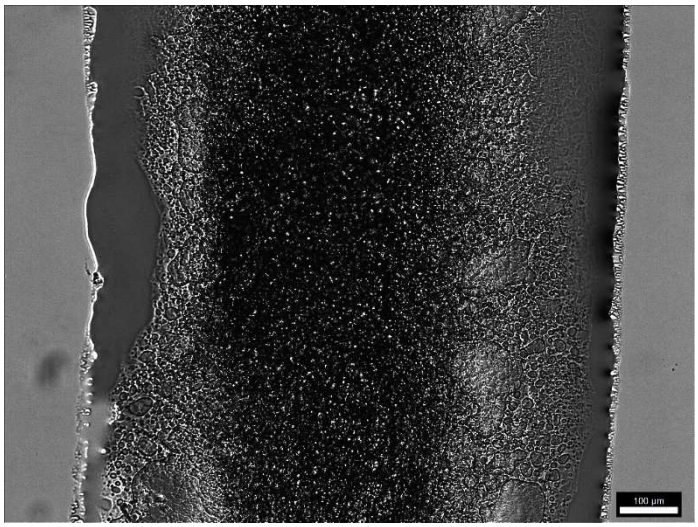

Figure 3-14 Printed 750μm thick line of cured PNIPAM-alginate. Pores are water-rich regions formed during gelation process. Channels on either side are unreacted solution, meaning final gel is smaller than extruded line. Image taken with Leica microscope by Abraham Mauleon Amieva.

Minimum resolution has not been tested fully since this was not a primary aim. However, at least 500μm horizontal resolution has been achieved, with 200 μm resolution in the vertical direction. As is standard in 3D printing, Z dimension resolution is higher than XY due to the inevitable effects of gravity.

An additional consideration for printing PNIPAM-alginate hybrids is the unavoidable presence of an unreacted outer layer consisting of alginate and NIPAM monomer, where the radicals created by the photoinitator form peroxide radicals rather than inducing

polymerisation.[29] This manifests as a thin (~50μm) layer of alginate and monomer solution on the surface of the print, shown in Figure 3-14. While the NIPAM monomers will not have crosslinked, there is no inhibitory effect on the alginate component when placed in $CaCl_2$, leading to the formation of a thin alginate-NIPAM shell around the areas of the piece in contact with air.

This can be easily removed by stretching the entire piece to generate cracks in this outer, much less elastic layer, and gently rubbing to remove them. This reduces the size of any prints created by a predictable amount. It also limits the smallest dimension that can be achieved in PNIPAM-alginate to the thickness of this layer (in the absence of other mitigating strategies such as the inclusion of oxygen scavengers[1] or processing in an inert environment[30]).

One further complexity is that, if the humidity in the environment is insufficient, the blend dries and NIPAM crystallises before polymerisation can take place. Once crystallised, the radicals cannot penetrate the monomer and no crosslinking will occur until the mixture is redispersed. This case is shown in Figure 3-15.

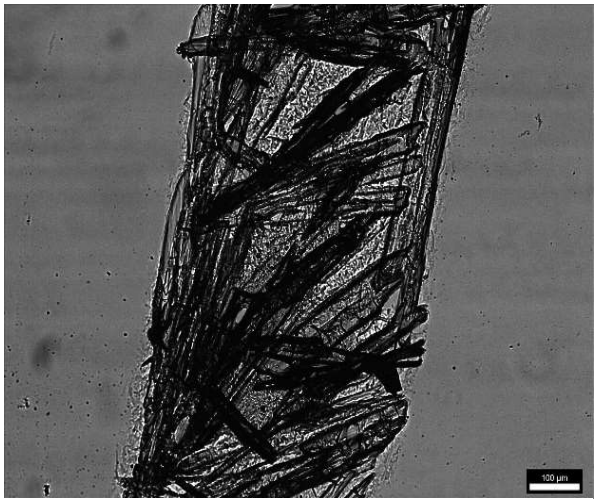

Figure 3-15. Crystallized 510μm-thick line of PNIPAM-alginate. If the humidity is too low, the PNIPAM-alginate solution crystallizes rather than polymerising and crosslinking.

Since the UV illumination inevitably creates some heating, this places an extra constraint on the minimum PNIPAM-alginate resolution possible. Smaller samples exhibit a larger surface-to-volume ratio, drying more rapidly, and increases their temperature more rapidly if exposed to heat. During printing, adequate humidity (found experimentally as >70%) was monitored using a temperature and humidity sensor (Amazon UK). If necessary, humidity was raised with the addition of an open water container with immersed tissue paper to increase evaporation rates.

3.2.4.2 ACCESSIBILITY

The entire process described above for 3D printing avoids any legal restrictions on accessibility, as all components are licenced according to the GPL and published on a freely available repository. Limitations on

access to parts are minimised due to the use of standard components and provision of all designs, enabling adaptations to accommodate changes required. A price breakdown (neglecting labour costs) is provided in Table 3.1. Excluding part printing time, a build could be completed in two days, assuming no particular familiarity with 3D printers but a beginner level of soldering and familiarity with hand tools.

Component	**Cost**
Kossel mini body, printed, and all components required for assembly	£499
265nm UV LEDS – 8@$9USD*	£56.16
365nm UV LEDS – 8@$2.7USD*	£16.85
PCB design and manufacture - $45 USD	£35.10
30V Power supply	~£20 (if bought new – in this case used from lab)
Transistor	0.15p
Connector parts: Silicone tubing, barb union, luer union	£30
Extruder parts: linear bearings, regular bearings, threaded bar	£15
Second hand fridge	£250
Focusing element, bolts, heatsink	Used found components
Total:	£923.28

Table 3.1 Cost of components of printer. *Converted at 1USD = 0.78GBP, values taken from xe.com 23/11/2018

Comparing to the off-the-shelf solutions benchmarked in 3.2.2, this combination of equipment is at least a factor of 4 cheaper than other extrusion printers. It additionally has two 'advanced' features only seen on higher range bioprinters – the ability to operate at temperatures below ambient, and UV curing. Further, since the bioprinters only implement UV for blanket curing or disinfecting, the on-head mounting allows modulated and localised exposure, allowing for more options during print. The potential of this will be explored further in Chapter 4. The small build volume allows containment in a refrigerator in place of dynamic chilling control, providing an inexpensive, controlled, chilled and humid environment suitable for gel processing.

3.2.5 ISSUES AND IMPROVEMENTS

Since the commencement of this project large strides have already been made in the availability of OS gel printers, to which this project is a small, simple contribution. The large volume extruder published in Hardware X by Pusch et al.[24] seems promising, and for a budget in the thousands the Discov3ry and Hyrel printers have produced good results.[27,31] It is suggested that any other researchers building their own equipment assess what is available on a regular basis to critically evaluate the current best option, including the possibility of hybridising self-built and integrated systems.

The system presented here has 10 ml print volume and a 0.5 mm precision, sufficient for this stage of the project, but further developing work would benefit from larger volumes and higher precision. For this purpose improving the design by incorporating aspects from the Large Volume Extruder[24] and auger-based designs would be of interest. The low shear exerted by an auger-based design could reduce the drooling seen, as this originates from shear thinning and viscoelastic lag in the materials. This could also be reduced by dropping the distance between syringe and printhead. Previously, delta printers have been modified to have a motor mounted on the effector, but this affects mechanical precision as the increased weight slows deceleration. The only other option would be to move to a Cartesian print body, but this would limit the curing patterns and speed possible. A screw-driven system would be the easiest upgrade to try, and open source designs are now available.[32] A miniature servo that deployed a 'tray' under the nozzle to catch any unwanted drops, or retracted the needle, would also be an option.

The LED circuits are inefficient due to the unnecessarily high currents used and remain highly lossy in operation, particularly since cooling is being maintained. The circuit could be redesigned to integrate a voltage converter, or a higher voltage could be supplied initially to drop the current. Re-adding the original fan mounted on the effector head would be one easy way to cool it further, requiring just a tweak of the design to allow space for the mount. Another desirable improvement would be to add a height probe to the head, to detect misalignment in the bed and correct for it, allowing greater precision in surface printing.

To the knowledge of the author, no other G-code controlled UV-mounted head has been implemented. This has great potential even at this early stage, for which further evidence and applications will be provided in Chapter 4. Simple improvements could be made by reducing the size of the focal spot via a lens or a true parabolic mirror

enclosure. This could be created cheaply by 3D-printing the shape and then adding a reflective coating. Alternatively, a fibre-optic cable could be used, reducing heating effects or even a UV laser as seen in the work of Llewellyn-Jones et al.[33]

3.3 CONCLUSION

A fully open-source platform capable of proving the extrusion, chilling and curing capabilities required to process PNIPAM-alginate double network gels was sought. An appropriate system was developed and documented to enable replicability. The system produced combines existing designs for a delta printer and an open source syringe pump using microfluidic components and 3D printed parts, and has successfully been used to process silk, cellulose, nanocellulose crystals and alginate. Adding enclosure in a chilled environment and LED curing elements integrated with the on-board printer control produces a printer capable of processing shaped PNIPAM-alginate double network gels, with a resolution of 0.5 mm in *x* and *y* dimensions, and 0.1 mm in the *z* dimension. Improvements to resolution of the gel extrusion and of the UV curing area illuminated would be desirable, and could be achieved using a progressive cavity pump and improved optics. However, at the current design stage, performance is comparable to that of off-the-shelf models. All processes are tailorable, from design to firmware, and costs for build are at least 4× lower than existing products (neglecting labour). Integration of an on-head UV curing element allows UV exposure to be modulated as another printing variable, it is believed, for the first time. This enables exciting applications that will be shown in Chapter 4.

3.4 REFERENCES

(1) Sydney Gladman, A.; Matsumoto, E. A.; Nuzzo, R. G.; Mahadevan, L.; Lewis, J. A. Biomimetic 4D Printing. *Nat. Mater.* **2016**, *15* (4), 413–418. https://doi.org/10.1038/nmat4544.

(2) Bakarich, S. E.; Gorkin, R.; in het Panhuis, M.; Spinks, G. M. 4D Printing with Mechanically Robust, Thermally Actuating Hydrogels. *Macromol. Rapid Commun.* **2015**, *36* (12), 1211–1217. https://doi.org/10.1002/marc.201500079.

(3) Ober, T. J.; Foresti, D.; Lewis, J. A. Active Mixing of Complex Fluids at the Microscale. *Proc. Natl. Acad. Sci. U. S. A.* **2015**, *112* (40), 12293–12298. https://doi.org/10.1073/pnas.1509224112.

(4) Bakarich, S. E.; in het Panhuis, M.; Beirne, S.; Wallace, G. G.; Spinks, G. M. Extrusion Printing of Ionic–covalent Entanglement Hydrogels with High Toughness. *J. Mater. Chem. B* **2013**, *1* (38), 4939. https://doi.org/10.1039/c3tb21159b.

(5) Stark, P. B. Before Reproducibility Must Come Preproducibility World-View. *Nature*. 2018. https://doi.org/10.1038/d41586-018-05256-0.

(6) Chen, H.; Lun, Y.; Ovchinnikov, D.; Kokubo, H.; Oberg, K. C.; Pepicelli, C. V.; Gan, L.; Lee, B.; Johnson, R. L. Limb and Kidney Defects in Lmx1b Mutant Mice Suggest an Involvement of LMX1B in Human Nail Patella Syndrome. *Nat. Genet.* **1998**, *19* (1), 51–55. https://doi.org/10.1038/ng0598-51.

(7) Jones, R.; Haufe, P.; Sells, E.; Iravani, P.; Olliver, V.; Palmer, C.; Bowyer, A. Reprap - The Replicating Rapid Prototyper. *Robotica* **2011**, *29* (1 SPEC. ISSUE), 177–191. https://doi.org/10.1017/S026357471000069X.

(8) Bij, E. van der; Serrano, J.; Wlostowski, T.; Cattin, M.; Gousiou, E.; Sanchez, P. A.; Boccardi, A.; Voumard, N.; Penacoba, G. Open Hardware for CERN's Accelerator Control Systems. *J. Instrum.* **2012**, *7* (01), C01032–C01032. https://doi.org/10.1088/1748-0221/7/01/C01032.

(9) Nilsen, V.; Anelli, G. Knowledge Transfer at CERN. *Technol. Forecast. Soc. Change* **2016**, *112*, 113–120. https://doi.org/10.1016/J.TECHFORE.2016.02.014.

(10) Open Source Hardware Association. Definition (English) – Open Source Hardware Association

https://www.oshwa.org/definition/ (accessed Nov 22, 2018).

(11) Pearce, J. M. The Future of Open-Source Hardware and Science. In *Open-Source Lab*; 2014; pp 255–263. https://doi.org/10.1016/B978-0-12-410462-4.00007-X.

(12) Dryden, M. D. M.; Fobel, R.; Fobel, C.; Wheeler, A. R. Upon the Shoulders of Giants: Open-Source Hardware and Software in Analytical Chemistry. *Anal. Chem.* **2017**, *89* (8), 4330–4338. https://doi.org/10.1021/acs.analchem.7b00485.

(13) Pearce, J. M. The Case for Open Source Appropriate Technology. *Environ. Dev. Sustain.* **2012**. https://doi.org/10.1007/s10668-012-9337-9.

(14) Ozbolat, I. T.; Moncal, K. K.; Gudapati, H. Evaluation of Bioprinter Technologies. *Addit. Manuf.* **2017**, *13*, 179–200. https://doi.org/10.1016/J.ADDMA.2016.10.003.

(15) Sun, J.; Zhou, W.; Yan, L.; Huang, D.; Lin, L. Extrusion-Based Food Printing for Digitalized Food Design and Nutrition Control. *J. Food Eng.* **2018**, *220*, 1–11. https://doi.org/10.1016/J.JFOODENG.2017.02.028.

(16) Sher, D. The Top 10 Bioprinters https://3dprintingindustry.com/news/top-10-bioprinters-55699/ (accessed Nov 23, 2018).

(17) 3ders.org - Introducing CELLINK's BIO X, the "most user-friendly" 3D bioprinter http://www.3ders.org/articles/20170113-introducing-cellink-bio-x-most-user-friendly-3d-bioprinter.html (accessed Nov 23, 2018).

(18) Think3dPrint3D. Kossel Delta Printer Kit https://www.think3dprint3d.com/3D-Printer-Kits/Kossel-XLplus-3dPrinter-Kit (accessed Nov 27, 2018).

(19) Rocholl, J. Kossel Mini https://github.com/jcrocholl/kossel.

(20) RepRap project. RAMPS 1.4 - RepRap https://reprap.org/wiki/RAMPS_1.4 (accessed Nov 23, 2018).

(21) Naficy, S.; Gately, R.; Gorkin, R.; Xin, H.; Spinks, G. M. 4D Printing of Reversible Shape Morphing Hydrogel Structures. *Macromol. Mater. Eng.* **2017**, *302* (1), 1600212. https://doi.org/10.1002/mame.201600212.

(22) Wijnen, B.; Hunt, E. J.; Anzalone, G. C.; Pearce, J. M.; Miller, K.; Voas, J.; Costello, T.; Glynn, L.; Hallgren,

K.; Houck, J.; et al. Open-Source Syringe Pump Library. *PLoS One* **2014**, *9* (9), e107216. https://doi.org/10.1371/journal.pone.0107216.

(23) Horne, R. Reprap development and further adventures in DIY 3D printing: Universal Paste extruder - Ceramic, Food and Real Chocolate 3D Printing... https://richrap.blogspot.com/2012/04/universal-paste-extruder-ceramic-food.html (accessed Jul 18, 2018).

(24) Pusch, K.; Hinton, T. J.; Feinberg, A. W. Large Volume Syringe Pump Extruder for Desktop 3D Printers. *HardwareX* **2018**, *3*, 49–61. https://doi.org/10.1016/J.OHX.2018.02.001.

(25) Bakarich, S. E.; Gorkin, R.; Naficy, S.; Gately, R.; in het Panhuis, M.; Spinks, G. M. 3D/4D Printing Hydrogel Composites: A Pathway to Functional Devices. *MRS Adv.* **2015**, 1–6. https://doi.org/10.1557/adv.2015.9.

(26) Naficy, S.; Gately, R.; Gorkin, R.; Xin, H.; Spinks, G. M. 4D Printing of Reversible Shape Morphing Hydrogel Structures. *Macromol. Mater. Eng.* **2017**, *302* (1), 1600212. https://doi.org/10.1002/mame.201600212.

(27) Sears, N. A.; Dhavalikar, P. S.; Cosgriff-Hernandez, E. M. Emulsion Inks for 3D Printing of High Porosity Materials. *Macromol. Rapid Commun.* **2016**, *37* (16), 1369–1374. https://doi.org/10.1002/marc.201600236.

(28) Arduino. What Is Arduino?

(29) Mucci, V.; Vallo, C. Efficiency of 2,2-Dimethoxy-2-Phenylacetophenone for the Photopolymerization of Methacrylate Monomers in Thick Sections. *J. Appl. Polym. Sci.* **2012**, *123* (1), 418–425. https://doi.org/10.1002/app.34473.

(30) Wang, J.; Lin, L.; Cheng, Q.; Jiang, L. A Strong Bio-Inspired Layered PNIPAM-Clay Nanocomposite Hydrogel. *Angew. Chemie - Int. Ed.* **2012**, *51* (19), 4676–4680. https://doi.org/10.1002/anie.201200267.

(31) Mulakkal, M. C.; Trask, R. S.; Ting, V. P.; Seddon, A. M. Responsive Cellulose-Hydrogel Composite Ink for 4D Printing. *Mater. Des.* **2018**, *160*, 108–118. https://doi.org/10.1016/J.MATDES.2018.09.009.

(32) Moineau Extruder by coricoco - Thingiverse https://www.thingiverse.com/thing:2424818 (accessed Nov 30, 2018).

(33) Llewellyn-Jones, T. M.; Drinkwater, B. W.; Trask, R. S. 3D Printed Components with Ultrasonically Arranged Microscale Structure. *Smart Mater. Struct.* **2016**, *25* (2), 02LT01. https://doi.org/10.1088/0964-1726/25/2/02LT01.

4 LIGHT-INDUCED GRADIENTS IN PNIPAM-ALGINATE PRINTS

4.1 ABSTRACT

An existing 3D-printable PNIPAM-alginate formulation was characterised in terms of the molecular weight, copolymer formulation, and elastic moduli of the component gels both singly and as an interpenetrating network gel. The viscoelastic properties of the uncured polymer blend were found to depend dramatically on the order of preparation, which was attributed to complexation effects. The blend was successfully processed into shaped, thermoresponsive gels using the open-source equipment and techniques documented in Chapter 3, demonstrating the applications of this accessible technology.

Final pieces were printed in flat beam, disc and flower shapes. Following full crosslinking, these adopted curved configurations, both in in equilibration with water at ambient temperature and at temperatures above the lowest critical solution temperature (LCST). The radii of curvature differed in both magnitude and direction as a function of the thickness of the piece and the direction of curing illumination. This light-induced phenomenon is previously undocumented and could provide a facile route to programmable complex shape change in shaped gels. However, while a high sensitivity shows potential for programmed shape change, it inhibits sample reproducibility. Therefore, further investigation into the relation of curvature to dimensions would be required to accurately predict equilibrium configurations.

The effect was theorised to originate from either a difference in crosslinking density or pore structure. Raman spectroscopy indicated a high similarity between both sides of a dried bending sample, making a difference in chemical bonds unlikely. Imaging of pores was attempted using scanning electron microscopy (SEM) and confocal microscopy, highlighting issues with reliance on dried imaging methods. Due to within-sample structural variation and small feature size, more data would be required to draw statistically valid conclusions, although a previously-undocumented population of sub-0.5 μm^2 pores was recorded. A hypothesis for the origin of the effect is proposed, based on osmotic gradients between first-cured and uncured polymer blend.

4.2 INTRODUCTION

As outlined in Chapter 1, the working material is a double network hydrogel formed from the covalently bonded thermoresponsive network poly-n-isopropyl alcohol (PNIPAM) interpenetrated with a physically bound strong alginate network, crosslinked with divalent calcium cations. This gel was selected as it had already been demonstrated as suitable for responsive 3D printing, was non-toxic, abundant, and low cost.

4.2.1 THERMORESPONSIVE POLYMER: POLY N-ISOPROPYL ACRYLAMIDE

One of the best characterised responsive hydrogel materials is poly-n-isopropyl acrylamide, PNIPAM. Above approximately 32 °C it becomes energetically advantageous for the polymer to preferentially interact with itself rather than the solvent, and its polymers coil in on themselves. This coil-globule transition occurs at a temperature known as the LCST, the lowest critical solution temperature. The exact details of the LCST are affected by molecular weight,[1] temperature of processing,[2] and crosslinking environment [3], but the result is the same: a gel that contracts to approximately 40% of its original volume.

The degree of thermally-triggered contraction depends on the solvent and the level of crosslinking between the polymers. Higher levels of crosslinking cause a decreased ratio between the swollen and contracted states: while the minimal volume occupied is the same, a higher degree of cross linking imposes a constraint on the free gel which leads to a smaller volume in equilibrium. This has been shown experimentally many times,[4] and has been described by Flory and Rehner among others.[5]

While synthesis of PNIPAM gels may be achieved in a number of ways,[3] commonly polymerisation and crosslinking are induced simultaneously *via* free radical or redox reactions within a concentration of monomer (isopropyl acrylamide) and a crosslinking agent (often methylene bisacrylamide). The chemical structure of the crosslinked gel and the crosslinker methylene bisacrylamide (MBA) are shown in Figure 4.1.

The advantage of the free radical route is that the process of gelation may be triggered externally without contact, for example by illumination of the correct wavelength combined with a photoinitiator such as diethoxyacteophenone (DEAP).[6] Redox-triggered gelation is also possible, which allows initiation inside opaque moulds and in gels with a high percentage of opaque filler.[7]

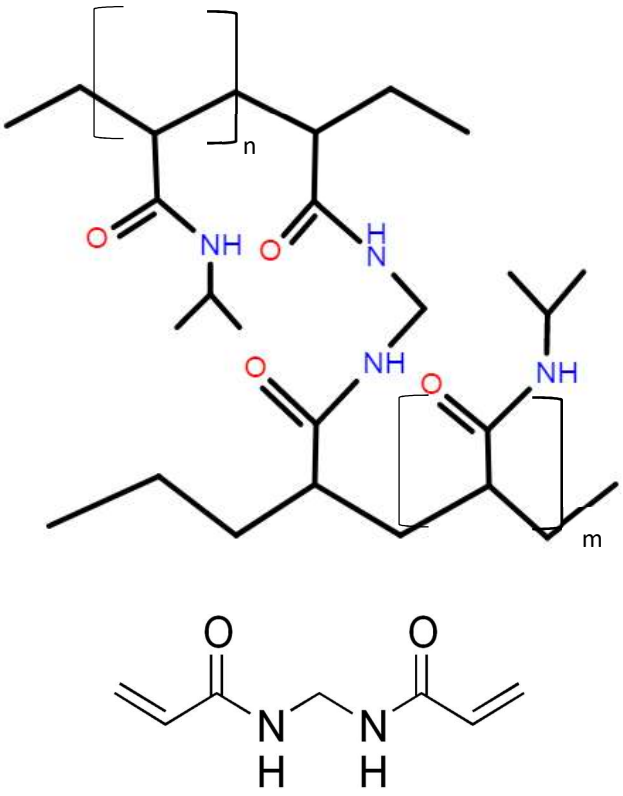

Figure 4.1. The chemical composition of poly-N-isopropyl acrylamide gel. Top: a polymer of n units is shown crosslinked with a polymer of m units. Bottom: the chemical structure of methylene bis-acrylamide, a commonly used crosslinking agent.

At a microscopic level, the effect of the degree of crosslinking is evident under SEM, with clear pores visible that decrease as the weight percentage of crosslinking agent added increases.[4] This is supported by Raman microscopy imaging which confirms that PNIPAM gels segregate at a microscopic scale into water- and polymer-rich regions, forming a micrometer-scale pore structure.[8] This length scale also contracts during the thermal transition. At the molecular level, UV Raman spectroscopy has clarified the change in conformation which underlies the packing transition of the amide groups, whereby these functional groups orient themselves inwards, forming hydrophobic pockets.[9]

This contraction may be triggered by heating in solution or in air, and is fully reversible. With the addition of nanoparticles, the PNIPAM LCST transition may be triggered externally by laser or incoherent light [10,11] or inductive heating. [12] The nature of the thermal contraction is affected by the ionic environment, with the 'sharp, yet continuous' native transition becoming a discontinuous transition in the presence of higher ion concentrations.[13]

PNIPAM has been shown to be non-cytotoxic to epithelial, smooth muscle, and fibroblast cells, and to exhibit sensitivity in endothelial cells depending on the source. It is considered a candidate for medical applications, but requires application-specific cell testing.[14]

However, PNIPAM in its native state is brittle and weak. Its performance has been improved by the inclusion of laponite clay disks, graphene oxide, and metallic nanoparticles, among others.[7,12,15,16] Another simple and promising route to improving mechanical performance is the inclusion of another hydrogel to form an

interpenetrating network. Many other polymer networks have been trialled to improve the properties of PNIPAM, including silk fibroin, cellulose, poly(acrylamide), and alginate.[17] It is difficult to directly compare their properties due to the different weight ratio of components used, but according to the principles of double network gels described by Gong, one expects both a high yield stress and strain from an additional network with physical crosslinks. This is because reversible bonds are able to dissipate the energy by peeling apart electrostatic bonds, rather than leading to rupture of the permanent chemically bonded PNIPAM network. Thus, properties such as the elastic modulus, the yield strength and the fracture toughness are seen to improve. [18]

4.2.2 POLYSACCHARIDE: ALGINATE

Within this subcategory of polymers that form physically crosslinked gels, alginate is an attractive candidate for combination with PNIPAM into a durable, 3D printable hydrogel. It is readily crosslinked by the addition of cations, is cheap and abundant, is generally regarded as safe, is bio-degradable, and is well-studied.[19]

Alginate is a linear polysaccharide formed by the monomer units guluronic acid (G) and mannuronic acid (M). The ratio and ordering of these two units varies depending on the species, season and age of the algal form that it was harvested from. The structure however will always consist of blocks of G, blocks of M, and blocks of alternating MG – the lengths of these respective sections are what varies within the polymer depending on the source species, the season, and the place of origin.[20,21]

Alginate gels are formed by chelation of cations within the pockets formed by the G-units, according to a concept known as the egg-box model shown in Figure 4.2. Here, the cations, attracted by the negatively charged carboxyl groups, enter the nanopockets, first binding in pairs and then into larger multi-strand junctions.[22] Accordingly, the properties of alginate gels vary in their tensile strength and yield stress depending on the M:G ratio and average G-block size, as these directly relate to the number and nature of crosslinks.[21,23] Choice of cation species also affects the mechanical properties of the get created, and this has been used to create IPN alginate ‘grippers’.[16,24]

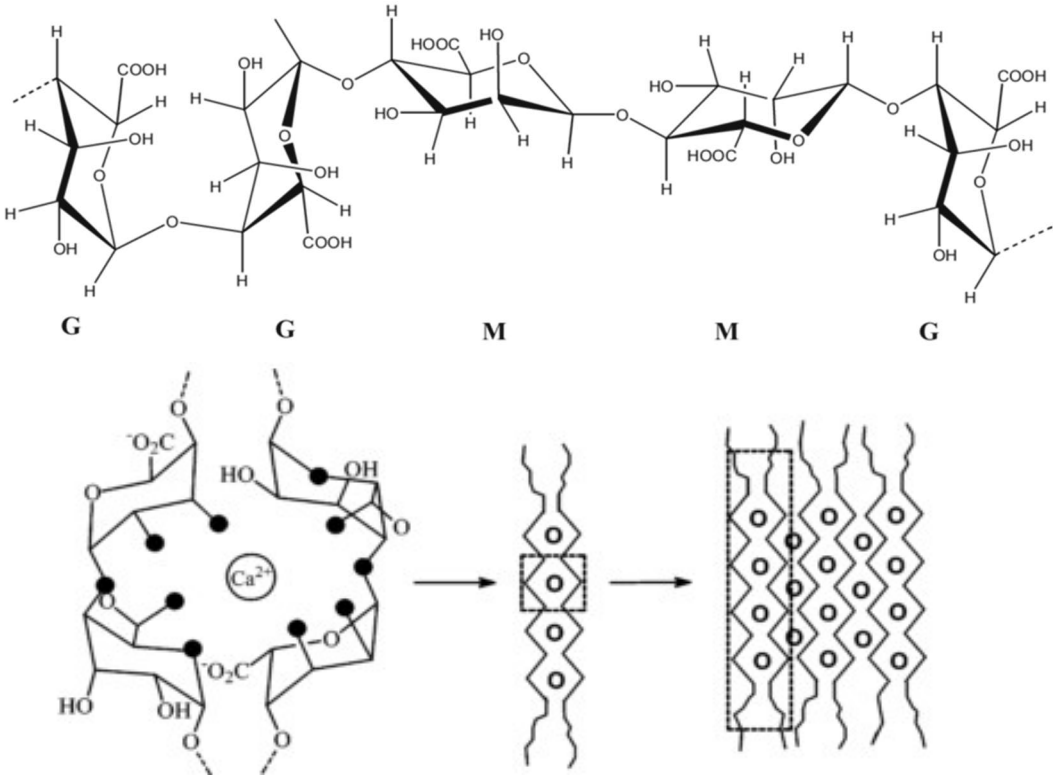

Figure 4.2. The components of the biopolymer alginate. Top, guluronate (G) and mannuronate (M) are shown in their potential configurations. Bottom, the binding of alginates into gels proceeds by the chelation of an ion between two facing G-units (bottom left) which is then followed by other sites between the two strands, and finally combined into a multi-strand junction. Figure adapted from Fang et al. [22]

Basic sample preparation was adapted from the work of Bakarich,[25,26] with a change of photocrosslinker from alpha ketoglutaric acid to dimethoxy phenylacetophenone (DMPA) to increase stability of the solution (detailed in section 2.5) and allow irradiation through glass, enabling the production of entirely enclosed moulded samples triggered to cure by UV light. Formulation is given in Materials, section 2.1.

4.2.3 DOUBLE-NETWORK PROCESSING STAGES

The material passes through three distinct stages during processing: first as a viscous liquid polymer blend with only weak alginate crosslinks, then as a weak gel with a fully-crosslinked PNIPAM network but still only weak alginate crosslinking, and finally as a strong double network gel, with full alginate crosslinking surrounding the fully crosslinked PNIPAM network.

4.2.3.1 BEFORE EXTRUSION: A VISCOUS POLYMER BLEND

The initial gel polymer blend is viscous due to the addition of 0.01M calcium chloride. These calcium ions lightly cross-link the alginate, creating a high viscosity blend suitable for printing and otherwise shaping (see section 4.4.3.1).

Rheological experiments reveal that at very low shear rates, <0.01 s^{-1}, the viscosity of the lightly-ionically-crosslinked polymer blend is high. This is required for printing applications, as it corresponds to a negligible spreading on the print bed when in position. However, when shear is applied, the crosslink density is sufficiently low for the viscous shear modulus to dominate over elastic shear modulus, causing the liquid to flow under the shear regimes accessible to the printer. The viscosity may be adjusted by modifying the number of initial crosslinks *via* the molarity of the $CaCl_2$ solution added, or by increasing the volume fraction of alginate or PNIPAM. However, all changes will also affect the final cured gel properties.

Given the focus of this investigation was to find novel routes to modulating thermoresponsive behaviour, and previous investigations have assessed the results of modifying crosslinker concentration and PNIPAM:alginate ratio,[27–30] here the composition of the gel was kept constant.

4.2.3.2 FORMATION OF FIRST NETWORK: UV-INITIATED CROSSLINKING

Once the uncured gel is in position, illumination by deep UV light cleaves 2,2-dimethoxy-2-phenylacetophenone (DMPA) a type I photoinitiator, into dimethoxybenzyl and benzoyl radicals.[31] The dimethoxybenzyl radical then degrades further into methyl benzoate and methyl radicals (shown in Figure 4.3Figure 4.4). Each radical thus produced is then available to initiate the free radical polymerisation of the isopropyl acrylamide through the opening of the vinyl bond. The UV-Vis absorption spectrum of DMPA as provided by the manufacturer is shown in Figure 4.4, highlighting the relevant frequencies to trigger activation.

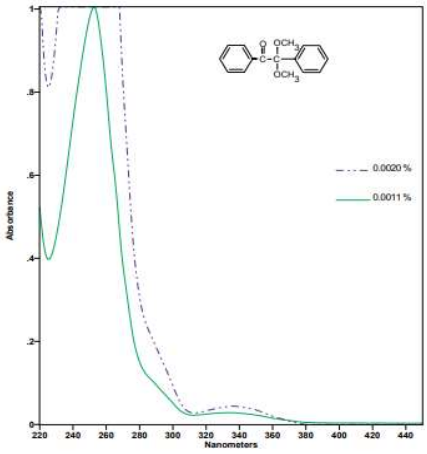

Figure 4.4. UV-Vis absorption spectrum of 2,2-Dimethoxy-2-phenylacetophenone. Data provided by manufacturer, Sigma Aldrich.

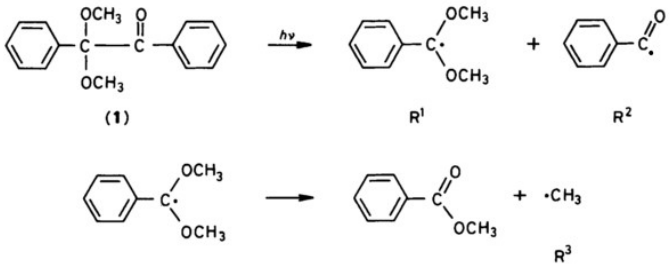

Figure 4.3. Major reaction products of 2,2-Dimethoxy-2-phenylacetophenone following illumination by deep UV light. From Fischer et al. [31].

Crosslinks between growing polymers of poly-N-isopropyl acrylamide are formed by the incorporation of methylene bis acrylamide (MBA, shown in Figure 4.1) in place of IPAM monomers, forming a bridge between two polymer chains. The crosslink density of the gel is affected by the relative concentration of MBA until a saturation point is reached.[30] Results are relatively insensitive to the amount of cross-linking agent used when small amounts are present.[32]

A higher crosslink density reduces the swelling of pure PNIPAM gels at temperatures below the LCST, due to geometric constraints on the motion of the polymers, as predicted by the model described in section 1.4.1. However, the minimum volume occupied by the network is insensitive to the crosslink density, as at this stage the packing of the functional groups is the limiting factor, rather than the larger scale polymer configuration or any longer-range forces.[33]

One therefore expects the swelling ratio between ambient and high temperature volumes to decrease with crosslink density, and this has been demonstrated experimentally, showing that for both PNIPAM and PNIPAM interpenetrated with an alginate network, a greater crosslink density decreases the swelling ratio.[4,30] Zhang *et al.* observe smaller PNIPAM pore sizes as the proportion of MBA is increased. Petrusic *et al.* also report that the swelling ratio increased for alginate/PNIPAM blends relative to pure PNIPAM, probably due to ionic repulsion;

however, a relatively greater percentage of alginate in the blend decreased the swelling ratio due to the additional constraint of the alginate chains.[30]

4.2.3.3 FORMATION OF SECOND NETWORK: IONIC CROSSLINKING

With the PNIPAM network formed, a secondary alginate network is formed interpenetrating with it by immersing the now-fixed sample in a bath of 0.1M $CaCl_2$ for 2 days. Following this, samples are placed in deionised water for at least 48 h with a change of water every 24 h to remove unreacted monomer and allow swelling to an equilibrium state.

4.2.3.4 OBSERVATION OF ILLUMINATION-BASED ASYMMETRY

As mentioned in Section 1.5, to produce prints with non-trivial shape-change requires some sort of variation of responsive properties is required throughout the sample. During the fabrication of initial samples an intriguing phenomenon was observed: samples showed a tendency to bend. The gels are observed to curve with a radius of curvature directed towards the source of illumination during the formation of the PNIPAM gel network: ie. the side with more illumination contracts more when heated.

The configuration of the gel during curing – on top of a glass slide with the source of illumination located above – means that that this is not the only asymmetry: there is also a difference with respect to oxygen exposure, initial drying effects, and potentially sedimentation and heating. However, these can be eliminated as first-order contributors towards the phenomenon by a simple experiment. If the sample is prepared in identical circumstances with only the light source moved (illustrated in Figure 4.5), the curvature is observed to change to reflect the new location of the light source. This demonstrates that the level of illumination is the primary determinant of the different behaviour of the sample faces.

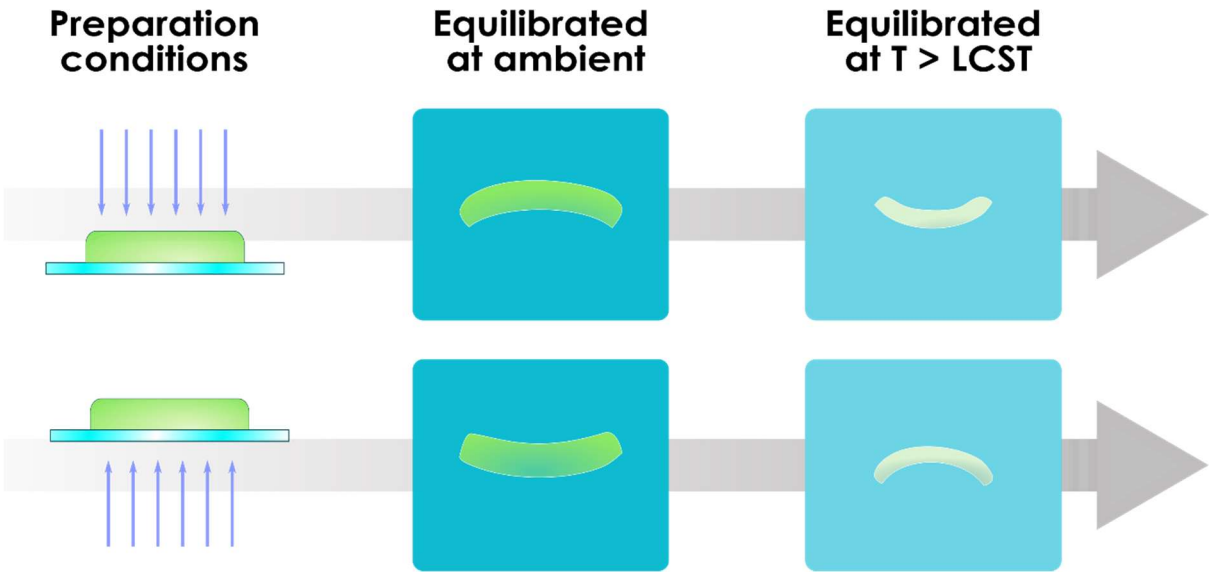

Figure 4.5 Schematic showing the behaviour of gel samples (left, green) produced in identical configurations save for the direction of the illumination (violet). Keeping all other variables constant, a rotation of the illumination by 180° produces a rotation of the asymmetric contracting effect by 180°, implying that this is the key origin of the observed effect.

This is an interesting phenomenon, as prior work has required the manual introduction of a gradient of some other element in order to produce such effects. This has been achieved with a diffusion-based chemical gradient,[34] diffusion-based substitution with non-thermally sensitive monomers,[35] templating around silica particles gradated by electrophoresis,[36] and sedimentation of PNIPAM with reactive crosslinking groups,[37] all of which are time consuming and require additional fabrication stages.

An examination of the literature suggests that this phenomenon has not been observed before in PNIPAM-based systems. The most relevant work is that of Kim et al. demonstrating curvature shaped by variation in density of photoinitiated crosslinks. This work used PNIPAM copolymerized with benzophenone pendant groups, the conversion rate of which is proportional to the light exposure and to the final expansion ratio and stiffness.[37] However, this was a copolymer based system, and had the limitations that the variation imposed by lithography is constrained to a 2D surface – further, the plane of a 2D surface - and, as the contracted PNIPAM volume is not a function of crosslinking, the only shape change that can be triggered by heating is a return to a flat configuration. Additionally, while the group made use of a half-tone based masking approach to reduce the number of masks needed, the need for prior construction of masks with the appropriate spacing is still a production limitation.

Contrary to this and the examples given in section 2.3, the method of introducing anisotropy is rapid, tailorable, facile, and can be incorporated in the production method already used for 3D printing hydrogels. Aims were therefore to explore the variables involved in the phenomenon, investigate potential mechanisms, and create or validate a mathematical model enabling the design of a print that would produce a specific curvature.

In this chapter, initial work focuses on characterising the materials used to enable subsequent calculations and replicability; finding the M:G ratio of alginate and the average molecular weight between crosslinks of both PNIPAM and alginate. The next step was to extract material properties such as the uniaxial and shear elastic moduli from the samples, which required the generation of protocols for creating testable samples – that is, samples with reproducible properties in the formats used in literature. With these data, observations of the deformation behaviour of simple shapes such as beams and discs could be compared to theoretical descriptions such as the Timoshenko model. Finally, investigations into the molecular and microporous composition of the illuminated and non-illuminated sides of the gel were conducted to investigate the cause of the effect.

4.3 METHODS DEVELOPMENT

The samples required for compression testing, rheological testing and simple deformations were cylinders, discs, and beam structures, respectively.

4.3.1 GEL PRECURSOR MIXING PROCESS

To form the gel precursor for initial extrusion, 450mg of alginic acid and 3g of isopropylacrylamide (IPAM) were weighed and blended, dry, in a THINKY ARE-250 planetary mixer for 2 minutes at 2,000RPM to maximise blending of components of the dry mix and ensure Ca^{2+} ions encountered both reagents simultaneously. Then 15ml of 0.01M CaCl2 was added, and the wet mixture blended for 20 minutes at 2,000RPM, again in the THINKY ARE-250. The blend was allowed to rest for 24h in a sealed container to ensure the biopolymers were completely hydrated (following the recommendation of Michael Avery, pers. comm, as recommended in Song et al.[38]). Immediately before gel shaping and formation to retain maximum reactivity and prevent premature gelation, 40mg of DMPA and 15mg of MBA were added to the 15ml of solution, blended for 2 minutes at 2,000RPM in blend mode and then 2 minutes in degas mode at 2,200RPM on the ARE-250.

The use of the Thinky mixer allows even blending of relatively highly concentrated alginate solutions without the chain shortening damage caused by sonication, and much more rapidly than with magnetic stirring. Notably, the Thinky mixer permitted the introduction of both IPAM and alginate to the solution at the same time; the prior methodology by Bakarich et al. required first blending of IPAM with $CaCl_2$, MBA as crosslinker, and alpha ketoglutaric acid as photoinitiator with solution alginate added as a final step. If this order was varied the mixture separated and precipitated.

The choice of different mixing protocols made a distinct difference to the viscosity of the blend produced. Mixtures where IPAM was blended with $CaCl_2$ solution initially had a notably lower viscosity than those where alginate encountered the Ca^{2+} ions first. Alginate first or simultaneous mixes were sufficiently gelled to be invertable in a vial, while IPAM-first mixes flowed. However, following ageing, the IPAM-first mixtures converged on the behaviour of the simultaneous blends. This behaviour was subsequently investigated in section 4.4.3.

Air bubbles were visible by eye in the blend, and vacuum degassing was considered and attempted. However, due to the high viscosity of the blend, six repeats of 15 minute cycles of dropping to low pressure – on the order of 10Pa – followed by a return to atmospheric pressure were insufficient to remove visible bubbles (>100microns). This was time consuming, added another cost and accessibility barrier to reproduction, and may still have been insufficient to prevent the inclusion of air bubbles within final prints as a result of print processing. This stage was therefore discarded, and all samples, both printed and cast, can be expected to contain defects from bubbles.

4.3.2 CURING PROCESS

For printing purposes, it is advantageous if the curing reaction proceeds as quickly as possible; this shortens the overall print time and prevents crystallisation of unreacted monomer in a low humidity environment. However, it has been observed that phase separation of the two gels may take place if the cross-linking of the UV network happens too quickly. This is apparent by opaque regions visible in the gels. This can be minimized by conducting the exposure at temperatures below 15° C, as noted in the supplementary material to Bakarich et al. [39]

Cast gels were formed using the methods described in section 4.3.3, and cured using a 254nm 6W UV lamp (Model UVS-26 EL UVP) in a UVP 95007201 CHROMATO-VUE C-10 mini UV-viewing cabinet. Printed gels were

produced following the methodology in section 3.2.3.7 and were cured in the printer, as documented in Chapter 3. Curing measurements of UV absorption as a function of time were taken by aligning a quartz cell containing a 0.8mm thick sample of gel between the UV lamp and a UV radiometer sensitive to 254nm wavelengths. The intensity of the radiation arriving at the detector was recorded every 15 seconds to investigate the changing opacity of the sample over time.

Following photocuring of the PNIPAM network, fixing the blend in the desired shape, gels were placed in 0.1M $CaCl_2$ for 24 hours, before swelling in DI water for 48 hours to an equilibrated state, changing every 24h to remove any unreacted monomer, crosslinker or photoinitiator species.

Samples were then sectioned further, if appropriate, and stored in DI water until testing. All samples were patted dry on towels before testing or examining, to remove surface water.

4.3.3 SAMPLE PREPARATION METHODS

Initial material characterisations were performed using cast, rather than printed, gel samples to eliminate additional sources of variation caused by print properties. Cast samples were prepared through two methods as appropriate for different applications.

4.3.3.1 FOR CURED GEL RHEOLOGY AND OPTICAL MEASUREMENTS

For viscoelastic rheological measurements and optical thermomechanical measurements, samples were cut from the centre of cast sheets to remove unrepresentative strain effects caused by boundary conditions. Strain effects in z were unavoidable in this method and derived from the need for two reproducible flat surfaces on the top and bottom face of the cylinder. This is a limiting factor on the quality of the results. Said sheets were created by placing rubber spacers of the desired height between two glass surfaces, one quartz and one silicate, filling with polymer blend, and securing the sides together using plastic bolts on both sides. A schematic is shown in Figure 4.6.

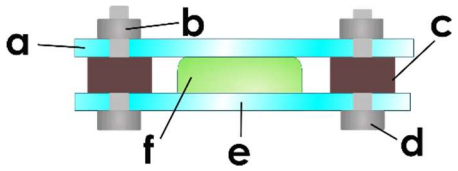

Figure 4.6. Casting process sketch. Two glass plates (a and f) contain the sample. A is quartz glass, transparent to UV. Each plate contains four holes. Bolts (d) are inserted into each hole, with spacers (c) to keep the plates a fixed distance apart. Polymer blend (f) is added and nuts (b) are screwed onto the bolts to fix it together.

For the rheological samples, the sectioning was done using custom 'cookie cutters' matched to the 20mm diameter of the rheometer geometry and 3d printed on a standard heated-plastic based extrusion system using poly lactic acid (PLA), a commonly used 3D printable biodegradable plastic. This gave a reproducible shape and size but created a rougher edge.

The dimensions of samples for optical measurements were chosen to be large enough to minimize error when recording size changes on the order of -30% linearly with a camera of sensor size 1776 x 3000 pixels (corresponding to approx. 55 pixels/mm when the sample was correctly aligned in the viewer), but to not take too long to print when produced on a 3D printer, and fit on the largest glass slides available (58x76mm) for ease of transport before curing. The z height was determined by the smallest available spacer value which exceeded the minimum number of layers required to constitute a bulk 3D print (5) multiplied by the maximum acceptable resolution in z (0.5mm), and was chosen as 3mm.

4.3.3.2 SHAPE CHANGING SAMPLES

For measurements which required the production of more complex shapes, 3D printed gel samples were prepared using the methods and parameters given in 3.2.3.7 and on the system described as a whole in Chapter 3.

4.3.4 DEVELOPMENT OF TESTING METHODS

Mechanical testing of soft, slippery materials such as gels has as yet few established standards, particularly when compared to those existing for traditional engineering materials. Methods were therefore developed specifically for this application, based where possible on those found in literature, or adapted from protocols for testing rubbers or biological tissues.

4.3.4.1 SHAPE CHANGE TESTING

To measure the shape-change of the gels, samples needed to be immersed in water baths both at ambient temperature and at temperatures of over 40 °C, and photographed with a clear scale indicator. Challenges included a low opacity and a high mobility during testing due to convection currents in the water baths and low inertia.

Therefore, a simple mounting rig was designed and laser-cut from clear 3mm thickness acrylic. This mount slots together over the edge of a square glass tank, fixed in place with Sugru, an air-drying water-proof silicone putty. The arm of the rig contains a small cut out square.

Small laser-cut clear hooks were glued to the samples using cyanoacrylate, chosen to minimise the disruption to the gel network and creation of potential fracture initiation sites. This minimizes rotation and translation of samples during an exchange of water and ensures they are anchored in the same fixed position. Increased contrast and distortion reference was provided by dark gridded paper, laminated and inserted as a backdrop.

Images were taken using a Moto 4 mobile phone, arranged on a tripod to provide a constant viewpoint. Images were corrected for any distortion using a cage transform in GIMP (GNU Image Manipulation Program) using the gridded background as a reference. The 3mm thick sample holder was used to assign a scale to the sample using ImageJ. The thickness of each sample was taken as an average of 10 measurements across the thickness, reported as a mean with errors from standard deviation. The length of each side, exposed and unexposed, were recorded using the segmented line feature. Finally, the curvature of the strip was recorded by assigning 20 points along the unilluminated side of the sample and performing a fit to a quadratic function. If the radius corresponding to maximum curvature was not parallel with the y-axis when these points were plotted, the image was rotated before analysis to achieve this, as the fit used did not include a rotational variable.

4.4 RESULTS AND DISCUSSION

4.4.1 DETERMINATION OF ALGINATE CHARACTERISTICS

As mentioned in section 4.2.2, alginate shows substantial variation in the distribution of its two constituent monomers, mannuronate (M) and guluronate (G). The behaviour of the polymer varies greatly as a function of its molecular weight, the M:G ratio, and the distribution of M versus G-units,[21,23,40] none of which properties are provided or characterised by the manufacturer as standard. As a result, it is essential to characterise the alginate source to allow comparison to others' work.

4.4.1.1 MOLECULAR WEIGHT

Molecular weight was determined using viscometry as described in Materials and Methods. The solute used was 0.1M NaCl solution to reduce viscosity and therefore experiment times, following Mackie.[41]

The intrinsic viscosity and the specific viscosity were both plotted as a function of concentration. Linear fits were used to extrapolate the intrinsic viscosity, [η], yielding values of 371±1 and 360±6 dL/g. These were then converted to molecular weight following the Mark-Houwink equation as given in Materials and Methods. K and a were assigned as 0.0178 and 1 respectively, following Mackie for a matched M:G alginate ratio and solute.[41]

4.4.1.2 G:M RATIO AND DISTRIBUTION

The G:M ratio may be determined by the unique signatures of the anomeric protons in the H^1 NMR spectra of the G units, and those of combinatorial sequences of G and M. Following the process defined by ASTM F2259-10,[42] NMR was kindly performed on the sample by Sarah Michel, and the spectrum in Figure 4.7 produced.

Using the Mark-Houwink-Sakurada parameters following Mackie et al.[41] and combining the two values as a weighted average, the molecular weight was found to be 20.6 ± 0.6 kDa, corresponding to an average degree of polymerisation of 98.2 for the MG distribution found in the following section.

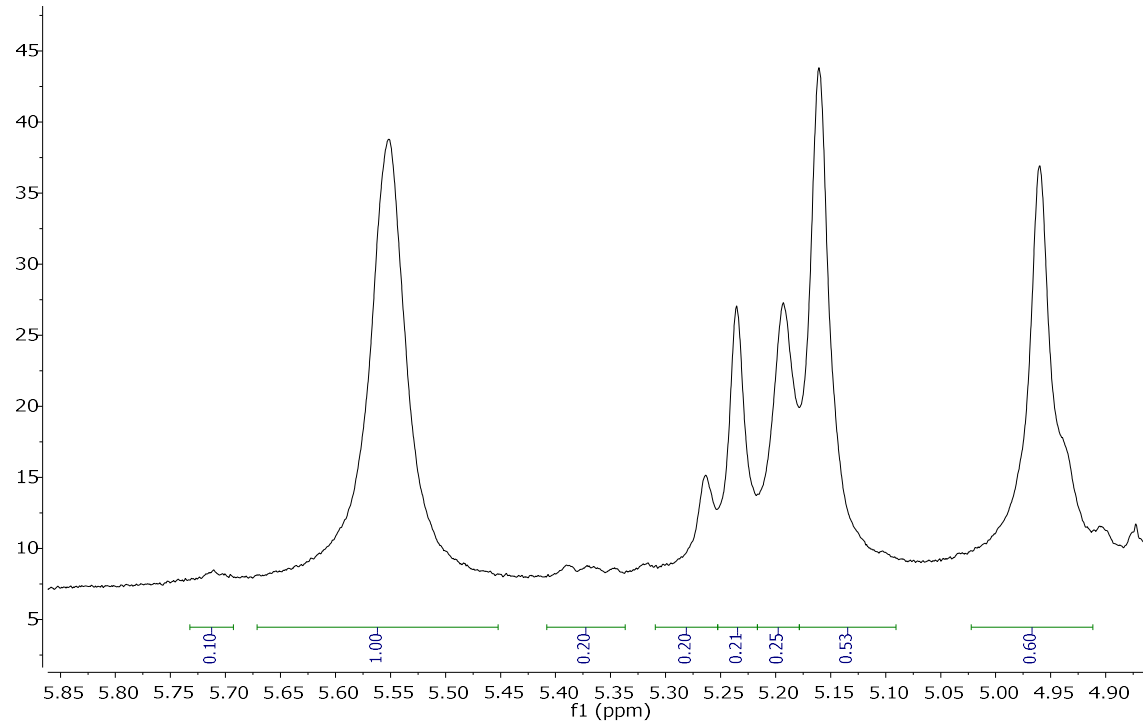

Figure 4.7. H^1 NMR spectrum of alginate used in this thesis, showing peaks integrated to determine the ratio of guluronate to mannuronate monomer units.

The spectrum of Figure 4.7 was analysed according to the processes laid out in ASTM F2259-10. Following a comparison of the peak intensities, and area integrations, the proportions and statistical distribution of the monomers were calculated and are presented in Table 4.1. Here N(G,M) gives the number average block length of G and M respectively, and N(G>1) the number average block length of G when single G units are discounted (that is, when only blocks long enough to participate in the egg-box stage of ion binding are considered).

Ratio M:G	1.12 ± 0.01
N(G)	2.92 ± 0.1
N(G>1)	4.9 ± 0.5
N(M)	2.6 ± 0.1
F(G)	0.528767
F(M)	0.471233
F(GG)	0.347945205
F(MM)	0.290410959

F(GM)	0.180821918
F(GGG)	0.259739392
F(MGM)	0.092616104
F(GGM)	0.088205814

Table 4.1. Relative frequencies of G, M and monomer sequences. F(X), where X is a monomer sequence, indicates the relative strength of signal deriving from that sequence compared to the strength of the polymer as a whole.

The alginate source used here is notably rich in guluronic acid, with 53% guluronic acid content. The signal strength for the triad MGM – indicating a lone G unit – compared to the overall G signal indicates that 9.56% of guluronate residues are found in this format, leaving the majority of G units to participate in bonding. One therefore expects an average of 48.2 G units participating in binding per polymer, arranged in blocks of average size 4.9, and with approximately 5 flexible units between each pair.

The high proportion of binding G blocks will result in multiple rigid, rod-like junction regions, on average 4.9 units long along the long axis, connected by more flexible chain sections. From SAXS of crystallized guluronate, it is known that the unit cell, consisting of two molecules, has dimensions 8.6 x 8.7Å.[43] Since each G-pocket is this gives an aggregated region of approximately 43-50nm long. Estimates for the persistence length of alginate vary between one monomer unit – an ideally flexible chain – to approximately 17.[44]

This information was combined with the molecular weight and converted to a degree of polymerisation using a weighted average monomer mass, again according to the ASTM process, yielding a value of 7– this is significantly lower than the value found via viscometry, and likely reflected breakdown due to the heating and hydrolysis processes conducted in preparation for NMR rather than the state of the polymer as used.

4.4.2 DETERMINATION OF PNIPAM CHARACTERISTICS

4.4.2.1 MOLECULAR WEIGHT

To determine the average degree of polymerisation PNIPAM was polymerised in the absence of crosslinking agent, at the same ratio (0.5% PI to monomer by weight) and at the same polymer fraction (0.2) in DI water using the same light source. The polymer thus formed was characterised for molecular weight by differential viscometry. Fujishige shows that at 25°C and above the relationship between reduced viscosity and

concentration for PNIPAM departs from linearity.[45] Therefore, an Ostwald viscometer in a water bath was used for this stage to enhance thermal stability. The temperature was held at 21±0.2°C, with higher temperatures occurring during the testing of higher concentrations. Results are presented in Figure 4.8.

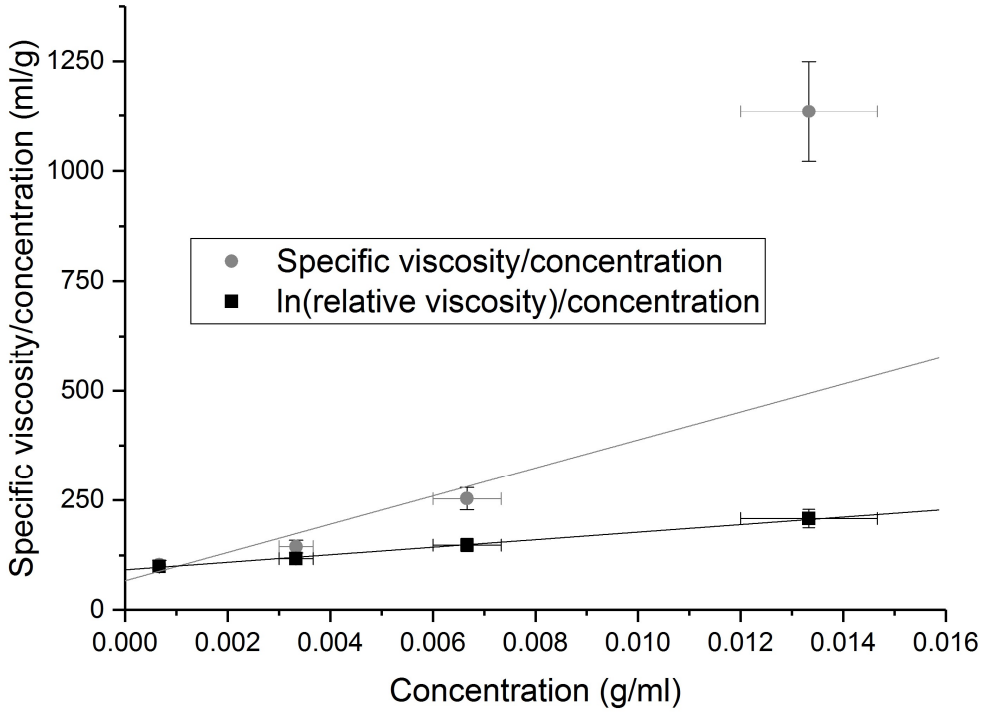

Figure 4.8. Relationship between concentration and reduced viscosity for a polyisopropyl acrylamide sample of unknown molecular weight, measured using differential viscometry. Viscosity errors are assigned through standard error propagation of the error on the mean, with each measurement taken 4 times. Concentration errors derive from the precision of the pipette.

It is obvious that the highest concentration point (13.3g/ml) for the reduced viscosity does not lie on the trend expected from the other values. A fit including this point yields an uninformative intrinsic viscosity of 60±50 ml/g, and a low adjusted R^2 of 0.46. This point may be unreliable due to a viscosity which exceeds the laminar flow regime for this capillary with – the value is only 30% over the maximum used by Fujishige,[45] but could still cross the transition. Another possibility is the 0.4°C increase in temperature during the process. Details of the sensitivity of the behaviour of dilute PNIPAM between 20°C and 25°C are not available, but the data from Qu and Zhou suggests some effects begin at 20°C.[46]

Fitting to the inherent viscosity data and the three other reduced viscosity points gave $[\eta]$ as 93 ± 2 ml/g (R^2 = 0.99) and 84 ± 15 ml/g (R^2 = 0.47). This suggests the true value lies in the range 80 ± 20 ml/g, and this value was used for subsequent calculations.

4.4.2.2. AVERAGE DISTANCE BETWEEN CROSSLINKS IN A PURE PNIPAM GEL

Volumetric swelling ratio for a pure PNIPAM gel was found by the method described in section 2.2.5 as 13.3 when calculated by volume and 13.7 when calculated by mass, corresponding to a polymer fraction of 0.075±0.008 for an ideal, transparent PNIPAM gel, and of 0.14±0.1 for gels with higher opacity (corresponding to a more heterogenous network). Both are calculated below because they bound the conditions which PNIPAM may take up within a double network gel – either totally extended and transparent, or contracted and opaque.

Molecular weight between crosslinks (M_c) is calculated using the following equation:[47]

$$\frac{1}{\overline{M_c}} = \frac{2}{\overline{M_n}} - \frac{\left(\frac{\bar{v}}{V_1}\right)[ln(1-v_2) + v_2 + \chi_1 v_2^2]}{[(v_2)^{1/3} - v_{2s}]}$$

Equation 4.1

Here $\bar{M}_n$ is the average polymer mass in the absence of crosslinking, found in section 4.4.21, V_1 is the molar volume of solvent (18 $cm^3\ mol^{-1}$ for water), $\bar{v}$ the specific volume (reciprocal of density, volume/mass) of the dry polymer (taken from density measurements of the amorphous dry material), v_2 the polymer fraction in the swollen state (found above; the reciprocal of the swelling ratio), and χ_1 is the Flory interaction parameter.

The parameter χ_1 is a function of both polymer volume fraction ϕ and temperature T. To third order it can be evaluated with the following expansion:

$$\chi_1 = x + yT + \varphi(a + bT) + \varphi^2(c + dT) + \cdots$$

Equation 4.2

Here x, y, a, b, c and d are numerical coefficients. These were taken following Afroze et al.,[48] and evaluate to 0.364 for a volume fraction of 0.075, and 0.435 for a volume fraction of 0.14, both at 21°C.

This gives the molecular weight between crosslinks as 7.00±0.03 kDa for ideal transparent gels and 3.5±0.1 kDa for opaque gel. For a monomer mass of 113.16 g/mol, the degree of polymerisation is therefore 61.8±0.3 for transparent and 31±1 for opaque gels. Taking the length of one monomer unit as approximately that of two C-C

bonds, or 0.3nm, this yields an average expected distance between crosslinks of 18.5±0.1nm in transparent gels and 9.3±0.3nm in opaque, and presumably something between for the PNIPAM network in a translucent PNIPAM-alginate gel.

From the ratio of monomer to crosslinker, the average distance between crosslinks is expected to be ~272 polymer units, notably higher than both calculated through swelling methods. Verification of the percentage of monomer reagent contributing to the final polymer network was conducted according to the protocol detailed in section 2.2.5, and determined that 65±11% of solid reagents in the gels were fixed in the network for pure PNIPAM. This adjusts the expected degree of polymerisation to 110±12, still higher than the prediction from swelling-based calculation.

This suggests that additional contributors are confining the swelling of the gel. These could be charge or hydrophobic mediated inter-chain interactions, or joins formed by entanglement between PNIPAM networks during polymerisation rather than incorporation of MBA units.

Taken overall, this suggests that swelling-based measurements are a more appropriate way to record and characterise network properties than stoichiometric calculations alone. A low concentration of crosslinker was used due to the advantageous properties of double network gels with only a lightly crosslinked covalent network.[49,50] However, it is clearly undesirable to waste monomer unnecessarily, and it is unclear what role unreacted monomer or un-crosslinked polymer could be playing in the composite. This could be examined further through additional stoichiometric measurements with varying concentrations of crosslinker, or the complementary use of inverse size exclusion chromatography or NMR cryoporosity measurements to investigate the resulting gel structure.[51,52] The issue of obtaining an accurate picture of a double hydrogel in its native state will be returned to in section 4.1.1.2.

4.4.3 UNCURED NIPAM-ALGINATE POLYMER-BLEND PROPERTIES

First, the properties of the polymer blend before UV-curing were assessed, to validate printability and production methods.

4.4.3.1 SHEAR RAMPS

Shear ramps were performed uncured PNIPAM-alginate solution to assess the shear thinning behaviour and quantify the observed preparation-order variance described in section 4.3.2. within the limits previously identified as relevant to extrusion-based 3D printing, shown in Figure 4.9. A shear rate of $0.01s^{-1}$ reflected conditions at rest on the bed, and a rate of $500s^{-1}$ the maximum relevant strain while extruding.[53]

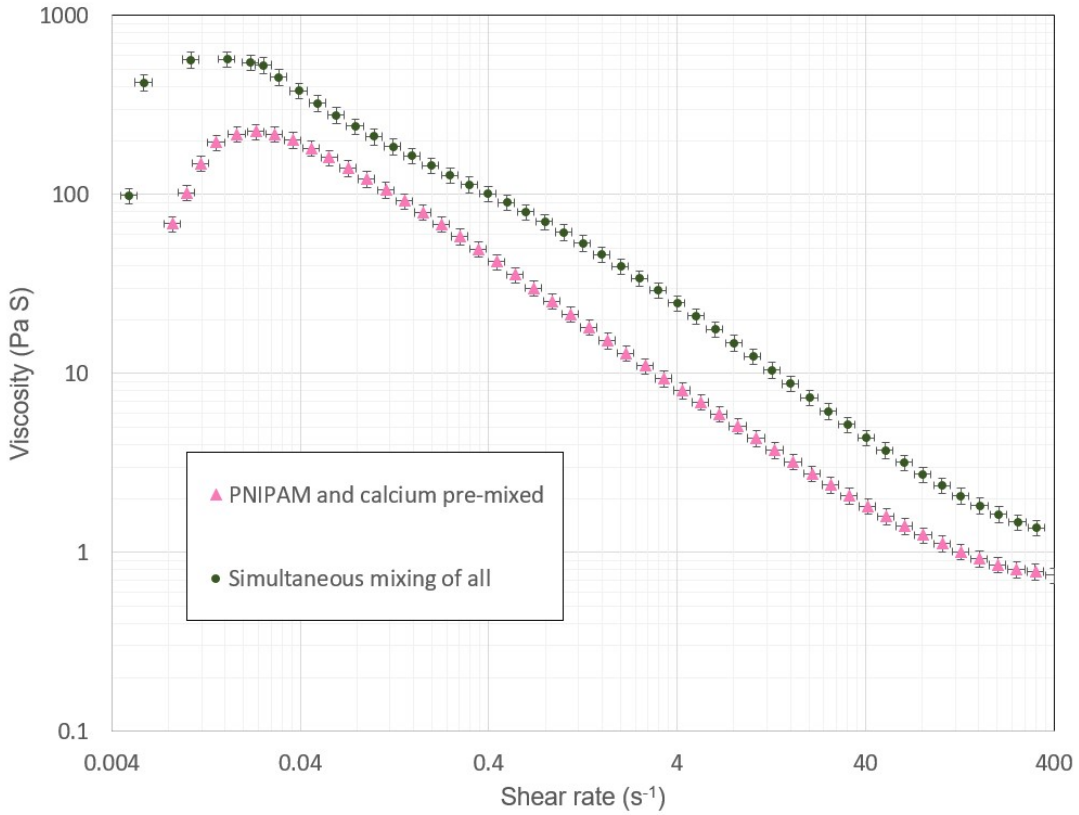

Figure 4.9 Viscosity-shear rate measurements comparing the behaviour of polymer blends with NIPAM and calcium components blended together before adding alginate, or all components blended simultaneously.

The blend where dissolved calcium chloride and NIPAM monomers were first dissolved in aqueous, and then alginate added by stirring, had a maximum shear stress of less than half of the blend with all components added and blended simultaneously. Both examples had the same shear history and ageing characteristic.

Higher viscosity at low shear rates indicates that a simultaneous mix is more suitable for holding its shape on the printbed. While the higher resistance to flow with respect to the pre-mixed solution remains at all shear rates, substantial shear-thinning behaviour is still seen. This demonstrates both both blends may be successfully extruded. Due to the higher viscosity at low shear, and ease of production, simultaneous blending was used for all subsequent work. The origin of this phenomenon was of interest, however, and further investigations into

the mechanism of action and the relevant timescale for ageing processes to rebuild the structure were conducted.

4.4.3.2 ZETA POTENTIAL MEASUREMENTS

The alginate-calcium network is the dominant contributor to viscosity in the alginate-NIPAM-$CaCl_2$ aqueous solution, and its high viscosity at low concentrations is part of its appeal as a working material. Since this network is bound by charge, zeta potential measurements were relevant to assess the electrostatic interactions of the double network solution. Measurements were taken as described in section 2.2.7 and are given in Table 4.2.

NIPAM monomer	-(27.25 ± 4.3)
Alginate	-(49.69 ± 4.1)
NIPAM + $CaCl_2$	-(9.2 ± 2.1)
NIPAM + Alginate + $CaCl_2$	-(31.9 ± 3.9)

Table 4.2. Zeta potential values for components of the double network gel, in milliVolts.

The negative value for alginate is as expected for the anionic polymer, which derives its charge from the carboxylate ion on each sugar ring; the net charge on the polymer depends on the pH of the solution. This negative charge is of course the mechanism by which the divalent calcium cations bind the alginic acid polymers into a gel.

However, the fact that the zeta potential for NIPAM combined with calcium chloride is less negative than the NIPAM alone suggests that the calcium ions are forming a coordination complex with one or more isopropyl acrylamide molecules. This would reduce the availability of ions to bind alginate polymers. The sequestration of ions that would otherwise increase binding could explain the lower viscosity of solutions in which calcium and NIPAM were blended first. The significant effect of assembly processes for low-molecular weight gelators, even while maintaining the same ratios of components, has been documented by Draper *et al.*[54]

However, alginate polymers are still more negatively charged then NIPAM or PNIPAM, and over time, calcium ions could be expected to migrate toward the greater negative charge on the alginate. There they could form the more stable ‘egg-box’ configuration, creating crosslinks and showing the age-related viscosity increase

observed. To determine if the timescale of this restructuring is relevant when constructing samples, the three-stage thixotropy test protocol detailed in section 2.2.2.3 was performed.

4.4.3.3 SHEAR-REBUILD PROCESSES

A three-stage shear-rebuild protocol was developed that mimicked the processes undergone by the polymer blend when creating samples (see section 2.2.2.3). Data were collected for alginate and NIPAM-alginate as used in creating shape changing hydrogels, and results are shown in Figure 4.10 and Figure 4.11 respectively. Both showed a clear two-phase rebuild process following disruptive shearing. This occurred in approximately 20 seconds, before attaining a steady state that persisted for the duration of observation (terminated after 600 s for initial studies and after 150 s for data collection).

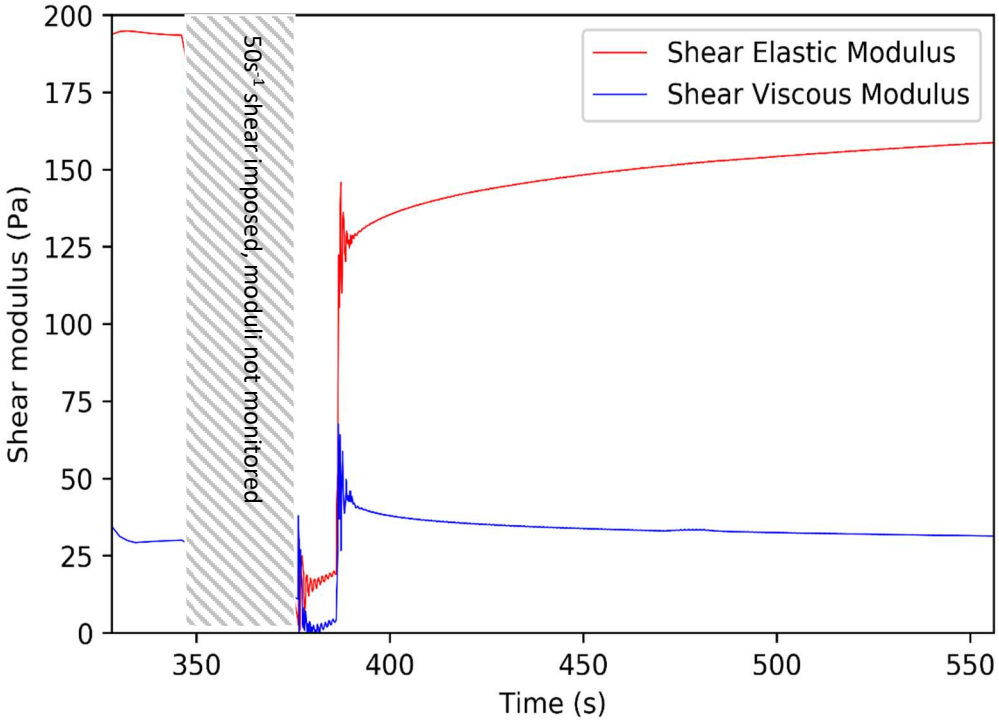

Figure 4.10. Three-stage rebuild behaviour for 2% wt alginate with 0.01$CaCl_2$. The experiment begins at t=0 with an initial rest period to allow temperature equilibration, and therefore measurements start at ~330 s

However, the values attained after rebuilding were significantly lower than those measuring during the initial oscillation phase. In the case of alginate alone the data obtained post-shearing show a regain of 75% of the elastic shear modulus recorded in the initial stage, and in the case of the full NIPAM-alginate blend as used in printing, 40% of the value measured in the initial section. While a reduced modulus could be expected, as the oscillation used to measure will disrupt the material slightly, this difference implies that on a timescale of hours the viscosity of the NIPAM-alginate blend would increase further. The elastic shear modulus of the alginate blend

was more than 4 times greater than when NIPAM was added, suggesting the addition of the monomer inhibits interactions between the polysaccharide strands.

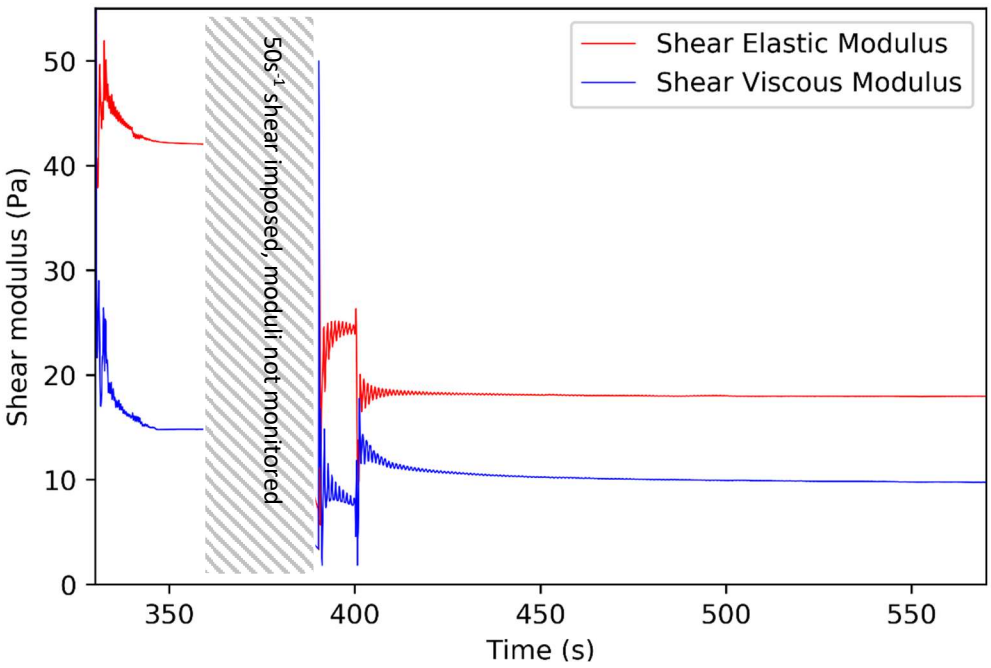

Figure 4.11 Three-stage rebuild behaviour for NIPAM-alginate polymer blend.

The two-stage rebuilding is intriguing and has not been recorded previously in literature. It is hypothesized that the two stages represent the formation of hydrogen bonds and electrostatic bonds respectively. If so, the method could potentially reveal information about the behaviour of different bonds in alginate-based blends. However, much more research would be needed to determine this. Some additional studies of the effect of additional components on the behaviour of NIPAM-alginate blend during this test have been conducted, and are presented in section 6.2 and section 7.3 with preliminary analysis.

There are implications for 3D printing scenarios and for sample preparation. Clearly over time the post-shearing steady state elastic and viscous shear moduli transition to the value recorded before shearing, and possibly still higher if loading reduces sample integrity before the first recordings are taken. Therefore, the amount of time the polymer is left undisturbed before extrusion will affect the viscosity of the blend and therefore its extrusion rate. The time elapsed between forming into the desired shape and curing may also affect the properties of the final sample, since the structural rebuilding will be continuing at rest and may be 'locked in' at the level reached by the time the monomer is polymerised and crosslinked.

This could be a subject of further study and would be required if an application requiring high reproducibility or fine tuning of mechanical parameters were identified. However, given the focus of this work on shape change, it is sufficient that the time-dependence of the material is noted and that times between shaping and curing should be matched for all samples to within a few minutes to prevent significant variation.

During printing, there is a possibility that cure-on-deposition systems as used by Sears et al.[55] would 'lock in' the less viscous structure. The slow curing rate used in this study (light curing took approximately 25 minutes) mean that the different ages of first versus last layers printer (typical print duration 8 minutes) were unlikely to have a large effect, but the possibility is noted.

4.4.4 CURED PNIPAM-ALGINATE GEL PROPERTIES

4.4.4.1 GELATION PROCESS

PNIPAM gels show a decrease in intensity of light transmission following crosslinking.[56] This has implications for the light dose delivered to lower layers and the maximum sample dimensions, as well as providing insight into the formation of the gel network. Simple exposure of a thick sample of uncured polymer indicated the maximum penetration depth of UV for curing was approximately 8mm. To monitor the process, measurements were taken as described in Section 4.3.2, and results are shown in Figure 4.12.

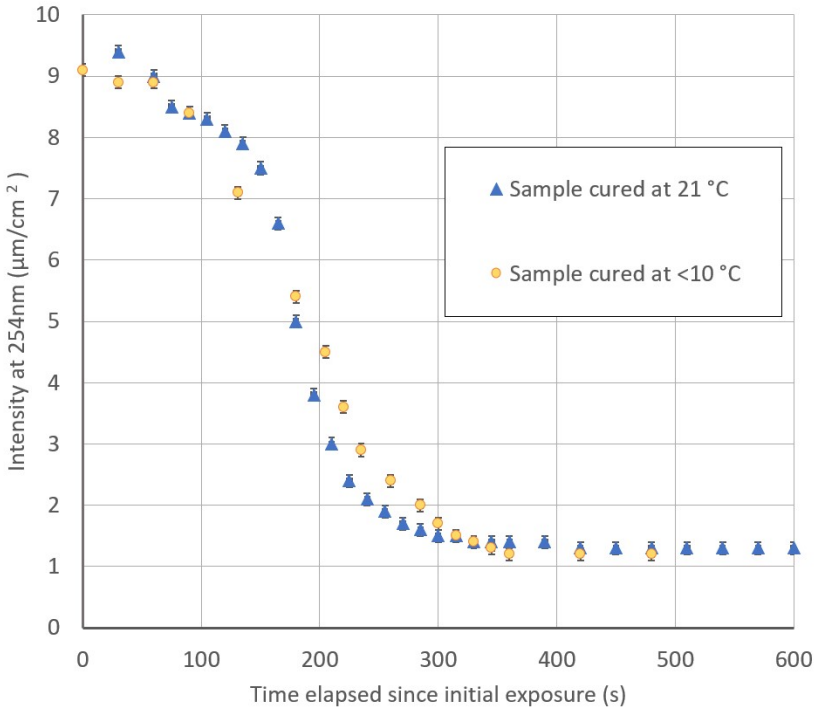

Figure 4.12 Transmission intensity of deep UV light through a PNIPAM-alginate system as a function of time, for samples held at ambient (blue triangle) and chilled (yellow circle) temperatures. Errors are derived from instrumental sensitivity and if not visible are smaller than markers.

The decrease in optical transmission during curing for PNIPAM and related gels has been attributed to the formation of 'frozen in' inhomogeneities in the gel network, and is proportional to the rate of crosslinker added.[56] This implies the measurement of transmission intensity is indicative of the rate of gelation.

This is further supported by the shape of the graph, which corresponds to the sigmoidal form predicted by kinetic modelling of free-radical network polymerisation.[57] The rate of gelation has implications for the properties of the gel formed; at a slower rate of reaction, the incipient gel network has greater time to relax and even out inhomogeneities before they become fixed by crosslink formation.[56] This is thought to be the origin of improved gel properties when prepared at lower temperatures.[2]

The minimum transmission level recorded is slightly above 1 $\mu W/cm^2$, showing that photoinitiation can still take place under a layer of cured gel, albeit at a slower rate. However, since only one frequency of UV is monitored it would be desirable to perform a full-spectrum characterisation of the UV sources used, as the range of phototriggering frequencies is broad (see Figure 4.4), and it is possible that multiple photon energies contribute to the crosslinking and polymerisation activity.

4.4.4.2 FOURIER-TRANSFORM INFRA-RED SPECTROSCOPY

Data from FTIR confirms the successful combination of both networks, as the spectra obtained from PNIPAM-alginate (Figure 4.13) contain features of both PNIPAM and alginate gels measured separately (also shown).

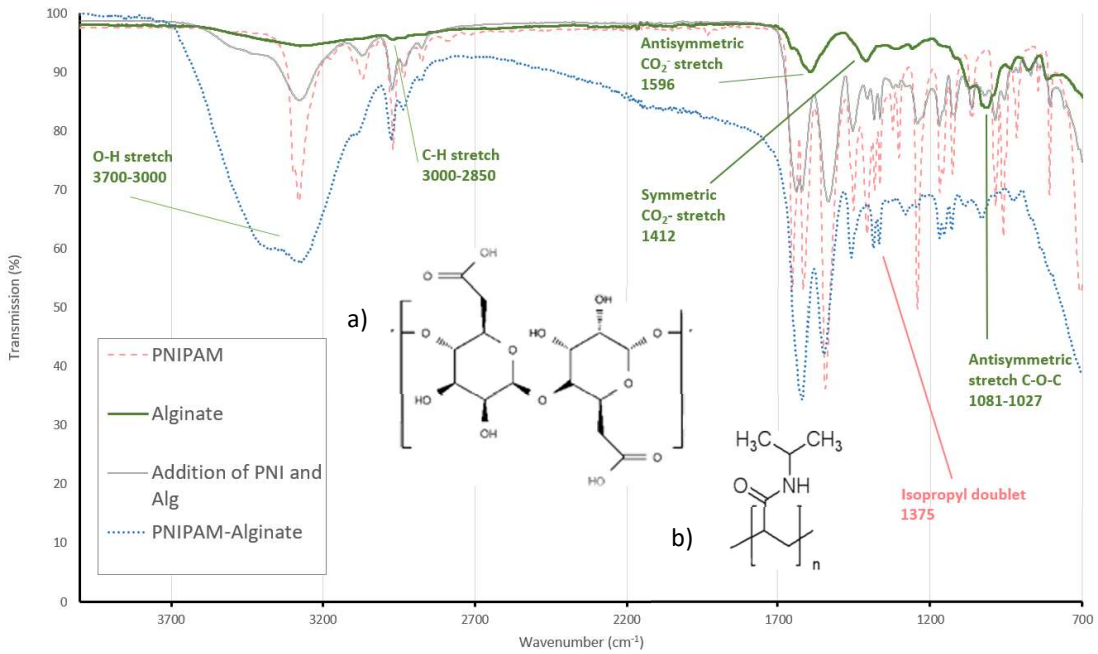

Figure 4.13 FTIR spectroscopic data from gels of PNIPAM, alginate and PNIPAM-alginate. Also shown is the spectrum expected from a linear unweighted combination of PNIPAM and alginate. Inset: the chemical structure of alginate (a) and of PNIPAM (b). Features characteristic of PNIPAM (the isopropyl doublet at ~1377)[58] and of alginate (the antisymmetric C-O-C stretch around 1081-1027)[59] are indicated. These can clearly be seen in the spectrum of both.

Significant changes are visible in the FTIR spectra of PNIPAM-alginate, but as for Raman spectroscopy, deconvolution would be necessary to thoroughly analyse the data. However, it can be concluded that PNIPAM-alginate as measured contains contributions from both alginate and PNIPAM molecules, and also differs from a linear sum of the two spectra.

This hypothetical linear sum is also shown in Figure 4.13 (grey line). While it is similar to the combined spectrum as measured, there are some differences – for example the lack of a double peak at ~1620cm^{-1} and the shift of the C-O-C antisymmetric stretch from 1022 cm^{-1} in alginate to 1028cm^{-1} in PNIPAM-alginate. This latter is associated with a decrease in hydrogen bonding and may result from the alginate being physically interpenetrated with the PNIPAM.[60,61] Similarly, the blueshift seen for the C-H stretching peak, found at 2970 cm^{-1} in PNIPAM and alginate separately, and at 2975 cm^{-1} in PNIPAM-alginate may indicate an increase in the number of water molecules around each methyl group.[62,63] Such changes would be representative of direct or indirect interactions between the PNIPAM and alginate molecules.

Further analysis of the spectra of PNIPAM-alginate structures could reveal details of the interaction between networks in this double network gel and elucidate some of the as-yet-unknown mechanism behind the high toughness of such structures.[64]

4.4.5 DETERMINATION OF ELASTIC CONSTANTS

To gain predictive power over the finished materials, elastic constants for the material were required, ideally both below and above the LCST. Rheology is a rapid, well characterised method to quantify the magnitude of the elastic and viscous shear moduli in a gel-like material and determine the frequency dependence. For shape-changing applications the response time of the gel is on the order of seconds, giving the timescale of interest. The calculation of elastic constants permits both calculations of the theoretical conformation expected and comparisons to others' work.

4.4.5.1 SHEAR ELASTIC BEHAVIOUR

Shear modulus measurements of cured gels are a common measurement modality for the hydrogel community due to equipment availability and ease of measurements. For these purposes, samples of opaque PNIPAM (referred to as PNIPAM(O)) and transparent PNIPAM (referred to as PNIPAM(T)), with high and low degrees of variation in crosslink density respectively, samples of alginate, and samples of PNIPAM-alginate were tested for their elastic and viscous shear moduli as a function of strain. Data are presented in Figure 4.14.

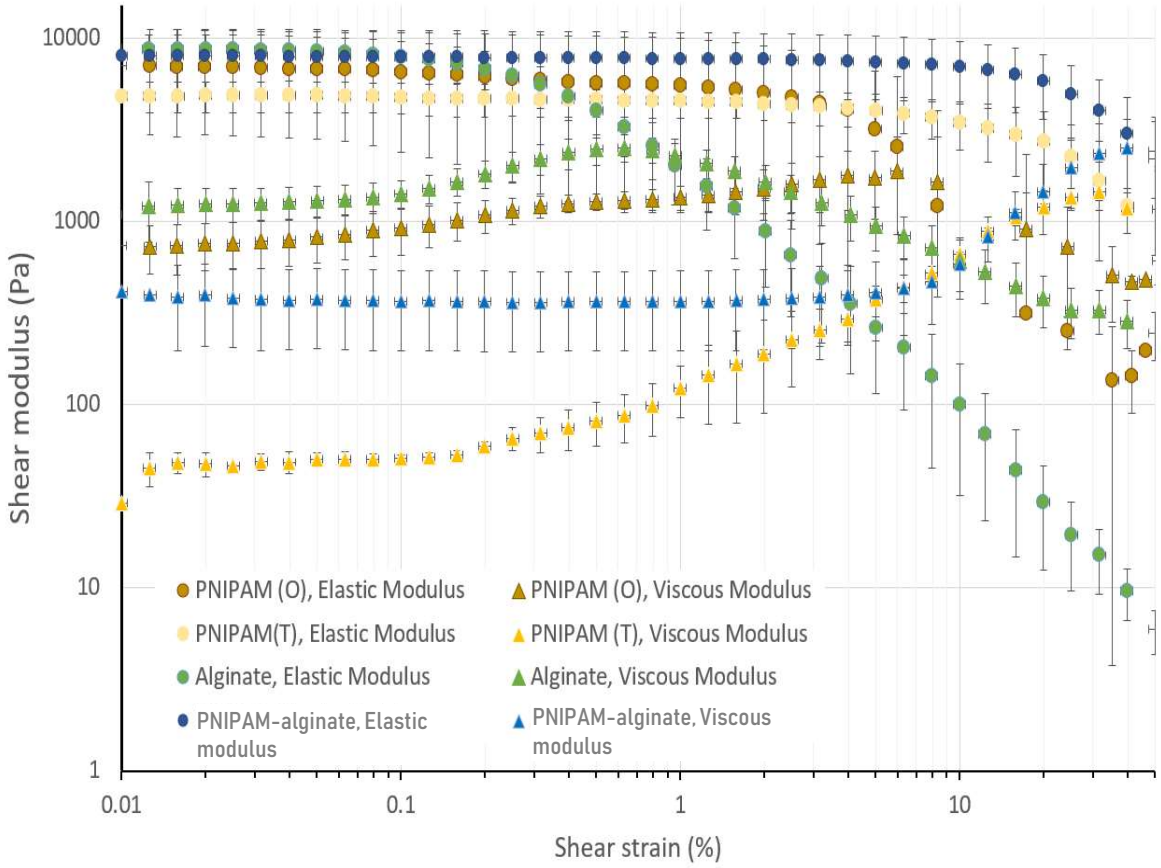

Figure 4.14. Elastic (circle) and viscous (triangle) shear moduli of gels as tested using rheometry as described in Materials and Methods. Error bars are standard error on the mean taken from three samples.

From the data in Figure 4.14, PNIPAM (T) has an elastic shear modulus of 4.8±9 kPa, PNIPAM (O) a modulus of 7 ± 4 kPa. Puleo et al. find a compatible value of 6.5 kPa.[65] Crossover between elastic and viscous regions occurred after 12% strain. Large errors likely derive from issues of sample reproducibility – these measurements were made at the beginning of the project and sample preparation improved throughout.

Alginate was the stiffest gel measured with an elastic shear modulus of 8.8±1.6 kPa. However, the LVER for alginate was the smallest of the samples measured, as expected from the flexible nature of the ionic crosslinks, and a crossover between elastic and viscous behaviour was seen at under 1% strain. This is larger, but on the order of, the values found by Stokke et al. for various alginate stocks using the same weight percentage and a similar protocol.[66]

PNIPAM-alginate, as expected, combined the desirable characteristics of both components: this gel was stiffer, at 8 ± 3 kPa, and retained an elastic-dominated response up to a strain of 12%.

4.4.5.2 UNIAXIAL ELASTIC CONSTANTS

Compression data were taken as given in Materials and Methods to compare the behaviour of PNIPAM and alginate gels separately to the composite double-network gels. Results were transformed into true stress and strain and are presented in Figure 4.15, Figure 4.16Figure 4.17. While the assumption of constant volume is not exact for the alginate gels used in this study, the magnitude of the deviation is small and should not affect the qualitative conclusions presented here. Each series represents a sample, and each graph shows a separate composition.

The behaviour of the gels is in accordance with prior work on double network hydrogels by Gong, de Moura, and others.[27,49,67] The maximum recorded yield stress of PNIPAM-alginate, at ~185kPa, is significantly greater than the sum of that of plain alginate gels, ~28kPa, and plain PNIPAM, at ~13kPa.

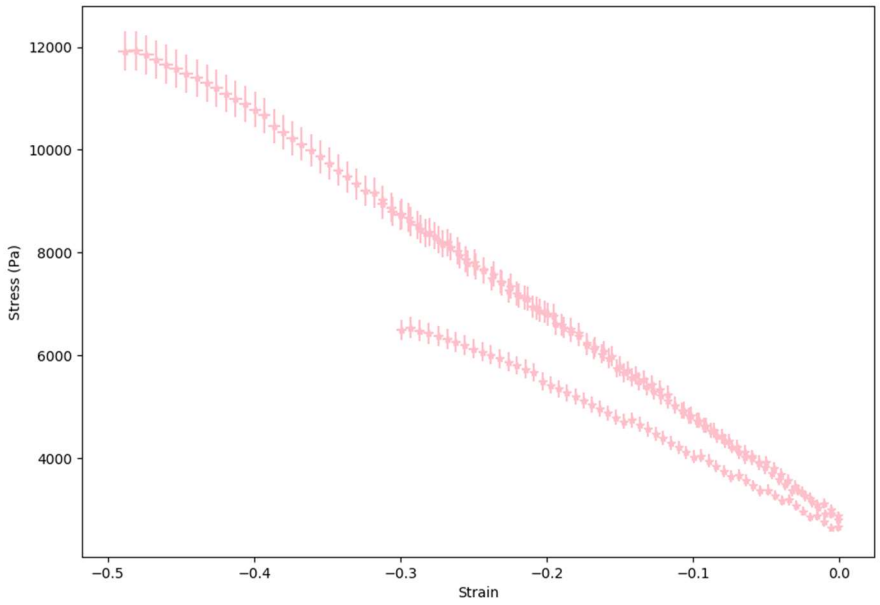

Figure 4.15. Compression data for PNIPAM gels, converted into true stress and strain and shown to failure. For visibility, only every fifth data point is shown.

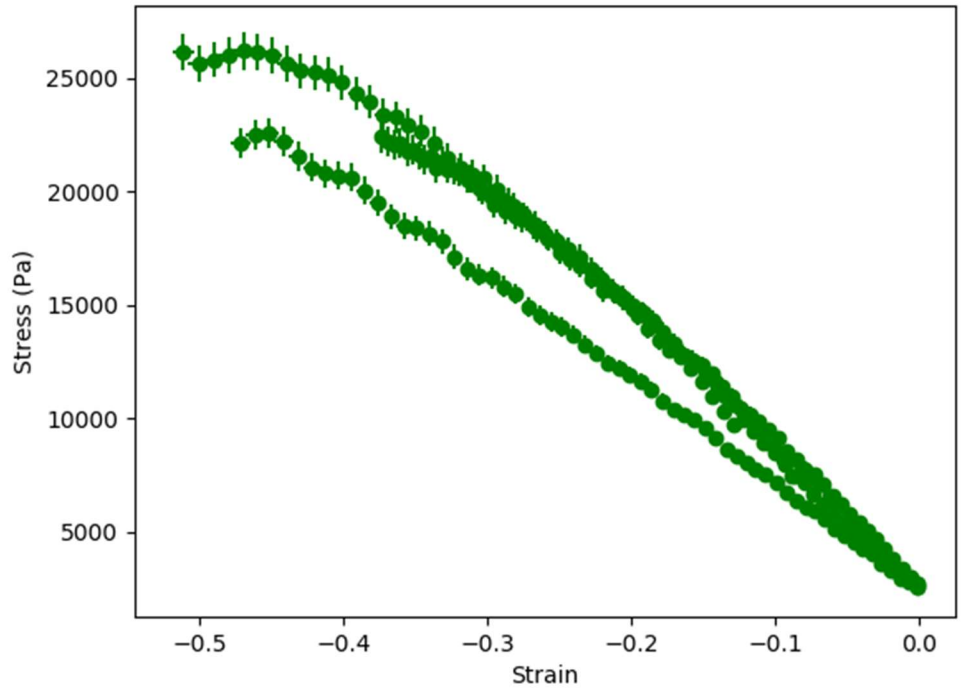

Figure 4.16 Compression data for alginate gels, converted into true stress and strain and shown to failure. For visibility, only every fifth data point is shown.

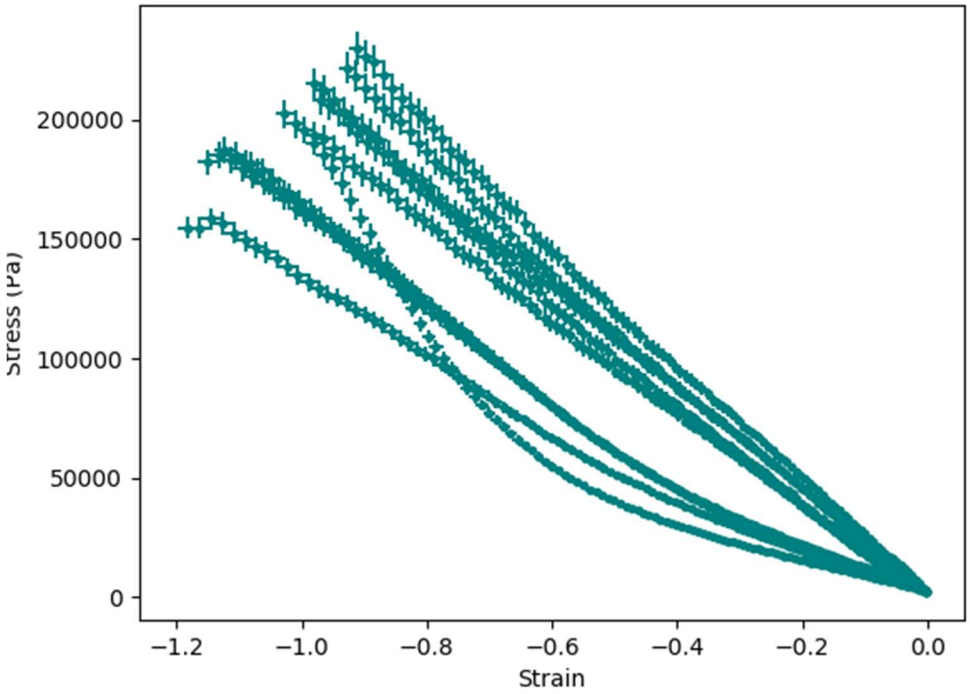

Figure 4.17 Compression data for PNIPAM-alginate gels, converted into true stress and strain and shown to failure. For visibility, only every fifth data point is shown.

Within the elastic limit, taken here as $\epsilon < |0.01|$, linear fits to the data were used to determine the Young's modulus of each of the materials. An enlarged graph of this region for each composition is shown in Figure 4.18, Figure 4.19, and Figure 4.20. These show that at small strain, a linear fit is appropriate. While there is significant variation in gradient for samples within each batch, the fit for each individual trend to the data points is fair. This suggests the origin of variation is sensitivity to sample preparation, creating a high standard error on the mean. Comparing to the full data series of Figure 4.17 shows strain hardening. This matches expectations for double-network models, namely that the toughness of the composite gel derives from the work of plastically deforming the bonds within. [49,64]

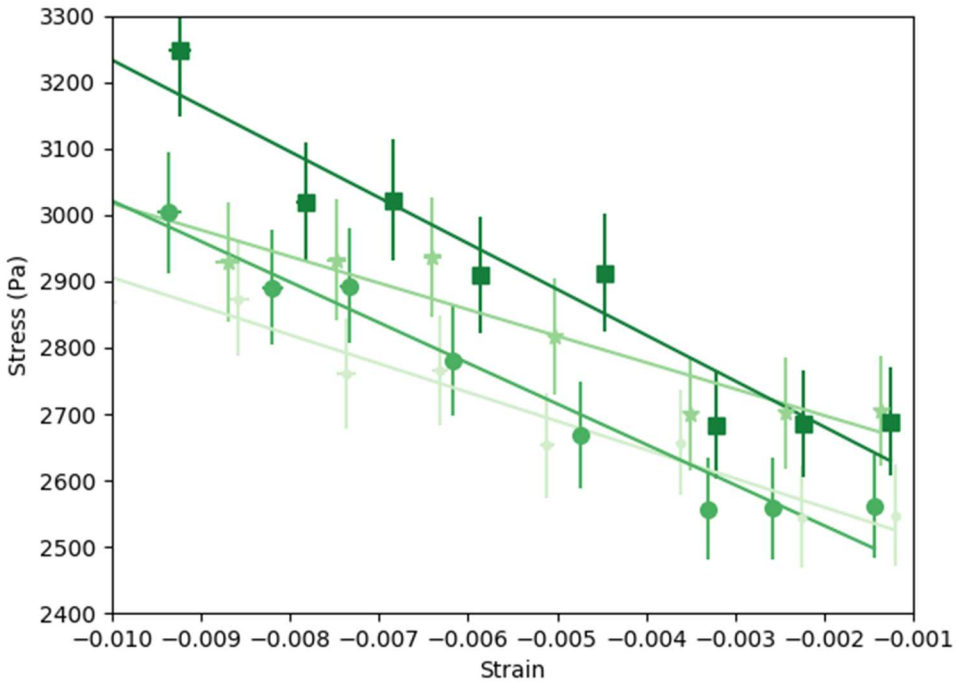

Figure 4.18 Stress-strain data from small-strain region for alginate samples, with linear fits used to calculate the Young's Modulus.

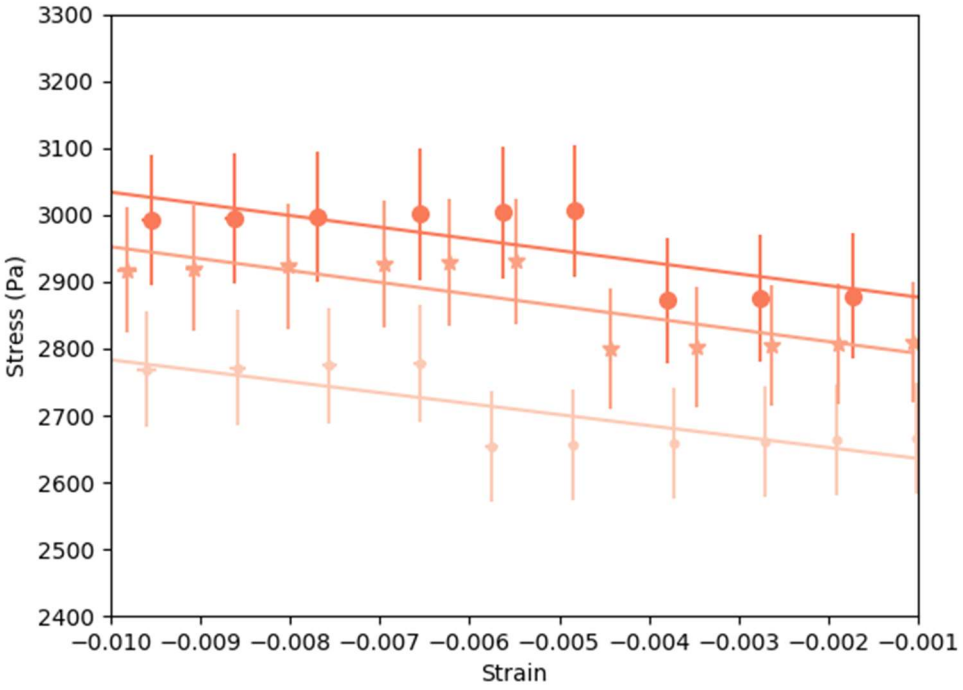

Figure 4.19 Stress-strain data in small strain region for PNIPAM samples, shown with linear fits used to calculary Young's Modulus.

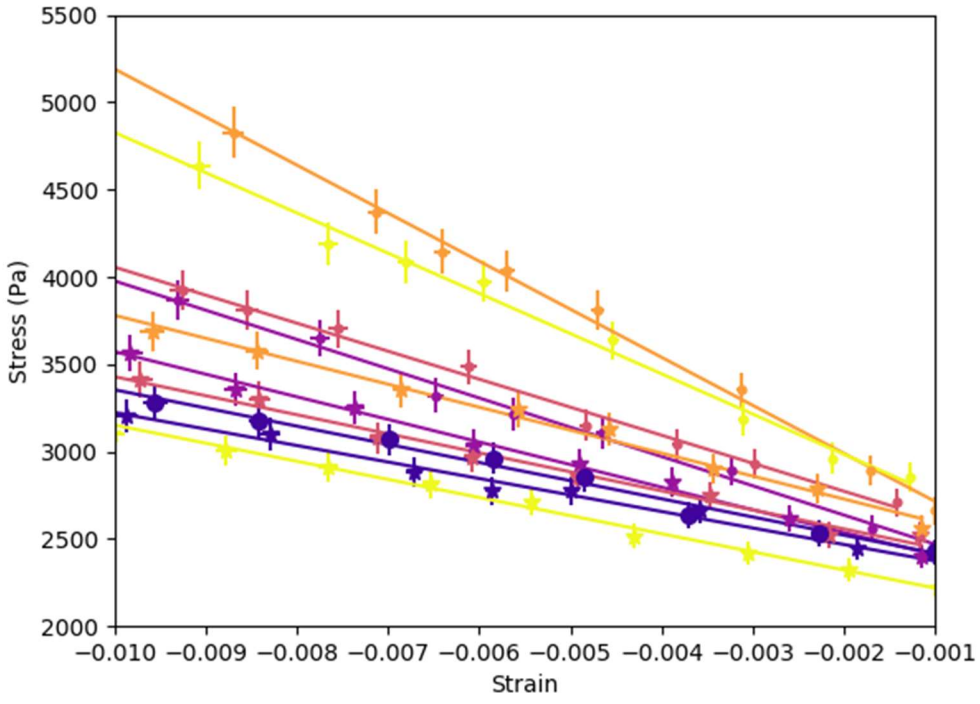

Figure 4.20 Stress-strain data in small strain region for PNIPAM-alginate samples, shown with linear fits used to calculate Young's Modulus

The Young's moduli found from these fits are for PNIPAM 17.2±0.5kPa, for alginate 53±7kPa, and PNIPAM-alginate 150±19 kPa. This shows an increase in stiffness which is again, as expected, non-additive. The modulus values obtained for PNIPAM-alginate are within error of the 170±3 kPa reported by Bakarich et al. for the same composition, obtained through tensile testing.[25]

A common theoretical assumption used in hydrogel characterisation is that $E \approx 3G$, arising from an assumption of isotropy, constant volume and relative incompressibility – ie. that K is large (see for example Doi [68]). Since E here is ~150±19 kPa, and G at most 7 ± 4 kPa, one of these assumptions clearly does not hold true here. This would indicate that either the results represent material values in different testing regimes, the bulk compressibility K differs between modes, or the samples of 7mm and 3mm thick respectively are not comparable.

During rheological gel testing the strains induced are positive and in shear mode. Conversely, compression testing exerts a normal, negative strain, bringing the polymers closer together. Polymers are generally expected to have a higher yield stress in compression than in tension, suggesting that the bulk compressibility affects the yield stress.[69] However, in this case the values for E obtained by compression agree with others' tensile testing results.

Viscoelastic materials also exhibit different behaviour depending on the strain rate applied. In this case the shear measurements were taken more rapidly (1Hz frequency) and so would be expected to have a higher value than the compression measurements.[70] At a rate of 1mm/min, compression tests theoretically allowed a longer time for material rearrangement and viscous relaxation, reducing the stress experienced by the materials.

There is little prior work on relevant hydrogels showing a systematic difference between tension and compression. One of the few examples is Puleo *et al*, where the fracture strain of pure PNIPAM was found to be 30% in tension and 79% in compression. This was attributed to the ability of water to redistribute in compression but not in tension.[65] However, this differs from the expectations of poroelasticity, which would suggest a higher resistance to deformation for samples within which fluids cannot redistribute,[71,72] such as when contained within non-porous plates during compression testing. While both predictions match what is seen, the interpretations of material behaviour differ. Work by Wang et al. also suggests that the decay behaviour measured is sensitive to the sample size, which may have played a role in the difference between these samples.[70]

In the absence of prior evidence for a systemic difference between the testing methods, the possibility of anisotropy in the samples must also be considered. This is also suggested by the work in 0. This could be further investigated by probing vertical cross-sections of both samples with nanoindentation or AFM to look for variation within the bulk. These techniques would also yield information about the bulk compressibility and the Poisson's ratio, thus investigating two possibilities simultaneously.[71]

4.4.5.3 MEASUREMENT OF THE ELASTIC RESPONSE ABOVE LCST

Measurements in 4.4.5.1 and 4.4.5.2 were taken in ambient conditions. To use a Timoshenko-type bilayer model to predict the heated configuration, the Young's modulus of gels above the critical transition would be required.

Compression measurements of gels held above the LCST, in the contracted state at a temperature of <50°C, were attempted for both shear and uniaxial testing. However, the results were highly variable between samples, ranging from a Young's modulus of 35kPa to 180kPa. A significant increase relative to ambient temperatures is predicted, both by literature and theory.[17,25,30,73] Since none of these results are of the magnitude expected, this suggests a problem with the methodology of the experiment. This could be due to the deformation of samples when heated, rendering the measurements of area used for stress-strain conversion inaccurate, or the samples not remaining in the collapsed state for the duration of the test, possibly due to confounding effects of compression.[74]

4.4.6 SHAPE CHANGE IN PRINTED PNIPAM-ALGINATE GELS

The general problem of predicting the deformation of hydrogel shapes as temperature-based contraction occurs is challenging, as it deals with the large-scale deformation of anisotropic viscoelastic structures, an inherently non-linear problem.[75] To investigate the previously undocumented phenomenon of illumination-based graded response, a reduced dimensionality system was selected for further examination. Target shapes of beams 60x3 mm in *x* and *y*, and with heights from 1-5 mm in 1 mm intervals, were generated using the printer system described in Chapter 3. These were printed in batches of three. Significant variation (± 0.3 mm) was seen in the output dimensions following the full curing and equilibration process. This may be due to unevenness in UV exposure or flow issues in the nozzle, for which suggestions for improvement are made in section 3.5.2. Due to

the non-zero viscosity of the gels before curing, spreading was seen in the prints. This resulted in the deformation sketched in Figure 4.21.

Samples were photographed in the conformation they assumed following equilibration at ambient temperatures, and also in their equilibrated conformation above LCST. Since the gels approximate neutral buoyancy to 1 part in 1000, gravitational effects are taken as negligible. All samples are suspended from a central point, mounted with the un-illuminated face attached to the suspension point using the method described in 4.3.4.1.

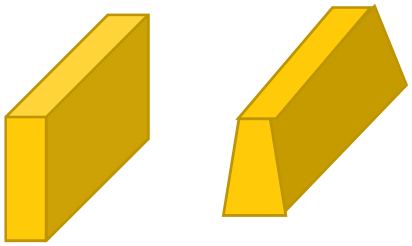

Figure 4.21. Sketch of print deformation resulting from flow of uncured polymer. The largest effect seen was on the 5mm high samples which were 5.8mm in width at base and 2.6mm at the top.

4.4.6.1 SWOLLEN EQUILBRIUM CONFIGURATIONS FOR GRADATED BEAMS

Considering first the case of ambient temperature, qualitatively changes are seen in the shape adopted by the beams, as shown in Figure 4.22. Increased curvature is seen in the thinner samples. While the equation for beam bending produced by Timoshenko[76] predicts an increase in radius of curvature with height of beam, presuming all other variables to be held constant this would be a linear relationship (see section 1.5.2). It should also be noted that the total angle subtended depends not only on the curvature but also on the aspect ratio of the shape. Morimoto and Ashida demonstrate that as beam length increases with respect to the height the effects of the free ends of the beam are reduced. Curvature therefore tends towards a circular configuration rather than a parabola with increasing aspect ratio.[77]

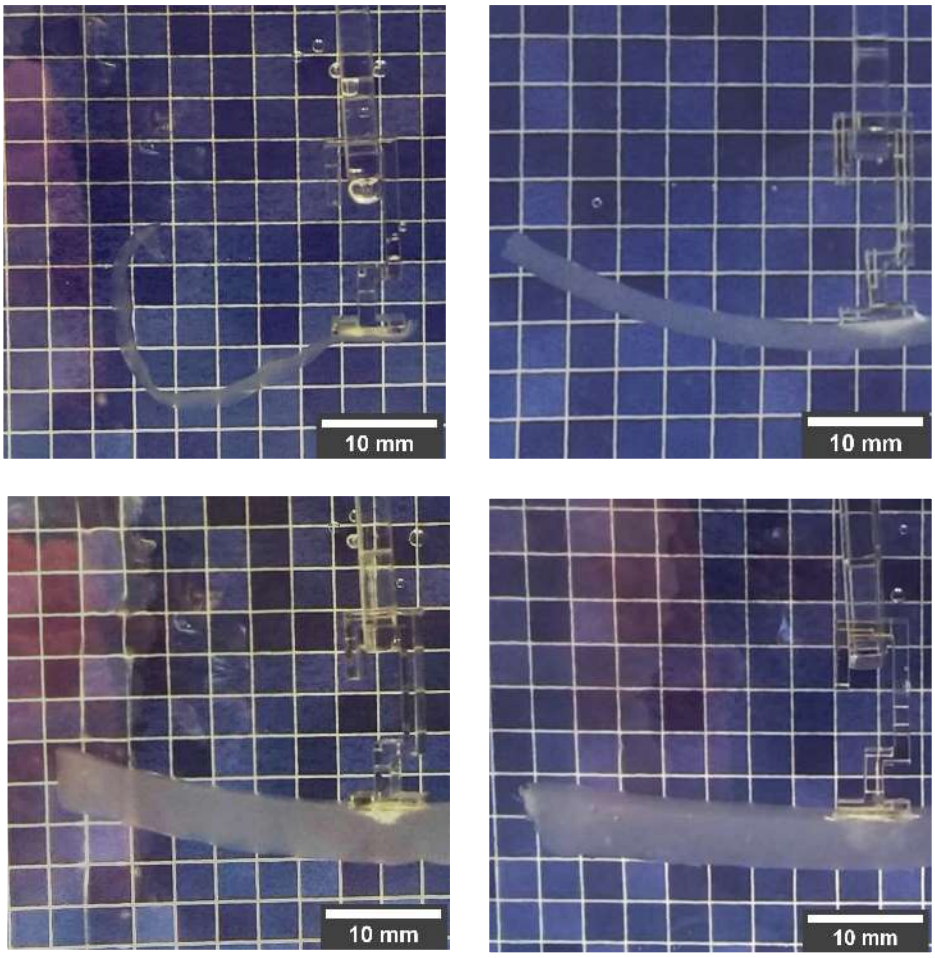

Figure 4.22. Equilibrium configurations taken up by beams printed flat and then allowed to equilibrate. L-R, beam heights of 1mm, 2mm, 4mm and 5mm thick. While samples vary, curvature opposes the direction of illumination (all samples are mounted with the illuminated side facing down) and the degree of curvature decreases with thickness.

Not all samples produced exhibited well-shaped, consistent bends under ambient conditions, and therefore these samples were rejected. The 3mm height sample batch was particularly variable, as shown in Figure 4.23. This could be a particular sensitivity of this dimension: it seems likely that if the equilibrium configuration is closer to flat then small variations in mounting, humidity or light intensity during manufacture will be sufficient to change the configuration. Alternatively, this could be a batch production issue; while the origin of the bending phenomenon is unknown (see section 4.4.8 for further investigations), it is hard to say what is necessary to reduce or control it.

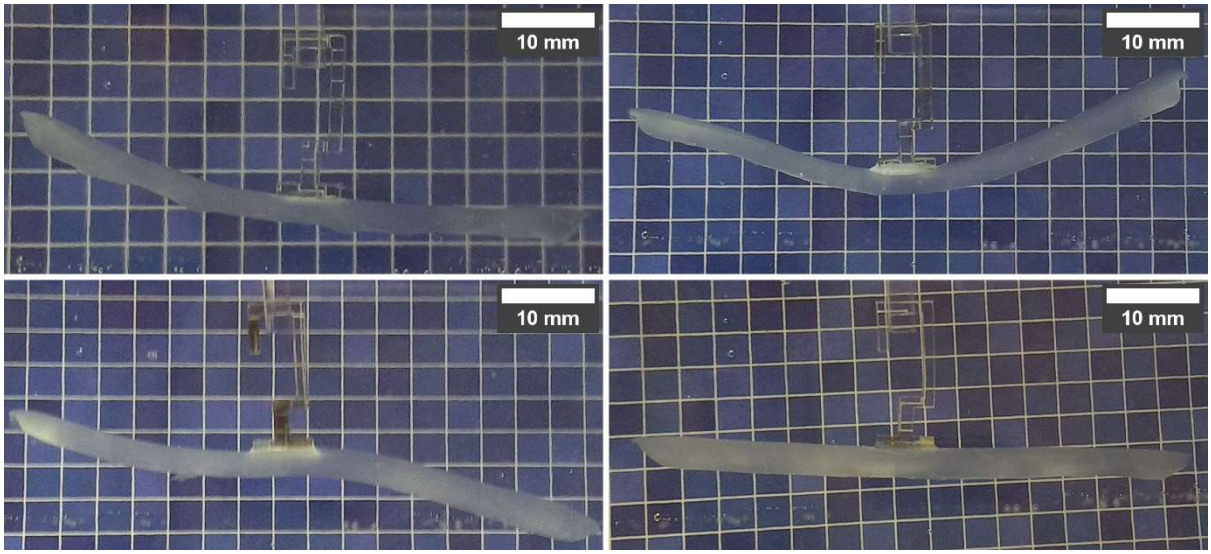

Figure 4.23. Examples of 3mm beams in ambient conditions and the variation shown in their configurations.

Producing samples one at a time would be a slow, but simple, testing step. The current illumination spot size and sample spacing means multiple samples are illuminated at once and the light beams may not be approximately parallel to the print bed for all samples, or of equal intensity throughout the spot. This is supported by the observation that of three 5 x 3 x 3mm beams, one curves left at maximum contraction, the other right, and the third straight up (see Figure 4.27 for an illustration and further discussion). The distortion of the printed samples from the target shape, forming a trapezoidal prism rather than a true rectangular beam (shown in Figure 4.21), may also play a role. If a series of single-sample prints showed improvement, the next step would be to improve light collimation with methods detailed in section 3.2.5.

4.4.6.2 CONTRACTED EQUILBRIUM CONFIGURATIONS FOR GRADATED BEAMS

During heating, the beams initially display bending behaviour to take up well-shaped parabolas, arcs of ellipse, and circles. Thinner samples are generally quicker to respond (deforming substantially within seconds).

Figure 4.24 shows an example of deformation over time with stills taken at 4 second intervals.

For such thin samples, curvature is greatest for the first few minutes of immersion and then straightens out to stabilise at the shapes seen in Figure 4.25. This could be due to the initial contraction of the skin of the sample

causing a differential stress relative to the still-swollen inside, which is then relieved as hot water molecules diffuse throughout the sample and the contraction state becomes uniform across the sample.

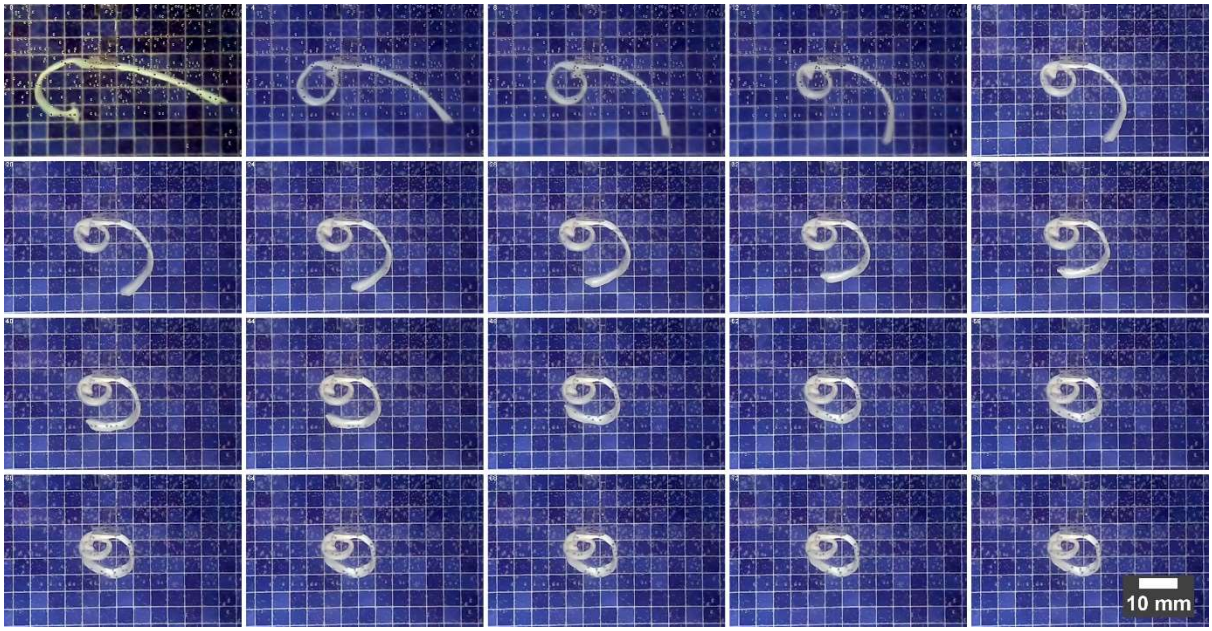

Figure 4.24 Timelapse series of a 1.3±3mm x 5mm x 65mm gel strip, initially at 21 °C, immersed in 50 °C water at T=0. Images are 4 seconds apart and start in the top left, progressing left to right. Total sequence thus represents 192 s.

After being held at a temperature of <50 °C for 1 h a stable contracted configuration is reached. These samples are less regular than the swollen gels due to bubbles in the gel, but many still show a pronounced curve and change in conformation beyond a simple scaling (Figure 4.25). Interestingly, the direction of the final curvature depends on the height of the sample. Thin samples (<2mm initially) adopt a final curvature with a radius parallel to the original illumination (the inverse of the ambient direction of curvature) and thicker samples (>4mm) finish with curvature opposing direction of illumination (parallel to the ambient curvature, but with a decreased radius of curvature).

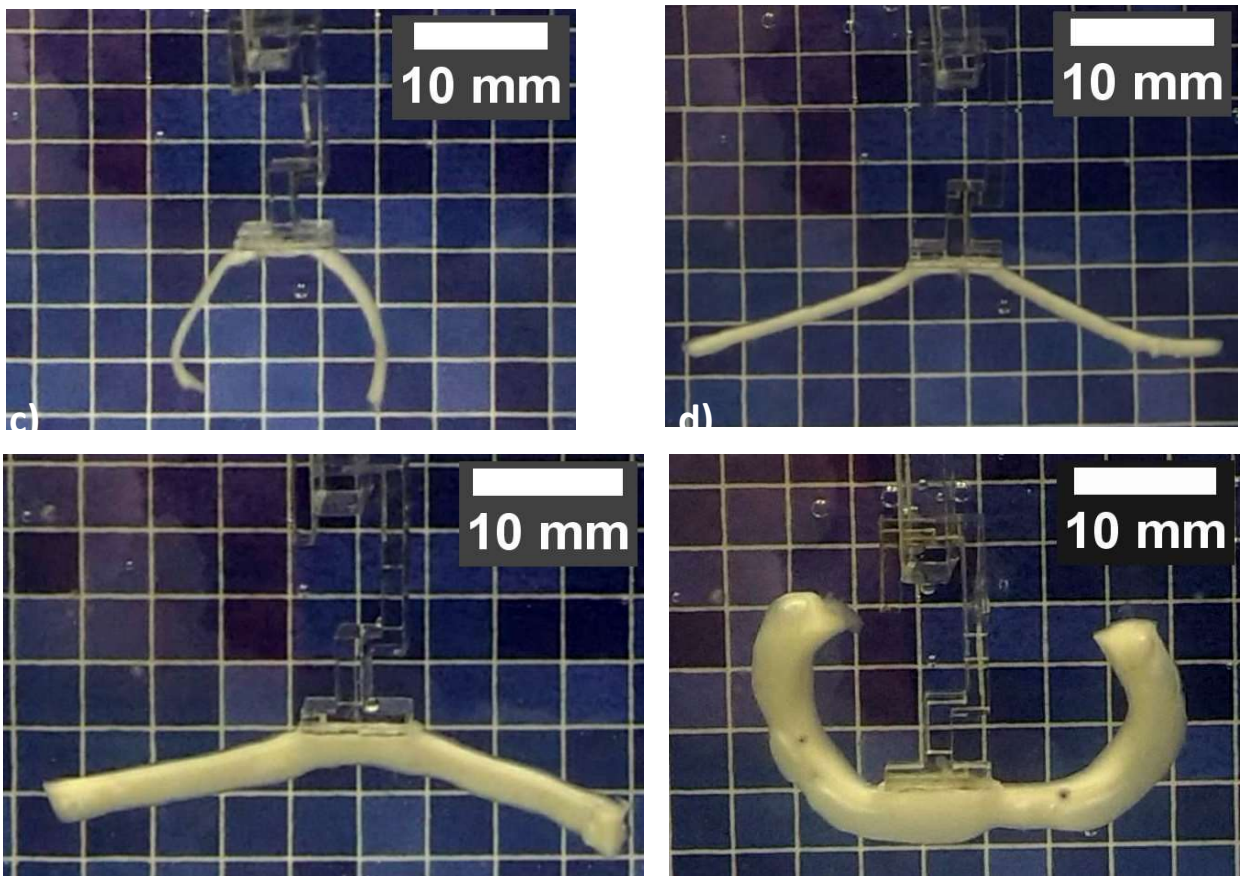

Figure 4.25. Series showing trend of curvature with increasing height for the final, maximally contracted configuration. Sample heights as printed (ie before contraction): a) 1mm, b) 2mm, c) 4mm, d) 5mm. Magnitude and direction of curvature both change consistently for all samples.

In their maximally contracted configuration, samples between 2 and 3mm thick produce an angled joint, rather than a continuous curve. This is thought to arise from the forced strain caused by adhesion to the sample holder preventing the contraction of one side of the test piece, creating an elastic strain which is relieved by the adoption of a bent configuration. This provides an illustration, both of the effect of sample testing protocols, and also of how this material could be used to actuate joints, as well as continuous bends.

4.4.6.3 ILLUMINATION DEPENDENCE OF EFFECT

The relevance of the illumination direction is highlighted in the case of beams which collapsed between printing and curing. Originally constructed as 5 x 3 x 60 mm (z-y-x), instabilities caused them to tilt during curing, as shown in Figure 4.26.

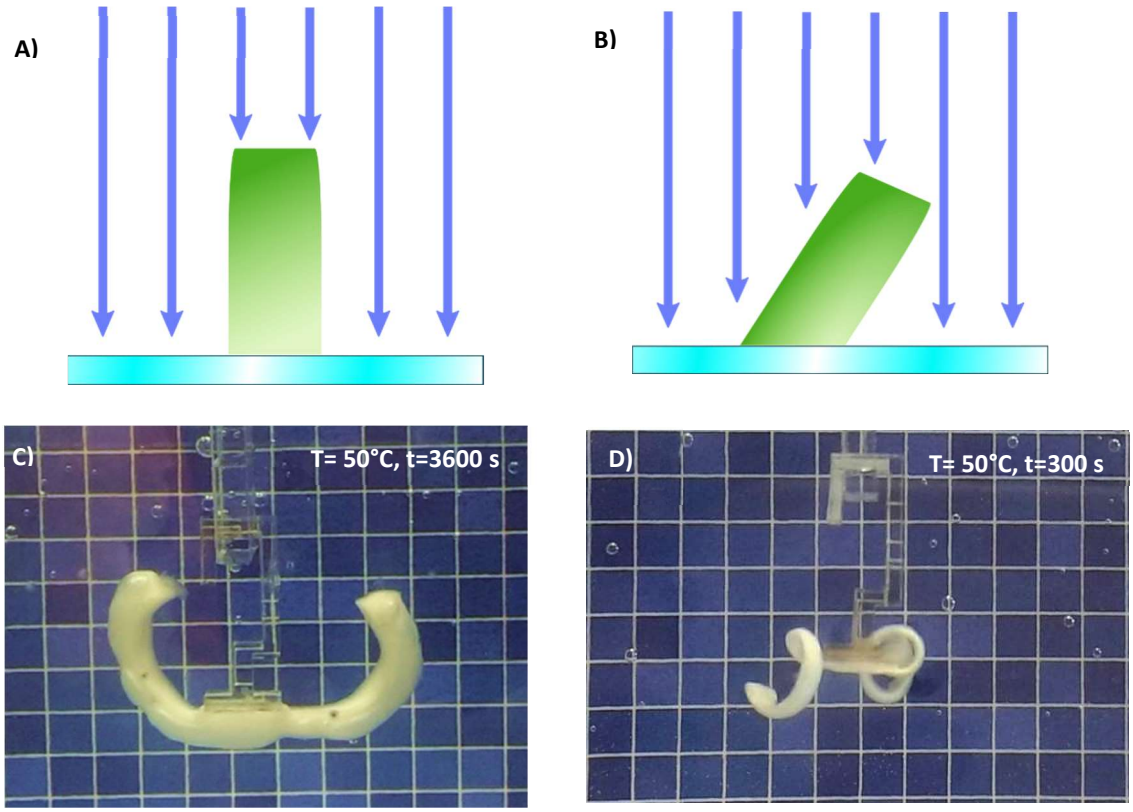

Figure 4.26. Two beams printed at 5 x 3 x 60 mm and cured with illumination directly from above. (A) is as printed and B) tilted following print. The different illumination directions with respect to the printed parts impose different contraction gradients leading to plane elliptical (C) and helical (D) deformation.

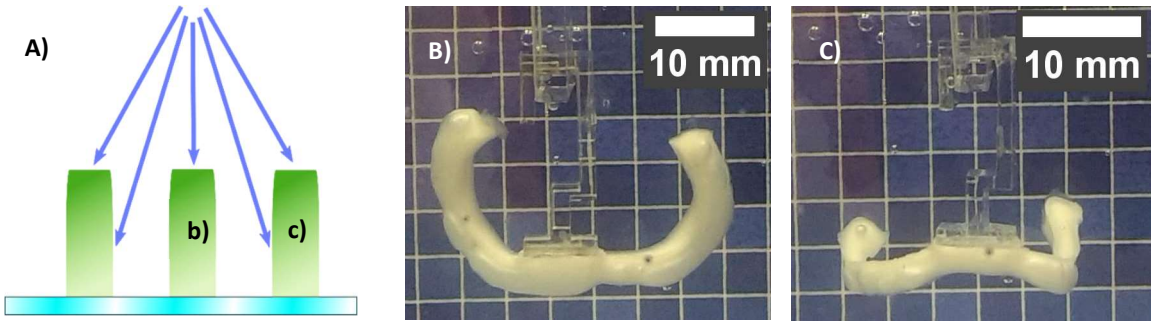

Figure 4.27. Illustration of theorised origin of off-plane bending in thick samples. If the light source used during curing (as seen in A) is not approximately parallel, then beams b) and c) receive different gradient exposures during curing. This could explain the observed behaviour of one beam in three that curves in the z-direction (B) and one that contracts both in z and x directions (C).

This caused the curing differential to occur, firstly through a smaller thickness, and secondly at an angle through the piece. The thermoresponsive gradient thus produced contracts into a helical, rather than planar, curve, shown in Figure 4.26 d). This underscores the importance of directional curing as a variable, since the biggest difference between the two printed pieces shown in Figure 4.26 is illumination.

While variation is seen between beams in the same orientation printed at the same time, these do not show differences in helical versus planar curvature: rather in direction of curve, with a component perpendicular to the length of the beam. This would be compatible with illumination over three samples which is not parallel, as illustrated in Figure 4.27.

If these interpretations are correct, it suggests the intriguing possibility of using the process of curing to add different functionalities to the same print. The integrated curing modulation demonstrated in section 3.2, easy to incorporate into G-code during slicing or post-print, could modify the dose delivered. Illumination direction could be controlled modestly by some overriding of the firmware to alter the effector angle while rastering post-cure, or placing a sample off-centre to a light source with a large half-angle and moving the head relative tp the sample. Alternatively, if a directional light source were mounted on a ball joint adjustable by servos, a hemisphere of solid angle could be accessible while printing.

With more precise control over light direction, the figures presented in section 4.4.7 to summarize the relationship between radius of curvature and sample height could be improved. Inspired by Figure 4.26, helical configurations could also be explored, with pitch and radius as independent variables.

4.4.6.4 TWO-DIMENSIONAL CASES

Extending into a two or two-and-a-half dimension (as only low surface features are possible currently) print allows a demonstration of the potential utility of such a system. A flower or gripper shape, capable of opening and closing, is a common demonstration model for the field. A five-pointed flower shape with decorative ridges and centre was produced using the same methods. The change in shape between immersion in water at ambient temperature and at 50 °C for such a sample is shown in Figure 4.28.

One of the petals shows different curvature to the others: this is attributed to receiving a different curing dose due to the incompatibilities between the fivefold symmetry of the print and the rectilinear direction of the curing raster.

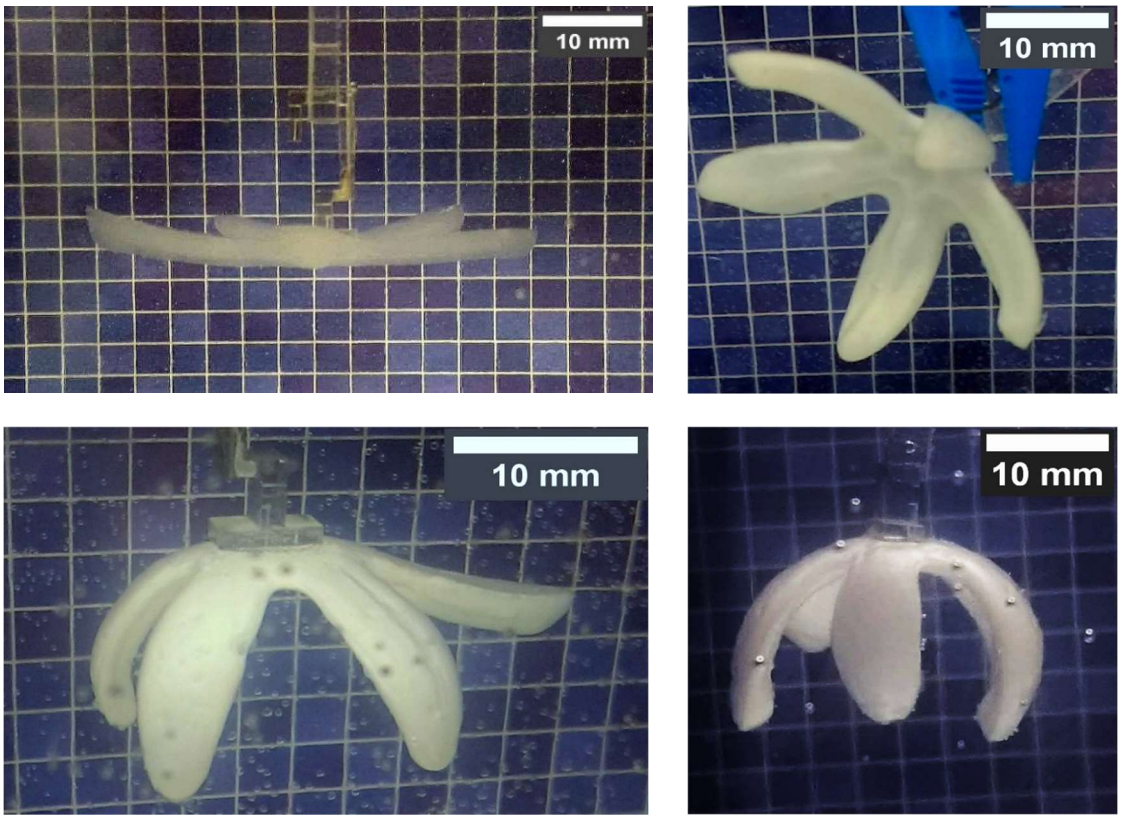

Figure 4.28. Top: left, a 3D printed flower at embient temperature, showing slight bowing towards sample mount. Right: initial curvature of flower following immersion for 2 minutes; detailed features visible. Bottom left: shape following 20 minutes immersion. Note difference angles of petals. Bottom right: maximally contracted configuration following 1h immersion at 50 °C. Tangents to petal tips now form an obtuse angle with respect to the original printed plane. At full contraction, the widest point is 17mm across; less than half of that at ambient.

The behaviour of this sample is similar to five beams as seen in the previous section, joined at a central point. A distinctly different behaviour is seen for circular discs, which in some cases change their Gauss curvature when heated: shown in Figure 4.29 and Figure 4.30.

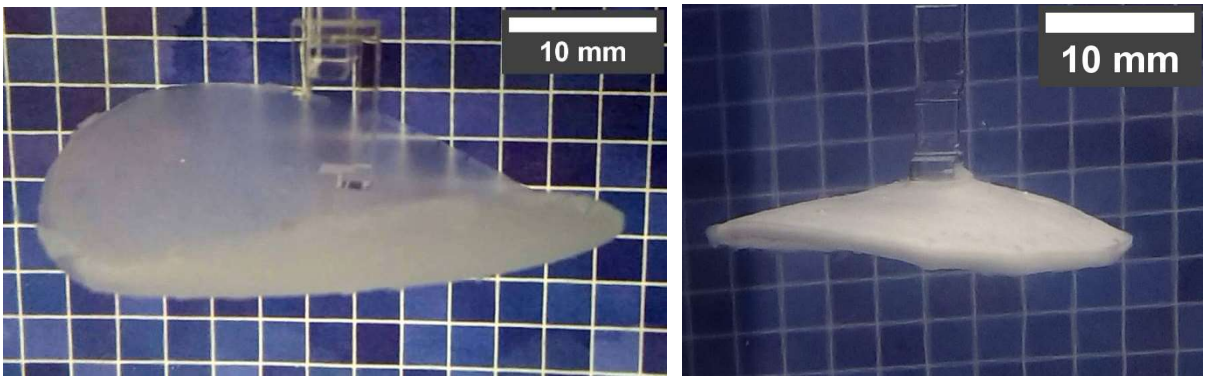

Figure 4.30. Disc of radius 20mm and height 2mm, demonstrating a switch in curvature: net curvature is upwards (away from original illumination) before heating and downwards (towards illumination) after.

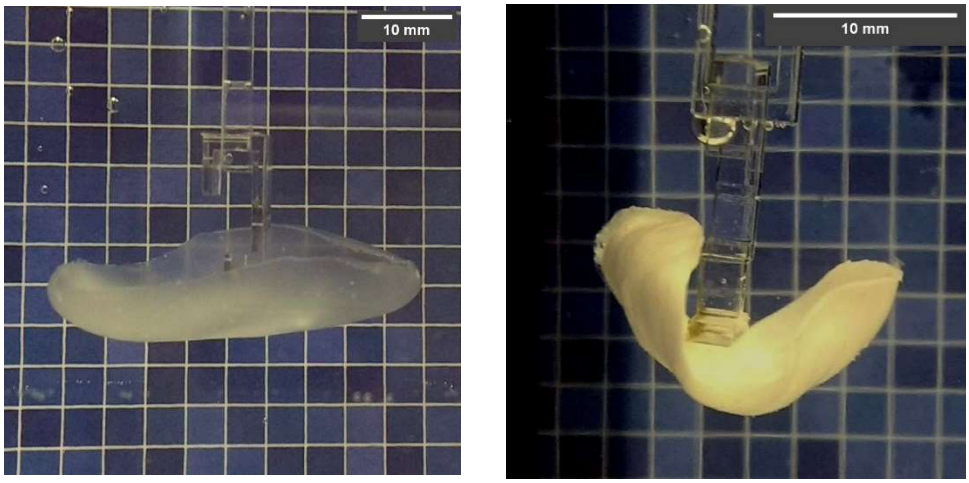

Figure 4.29. Disc of 20mm in radius and 1mm in depth in ambient conditions (left) and after 15 minutes in water at 50°C (right). This view is from the side and so backing squares are further away: see scale bar for accurate size reference.

An uniform bending into a bowl shape has a high elastic energy cost for the shape. Therefore it is energetically advantageous for the symmetry to be broken and for a 'taco' shape, of a circle bowed into a cylinder, to be formed. This configuration has a curvature of zero in one direction and thus a reduced bending energy. This could be the origin of the behaviour seen in Figure 4.29, as the contracted material is stiffer and therefore would require more energy to deform if the initial bowl configuration was retained. Due to the sensitive nature of gel systems there are many potential sources of symmetry breaking, although it seems likely that in this system the deciding factor is the geometry of the sample mount. For a thicker gel disc, as shown in Figure 4.30, the energy cost is too high even below the LCST to retain a spherical geometry. However, following the effects of thermal contraction the direction of curvature inverts, analogously to the beam situation. The geometry adopted will

minimize the strain energy of the system and is likely to be a function of the gradient and the radius: height ratio, as well as any external influences such as the mount.

The examples presented in this section show definitively that shaped PNIPAM-alginate gels prepared using the equipment in Chapter 3 undergo large, non-trivial changes in surface curvature and configuration upon simply placing into hot water. These changes differ depending on sample geometry and curing conditions. As a function of these variables, sample curvature may be dramatically increased, decreased, and in some cases inverted as the gel is transferred from ambient to heated water. This demonstrates a rich selection of potential mechanisms for actuating systems. For some samples the macroscale configuration changes over time as the heated solvent permeates the sample, leading for example to a beam which curls up and then extends itself.

While it would be desirable to have more reproducible samples and therefore more precise control over the final contracted shapes, the behaviour documented above demonstrates the potential of the technique. To explore deformation of 2D surfaces a method of collecting data on the topology of a curved surface would be desirable, such as laser scanning or photogrammetry techniques.[78] A more precise understanding of the phenomenon would benefit from more reproducible samples, which in turn would result from an understanding of the relevant phenomena that must be controlled to see the result.

4.4.7 MATHEMATICAL MODELS OF BEAM DEFORMATION

While the specimens processed showed substantial variance, a sketch of the variation in minimum radii of curvature as a function of beam thickness in both ambient and contracted states can be made, and are shown in Figure 4.31 and Figure 4.32 respectively.

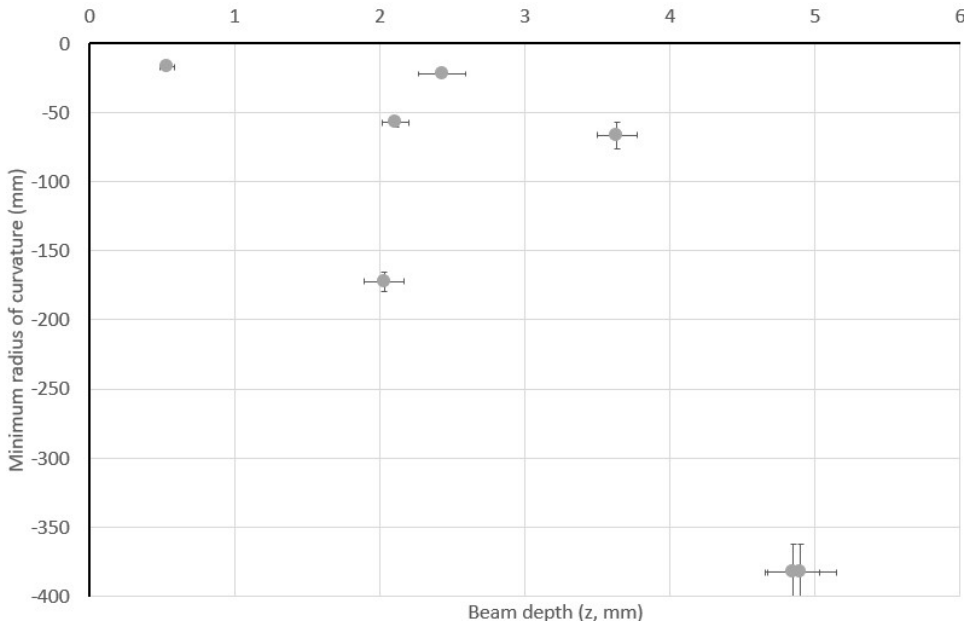

Figure 4.31 Minimum radius of curvature for PNIPAM-alginate gel beam samples equilibrated at ambient, as a function of their height when fully swollen. Errors in x come from the standard deviation of 10 measurements of thickness and in y from the covariance of the coefficient of the quadratic term when fitted; if not visible these are too small to see.

Figure 4.31 shows negative curvature (here defined as away from the direction of illumination during preparation), increasing as a function of h. It is not clear whether the increase is linear or non-linear – for simplicity it will assumed to be linear.

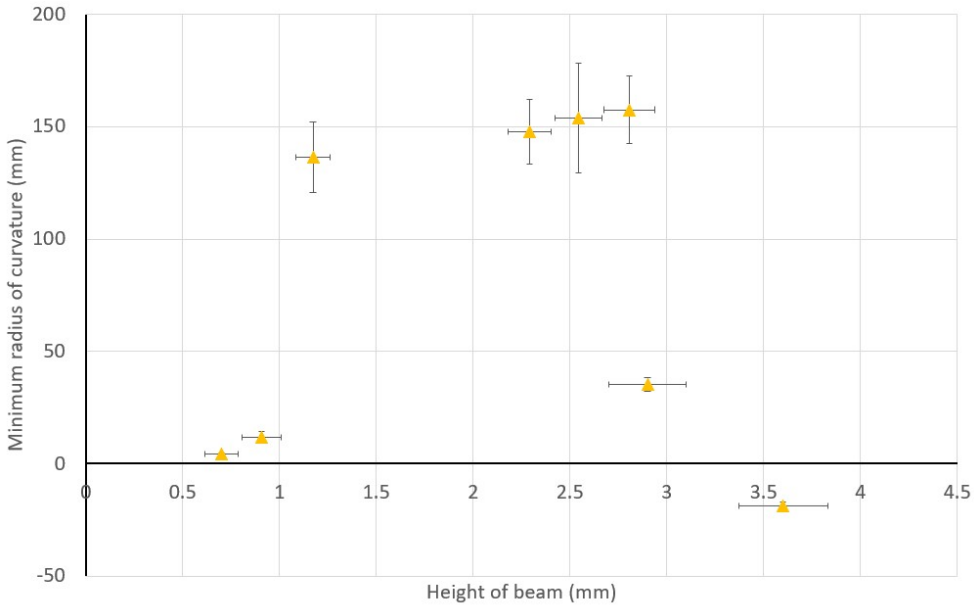

Figure 4.32 Minimum radius of curvature for fully thermally contracted PNIPAM-alginate gel beam samples, as a function of their height when at full contraction. Errors are as described in Figure 4.31 caption.

Figure 4.32 shows more complex behaviour: the smallest radius of curvature (corresponding to greatest curvature) occurs for the thinnest samples. The radius increases, (samples become straighter), before decreasing again and becoming negative for the thickest sample. The samples with a radius above 100mm are those which show bending – this measurement may have been affected by the sample holder. The general shape is non-monotonic, and changes sign at the highest value.

Comparing these shapes to the predictions made by models of beam bending, such as the Timoshenko bilayer equation (see section 1.5.1) could give insight into the material properties underlying the deformation. In this section scaling arguments are used to consider the bending behaviour which would be exhibited by simple 1D beams with different contraction-depth profiles and, by comparing these to the results found experimentally, assess the suitability of a Timoshenko-type model for this bending behaviour.

As a simplifying assumption, each layer will be treated as an elastic body, disregarding the complex time-based responses of the material (see section 4.4.5.2 for discussion). In the following section, two bilayer approximations were compared to the behaviour depicted in Figure 4.31 and Figure 4.32. While no discontinuities are visible in the samples, the bilayer strip is a standard analytical model in the field.[79–81] Due to its simplicity of application, particularly compared to a full continuum elasticity treatment, was trialled for effectiveness. The two situations considered are shown conceptually in Figure 4.33.

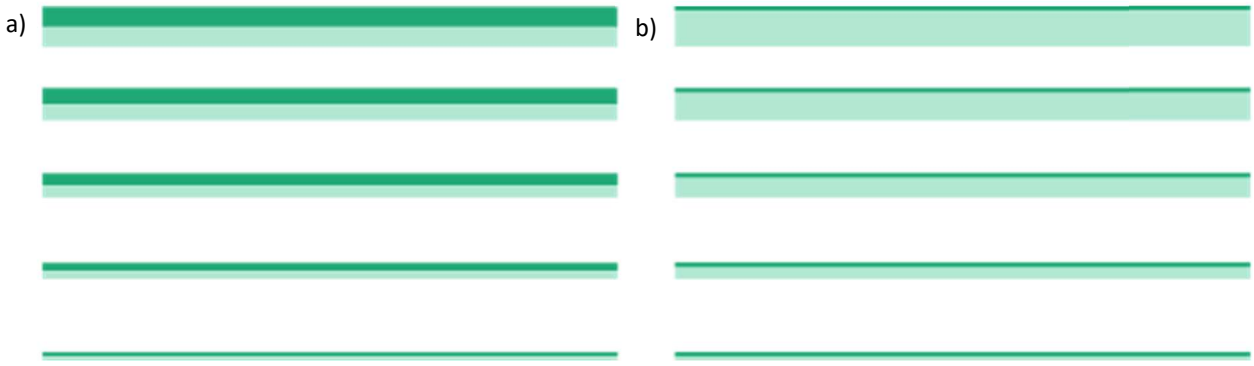

Figure 4.33 Schematics of the models considered in this section as potentially representing the behaviour of samples created and tested in section 4. 4.6. Light green represents a low level of contraction, λ_{low}. Dark green a higher level of contraction, λ_{high}. In the Timoshenko equation (1.8), the overall difference in contraction λ is $\lambda_{high} - \lambda_{low}$. Model a) takes m as constant and only varies h. Model b) considers a fixed thickness of λ_{high}. In this situation varying sample height, h, affects the ratio between the heights of λ_{high} and λ_{low} regions, parametrised in the Timoshenko equation as m.

For convenience, the Timoshenko equation for bending of a bilayer beam introduced in section 1.5.1 is reproduced here:

$$\kappa = \frac{1}{R} = \frac{6\Delta\lambda(1+m)^2}{h\left[3(1+m)^2 + (1+mn)\left(m^2 + \frac{1}{mn}\right)\right]}$$

Equation 4.3

Here K is the curvature and *R* is the radius of curvature. Defining α_1 and α_2 as the linear expansion ratios of each layer when separate (here a temperature increase causes contraction and therefore $\alpha_1, \alpha_2 < 1$), $\Delta\lambda$ is the difference between the contraction ratios $\alpha_1 - \alpha_2$. The sign of the difference gives the direction of curvature. a_1 and a_2 are the heights of the first and second layers respectively, after contraction; *h* is the total height (ie., $h = a_1 + a_2$); *m* is the ratio of a_1 and a_2; and *n* is the ratio of the Young's modulus of the layers 1 and 2, E_1/E_2.

Despite multiple investigations into potential differences between the sides (see section 4.7) , it has not been possible to measure a quantifiable difference between them. Therefore, m, $\Delta\lambda$, and n must all be considered as unknown functions of h. In the work described in section 4.4.6, the radius of curvature R is measured and the height h varied. For direct comparison to this form, Equation 4.3 may be inverted and separated:

$$R = \frac{h}{6\Delta\lambda(h)} f(m,n)$$

Equation 4.4

Where $f(m,n)$ is:

$$f(m,n) = \left[\frac{3(1+m^2) + (1+mn)\left(m^2 + \frac{1}{mn}\right)}{(1+m^2)}\right]$$

Equation 4.5

For some hydrogels, E (and therefore n) is a function of λ. However, analysis (full details of which are provided in the appendix) suggests that this is not the case for the system under study, and that the simplification of setting n=1 is applicable here. This is confirmed by Figure 4.34, demonstrating the exact value of n does not affect the general shape of the $f(m,n)$ curve, which is a continuous positive function with a minimum ≤ n, followed by a linear increase.

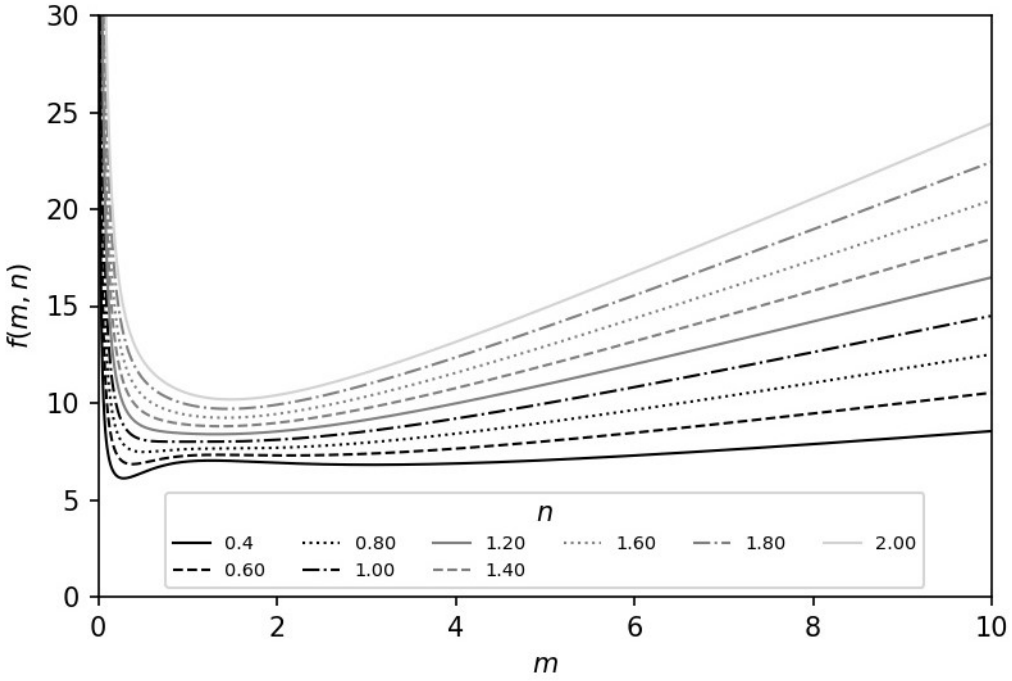

Figure 4.34. Dependence of f(m,n) on m for n in the range 0.4 – 2.0, corresponding to a Young's modulus ratio between the bilayers of $5E_1{:}2E_2$ and $E_1{:}2E_2$ respectively.

Thus f(m) can be evaluated for the two conditions presented in

Figure 4.33, firstly where m is constant and secondly where m is a function of h. The first case, a), is simple: with m constant and n fixed the term $f(m,n)$ evaluates to a constant and, if the relationship were to be valid in this case, the $h/6\Delta\lambda$ term must contain the observed behaviour of Figure 4.31 and Figure 4.32.

For case b), m can be described in terms of h:

$$m = \frac{a}{h - a}$$

Equation 4.6

Substituting this into Equation 4.5 yields Figure 4.35 for physically plausible different values of a, the thickness of the hypothetical higher contraction layer, in millimetres.

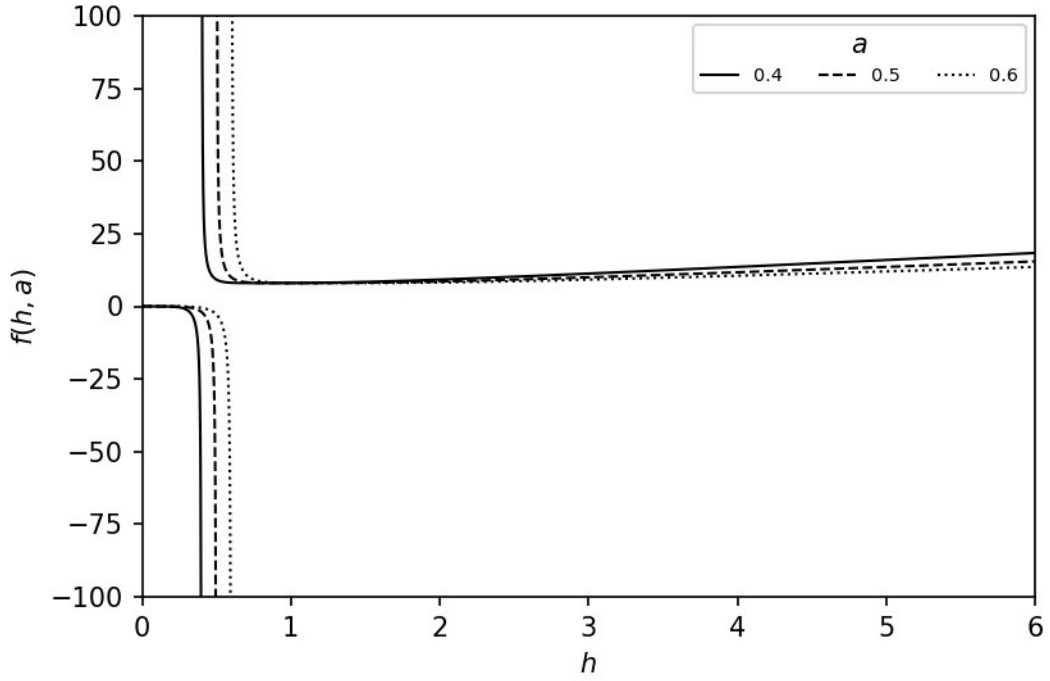

Figure 4.35 Dependency of f(m, n) as a function of h for the situation shown in Figure 4.33

Physically, h ≥ a > 0, and therefore for this situation, following an initial minimum the radius of curvature should increase with h.

The observed behaviour for samples equilibrated at ambient temperature (Figure 4.31) shows a linear increase, similar to that shown in Figure 4.35. The minimum value of h here is limited by surface effects (see section 3.2.4.9) and so the experimentally accessible portion of the graph may not include the non-linear region.

Comparing to Equation 4.4, for case a) of a fixed ratio between high and low contraction layer thickness the dependency on h would come from the $h/6\Delta\lambda$ term, implying $\Delta\lambda$ is a constant within error for the region measured. Physically, this would mean that the difference in swelling between the top and bottom following curing is not affected by the sample thickness. Given for all samples the lengths are the same during curing and

expand during equilibration to different amounts, this is observationally not true (Appendix, section 7.1.2), and can be rejected as a description.

For case b), a linear relationship between h and R emerges from $f(h,a)$ (following the initial minimum). Therefore, the $h/6\Delta\lambda$ term must reduce to a constant, implying Δλ is proportional to h. This is compatible with measurements in ambient conditions (see appendix) and therefore a reasonable description of Figure 4.31. However, there are relatively few data points and the trend could be non-linear; if so, a more complex model such as an elastic continuum treatment might be required.[77]

For the heated situation (Figure 4.32), the behaviour is more complex. A non-linear increase in radius is seen which crosses between positive and negative values, presumably discontinuously since R=0 is undefined. Neither $f(m,n)$ or h/6Δλ, where λ is a polynomial, describe such behaviour for either case. It seems that λ(h) would need to contribute this complex behaviour.

In summation, the Timoshenko bilayer model commonly used to calculate equilibrium configurations for bilayers of unequal contraction ratios is an adequate description of the conformation of these PNIPAM-alginate samples in ambient conditions. The best fit is with the assumption that a fixed-depth layer of higher linear contraction ratio is formed, regardless of thickness. This implies the difference between contraction ratios on the top and bottom surfaces decreases linearly with height; this makes intuitive sense, as in the limit of a very thick sample it seems likely no bending would take place.

However, the equilibrium forms produced by contraction are not amenable to such a treatment, showing a switch in sign which implies a discontinuity not present in any simple versions of the Timoshenko relationship. Thus, the behaviour of λ(h) is shown to be complex, possibly representing multiple competing effects.

In the next section, potential sources of the observed variation in expansion ratio λ are considered, and experiments conducted to test for measurable differences between illuminated and non-illuminated gel surfaces.

4.4.8 THE ORIGIN OF ASYMMETRY

It is clear from the bending behaviour described in 4.2.3.4 that some difference exists between the illuminated surface and the non-illuminated surface of a PNIPAM-alginate which causes them to have different expansion ratios, both in the ambient and the contracted state. To the eye and the optical microscope, they look identical.

One possibility for the varying behaviour between the illuminated and non-illuminated sides in samples is a difference at the molecular level. This could theoretically be a phase separation effect between the two components of the blend, or a variation in cross-link density or other configurational parameter in the PNIPAM network. The intensity of illumination is expected to affect the amount of free radicals available to trigger crosslink formation, providing a mechanism.

4.4.8.1 BONDING DIFFERENCES EXAMINED THROUGH RAMAN SPECTROSCOPY

Raman spectroscopy is a candidate to assess differences in molecular bonding and composition, as this technique is highly sensitive to changes in bond energy arising from mechanism stress,[82,83] orientational effects,[84,85] and hydrogen bonding,[86] among others. See section 2.4.3 for an overview of the concept. Within the PNIPAM-alginate literature, Raman spectroscopy has been used to track the molecular conformation of molecules as they undergo their phase transition between expanded and collapsed configurations[33], assess the effect of electrospinning,[87] and determine the characteristics of alginate from various sources,[88] which suggests that it might be able to shed some light on the origin of this phenomenon.

To test for different chemical characteristic on either face, such as a greater population of crosslinks between PNIPAM chains or a different proportion of PNIPAM to alginate, Raman spectroscopy was conducted according to the parameters given in section 2.4.3 on a dried sample, 1mm thick when hydrated, seen to exhibit bending.

Four spectra were taken for 25 seconds each (determined as the maximum exposure without saturating the detector) at each of 15 locations on both surfaces of a dried gel sample observed to exhibit the bending phenomenon. Images were taken of each location, and the resulting spectra analysed using lmfit, a Python package which implements the Levenberg-Marquardt least squares algorithm for peak fitting purposes.

The model chosen for the peaks was a combination of a linear fit and a Voigt peak, defined as a convolution of Gaussian and Lorentz peaks with a parameter defining the weighting between the two. This model was selected

to reflect the fact that neither relaxation effects (inherent to the system and modelled well by a Gaussian distribution) or decoherence effects (arising from the effects of motion and variation within the sample, and modelled well by a Lorentzian peak) are dominant with the irregular environment of a blended gel.[89]

The region between 1050-1700cm^{-1} was selected for study as it contains the bands expected to correspond to the amine groups involved in PNIPAM-PNIPAM crosslink formation. These are the N-C bond, at roughly 1158 cm^{-1}, the Amide III peak representing the overlap of CN and CH resonances at 1283 and 1322 cm^{-1}, the Amide II peak of the N-H deformation at approximately 1547 cm^{-1}, and the Amide I peak of the carbonyl stretch at 1642 cm^{-1} (values taken from Rockwood[87]) These key peaks are indicated on the example spectrum shown in Figure 4.36.

Peak characteristics were fitted using a customisation of peak-fitting code written by Chris Brasnett,[90] with the Voigt model specified above. The average height, location and width of each peak were computed for the fifteen samples from both the top and bottom surfaces (shown in Table 4.3). A chi-squared test was performed between the two sample groups, but no significant difference was found between any properties of the five peaks hypothesized to be relevant, or indeed any of the others. An example fit with the locations of the key peaks annotated is shown in Figure 4.36.

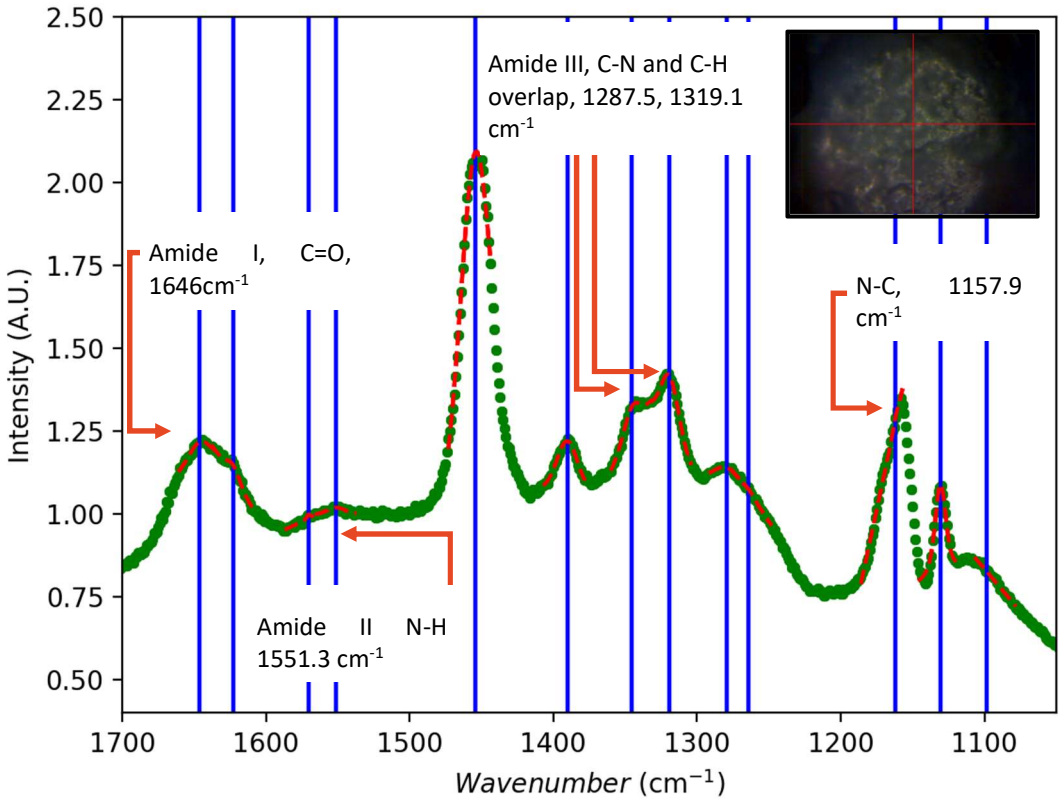

Figure 4.36. A typical Raman spectrum obtained from a dried PNIPAM-Alginate gel. Fits are shown in red and highlighted with blue vertical lines. Peaks identified as those deriving from amide groups and therefore potentially affected by the crosslinking involving them are labelled. Note, the fitting is less reliable in the difficult case of a peak with a shoulder (as seen around 1160), but bias can be expected to be consistent between spectra and therefore still able to detect systematic differences between the illuminated and unilluminated groups. Inset: optical image of scan location.

Values from top surface						
Peak identification	Wavenumber (cm^{-1})	Standard Deviation	Height (A.U.)	Standard Deviation	Width (cm^{-1})	Standard Deviation
C-C skeletal	1130.6	2.3×10^{-13}	2.5	0.0	3.4	8.9×10^{-16}
N-C bond	1157.9	2.3×10^{-13}	4.3	8.9×10^{-16}	9.5	0.0
Amide III C-N and	1287.5	4.5×10^{-13}	18.3	3.6×10^{-15}	38.3	7.1×10^{-15}
C-H overlap	1319.1	0.0	4.5	8.9×10^{-16}	4.4	8.9×10^{-16}
Methyl group	1345.3	0.0	4.1	8.9×10^{-16}	1.9	4.4×10^{-16}
Methyl group	1390.4	0.0	4.6	1.8×10^{-15}	3.3	1.3×10^{-15}
CH3 Scissors deformation	1453.2	0.0	7.8	3.6×10^{-15}	43.8	1.4×10^{-14}
CH3 Scissors deformation	1454.3	2.3×10^{-13}	7.4	0.0	39.1	0.0
Amide II N-H	1551.3	2.3×10^{-13}	3.9	4.4×10^{-16}	0.4	5.6×10^{-17}
Alginate – C-O-O	1622.9	2.3×10^{-13}	3.2	8.9×10^{-16}	0.7	1.1×10^{-16}
Amide I C=O	1646.1	2.3×10^{-13}	5.7	0.0	2.3	4.4×10^{-16}
Values from bottom surface						
Peak identification	Wavenumber (cm^{-1})	Standard Deviation	Height (A.U.)	Standard Deviation	Width (cm^{-1})	Standard Deviation

C-C skeletal	1130.6	3.4×10^{-9}	2.5	2.0×10^{-8}	3.4	$2. \times 10^{-8}$
N-C bond	1157.9	3.3×10^{-9}	4.3	4.0×10^{-10}	9.5	2.7×10^{-9}
Amide III C-N and	1287.5	5.5×10^{-3}	18.3	5.1×10^{-3}	38.3	3.7×10^{-2}
C-H overlap	1319.1	6.0×10^{-9}	4.5	7.0×10^{-9}	4.4	1.3×10^{-8}
Methyl	1345.3	2.0×10^{-7}	4.1	2.2×10^{-6}	1.9	1.6×10^{-6}
Methyl	1390.4	5.6×10^{-8}	4.6	5.5×10^{-8}	3.3	7.9×10^{-8}
CH3 Scissors deformation	1453.2	4.2×10^{-6}	7.8	4.3×10^{-6}	43.8	6.7×10^{-5}
CH3 Scissors deformation	1454.3	2.1×10^{-6}	7.4	2.0×10^{-6}	39.1	2.9×10^{-5}
Amide II N-H	1551.3	2.9×10^{-6}	3.9	9.6×10^{-6}	0.4	1.4×10^{-6}
Alginate – C-O-O	1622.9	1.6×10^{-7}	3.2	2.0×10^{-6}	0.7	6.7×10^{-7}
Amide I C=O	1646.1	1.4×10^{-7}	5.7	7.5×10^{-8}	2.3	5.9×10^{-8}

Table 4.3. Peak centres, heights and widths from the Raman spectra of the illuminated (top) and unilluminated (bottom) faces of a 1mm thick PNIPAM-alginate sample exhibiting bending. Peak fit parameters are assigned by automated peak fitting of a Voigt curve. Standard deviations are for the parameters shown, from 15 samples in each batch. Peak assignations derive from Rockwood and coworkers.

It was hoped that this methodology would detect differences in the chemical composition between the sides. Specifically, if there were a difference in the proportion of alginate and PNIPAM, or if the alginate and PNIPAM were binding somehow differently, this should show as a shift in the height or wavenumber of the peaks. This is not seen. Although not previously documented in literature, it was hypothesized that a change in crosslink density, since this involves substitution of a C-N-C bridge for the free amide groups (see Figure 4.1), would be reflected in a change in the amide I, II and III peaks, and the N-C bond. Due to the identical nature of the peaks

measured on both sides, it is concluded there are either no differences in crosslinking density for this dimension, or differences in crosslinking density do not affect the Raman spectra. This second possibility could be tested by taking spectra from gels with different percentages of MBA added and empirically different swelling ratios.

One detail that would not be detected using the approach above is a difference in the interaction with solvent. Dried gels were used for testing due to the difficulty of identifying peaks in wet samples, attributed to the large degree of variation in energy levels caused by random solvent molecules. However, this misses potential variation in water content, and also of density of the blended polymer.

4.4.8.2 PORE STRUCTURE INVESTIGATED THROUGH MICROSCOPY

An alternative cause of the observed effect was some difference in the micro-scale structure of the materials, such as a change in the average pore size, between exposed and unexposed faces. This had previously been observed to cause bending phenomena in responsive hydrogel samples exposed to an acetone gradient or hydrothermal precipitation.[34,37] Porosity has also been demonstrated to affect the mechanical response of biopolymer gels.[91]

Water-rich pore domains within the polymer were expected to be on the order of 10μm.[86] This determined the magnification required and focused attention on electron and confocal microscopy.[8,27]

4.4.8.3 SCANNING ELECTRON MICROSCOPY

Scanning electron microscopy (SEM) is suitable for imaging with a resolution of 1nm and was therefore appropriate for identifying micro-scale features. However, this introduced two problems. Firstly, standard SEM requires a vacuum to prevent loss of electron beam intensity and collimation; therefore, samples must be dried. It is unlikely that the water can be extracted from a water-rich material such as hydrogel without changing the structure substantially from the form it would take in a wet state, and since the wet state is the object of interest this raises questions about how relevant such data are.[92]

Secondly, hydrogels, and particularly hydrogels derived from polydisperse biopolymers, often acquire microscopic variation due to small-scale fluctuations in polymer density.[73] Therefore, to draw meaningful

conclusions about gel features a statistically valid, and representative, number of such features must be analysed.

To address the first problem a variety of hydrogel preparation methods were attempted and the results intercompared. These included critical point drying from solvent exchange with ethanol (a good solvent for PNIPAM);[93] critical point drying from solvent exchange with acetone (also a good solvent for PNIPAM);[93] air drying; and lyophilisation from aqueous phase. Samples were cut with a razor to expose inner surfaces, mounted on carbon pads, and coated with silver prior to imaging. Imaging was conducted according to the methods described in section 2.2.3.2 and example images are shown in Figure 4.37.

This process revealed polydisperse pore structures, with angular, irregular shapes, thin walls and ragged wall features. Each sample (sectioned from the same material block before processing) showed significant variation over the ~4mm surface prepared (for example, compare Figure 4.37 a) and b), from the same sample with the same processing) raising the question of which area could be considered representative throughout the sample.

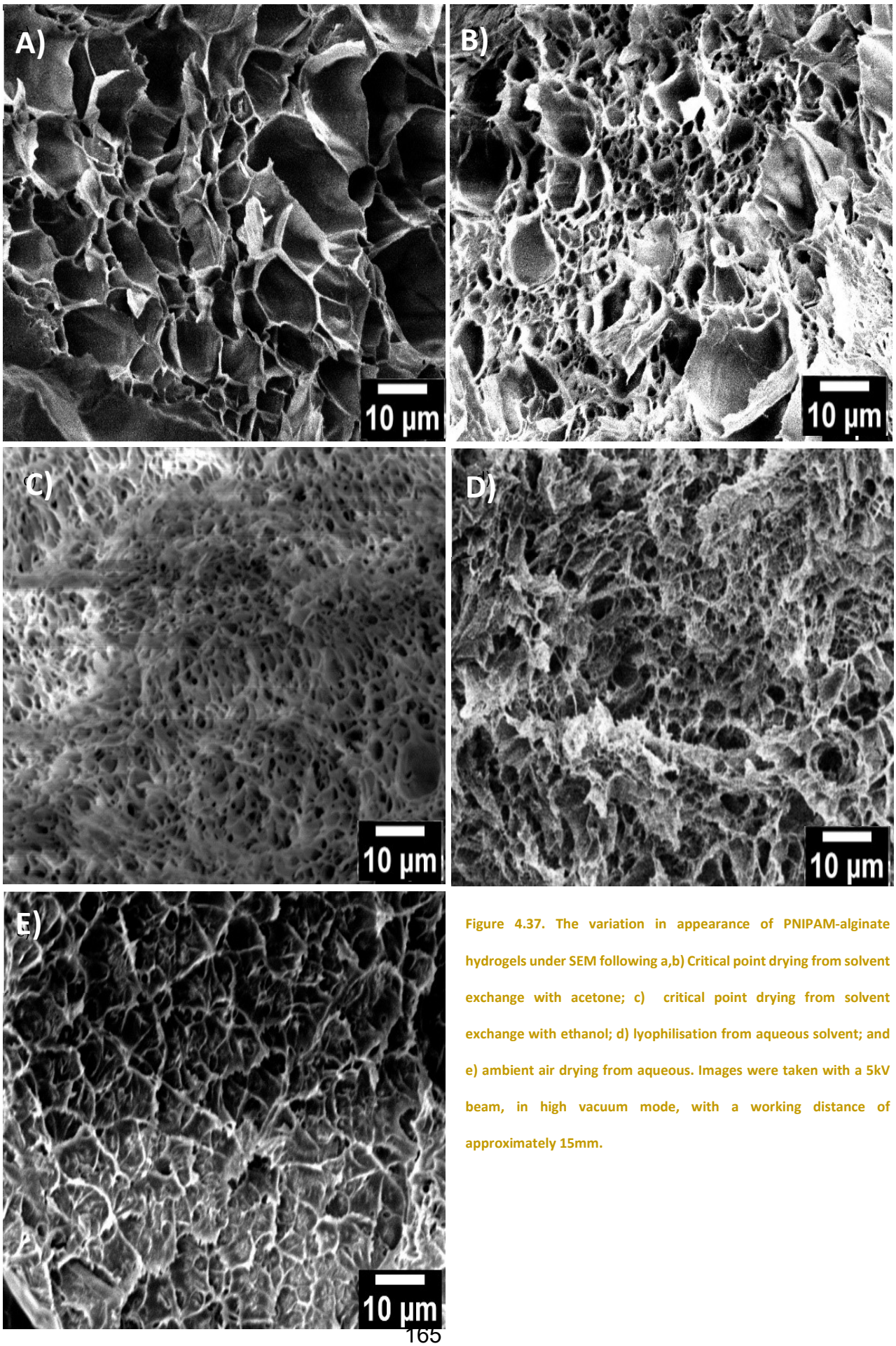

Figure 4.37. The variation in appearance of PNIPAM-alginate hydrogels under SEM following a,b) Critical point drying from solvent exchange with acetone; c) critical point drying from solvent exchange with ethanol; d) lyophilisation from aqueous solvent; and e) ambient air drying from aqueous. Images were taken with a 5kV beam, in high vacuum mode, with a working distance of approximately 15mm.

Samples varied depending on processing, with observations suggesting larger pores following air drying. This would be compatible with a longer time taken for the meniscus of water to pass through the gel, causing more disruption to the sample. A smaller-featured result seems to be obtained by critical point drying from ethanol, or lyophilisation. This may represent a shrinking from the native state or an accurate preservation of the smallest length scales in the gel: it is not possible to say based on this evidence. Post-preparation, all gels had significantly reduced in volume and deformed from their original hydrated size, making it doubtful their inner structure remained true to hydrated conditions.

Due to substantial levels of variation, deriving reliable statistics on the dimensions of pores within samples from the 2D images was not possible. Since any investigation into variation within pores as the source of the effect would require a valid baseline for measurement, a different approach, Environmental Scanning Electron Microscopy (ESEM), was trialled.

4.4.8.4 ENVIRONMENTAL SCANNING MICROSCOPY

A route to avoiding one of the problems highlighted in 4.1.1.2 is to use ESEM. This technique, described further in section 2.2.3.3, allows imaging of samples under higher pressure than pure SEM. This means samples can be imaged in a more representative state.

Following Stokes,[94] an initial pressure of 12 Torr (1,600Pa) and temperature of 18°C were selected. Relative humidity was held at 100%. However, under these conditions the gel surface appeared smooth, which was attributed to the absence of significant contrast between the electron density in the pores and in the walls. Reducing the pressure and temperature gradually to 5 Torr and 10°C revealed the presence of small deposits on the surface, probably small discontinuous pieces of gel created during preparation, were dried, but otherwise a smooth surface. Reducing further to 2.65 Torr created a textured surface. Round features resembling bubbles or craters of 1µm or smaller appeared at 2.25Torr. With further lowering of pressure, features up to 2µm were visible, forming lines or other ordered regions of larger pores. These changes are shown in Figure 4.38.

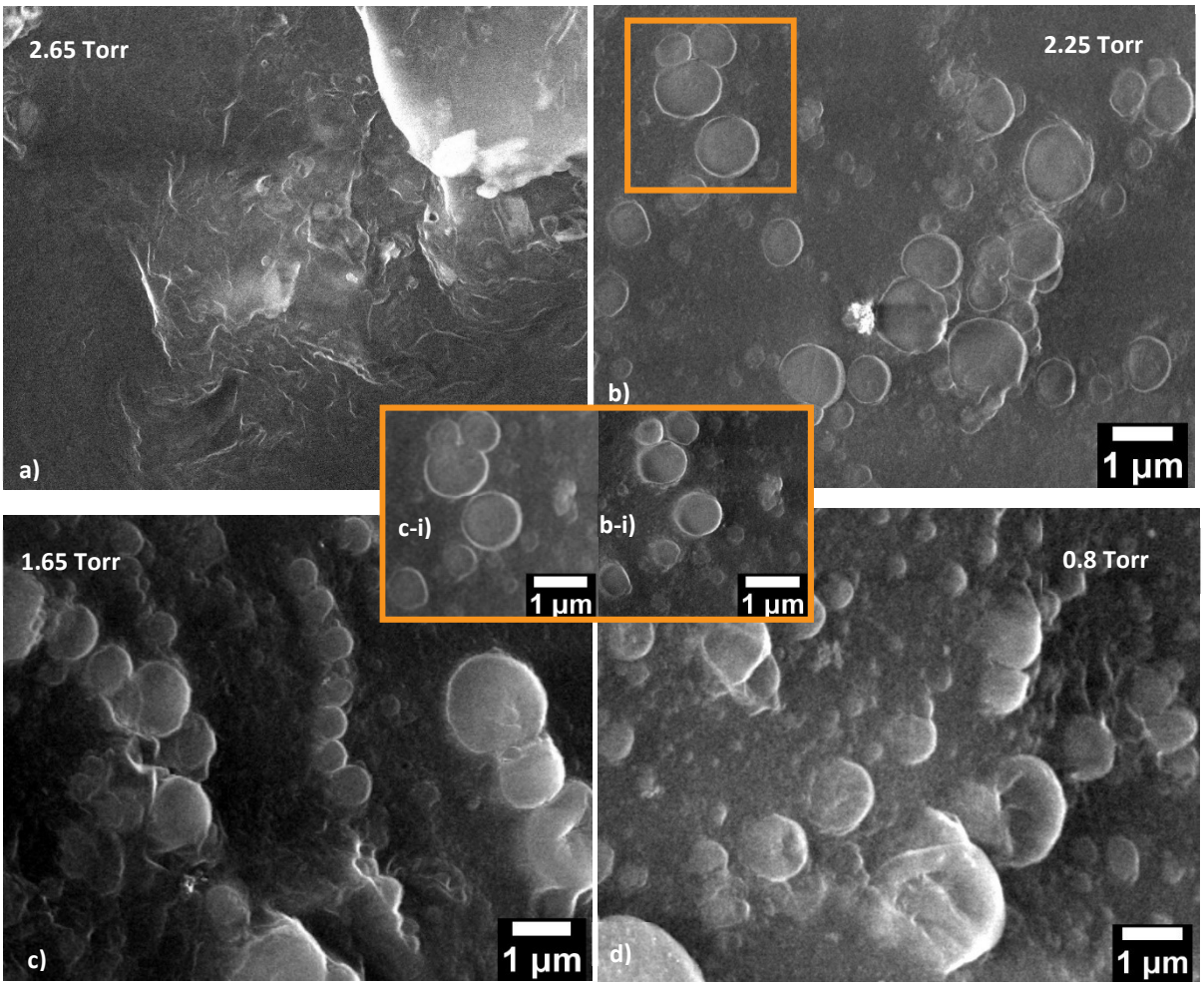

Figure 4.38 Environmental Scanning Electron Microscopy of PNIPAM-alginate hydrogels with no sample preparation. Pressure decreases from left to right and top to bottom. Sequence shows a) A textured surface with no pores visible at 2.65 Torr; b) crater or bubble features appearing at 2.25 Torr; c) increased prominence and indications of micro-scale grouping at 1.65 Torr; d) still further round features at 0.8 Torr. Insets b-i and c-i show the same feature at 2.25 and 1.65 Torr respectively, indicating clearly the size increase and merging of features due to pressure reduction.

The gradual appearance of indented circular features was attributed to the sublimation of water vapour, leaving an uneven surface with contours that then could be imaged with the electron beam. The water vapour inside these chambers then expanded, causing them to increase in size (as shown in Figure 4.38, inset b-i) and c-i) and merge. The alignment of pores into lines tens of microns in length is also visible in Figure 4.38 c). This demonstrated regional variation in the pores formed in the material, which should be borne in mind when sampling pore regions. The need for low pressures before pore features were visible and the shrunken appearance of the hydrogels following extraction from the instrument suggests that even environmental SEM does not produce images representative of the hydrated hydrogel.

This evidence of the change in sample with pressure suggests that the angular appearance of pores in high-vacuum SEM as seen in Figure 4.37 is not representative of the hydrated state, and that the size and shape of pores visible can be a function of the stage of dehydration during which observations are being made, as they expand and merge during depressurization. While many preparation methods stress the need for rapid drying to preserve structure, it is clear that processing parameters are very important and should accompany hydrogel SEM data when presented. The pore walls in a hydrated state are also significantly thicker than the dried images would suggest, meaning that a porosity measurement (ratio of pore area to solid material) would be overestimated from this state. The question of the real size of pores in a hydrated state is still unresolved by these studies, and so a final attempt at confocal microscopy, which can be conducted on samples in liquid, was attempted.

4.4.8.5 CONFOCAL MICROSCOPY

A sample exhibiting bending behaviour was freshly sectioned and imaged using confocal microscopy using the methods described in Chapter 2. Example microscopy images are shown in Figure 4.39. Bright areas were identified as bulk gel regions (presumably, preferentially bound by the hydrophobic rhodamine when freshly sectioned) and dark features as pores (regions of higher solvent concentration and therefore less fluorophore). A selection of images were taken along a linear distance of approximately 300 µm in the direction of illumination gradient.

From each image, ~130 pores of radius > 0.2µm were manually identified in ImageJ and areas measured. Total area was computed as a fraction of the gel area measured. Histograms of pore area data are presented in Figure 4.40. No significant difference in pore sizes or total porosity were

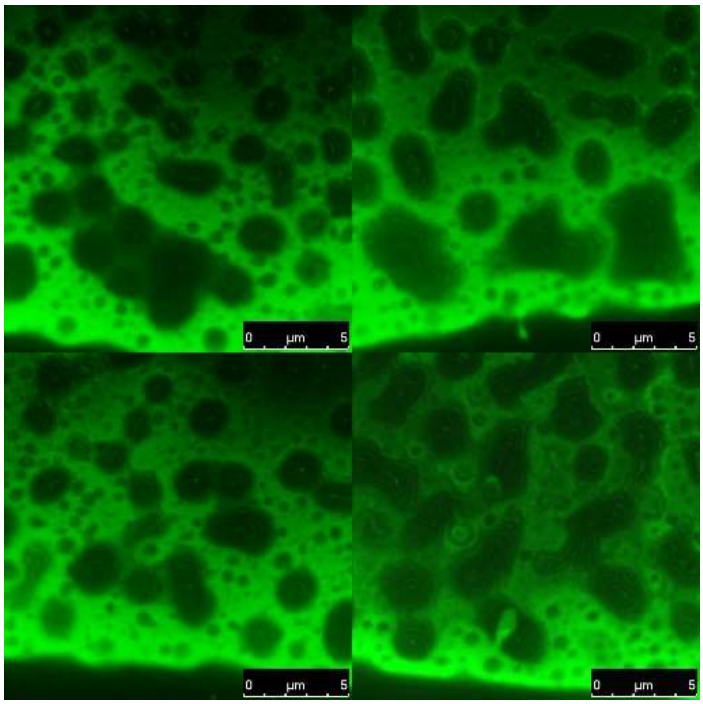

Figure 4.39 Four typical confocal microscopy images of PNIPAM-alginate gel. The striped contours within the large, irregular shaped blobs are believed to be an imaging artefact rather than a true feature.

noted across the range of the sample measured; it is possible that some difference would be evident across a larger scale. Sectioning the top and bottom of large samples (with the surface 'skin' removed to ensure a representative sample) as in Luo et al.[37] would be the quickest way to investigate this.

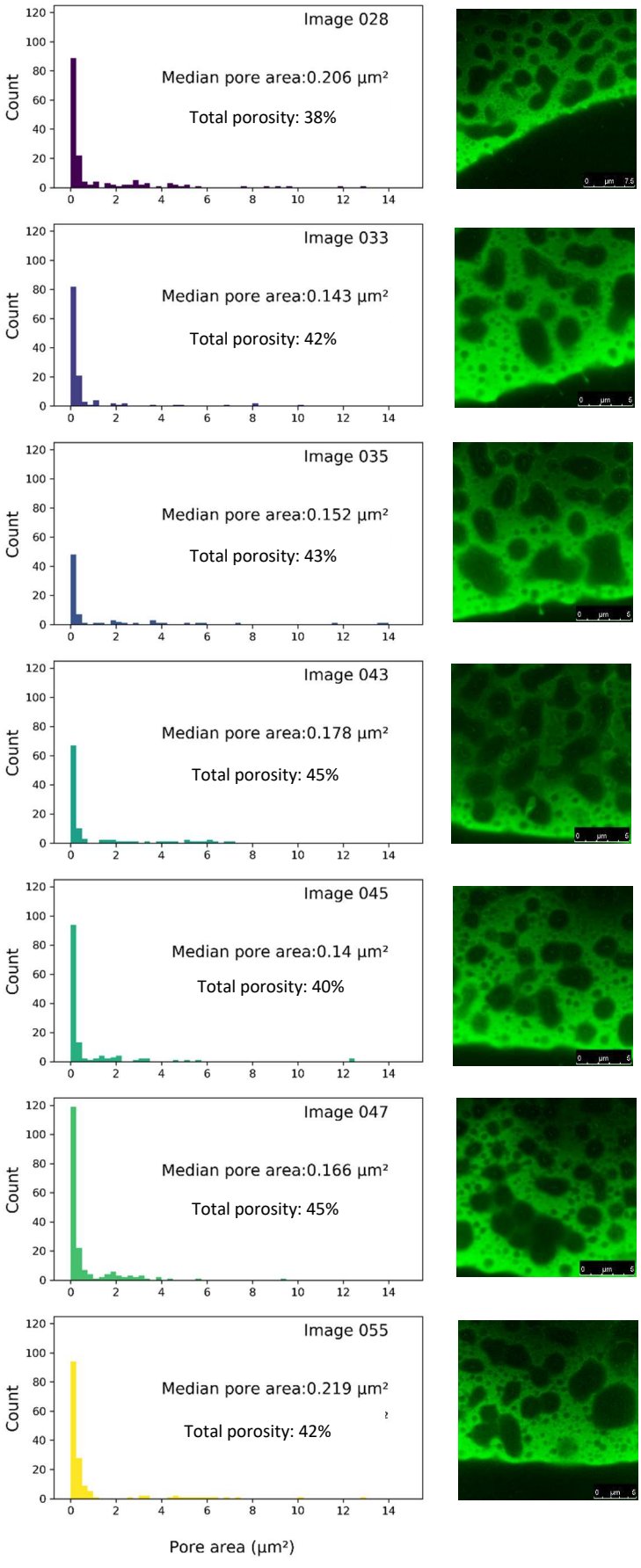

Figure 4.40. Pore size distribution as measured from 16 x 16 µm Images of hydrogel taken across 300µm of gradated gel. Pore sizes are plotted as histograms with a bin size of 0.5 µm²

However, Figure 4.40 clearly shows a large population of circular 0 - 0.5 µm^2 pores which have not been documented previously for PNIPAM-alginate. A smaller population of larger-area (0.5 - 5 µm^2) irregularly shaped pores is also observed. Larger sample sizes would be required for confirmation of systematic patterns in the population; however aggregated measurements from Figure 4.40 (corresponding to approximately 1,000 individual measurements) produces a histogram (Figure 4.41) which suggests the true pore size distribution may be multimodal.

Given the double-network nature of the gel, it is tempting to propose that the different pore sizes correspond to the two different gel components. However, while no prior work has used confocal microscopy to examine the pore structure of PNIPAM, alginate or their combination, and so no data from the same modality are available, data from other methodologies are incompatible with this hypothesis.

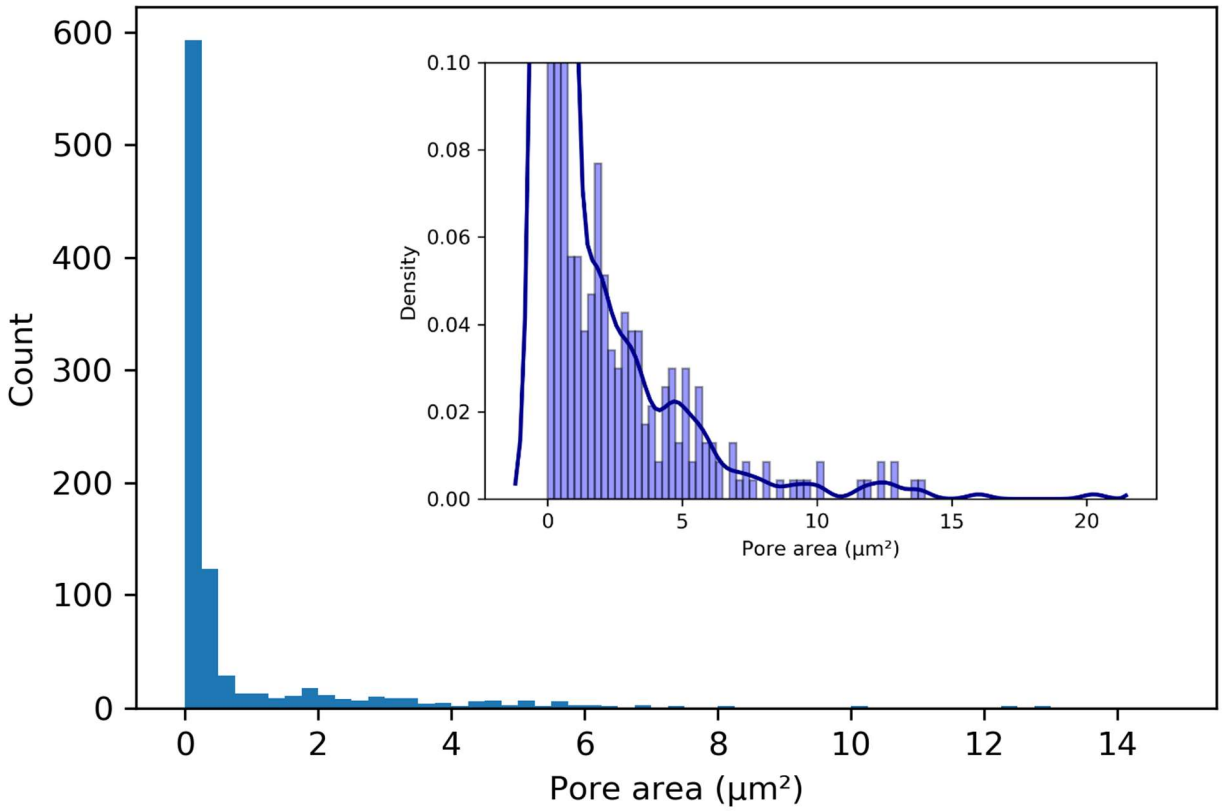

Figure 4.41. Histogram aggregated pore size data for all pores measured in Figure 4.40. Inset: The same data converted to probability density, with an increased y-scale for improved visibility. Line indicates a kernel distribution function with a bandwidth of 0.4µm. This is significantly larger than the bandwidths suggested by the Silverma 'rules-of-thumb', [107] **making under-smoothing unlikely.**

From existing measurements of dried gels, the larger pores of Figure 4.40 have similarities with those seen in gels of linear PNIPAM, found by Nguyen et al. have a pore size of 2.8 ± 0.9 µm as measured by cryoSEM.[95]

Alginate gels have been measured as nanoporous with pore sizes ~5-6nm for various molecular weights and M:G ratios, using a thermoporometry technique.[96] In observations taken for this work the smallest pores visible are 0.2µm, so alginate pores of that size would not be visible.

Most pores observed and reported in Figure 4.40 are much smaller than the PNIPAM-alginate pore size was recorded by de Moura and co-workers using SEM. The composition closest to that used in this work is reported with a uniform pore size of 16.0 ± 2.0 µm. Note that this is not exactly the same material as examined in this work, using a ratio of PNIPAM:alginate which is 1:0.017 by weight instead of 1:0.15. Petrusic et al. use a closer ratio of 1:0.2 but find a still larger pore value of 90 ± 27 µm.[30] Within both works it is shown that the addition of more alginate and more crosslinker reduces the measured pore size: therefore, if the work of de Moura were adjusted to match the proportions used in the work a still larger pore size would be expected.

This validates the concerns raised in section 4.4.8.3 and 4.4.8.4 that SEM preparations can systematically distort pore measurements. In this instance, comparisons between Figure 4.38 and Figure 4.40 imply SEM measurements can lead to an over-estimation of pore size in native states, under-estimation of wall size, and under-estimation of pore roundness, and potentially erase features such as the presence of a second population of smaller pores.

It seems likely that the large, irregularly shaped pores are those that have been previously observed under SEM following drying, and by Raman mapping.[8,27,30] The large quantity of small pores measured here by confocal microscopy has previously gone unnoticed and therefore neither been noted or remarked upon. Pore size affects many potential applications, including cellular interactions for biological applications,[52] mechanical properties for deployable subjects,[27] swelling ratio[27] and rate of thermal response.[17] Therefore, this fuller understanding of the porous structure of PNIPAM-alginate has consequences for many of the communities working with PNIPAM.

The regular shape and dimensions of the small pores are reminiscent of small, isolated regions of phase separation. The irregular shape of the larger pores suggests a more advanced state of demixing, perhaps with regions beginning to merge.

The general phenomenon of pore formation, microsyneresis, occurs during polymerisation, when the growing polymer network is unable to mix homogenously with the amount of solvent present. A phase separation results in which polymer-rich regions and solvent-rich regions separate: the latter manifest as pores.[73,97] Therefore, it is

tentatively suggested that the qualitatively different pores represent two distinct stages of microsyneresis during gel production, with different characteristic length scales and energies. These would depend on the entropy of mixing, and thus depend on the volume fraction of the difference polymer species, and the Florey-Huggins parameter χ (see section 1.4.1). For PNIPAM, χ is a sensitive function of polymer volume fraction, the polymer and solvent involved, and the temperature.[48]

Further testing on different ratios of PNIPAM and alginate blends, and the components singly, would give perspective on whether confocal pore measurements correlate as expected with macroscopic phenomena and whether the 0 - 0.5 μm^2 pores are a unique feature of PNIPAM-alginate processed as in this work, or have previously been overlooked in PNIPAM also. For more detail on the thermodynamics of pore formation, it would be interesting to quench gel formation after each cross-linking stage and examine the pore distribution. The issue of potential dependence of pore size on illumination dosage also remains an open question.

4.4.9 WORKING HYPOTHESIS FOR ORIGIN OF PNIPAM-ALGINATE MACROSCOPIC BENDING

From the evidence collected there is no definite answer for the interesting and promising bending phenomenon seen. However, some candidates can be assessed.

4.4.9.1 CROSSLINKING DENSITY VARIATION

At first glance it may seem that as the crosslinking and polymerisation is photo-triggered, gel sections exposed to more light would have a higher density of crosslinks. They would receive more energy and would also be the first macromolecules to form, which are expected to have a more tightly crosslinked structure.[56] This situation has been demonstrated; 10mm thick acrylamide gels have been shown to develop gradated crosslink density in the direction of illumination, as determined by swelling ratio.[98] However, this explanation does not fit the observed behaviour for PNIPAM-alginate.

Firstly, at ambient temperature the PNIPAM-alginate gels take up a configuration which expands more at the surface where most illumination is received. This is the inverse of what would be expected for a higher PNIPAM crosslink density in the gel, which Flory-Rehner swelling calculations suggest, and experimental results for PNIPAM confirm, constrain ambient swelling.[4,5,47] Secondly, the contracted PNIPAM-alginate gels adopt a curved configuration. The final configuration of PNIPAM-alginate is expected to be constrained by excluded volume

considerations, for which the crosslink density is not relevant to first order. Some experimentalists find that crosslinking degree does not affect the volume assumed following the LCST, as demonstrated by Zhang for PNIPAM and Petrusic for PNIPAM-alginate.[4,30] On the other hand, de Moura and co-workers do find a difference in contracted volume, perhaps as a result of the larger range of crosslinker values used – from 2.5% to 10% of the monomer mass.[27] The ratio of alginate:PNIPAM used in this work are closer to that of Petrusic et al. but use a crosslinker ratio closer to de Moura. It is possible that there are small variations in the final contracted volume between the samples reported by Petrusic et al, but whether these would be large enough to produce the magnitude of effect shown is unclear from the data provided.[30]

A higher density of crosslinks at the base could explain the behaviour seen in ambient conditions, but not easily the contracted behaviour. One would also expect a change in crosslink density to cause a difference in the Raman shifts seen on both sides, which is not observed, as detailed in section 4.4.8.1. A difference in the proportion of PNIPAM versus alginate would also be seen in these measurements. This explanation for the bending of the sample measured by Raman spectroscopy can therefore be set aside.

4.4.9.2 POLYMER VOLUME FRACTION VARIATION

However, the Raman spectra were taken on dried gels, and so a shift in the proportions of polymer and solvent would not be observed. This would correspond to a change in pore volume fraction or in the density of the polymer-rich regions surrounding the pores. A lower polymer volume fraction would have a larger equilibrium volume at ambient temperature, and attain a smaller volume in a contracted state, fitting what is observed at a macroscopic level in Section 0

Unfortunately, it was not possible to obtain clear, statistically valid information on the pore densities on each side of the bending samples. While previous studies have achieved imaging of a pore gradient,[37] the PNIPAM-alginate system presents difficulties due to its inhomogenous nature and the small scale of the pores (~0.2 -10 µm diameter) relative to the gradient dimensions to be observed (1-5 mm). Both conditions require many individual images to be processed to achieve relevant results. This could be improved with the commitment of more time or the creation of a digital image processing pipeline, potentially leveraging machine learning,[99] or stitching together of images. Alternative options would be fine sectioning followed by cryoporosity measurements,[52] thermoporometry with DSC,[96] or simple weight measurements as described in section 2.2.5.

The difficulty here would be sectioning fragile gels to sub-millimetre precision, as resins or other reinforcement may interrupt the native network structure.

4.4.9.3 FORMATION OF OSMOTIC PRESSURE GRADIENT VIA SLOW CURING

How could such a gradient occur? The hypothesis is that the illuminated, polymerised cross-linked top layer has a lower chemical potential than the bulk uncrosslinked monomer-rich polymer blend. This leads to an osmotic pressure gradient from bottom to top, and therefore a net flow of water towards the illuminated side. This creates a more water-rich region in the first areas to crosslink, which is preserved as more crosslinked are added between PNIPAM and alginate polymers.

This process would be limited by diffusion. No studies on diffusion behaviour of PNIPAM-alginate are available, but alginate is likely to dominate due to its higher characteristic diffusivity relative to acrylamides.[100,101] Assuming the alginate polymer blend shows Fickian behaviour, swelling would be inversely correlated with sample thickness, for a fixed amount of curing time.[102] This may be the origin of the observed linear relationship between radius of curvature and sample height in ambient equilibrium shown in Figure 4.31.

The more complex behaviour shown in Figure 4.32 is harder to explain. As theorised in section 4.4.7,competing effects which operate in different regimes are a possibility. If the osmotic gradient theory is valid, the amount of solvent transported will decrease with sample height. Possibly, when it drops below a key level, a second-order effect comes in to play, such as a higher percentage of crosslinking on the illuminated side, as described in 4.4.9.1. The sample measured in section 4.4.8.1 may have been too thin to show this phenomenon. Alternatively, there may be some change in the network structure due to changes in χ, temperature or Φ that lead to a more or less compact double-network.

The mechanism for the formation of an osmotic gradient could be the inclusion of more hydrophobic MBA units during crosslinking, or the conformational restriction of the crosslink on the polymers. Increased osmotic pressure with a higher crosslink density of MBA has been previously recorded for acrylamide gels by Mallam et al.[103]

Empirical testing of this theory would be relatively straightforward, requiring osmotic pressure readings from a crosslinked versus an uncrosslinked polymer blend, all other factors held constant. Unfortunately, access to an osmometer could not be arranged but this measurement would confirm or exclude the mechanism.

Why has this not been observed before? Possibly due to the increased viscosity of the PNIPAM-alginate system relative to PNIPAM alone, the relatively slow reaction rate of the UV system and photoinitiator, and the increased opacity which allows a curing gradient to be perceived. According to the Einstein-Stokes equation, a higher viscosity material would be expected to show lower mobility. With a localised photon source curing would therefore also be local.[100] For this phenomenon to be seen the time taken for water to diffuse a substantial fraction of the height of the gel must be on the order of curing times, which are of course increased by reduced optical transmission. This could be tested experimentally by measuring the diffusion rate of water-soluble dyes though uncured polymer and comparing to characteristic effect length scales from Figure 4.32.

4.4.10 FUTURE DIRECTIONS AND DEVELOPMENTS

In addition to determining the method of action of this effect, a more exact description of the parameters determining the gradient across a piece would be required to link a print to its final configuration. If the hypothesis given in section 4.4.9.3 is correct, then sample reproducibility could be improved by tighter control of humidity, illumination and timing. Following, if illumination-graded samples could be characterised well enough to relate gel printing dimensions and conditions to both ambient and contracted equilibrium configuration, this simple, accessible, cost-effective method could replicate a substantial amount of the capability previously demonstrated to create complex shape change (see section 1.5) in a one-step technique.[16,104,105]

While the method for developing macroscopic PNIPAM curvature detailed here does not yet match the precision of the surfaces created by lithographic methods,[106] the use of a light source on a computer-controlled head to provide variation in curing allows arbitrary complexity with no set up costs beyond the generation of path instructions. Further, that this equipment is also capable of producing shaped gels before curing allows a transition into at least a low-z 2.5D structured surface (full 3D would require overcoming limitations in printing high structures without prior curing). Finally, the method used is developed for PNIPAM-alginate, a durable, cheap material, and it can be performed using open-source, accessible technology as documented in Chapter 3.

4.5. CONCLUSION

In summation, this chapter documents an as-yet unrecorded phenomenon which permits the tailoring of curvature in a facile, easily automated manner across the surface of a 2.5D UV-cured tough PNIPAM-alginate gel. 1D samples have been created and characterised in terms of shape change, and some 2D samples indicate potential for future work in generating self-folding and rolling structures such as grippers. While sample variability is high due to uneven curing, it is shown that this also indicates potential for complex shape programming. Sample behaviour is compared with the commonly-used Timoshenko bilayer approach for predicting final curvature of a composite beam.

These predictions are compatible with data for the ambient equilibrium configuration, but indicate more complex behaviour for the heated contracted states as a function of height. This suggests that either competing phenomena may be operating to change the contraction ratios between the sides as a function of height, or a more complex mathematical model is required.

Physical observations of gradated differences throughout samples demonstrating bending were sought. A difference in crosslinking density seems to be unlikely based on Raman spectra. SEM and ESEM results were inconclusive, although they revealed the dependence of dried hydrogel pore structure on preparation methods. Confocal microscopy revealed a previously unrecorded population of pores of 0 - 0.5 μm^2 cross-sectional area pores, but many more observations would be required to draw statistically valid conclusions about pore size variation throughout the relevant length scales. Improved automation of processing could assist in gathering the relevant data.

Based on the evidence a suggestion for the origin of the bending effect – solute diffusion in the direction of increased crosslinking density – has been proposed. A comparison of osmotic pressure exerted by crosslinked versus uncrosslinked polymer blends would provide evidence for this mechanism. If correct, measurement of diffusion rates through cured gels could provide an explanation for the change of curvature direction, and control of humidity during curing could improve the reproducibility of samples.

4.6. REFERENCES

(1) Pamies, R.; Zhu, K.; Kjøniksen, A.-L.; Nyström, B. Thermal Response of Low Molecular Weight Poly-(N-Isopropylacrylamide) Polymers in Aqueous Solution. *Polym. Bull.* **2009**, *62* (4), 487–502. https://doi.org/10.1007/s00289-008-0029-4.

(2) Rathjen, C. M.; Park, C.-H.; Goodrich, P. R.; Walgenbach, D. D. The Effect of Preparation Temperature on Some Properties of a Temperature-Sensitive Hydrogel. *Polym. Gels Networks* **1995**, *3* (2), 101–115. https://doi.org/10.1016/0966-7822(94)00030-B.

(3) Schild, H. G. Poly(N-Isopropylacrylamide): Experiment, Theory and Application. *Prog. Polym. Sci.* **1992**, *17* (2), 163–249. https://doi.org/10.1016/0079-6700(92)90023-R.

(4) Zhang, X.-Z.; Wu, D.-Q.; Chu, C.-C. Effect of the Crosslinking Level on the Properties of Temperature-Sensitive Poly(N-Isopropylacrylamide) Hydrogels. *J. Polym. Sci. Part B Polym. Phys.* **2003**, *41* (6), 582–593. https://doi.org/10.1002/polb.10388.

(5) Flory, P. J.; Rehner, J. Statistical Mechanics of Cross-Linked Polymer Networks II. Swelling. *J. Chem. Phys.* **1943**, *11* (11), 521–526. https://doi.org/10.1063/1.1723792.

(6) Li, X.; Cai, X.; Gao, Y.; Serpe, M. J. Reversible Bidirectional Bending of Hydrogel-Based Bilayer Actuators. *J. Mater. Chem. B* **2017**, *5* (15), 2804–2812. https://doi.org/10.1039/C7TB00426E.

(7) Ma, X.; Li, Y.; Wang, W.; Ji, Q.; Xia, Y. Temperature-Sensitive Poly(N-Isopropylacrylamide)/Graphene Oxide Nanocomposite Hydrogels by in Situ Polymerization with Improved Swelling Capability and Mechanical Behavior. *Eur. Polym. J.* **2013**, *49* (2), 389–396. https://doi.org/10.1016/j.eurpolymj.2012.10.034.

(8) Rainer Appel; Wei Xu, and; Zerda, T. W.; Hu*, Z. Direct Observation of Polymer Network Structure in Macroporous N-Isopropylacrylamide Gel by Raman Microscopy. **1998**. https://doi.org/10.1021/MA971260C.

(9) Ahmed, Z.; Gooding, E. A.; Pimenov, K. V; Wang, L.; Asher, S. A. UV Resonance Raman Determination of Molecular Mechanism of Poly(N-Isopropylacrylamide) Volume Phase Transition. *J. Phys. Chem. B* **2009**,

113 (13), 4248–4256. https://doi.org/10.1021/jp810685g.

(10) Zheng, W. J.; An, N.; Yang, J. H.; Zhou, J.; Chen, Y. M. Tough Al-Alginate/Poly(N-Isopropylacrylamide) Hydrogel with Tunable LCST for Soft Robotics. *ACS Appl. Mater. Interfaces* **2015**, *7* (3), 1758–1764. https://doi.org/10.1021/am507339r.

(11) Zhu, C. H.; Lu, Y.; Peng, J.; Chen, J. F.; Yu, S. H. Photothermally Sensitive Poly(N-Isopropylacrylamide)/Graphene Oxide Nanocomposite Hydrogels as Remote Light-Controlled Liquid Microvalves. *Adv. Funct. Mater.* **2012**, *22* (19). https://doi.org/10.1002/adfm.201201020.

(12) Breger, J. C.; Yoon, C.; Xiao, R.; Kwag, H. R.; Wang, M. O.; Fisher, J. P.; Nguyen, T. D.; Gracias, D. H. Self-Folding Thermo-Magnetically Responsive Soft Microgrippers. *ACS Appl. Mater. Interfaces* **2015**, *7* (5), 3398–3405. https://doi.org/10.1021/am508621s.

(13) Hirotsu, S.; Hirokawa, Y.; Tanaka, T. Volume-Phase Transitions of Ionized N-Isopropylacrylamide Gels. *J. Chem. Phys.* **1987**, *87* (2), 1392–1395. https://doi.org/http://dx.doi.org/10.1063/1.453267.

(14) Cooperstein, M. A.; Canavan, H. E. Assessment of Cytotoxicity of (N-Isopropyl Acrylamide) and Poly(N-Isopropyl Acrylamide)-Coated Surfaces. *Biointerphases* **2013**, *8* (1), 19. https://doi.org/10.1186/1559-4106-8-19.

(15) Wang, J.; Lin, L.; Cheng, Q.; Jiang, L. A Strong Bio-Inspired Layered PNIPAM-Clay Nanocomposite Hydrogel. *Angew. Chemie - Int. Ed.* **2012**, *51* (19), 4676–4680. https://doi.org/10.1002/anie.201200267.

(16) Zheng, W. J.; An, N.; Yang, J. H.; Zhou, J.; Chen, Y. M. Tough Al-Alginate/Poly(N -Isopropylacrylamide) Hydrogel with Tunable LCST for Soft Robotics. *ACS Appl. Mater. Interfaces* **2015**, *7* (3), 1758–1764. https://doi.org/10.1021/am507339r.

(17) Haq, M. A.; Su, Y.; Wang, D. Mechanical Properties of PNIPAM Based Hydrogels: A Review. *Mater. Sci. Eng. C* **2017**, *70*, 842–855. https://doi.org/10.1016/j.msec.2016.09.081.

(18) Gong, J. P.; Katsuyama, Y.; Kurokawa, T.; Osada, Y. Double-Network Hydrogels with Extremely High Mechanical Strength. *Adv. Mater.* **2003**, *15* (14), 1155–1158. https://doi.org/10.1002/adma.200304907.

(19) Lee, K. Y.; Mooney, D. J. Alginate: Properties and Biomedical Applications. *Prog. Polym. Sci.* **2012**, *37* (1), 106–126. https://doi.org/10.1016/j.progpolymsci.2011.06.003.

(20) Johnson, F. A.; Craig, D. Q. M.; Mercer, A. D. Characterization of the Block Structure and Molecular Weight of Sodium Alginates. *J. Pharm. Pharmacol.* **1997**, *49* (7), 639–643. https://doi.org/10.1111/j.2042-7158.1997.tb06085.x.

(21) Mancini, M.; Moresi, M.; Rancini, R. Mechanical Properties of Alginate Gels: Empirical Characterisation. *J. Food Eng.* **1999**, *39* (4), 369–378. https://doi.org/10.1016/S0260-8774(99)00022-9.

(22) Fang, Y.; Al-Assaf, S.; Phillips, G. O.; Nishinari, K.; Funami, T.; Williams, P. A.; Li, L.; Yapeng Fang, *,†; Saphwan Al-Assaf, †; Glyn O. Phillips, †,‡; et al. Multiple Steps and Critical Behaviors of the Binding of Calcium to Alginate. **2007**. https://doi.org/10.1021/JP0689870.

(23) Drury, J. L.; Dennis, R. G.; Mooney, D. J. The Tensile Properties of Alginate Hydrogels. *Biomaterials* **2004**, *25* (16), 3187–3199. https://doi.org/10.1016/j.biomaterials.2003.10.002.

(24) Yang, C. H.; Wang, M. X.; Haider, H.; Yang, J. H.; Sun, J.-Y.; Chen, Y. M.; Zhou, J.; Suo, Z. Strengthening Alginate/Polyacrylamide Hydrogels Using Various Multivalent Cations. *ACS Appl. Mater. Interfaces* **2013**, *5* (21), 10418–10422. https://doi.org/10.1021/am403966x.

(25) Bakarich, S. E.; Gorkin, R.; Naficy, S.; Gately, R.; in het Panhuis, M.; Spinks, G. M. 3D/4D Printing Hydrogel Composites: A Pathway to Functional Devices. *MRS Adv.* **2015**, 1–6. https://doi.org/10.1557/adv.2015.9.

(26) Bakarich, S. E.; in het Panhuis, M.; Beirne, S.; Wallace, G. G.; Spinks, G. M. Extrusion Printing of Ionic–Covalent Entanglement Hydrogels with High Toughness. *J. Mater. Chem. B* **2013**, *1* (38), 4939. https://doi.org/10.1039/c3tb21159b.

(27) de Moura, M. R.; Guilherme, M. R.; Campese, G. M.; Radovanovic, E.; Rubira, A. F.; Muniz, E. C. Porous Alginate-Ca2+ Hydrogels Interpenetrated with PNIPAAm Networks: Interrelationship between Compressive Stress and Pore Morphology. *Eur. Polym. J.* **2005**, *41* (12), 2845–2852. https://doi.org/10.1016/j.eurpolymj.2005.06.007.

(28) Panhuis, M. in het; Bakarich, S.; Beirne, S. T.; Wallace, G. G.; Spinks, G. M. Extrusion Printing of Ionic-

Covalent Entanglement Hydrogels with High Toughness.

(29) Vasile, C.; Nita, L. E. Novel Multi-Stimuli Responsive Sodium Alginate-Grafted-Poly(N-Isopropylacrylamide) Copolymers: II. Dilute Solution Properties. *Carbohydr. Polym.* **2011**, *86* (1), 77–84. https://doi.org/10.1016/j.carbpol.2011.04.012.

(30) Petrusic, S.; Lewandowski, M.; Giraud, S.; Jovancic, P.; Bugarski, B.; Ostojic, S.; Koncar, V. Development and Characterization of Thermosensitive Hydrogels Based on Poly(N-Isopropylacrylamide) and Calcium Alginate. *J. Appl. Polym. Sci.* **2012**, *124* (2), 890–903. https://doi.org/10.1002/app.35122.

(31) Fischer, H.; Baer, R.; Hany, R.; Verhoolen, I.; Walbiner, M. 2,2-Dimethoxy-2-Phenylacetophenone: Photochemistry and Free Radical Photofragmentation. *J. Chem. Soc. Perkin Trans. 2* **1990**, *0* (5), 787. https://doi.org/10.1039/p29900000787.

(32) Anseth, K. S.; Bowman, C. N.; Brannon-Peppas, L. Mechanical Properties of Hydrogels and Their Experimental Determination. *Biomaterials* **1996**, *17* (17), 1647–1657. https://doi.org/10.1016/0142-9612(96)87644-7.

(33) Ahmed, Z.; Gooding, E. A.; Pimenov, K. V.; Wang, L.; Asher, S. A. UV Resonance Raman Determination of Molecular Mechanism of Poly(*N* -Isopropylacrylamide) Volume Phase Transition. *J. Phys. Chem. B* **2009**, *113* (13), 4248–4256. https://doi.org/10.1021/jp810685g.

(34) Zhao, Q.; Dunlop, J. W. C.; Qiu, X.; Huang, F.; Zhang, Z.; Heyda, J.; Dzubiella, J.; Antonietti, M.; Yuan, J. An Instant Multi-Responsive Porous Polymer Actuator Driven by Solvent Molecule Sorption. *Nat. Commun.* **2014**, *5*, 4293. https://doi.org/10.1038/ncomms5293.

(35) Hu, Z.; Zhang, X.; Li, Y. Synthesis and Application of Modulated Polymer Gels. *Science* **1995**, *269* (5223), 525–527. https://doi.org/10.1126/science.269.5223.525.

(36) Asoh, T.; Matsusaki, M.; Kaneko, T.; Akashi, M. Fabrication of Temperature-Responsive Bending Hydrogels with a Nanostructured Gradient. *Adv. Mater.* **2008**, *20* (11), 2080–2083. https://doi.org/10.1002/adma.200702727.

(37) Luo, R.; Wu, J.; Dinh, N.-D.; Chen, C.-H. Gradient Porous Elastic Hydrogels with Shape-Memory Property

and Anisotropic Responses for Programmable Locomotion. *Adv. Funct. Mater.* **2015**, *25* (47), 7272–7279. https://doi.org/10.1002/adfm.201503434.

(38) Song, K. W.; Kuk, H. Y.; Chang, G. S. Rheology of Concentrated Xanthan Gum Solutions: Oscillatory Shear Flow Behavior. *Korea Aust. Rheol. J.* **2006**, *18* (2), 67–81.

(39) Bakarich, S. E.; Gorkin, R.; in het Panhuis, M.; Spinks, G. M. 4D Printing with Mechanically Robust, Thermally Actuating Hydrogels. *Macromol. Rapid Commun.* **2015**, *36* (12), 1211–1217. https://doi.org/10.1002/marc.201500079.

(40) Mitchell, J. R.; Blanshard, J. M. V. Rheological Properties of Alginate Gels. *J. Texture Stud.* **1976**, *7* (2), 219–234. https://doi.org/10.1111/j.1745-4603.1976.tb01263.x.

(41) Mackie, W.; Noy, R.; Sellen, D. B. Solution Properties of Sodium Alginate. *Biopolymers* **1980**, *19* (10), 1839–1860. https://doi.org/10.1002/bip.1980.360191012.

(42) ASTM. *Standard Test Method for Determining the Chemical Composition and Sequence in Alginate by Proton Nuclear Magnetic Resonance (1 H NMR)*; 2012. https://doi.org/10.1520/F2259-10R12E01.Copyright.

(43) Atkins, E. D. T.; Nieduszynski, I. A.; Mackie, W.; Parker, K. D.; Smolko, E. E. Structural Components of Alginic Acid. II. The Crystalline Structure of Poly-?-L-Guluronic Acid. Results of X-Ray Diffraction and Polarized Infrared Studies. *Biopolymers* **1973**, *12* (8), 1879–1887. https://doi.org/10.1002/bip.1973.360120814.

(44) Vold, I. M. N.; Kristiansen, K. A.; Christensen, B. E. A Study of the Chain Stiffness and Extension of Alginates, in Vitro Epimerized Alginates, and Periodate-Oxidized Alginates Using Size-Exclusion Chromatography Combined with Light Scattering and Viscosity Detectors. *Biomacromolecules* **2006**. https://doi.org/10.1021/bm060099n.

(45) Fujishige, S. Intrinsic Viscosity-Molecular Weight Relationships for Poly(N-Isopropylacrylamide) Solutions. *Polym. J.* **1987**, *19* (3), 297–300. https://doi.org/10.1295/polymj.19.297.

(46) Wu, C.; Zhou, S. Thermodynamically Stable Globule State of a Single Poly(N-Isopropylacrylamide) Chain

in Water. *Macromolecules* **1995**, *28*, 45.

(47) Koetting, M. C.; Peters, J. T.; Steichen, S. D.; Peppas, N. A. Stimulus-Responsive Hydrogels: Theory, Modern Advances, and Applications. *Mater. Sci. Eng. R Reports* **2015**, *93*, 1–49. https://doi.org/10.1016/j.mser.2015.04.001.

(48) Afroze, F.; Nies, E.; Berghmans, H. Phase Transitions in the System Poly(N-Isopropylacrylamide)/Water and Swelling Behaviour of the Corresponding Networks. *J. Mol. Struct.* **2000**, *554* (1), 55–68. https://doi.org/10.1016/S0022-2860(00)00559-7.

(49) Gong, J. P.; Katsuyama, Y.; Kurokawa, T.; Osada, Y. Double-Network Hydrogels with Extremely High Mechanical Strength. *Adv. Mater.* **2003**, *15* (14), 1155–1158. https://doi.org/10.1002/adma.200304907.

(50) Gong, J. P. Why Are Double Network Hydrogels so Tough? *Soft Matter* **2010**, *6* (12), 2583. https://doi.org/10.1039/b924290b.

(51) Goto, M.; McCoy, B. J. Inverse Size-Exclusion Chromatography for Distributed Pore and Solute Sizes. *Chem. Eng. Sci.* **2000**, *55* (4), 723–732. https://doi.org/10.1016/S0009-2509(99)00352-8.

(52) Gun'Ko, V. M.; Mikhalovska, L. I.; Savina, I. N.; Shevchenko, R. V.; James, S. L.; Tomlins, P. E.; Mikhalovsky, S. V. Characterisation and Performance of Hydrogel Tissue Scaffolds. *Soft Matter* **2010**. https://doi.org/10.1039/c0sm00617c.

(53) Malda, J.; Visser, J.; Melchels, F. P.; Jüngst, T.; Hennink, W. E.; Dhert, W. J. A.; Groll, J.; Hutmacher, D. W. 25th Anniversary Article: Engineering Hydrogels for Biofabrication. *Adv. Mater.* **2013**, *25* (36), 5011–5028. https://doi.org/10.1002/adma.201302042.

(54) Draper, E. R.; Wallace, M.; Schweins, R.; Poole, R. J.; Adams, D. J. Nonlinear Effects in Multicomponent Supramolecular Hydrogels. *Langmuir* **2017**, *33* (9), 2387–2395. https://doi.org/10.1021/acs.langmuir.7b00326.

(55) Sears, N. A.; Dhavalikar, P. S.; Cosgriff-Hernandez, E. M. Emulsion Inks for 3D Printing of High Porosity Materials. *Macromol. Rapid Commun.* **2016**, *37* (16), 1369–1374. https://doi.org/10.1002/marc.201600236.

(56) Kara, S.; Okay, O.; Pekcan, O. Real-Time Temperature and Photon Transmission Measurements for Monitoring Phase Separation during the Formation of Poly(N-Isopropylacrylamide) Gels. *J. Appl. Polym. Sci.* **2002**. https://doi.org/10.1002/app.11173.

(57) Wen, M.; Scriven, L. E.; McCormick, A. V. Kinetic Gelation Modeling: Kinetics of Cross-Linking Polymerization. *Macromolecules* **2003**, *36* (11), 4151–4159. https://doi.org/10.1021/ma010309i.

(58) Soledad Lencina, M. M.; Iatridi, Z.; Villar, M. A.; Tsitsilianis, C. Thermoresponsive Hydrogels from Alginate-Based Graft Copolymers. *Eur. Polym. J.* **2014**, *61*, 33–44. https://doi.org/10.1016/j.eurpolymj.2014.09.011.

(59) Lawrie, G.; Keen, I.; Drew, B.; Chandler-Temple, A.; Rintoul, L.; Fredericks, P.; Grøndahl, L. Interactions between Alginate and Chitosan Biopolymers Characterized Using FTIR and XPS. *Biomacromolecules* **2007**, *8* (8), 2533–2541. https://doi.org/10.1021/bm070014y.

(60) Hou, L.; Wu, P. Exploring the Hydrogen-Bond Structures in Sodium Alginate through Two-Dimensional Correlation Infrared Spectroscopy. *Carbohydr. Polym.* **2019**, *205*, 420–426. https://doi.org/10.1016/J.CARBPOL.2018.10.091.

(61) Sun, B.; Lin, Y.; Wu, P.; Siesler, H. W. A FTIR and 2D-IR Spectroscopic Study on the Microdynamics Phase Separation Mechanism of the Poly(N-Isopropylacrylamide) Aqueous Solution. *Macromolecules* **2008**, *41* (4), 1512–1520. https://doi.org/10.1021/ma702062h.

(62) Speer, M. Raman Spectroscopy as a Technique for Studying the Structure and Mechanism of the Volume Phase Transition of PolyN(Isopropylacrylamide), University of Pittsburgh, 2013.

(63) Schmidt, P.; Dybal, J.; Rodriguez-Cabello, J. C.; Reboto, V. Role of Water in Structural Changes of Poly(AVGVP) and Poly(GVGVP) Studied by FTIR and Raman Spectroscopy and Ab Initio Calculations. *Biomacromolecules* **2005**, *6* (2), 697–706. https://doi.org/10.1021/bm049461t.

(64) Gong, J. P. Why Are Double Network Hydrogels so Tough? *Soft Matter* **2010**, *6* (12), 2583. https://doi.org/10.1039/b924290b.

(65) Puleo, G. L.; Zulli, F.; Piovanelli, M.; Giordano, M.; Mazzolai, B.; Beccai, L.; Andreozzi, L. Mechanical and

Rheological Behavior of PNIPAAM Crosslinked Macrohydrogel. *React. Funct. Polym.* **2013**, *73* (9), 1306–1318. https://doi.org/10.1016/J.REACTFUNCTPOLYM.2013.07.004.

(66) Draget, K. I.; Stokke, B. T.; Yuguchi, Y.; Urakawa, H.; Kajiwara, K. Small-Angle X-Ray Scattering and Rheological Characterization of Alginate Gels. 3. Alginic Acid Gels. *Biomacromolecules* **2003**, *4* (6), 1661–1668. https://doi.org/10.1021/bm034105g.

(67) Sun, J.-Y.; Zhao, X.; Illeperuma, W. R. K.; Chaudhuri, O.; Oh, K. H.; Mooney, D. J.; Vlassak, J. J.; Suo, Z. Highly Stretchable and Tough Hydrogels. *Nature* **2012**, *489* (7414), 133–136. https://doi.org/10.1038/nature11409.

(68) Doi, M. *Soft Matter Physics*; OUP Oxford, 2013.

(69) Young, R. J.; Lovell, P. A. 5.4.4. Pressure Dependent Yield Behaviour. In *Introduction to Polymers*; 1992; pp 363–365.

(70) Zhao, Q.-M. W.; Mohan, A. C.; Oyen, M.; Zhao, X. Separating Viscoelasticity and Poroelasticity of Gels with Different Length and Time Scales. *Acta Mech. Sin.* **2014**, *30* (1), 20–27.

(71) Oyen, M. L. Mechanical Characterisation of Hydrogel Materials. *Int. Mater. Rev.* **2014**, *59* (1), 44–59. https://doi.org/10.1179/1743280413Y.0000000022.

(72) Lopez-Sanchez, P.; Rincon, M.; Wang, D.; Brulhart, S.; Stokes, J. R.; Gidley, M. J. Micromechanics and Poroelasticity of Hydrated Cellulose Networks. *Biomacromolecules* **2014**, *15* (6), 2274–2284. https://doi.org/10.1021/bm500405h.

(73) de Gennes, P.-G. *Scaling Concepts in Polymer Physics*, 1st ed.; Cornell University Press: London, 1979.

(74) Suzuki, A.; Sanda, K.; Omori, Y. Phase Transition in Strongly Stretched Polymer Gels. *J. Chem. Phys.* **1997**, *1071* (10), 1214–10003. https://doi.org/10.1063/1.474880.

(75) Audoly, B.; Pomeau, Y. *Elasticity and Geometry: From Hair Curls to the Non-Linear Response of Shells*, First.; Oxford University Press, 2010.

(76) Timoshenko, S. Analysis of Bi-Metal Thermostats. *J. Opt. Soc. Am.* **1925**, *11* (3), 233–255.

https://doi.org/10.1364/JOSA.11.000233.

(77) Morimoto, T.; Ashida, F. Temperature-Responsive Bending of a Bilayer Gel. *Int. J. Solids Struct.* **2015**, *56–57*, 20–28. https://doi.org/10.1016/J.IJSOLSTR.2014.12.009.

(78) Baqersad, J.; Poozesh, P.; Niezrecki, C.; Avitabile, P. Photogrammetry and Optical Methods in Structural Dynamics – A Review. *Mech. Syst. Signal Process.* **2017**, *86*, 17–34. https://doi.org/10.1016/J.YMSSP.2016.02.011.

(79) Shim, T. S.; Kim, S.-H.; Heo, C.-J.; Jeon, H. C.; Yang, S.-M. Controlled Origami Folding of Hydrogel Bilayers with Sustained Reversibility for Robust Microcarriers. *Angew. Chem. Int. Ed. Engl.* **2012**, *51* (6), 1420–1423. https://doi.org/10.1002/anie.201106723.

(80) Stoychev, G.; Zakharchenko, S.; Turcaud, S.; Dunlop, J. W. C.; Ionov, L. Shape-Programmed Folding of Stimuli-Responsive Polymer Bilayers. *ACS Nano* **2012**, *6* (5), 3925–3934. https://doi.org/10.1021/nn300079f.

(81) Reyssat, E.; Mahadevan, L. Hygromorphs: From Pine Cones to Biomimetic Bilayers. *J. R. Soc. Interface* **2009**, *6* (39), 951–957. https://doi.org/10.1098/rsif.2009.0184.

(82) Xu, P.; Loomis, J.; Bradshaw, R. D.; Panchapakesan, B. Load Transfer and Mechanical Properties of Chemically Reduced Graphene Reinforcements in Polymer Composites. *Nanotechnology* **2012**, *23* (50), 505713. https://doi.org/10.1088/0957-4484/23/50/505713.

(83) Rusli, R.; Eichhorn, S. J. Determination of the Stiffness of Cellulose Nanowhiskers and the Fiber-Matrix Interface in a Nanocomposite Using Raman Spectroscopy. *Appl. Phys. Lett.* **2008**, *93* (3), 033111. https://doi.org/10.1063/1.2963491.

(84) Kizil, R.; Irudayaraj, J. Raman Spectroscopy. In *Food Engineering Series*; 2014. https://doi.org/10.1007/978-1-4939-0311-5_5.

(85) Mendez, J.; Annamalai, P. K.; Eichhorn, S. J.; Rusli, R.; Rowan, S. J.; Foster, E. J.; Weder, C. Bioinspired Mechanically Adaptive Polymer Nanocomposites with Water-Activated Shape-Memory Effect. *Macromolecules* **2011**, *44* (17), 6827–6835. https://doi.org/10.1021/ma201502k.

(86) Ahmed, Z.; Gooding, E. A.; Pimenov, K. V.; Wang, L.; Asher, S. A. UV Resonance Raman Determination of Molecular Mechanism of Poly(*N* -Isopropylacrylamide) Volume Phase Transition. *J. Phys. Chem. B* **2009**, *113* (13), 4248–4256. https://doi.org/10.1021/jp810685g.

(87) Rockwood, D. N.; Chase, D. B.; Akins, R. E.; Rabolt, J. F. Characterization of Electrospun Poly(N-Isopropyl Acrylamide) Fibers. *Polymer (Guildf).* **2008**, *49* (18), 4025–4032. https://doi.org/10.1016/J.POLYMER.2008.06.018.

(88) Campos-Vallette, M. M.; Chandía, N. P.; Clavijo, E.; Leal, D.; Matsuhiro, B.; Osorio-Ro, I. O.; Torres, S. Characterization of Sodium Alginate and Its Block Fractions by Surface-Enhanced Raman Spectroscopy. https://doi.org/10.1002/jrs.2517.

(89) Bradley; Michael S. Lineshapes in IR and Raman Spectroscopy: A Primer. *Spectroscopy* **2015**, *Volume 30* (Issue 11), 42–46.

(90) Brasnett, C. LipidSAXS https://github.com/csbrasnett/lipidsaxs.

(91) De Cagny, H. C. G.; Vos, B. E.; Vahabi, M.; Kurniawan, N. A.; Doi, M.; Koenderink, G. H.; Mackintosh, F. C.; Bonn, D. *Porosity Governs Normal Stresses in Polymer Gels*; 2016.

(92) Adams, D.; J., D. Does Drying Affect Gel Networks? *Gels* **2018**, *4* (2), 32. https://doi.org/10.3390/gels4020032.

(93) Bischofberger, I.; Calzolari, D. C. E.; De Los Rios, P.; Jelezarov, I.; Trappe, V. Hydrophobic Hydration of Poly-N-Isopropyl Acrylamide: A Matter of the Mean Energetic State of Water. *Sci. Rep.* **2015**, *4* (1), 4377. https://doi.org/10.1038/srep04377.

(94) Stokes, D. Investigating Biological Ultrastructure Using Environmental Scanning Electron Microscopy (ESEM). *Sci. Technol. Educ. Microsc. an Overv. Investig.* **2003**, *2* (January 2003), 564–570.

(95) Nguyen, H. H.; Payré, B.; Fitremann, J.; Lauth-de Viguerie, N.; Marty, J.-D. Thermoresponsive Properties of PNIPAM-Based Hydrogels: Effect of Molecular Architecture and Embedded Gold Nanoparticles. *Langmuir* **2015**, *31* (16), 4761–4768. https://doi.org/10.1021/acs.langmuir.5b00008.

(96) Boontheekul, T.; Kong, H.-J.; Mooney, D. J. Controlling Alginate Gel Degradation Utilizing Partial Oxidation and Bimodal Molecular Weight Distribution. *Biomaterials* **2005**, *26* (15), 2455–2465. https://doi.org/10.1016/J.BIOMATERIALS.2004.06.044.

(97) Okay, O. Macroporous Copolymer Networks. *Prog. Polym. Sci.* **2000**. https://doi.org/10.1016/S0079-6700(00)00015-0.

(98) Li, S.; Yang, W. Fabrication of Poly(Acrylamide) Hydrogels with Gradient Crosslinking Degree via Photoinitiation of Thick Polymer System. *Polym. Adv. Technol.* **2011**. https://doi.org/10.1002/pat.1623.

(99) Arganda-Carreras, I.; Kaynig, V.; Rueden, C.; Eliceiri, K. W.; Schindelin, J.; Cardona, A.; Sebastian Seung, H. Trainable Weka Segmentation: A Machine Learning Tool for Microscopy Pixel Classification. *Bioinformatics* **2017**, *33* (15), 2424–2426. https://doi.org/10.1093/bioinformatics/btx180.

(100) Nölle, J. M.; Primpke, S.; Müllen, K.; Vana, P.; Wöll, D. Diffusion of Single Molecular and Macromolecular Probes during the Free Radical Bulk Polymerization of MMA-towards a Better Understanding of the Trommsdorff Effect on a Molecular Level. *Polym. Chem.* **2016**. https://doi.org/10.1039/c6py00590j.

(101) Cai, S.; Hu, Y.; Zhao, X.; Suo, Z. Poroelasticity of a Covalently Crosslinked Alginate Hydrogel under Compression. *J. Appl. Phys.* **2010**, *108* (11), 113514. https://doi.org/10.1063/1.3517146.

(102) Serrano-Aroca, Á.; Ruiz-Pividal, J.-F.; Llorens-Gámez, M. Enhancement of Water Diffusion and Compression Performance of Crosslinked Alginate Films with a Minuscule Amount of Graphene Oxide. *Sci. Rep.* **2017**, *7* (1), 11684. https://doi.org/10.1038/s41598-017-10260-x.

(103) Mallam, S.; Horkay, F.; Hecht, A.-M.; Geissler, E. *Scattering and Swelling Properties of Inhomogeneous Polyacrylamide Gels*; 1989; Vol. 22.

(104) Sydney Gladman, A.; Matsumoto, E. A.; Nuzzo, R. G.; Mahadevan, L.; Lewis, J. A. Biomimetic 4D Printing. *Nat. Mater.* **2016**, *15* (4), 413–418. https://doi.org/10.1038/nmat4544.

(105) Wu, Z. L.; Moshe, M.; Greener, J.; Therien-Aubin, H.; Nie, Z.; Sharon, E.; Kumacheva, E. Three-Dimensional Shape Transformations of Hydrogel Sheets Induced by Small-Scale Modulation of Internal Stresses. *Nat. Commun.* **2013**, *4*, 1586. https://doi.org/10.1038/ncomms2549.

(106) Na, J.-H.; Bende, N. P.; Bae, J.; Santangelo, C. D.; Hayward, R. C.; Ionov, L.; Kempaiah, R.; Nie, Z.; Studart, A. R.; Erb, R. M.; et al. Grayscale Gel Lithography for Programmed Buckling of Non-Euclidean Hydrogel Plates. *Soft Matter* **2016**, *12* (22), 4985–4990. https://doi.org/10.1039/C6SM00714G.

(107) Silverman, B. W. *Density Estimation: For Statistics and Data Analysis*; 1986. https://doi.org/10.1201/9781315140919.

5 THE EFFECTS OF ADDITION OF GOLD NANORODS TO PNIPAM-ALGINATE HYDROGELS

5.1 REFERENCES

Responsive printable materials require variable degrees of response to achieve useful and interesting shape changes. Prior work has successfully combined gold nanorods and other nanomaterials with PNIPAM, to create materials with a tailorable speed of response and the potential for remote action. However, PNIPAM is not printable in isolation, and the combination of PNIPAM-alginate hydrogels with nanoparticles has not been tested. A commercial source of gold nanorods was added to the PNIPAM-alginate composition presented in prior chapters and the results assessed for thermal response, swelling properties, and viscoelastic behaviour, using compression and rheology. While no significant thermal change was measured, it was found that the elastic shear modulus increased non-monotonically with concentration, peaking at a factor of six compared to the unmodified gel when the concentration was 1-2 μg/ml. This change was not reflected in compressive testing measurements of the Young's modulus, demonstrating the limitations of extrapolating from shear testing to compression. Potential mechanisms for the change in gel performance were examined using SAXS and rheology, and a theory based on network structure changes is suggested. The significant variation in gel mechanical performance at such a low concentration is indicative that the addition of nanoparticles can have an unexpected and hard to predict effect on hydrogel matrix properties.

5.2 INTRODUCTION AND BACKGROUND

It is evident that for smart material prints to change shape, rather than just rescale while retaining the same proportions, the comprising materials must vary spatially in their response to stimuli. This could be achieved in multiple ways. Different stiffnesses, as in plant-inspired hygroscopic materials, can constrain movement.[1] Alternatively, varying sensitivity to external triggers can affect the onset of response, for example, triggering at different temperatures;[2] or exert different magnitudes of response.

As described in the introduction, there are many ways this could be implemented with hydrogels. Many authors have explored the route of combining different gel compositions, or responsive gels with stiff materials.[3–5] These have been achieved using layer-by-layer assembly,[6] photopatterning,[7] soft lithography[8] or manual fabrication

from dissimilar components (as shown in Figure 5.1).[9] These processes are inherently geometrically limited, and the multiple stages limit mechanisation and scale-up of production.

An alternative and appealing option is to create a 3D printed object using multiple materials, ready to actuate straight off the print bed. This has been demonstrated by Naficy *et al.* with a combination of responsive and non-responsive printable hydrogels.[10] In that work, bending angle was determined by the Timoshenko equation given in Chapter 1.5.1. Since two binary materials were used, no sequential deployment analogous to that shown in Chapter 1.2.1.1 for SMPs was possible.

Additional materials for printing responsive hydrogel objects are desirable, and a 'family' of gels which vary in response would be ideal. This requires at least two printable gels, similar enough to be processed together on the same printer, but different enough when cured to cause shape change of the overall print. One promising route to this is the addition of a small weight percentage of some other component to the existing printable PNIPAM-alginate.

Prior existing examples within printed shape-changing materials have used ions for selective reinforcement,[11] dyes for selective sensitisation,[12] and high aspect ratio nanocellulose for orientation-specific responses.[13] Since concentration can be varied smoothly, this also raises the prospect of grading properties smoothly across the print, allowing for optimisation.[14]

5.2.1 PRIOR NANOCOMPOSITE MODIFICATION OF POLY-N-ISOPROPYL ACRYLAMIDE NETWORKS

Nanoparticles exhibit enhanced and novel effects due to their size, and due to their high surface-to-volume ratio blend well with matrix materials when used in composites. PNIPAM nanocomposites with concentration-dependent responses have been demonstrated multiple times. For example, polymer gels have been combined with single walled carbon nanotubes (SWNT) to enhance the speed of thermal response.[9] The same effect has been achieved through combination with graphene oxide (GO) flakes to create microvalves and self-folding structures.[15,16] Directional effects of inclusions has been exploited to create anisotropic effects, both though alignment of iron oxide particles in PNIPAM[17] and through the extrusion-based alignment of cellulose mentioned in previous chapters.[13]

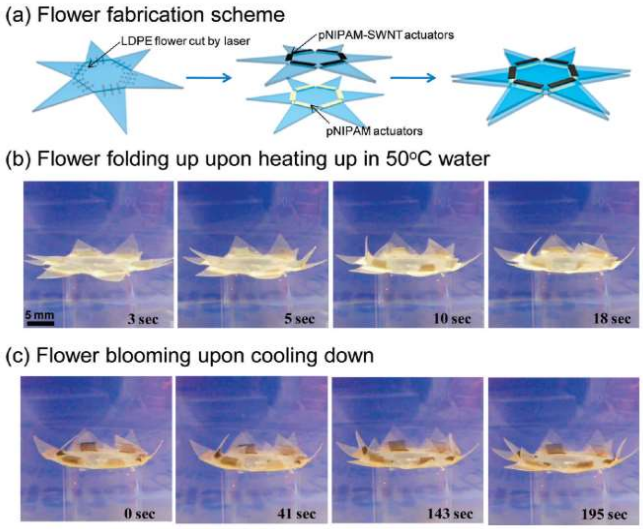

Figure 5.1. Hybrid PNIPAM/PNIPAM-SWNT actuators arranged to produce a flower with different folding rates for two rows of petals. From Zhang et al.[9]

Gold nanorods sized to exhibit plasmon resonance modes at 785 nm have successfully been used with PNIPAM hydrogels, allowing remote laser triggering through their sensitivity to IR frequencies.[18,19] This hybrid material was then incorporated into a dynamically adjustable microlens device.[20] Triggering in the infrared region is particularly appealing for biological applications as both PNIPAM and much of the human body are transparent in this range. Infrared triggering has already been used to deploy shape-changing implanted medical devices in animals.[21]

However, as mentioned in Chapter 4.2.1, PNIPAM in its native state is brittle and unsuitable for practical devices. Additionally, due to its viscosity, it cannot be printed with extrusion methods. Double network systems such as PNIPAM-alginate are a promising solution for rendering the material more tractable, both by enabling processing of uncured blends in a printer and by producing tougher, more resilient samples. It is therefore of interest to see if the sensitising effect of nanocomposites persists for a PNIPAM-alginatae double network gel, to what extent, and what other outcomes there are when such hydrogels are combined with these nanoinclusions.

As a starting point, gold nanorods (AuNR), with a plasmon resonance at 785 nm, were selected for combination with the PNIPAM-alginate system examined in Chapter 4. Firstly, it was hoped that AuNR in PNIPAM-alginate would enable remote triggering of gel contraction through IR laser stimulation of printed objects, as demonstrated conceptually with pure PNIPAM.[22] Secondly, it was possible that the addition of AuNR would modify the LCST for the PNIPAM-alginate composites as a function of its concentration, as previously shown for graphene oxide in PNIPAM,[23] enabling sequential deployment. Thirdly and finally, the addition of AuNR to PNIPAM-alginate could contribute reinforcing stiffening effects, as seen with in-situ synthesised gold particles in

PNIPAM.[24] These three possibilities were each suggested by the literature, and would increase the repertoire of 3D printable hydrogel materials available and the capacity of the models created from them.

It should be noted that this is a test model: the cost of gold nanorods as well as concerns about their toxicity[25] make other solutions, such as carbon nanotubes[9] or iron oxide nanoparticles,[7] attractive for future development. However, many nanoparticles carry toxicity concerns,[26] so this issue cannot be totally avoided if nanoparticles are to be used. Gold is non-toxic in bulk, gold nanorods are well studied, and available commercially in a well-characterised format. For novel applications, it is important that the number of variables in the existing system is reduced as much as possible to ease identification of the origin of effects. Additionally, the fact that CNTs, GO and iron oxide nanoparticle composites are black in colour presents challenges for use in a UV-based curing system, driving the choice of AuNR as a working material.

5.3 METHODS DEVELOPMENT

5.3.1 PROCESSING

For the preparation of nanoparticle-containing samples, the process described in Chapter 4 was modified by the addition of the appropriate volume of nanoparticles in aqueous media to the $CaCl_2$ solution (while retaining the same molarity of $CaCl_2$); from there the procedure was the same.

A nanoparticle suspension was added to the 15 ml synthesis batch volume in quantities from 0.5 to 3 ml: at a concentration of 30 μg/ml. This corresponds to a final concentration of 1-6 μg/ml in the hydrogel nanocomposites as prepared. This is a very low concentration, imposed by the cost and concentration of commercially available products, and it would be desirable to increase the weight percentage in future work. An increase in this concentration could be achieved through in-house synthesis to reduce the cost, a decreased sample size with proportional cost savings, or both. However, Hribar *et al.* observed photothermal effects in shape memory polymers modified with 1.8×10^{-13} M gold nanorods[27] – two orders of magnitude lower than the concentration used in this work. The following data will demonstrate that there is measurable variation in PNIPAM-alginate gel behaviour even at this low percentage, suggesting that a low concentration can still yield information about the effect of gold nanorods on double-network PNIPAM-alginate gels.

A potential confounding effect on all measurements taken on PNIPAM-alginate gels, with the addition of a nanoparticle suspension, is the presence in the suspension of the surfactant cetrimonium bromide (CTAB) and a weak organic acid citric acid at >0.1 wt.%. It is known that surfactants increase the equilibrium volume occupied by PNIPAM,[28] and its transition temperature.[29] The addition of CTAB to alginates has also been shown to decrease the hydrophilicity of binding parts of the polysaccharide chain, and to increase binding and aggregation through the promotion of both hydrophobic and electrostatic interactions.[30]

To assess whether the effects on the system could be explained wholly or partially by the presence of CTAB and citric acid being included with the nanoparticles, comparison samples were created with these components added, both separately and together, at an equivalent concentration to that delivered by the addition of a 3ml AuNR suspension in a 15ml batch synthesis (0.0002%wt). These samples are denoted Citric, CTAB or Citric and CTAB where referenced in the following sections.

5.4 RESULTS AND DISCUSSION

5.4.1 NANOPARTICLE CHARACTERISATION

The manufacturers of the gold nanorods used throughout this study state their dimensions as (10 x 35 nm) ± 10%. The percentage of particles conforming to this size is >90%, and their plasmon resonance is stated to occur at 785 nm. These characteristics were verified using DLS, a Zetasizer, transmission electron microscopy (TEM) and UV-Visible spectroscopic observations.

UV-Visible spectroscopy was performed at a dilution factor of 30, with deionized water, and yielded the spectrum shown in Figure 5.2.

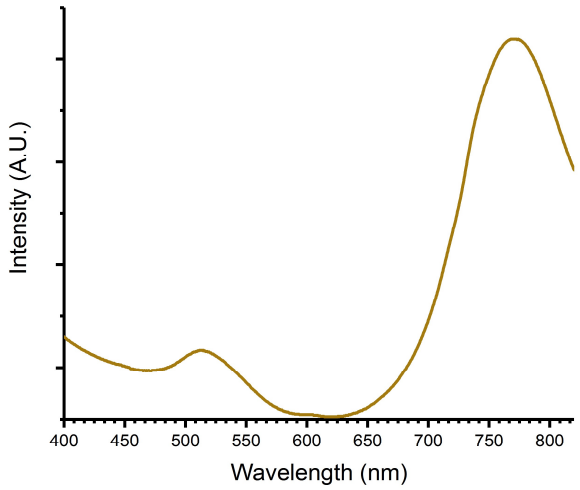

Figure 5.2. A typical UV-Visible spectrum from the gold nanorod suspension used for further experiments.

As stated by the manufacturers, the nanorods showed broad resonance peaks in the 785 (major) and 510 (minor) nm regions, consistent with a gold nanorod of the stated size. However, this was not conclusive evidence as it could also represent a mixture of materials with resonant peaks at 785 and 510 nm. To determine their dimensions further, transmission electron microscopy was used.

5.4.1.1 TRANSMISSION ELECTRON MICROSCOPY

TEM images of particles were taken to determine their sizes and aspect ratios (example images are shown in Figure 5.3), using parameters given in Materials and Methods.

A total of 75 particles from these images were measured using ImageJ, and yielded average dimensions of 34±4 nm in length and 12±4 nm in width. Of the 75 particles measured, 9 were approximately circular in cross-section, with the remainder well-formed rods. Electron diffraction patterns were taken of these anomalously shaped particles. (Figure 2, right). The radii of the first four rings were measured using ImageJ.

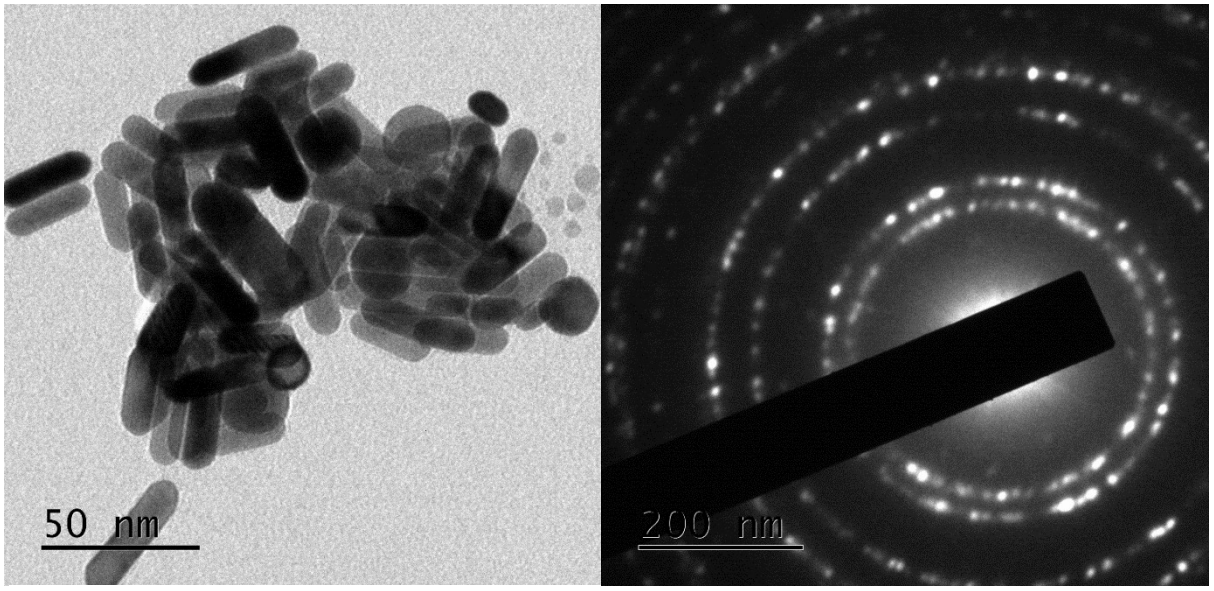

Figure 5.3. Left: A typical transmission electron microscopy image of the gold nanorods used for blending with PNIPAM-alginate hydrogels. Nanorods were observed to aggregate on the TEM grids but this is not thought to be representative of behaviour in solution. Right: A selective area electron diffraction (SAED) image of a circular aggregate.

TEM studies showed significant nanoparticle aggregation, but given the contrary evidence of zeta potential and DLS measurements (see 5.4.1.2), taken in solution, it is likely that this was caused by the drying process and the plasma treatment necessary for the particles to adhere well to the TEM grid.

Particle analysis of the TEM images revealed average dimensions of 11.8 ± 3.6nm and 33.9 ± 4.2nm for their width and lengths respectively (errors of approximately 20% of the total particle dimension). This is greater than the error stated by the manufacturer, of ± 10%. Around 20% of the particles observed from the TEM images were not rod-like – again, more than the manufacturer's value of 10%.

The electron diffraction pattern from the anomalous round particles was compared to the face-centred packing Bragg peaks expected from gold particles. The ratios between the first four peak spacings are expected to be 0.75:0.50:0.75, and were found by measurements of the ring diameters with ImageJ as 0.73:0.51:0.72, indicating compatibility with a face-centered cubic (FCC) structure. The lattice constant could not be determined as the scale on the image did not correspond with the real space distance between the peaks as projected. Based on the polycrystalline diffraction pattern shown, the compatibility of the peaks with the FCC atomic packing mode and the known potential for the AuNR synthesis used to create non-rod morphologies,[31] these are identified as gold nanoparticles rather than contaminants of other material.

The DLS value found for the hydrodynamic radius of the AuNR, 38.8±7.2nm, is compatible within errors with the values found via TEM and with the manufacturer's stated values. This means that there is probably an adsorbed double layer of CTAB molecules on the surface of the particles which is 3.2 ± 0.2nm thick.[32]

Overall, these measurements give us a picture of a rod, approximately 12x34nm, with a bilayer coating of surfactant which is positively charged. This can be usefully compared with the other characteristic dimensions of the system – the length of the average alginate G-block participating in binding is approximately 2.2 nm and the length of the more flexible regions in between is again approximately 2.2 nm (for full data and derivations see Section 4.4.1). While measurements from single networks cannot be expected to be reproduced exactly in interpenetrating networks, the degree of polymerisation between crosslinks in a pure PNIPAM gel found in Chapter 4 is 61.8 ± 0.2, corresponding to an average length between crosslinks of ~19 nm (see section 4.4.2 for methods). Figure 5.4 shows a sketch, to scale, which illustrates the relative sizes of the components.

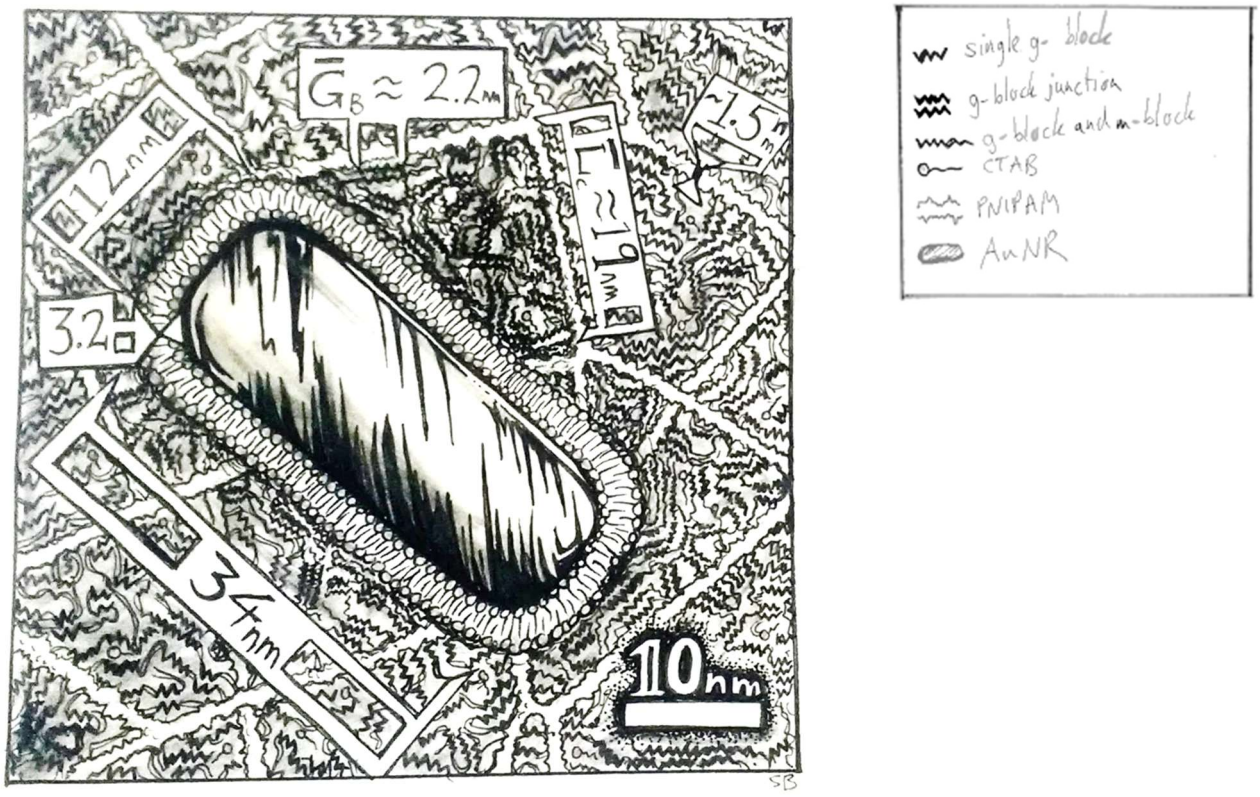

Figure 5.4. A schematic showing the relative sizes of the two gel networks and the AuNR components. The nanorod is 11.8 ± 3.6nm in width and 33.9 ± 4.2nm in length; Lc denotes average length between crosslinks for PNIPAM and is ~19nm, corresponding to 61.8±0.2 repeat units of monomer; G_B denotes average size of G-blocks in alginate, which are the primary units involved in binding during gelation,

here approximate 2.2 nm long, corresponding to 5 repeat units. The width of a PNIPAM strand is shown as approximately ten times the length of a C-C bond, ~1.75nm. The bilayer on the CTAB surface is taken to be 3.2 ± 0.2nm.[32] Hand-drawn by the author.

5.4.1.2 ZETA POTENTIAL & DYNAMIC LIGHT SCATTERING

The zeta potential of the gold nanorods, alginate and NIPAM were measured to determine their surface charge, and thus electrostatic interactions. Dynamic light scattering (DLS) was used to reveal average hydrodynamic radius of the particles.

These data suggest that in dilute solution the addition of AuNR results in binding to alginates and a decreased charge on the resulting complex. The addition of CTAB and citric acid, separately or together, has no effect larger than the error. However, the addition of the nanoparticle solution creates a complex with half the zeta potential of the alginate – NIPAM – $CaCl_2$ solution. This would support a decreased average electrostatic repulsion between the polymers upon the addition of nanoparticles.

Component	**Zeta potential (mV)**
NIPAM	-27.25 ± 4.3
Alginate	-49.69 ± 4.1
NIPAM + $CaCl_2$	-9.2 ± 2.1
NIPAM + alginate + $CaCl_2$	-31.9 ± 3.9
Au NR (with CTAB + Citric at <0.03%wt)	+31.6 ± 3.3
NIPAM + alginate + $CaCl_2$ + CTAB	-32.6 ± 3.3
NIPAM + alginate + $CaCl_2$ + citric acid	-32.0 ± 3.3
NIPAM + alginate + $CaCl_2$ + citric acid + CTAB	-28.9 ± 3.9
NIPAM + alginate + $CaCl_2$ + AuNR	-15.7 ± 3.9

Table 5.1. Zeta potential measurements for NIPAM, calcium chloride, alginate, CTAB, citric acid, and gold nanorods.

The zeta potential of the nanorods was measured as 31.6±3.3mV, from an average of eight runs, in the suspension as provided and at the concentration used in this work. This is compatible with the value found by Ferhan et al. (31.9 ±2.5mV) but slightly below other values found for CTAB-coated nanoparticles (around 40mV).[25,33–35]

DLS meaurements of AuNR showed the hygroscopic radius of the solvation sphere surrounding the nanorods to have a number averaged peak centred at 40 nm, with full width at half maximum of 7nm. This is compatible with the measurements observed with TEM, UV-Vis and with the manufacturer's stated specifications.

5.4.2 RHEOLOGY OF UNCURED POLYMER BLENDS WITH NANOPARTICLES

For printing as before, a high viscosity at low shear levels approximating print bed conditions, and a viscosity suitable for extrusion at the shear conditions generated by the syringe extruder were required. With these satisfied, small differences in rheology could be corrected for by adjusting software-derived extrusion parameters to modify the pressure as required. Therefore, rheological assessments of the viscosity of the material as a function of shear strain were conducted.

5.4.2.1 SHEAR RAMPS

Shear ramps were performed as in section 4.4.3.1 to assess printability and the affect of nanoparticles. Results are presented in Figure 5-5, and show a decrease in the viscosity of uncured gels with an added nanoparticle solution. This indicates a decrease in the interaction strength between components in the blend. Shear thinning behaviour was seen at all nanoparticle loadings, indicating suitability for extrusion printing. The yield strength of the gel was decreased relative to plain gel, showing suitability for extrusion at an equal or lowered mechanical pressure exerted by the syringe. The decrease in viscosity by an order of magnitude at low shear might cause some loss of resolution during print as the gel would tend to flow more on the bed. There could also be issues with over-extrusion as a more viscous material would take longer to stop flowing when pressure was removed. However, these issues could potentially be addressed with extrusion parameters, and these data demonstrate that the nanoparticle-modified gel could be processed with existing equipment.

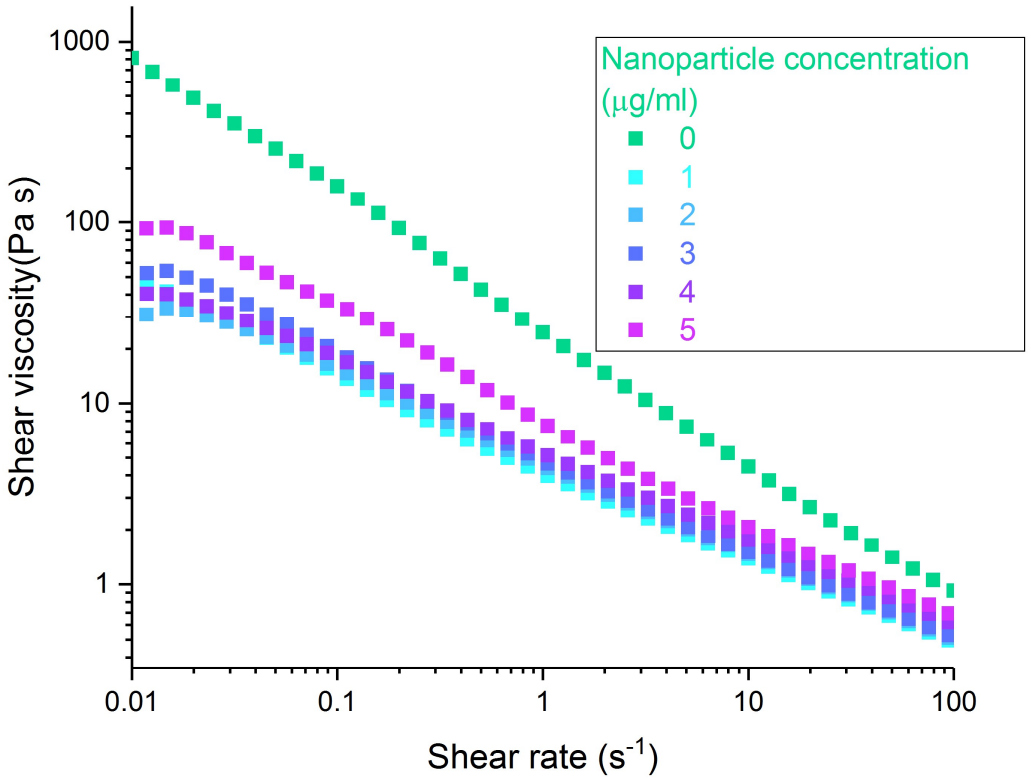

Figure 5.5. Viscosity changes as a function of shear rate for concentrations of between 1-5μg/ml of gold nanorods added to uncured PNIPAM-alginate gel.

5.4.3 LASER RESPONSE

Having established the printability of gold nanorod-laden PNIPAM-alginate gels, their response to infra-red laser stimulation was assessed. Notably, laser-triggered behaviour relies solely on the plasmon resonance of the nanoparticles and so no response would be expected from a PNIPAM-alginate sample without NPS.

A sample bed capable of rastering in two parallel directions was kindly lent by Dr Chris Hutton, who also provided a custom Labview interface. A 40 × 3 × 20mm sample of PNIPAM-alginate with a 2 μg/ml concentration of nanorods was placed on the stage and illuminated with a 0.22 mW laser, pulsed at 1 kHz. The frequency profile was a 30 nm FWHM bandwidth at 800 nm. The spot profile was approximately 3 mm in diameter and Gaussian in shape, corresponding to an average intensity of 3.2 mW/cm^2. Due to the pulsed nature of the setup, the peak energy transmission was 62 kW/cm^2. No response was seen following exposure for 500 seconds.

It is possible that the pulsed nature of the laser did not allow sufficient time for the heat generated by the nanoparticles to reach the PNIPAM polymers, or that insufficient average power was provided to trigger the contraction against the opposition of the alginate gel. In favour of the suggestion that more power was required to trigger a response, successful work triggering contraction of electrospun PNIPAM-AuNR hydrogels has used a 2 W laser.[36] While the system used did have the capacity to go higher, there were safety concerns around the possibility of burning samples or generating unwanted reflections from the set up (shown in Figure 5.6). Moreover, this is a very high-power requirement, meaning that a shape-changing technology which required such a source would be limited in its applications.

Another possibility is that the concentration of nanoparticles was too low. Unpublished work presented by Ximin He at SMASIS 2016, Stowe, Vermont, USA demonstrated 'artificial phototropism' via photothermal responses of PNIPAM pillars composited with gold nanoparticles. While these shapes were formed using soft lithography techniques, this shows the concept for laser triggered deformation of shape-changing gels at the micron scale is possible. However, it is still unknown how the presence of alginate would change the results.

The experimental setup used pillars 1 mm × 8 mm in dimensions, with a 500 mW laser and a concentration of 465 μg/ml of nanoparticles. It seems reasonable that a similar concentration, if not more, would be required in a PNIPAM-alginate composite. As mentioned in Section 5.2.1, while it would be desirable to investigate this to explore the original idea of 3D printed remote-controlled shape changing gels, creating samples of the size used in this thesis would require some methodological changes.

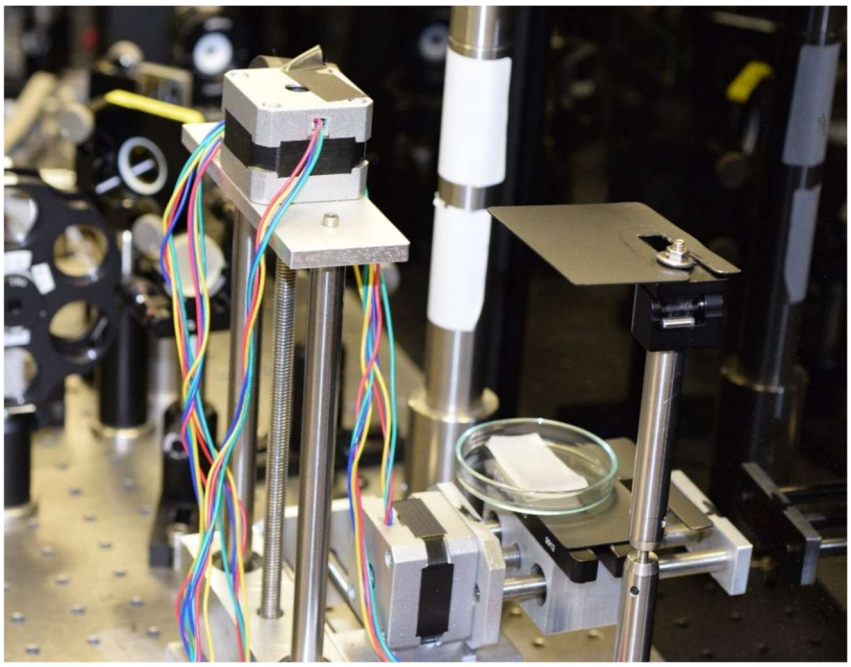

Figure 5.6. PNIPAM-alginate gel set up for laser testing. Sample (centre bottom, in petri dish) is exposed to beam from above, while the two motors raster in the *x* and *y* directions respectively.

5.4.4 DIFFERENTIAL SCANNING CALORIMETRY

To assess the potential for staged deployment through different concentrations of nanoparticles, differential scanning calorimetry was performed as stated in Chapter 2. Full DSC results are presented in Figure 5.7Figure 5.7, and the extracted parameters, the onset time of transition, the rate of transition, and the energy required to transition, are shown in Figure 5.7.

All samples showed a pronounced endo- (on heating) and exo- (on cooling) -thermic peak corresponding to the characteristic LCST transition between 30 and 40°C, and matching that seen in literature. Physically, this represents an increased amount of thermal energy contributing to molecular reconfiguration – the methyl groups folding together to reduce the surface area exposed to water[37] - rather than increasing the temperature of the sample. This is the DSC signature of the macroscopic gel contraction seen.

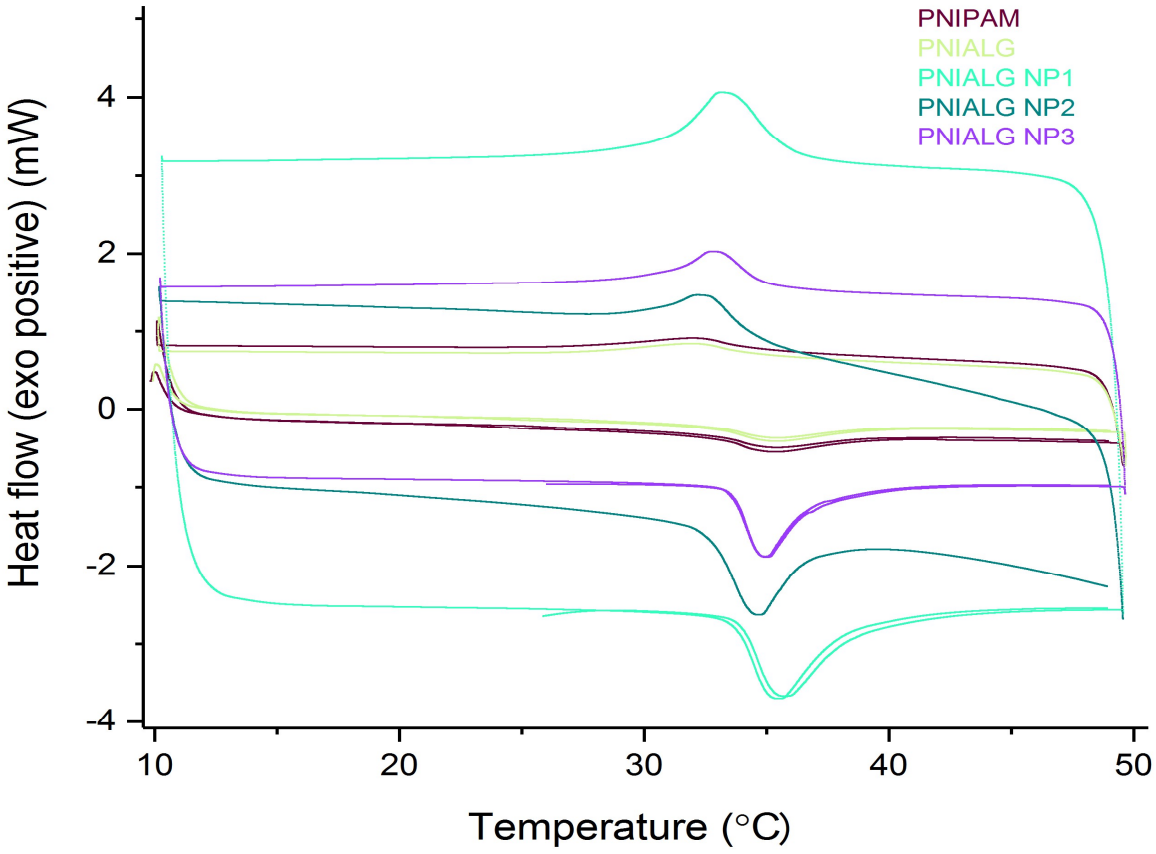

Figure 5.7. DSC data from approximately 2mm cubed gel sections of PNIPAM, PNIPAM-alginate, and PNIPAM-Alginate with 1, 2 and 3ml of added AuNR solution.

The area within the curve represents the energy absorbed by the sample. The magnitude of the difference in heat flow is likely to be due to differing amounts of hydration within the samples. A drier gel would be expected to show a smaller change in energy during heating or cooling as a result of its lower specific heat capacity. Correspondingly, such a gel would also have fewer isopropyl groups in contact with water able to exchange energy and reorient during the LCST transition, resulting in less energy absorbed or emitted during this process and a decrease in the magnitude of the peak. While all samples were sealed into pans for testing, some were sealed a week before testing. It could be the case that significant amounts of water were lost due to issues with the sealing press.

The location of these peaks varied depending on the sample composition, as does the height of the peak and its total area. The peak centre, the onset temperature for the endothermic peak while heating, and the energy of transition were calculated for different nanoparticle compositions and are shown in Figure 5.9. Pure PNIPAM at

a matched polymer fraction, and PNIPAM-alginate with only CTAB added, were also compared and are presented in Figure 5.9.

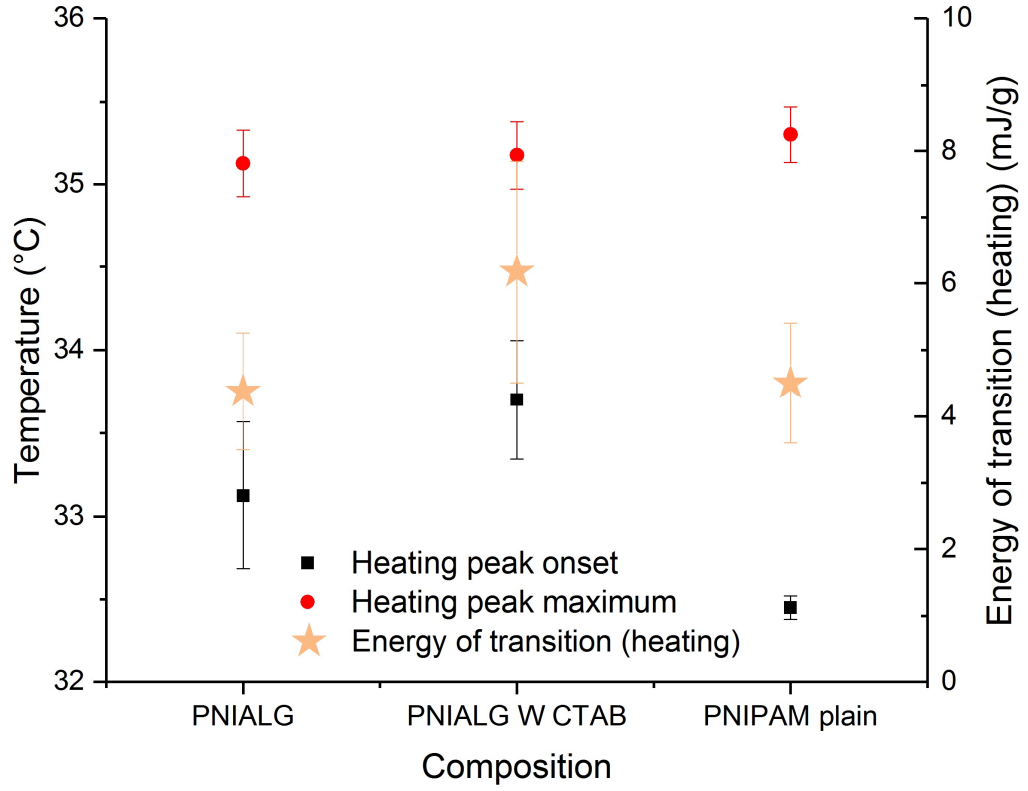

Figure 5.8. Key values relating to the thermal transition of pure PNIPAM, PNIPAM-Alginate and PNIPAM-Alginate with CTAB at equivalent concentrations to 3ml of nanoparticle solution. Left axis shows temperature and indicates the onset of the transition as black squares and the peak of the transition as red circles. Right axis shows the energy consumed and corresponds to the yellow stars. Error bars represent standard error on mean from two heating cycles.

PNIPAM without additives shows the lowest temperature of onset and energy of transition. The addition of other materials could be expected to inhibit the polymer's ability to reconfigure, requiring more energy and increasing the onset temperature. The peak maximum is very similar for all compositions. PNIPAM-alginate with CTAB shows the highest energy of transition and latest time of onset; approximately one degree after pure PNIPAM. However, variation in transition temperatures could be due to variation in hydration, as noted earlier.

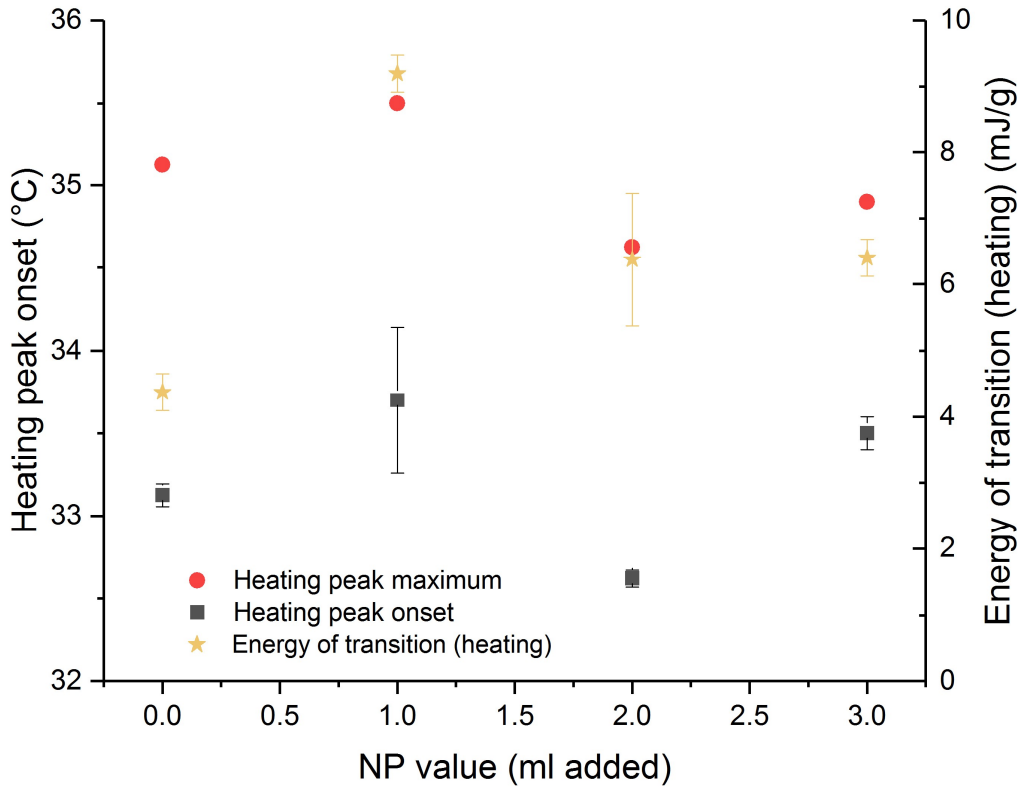

Figure 5.9. Key values relating to the thermal transition of PNIPAM-alginate with 0, 1, 2 and 3ml of nanoparticle solution added. Left axis shows temperature and indicates the onset of the transition as black squares and the peak of the transition as red circles. Right axis shows the energy consumed and corresponds to the yellow stars. Values are means calculated from two heating cycles and errors bars represent the standard error. For the peak maximum series, error bars are too small to be visible.

Comparing the nanoparticle-bearing samples, higher transition temperatures are seen for concentrations which have larger heat capacities (see Figure 5.7) and are hypothesized to contain more water (1 and 3ml). Since the limiting factor on the response of PNIPAM is the diffusion rate of water multiplied by the distance it must travel and hydrogels shrink as they dehydrate, drier hydrogels would rid themselves of water more rapidly and at a lower temperature during heating. On the other hand, this theory would suggest that the energy of transition and temperature of onset would show synchronous trends, which is not seen here: 2.0ml of NP leads to the earliest onset, while PNIPAM-alginate with no additions has the lowest energy requirement.

More interesting explanations of the shift in the LCST temperature would be a change in the mobility of water moving out of the gel,[38] constriction of the isopropyl groups by additional binding to other chemical species in the gel,[29] tension in PNIPAM polymer chains,[39] or a change in PNIPAM polymer density, since the Flory-Huggins

interaction parameter, χ, is a function of both temperature and polymer concentration.[40] The likelihood of these effects will be evaluated further in future sections in conjunction with the results shown there.

As a result of the lack of samples tested at the same hydration level, the influence of the concentration of AuNR on PNIPAM-alginate thermal response is undetermined. However, even if the results persist in a better controlled experiment, the magnitude of the effect seems to be small – causing a shift of a degree or so. For comparison, prior work has used stages separated by 5°C increments of thermal response.[41] Given the long time taken for hydrogels to equilibrate, it seems possible this variation in thermal response would be comparable to variations in temperature found in an unmodified gel system. This makes it unpromising as a candidate for staged deployment of printed thermoresponsive PNIPAM-alginate.

5.4.5 VOLUME SWELLING RATIO

The third possibility then presents itself: could AuNR have a reinforcing effect upon the gels, changing their mechanical properties?

A key determinant of many mechanical properties of hydrogels is their polymer volume fraction, φ. This defines the volume of material taken up by polymers rather than solvent in the network when the hydrogel is swollen to equilibrium in a given solvent. Intuitively, it makes sense that a hydrogel with a lower level of hydration will be stiffer and less able to deform. For PNIPAM it is also of interest for predicting the thermal response, as it is one of the parameters which affects the polymer-solvent interaction parameter χ.[40] Finally, for a fixed number of crosslinks the swelling ratio affects crosslink density, which is, in simple gel models, linearly related to the elastic shear modulus. It was therefore of interest to measure the variation in polymer volume fraction as the concentration of nanoparticles varied.

Concentrations corresponding to 1-6 μg/ml of gold nanorods, and 0.1% by weight of CTAB and citric acid, were prepared and tested as detailed in materials and methods.

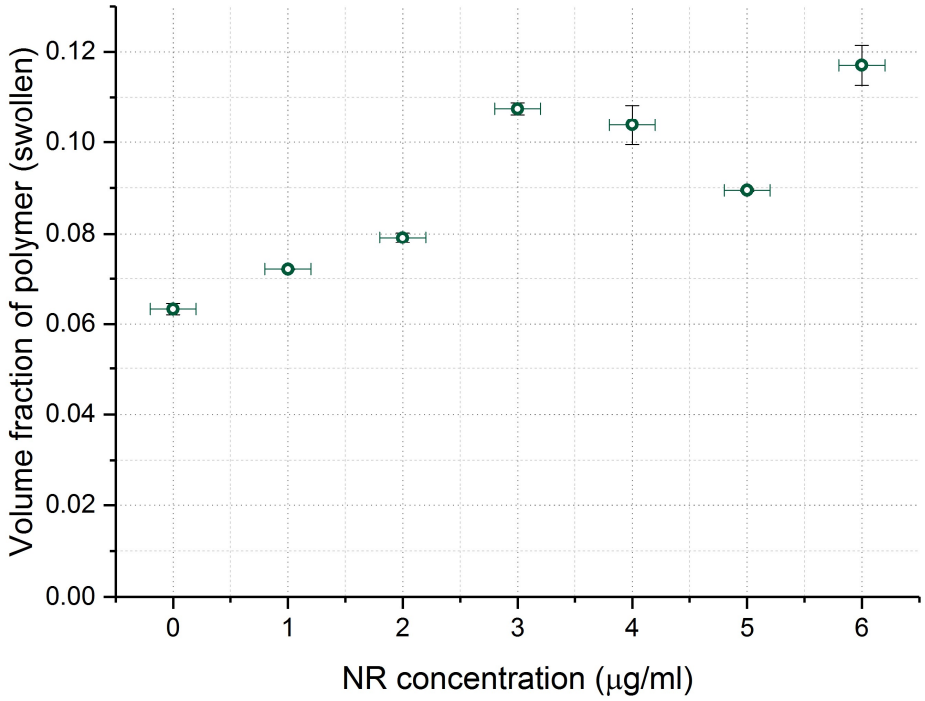

Figure 5.10. A comparison of the polymer volume fractions of PNIPAM-alginate double network gels with various concentrations of gold nanoparticles, evaluated when swollen to equilibrium at 20°C. Errors are the standard error on the mean (volume) and the error of the pipette (concentration).

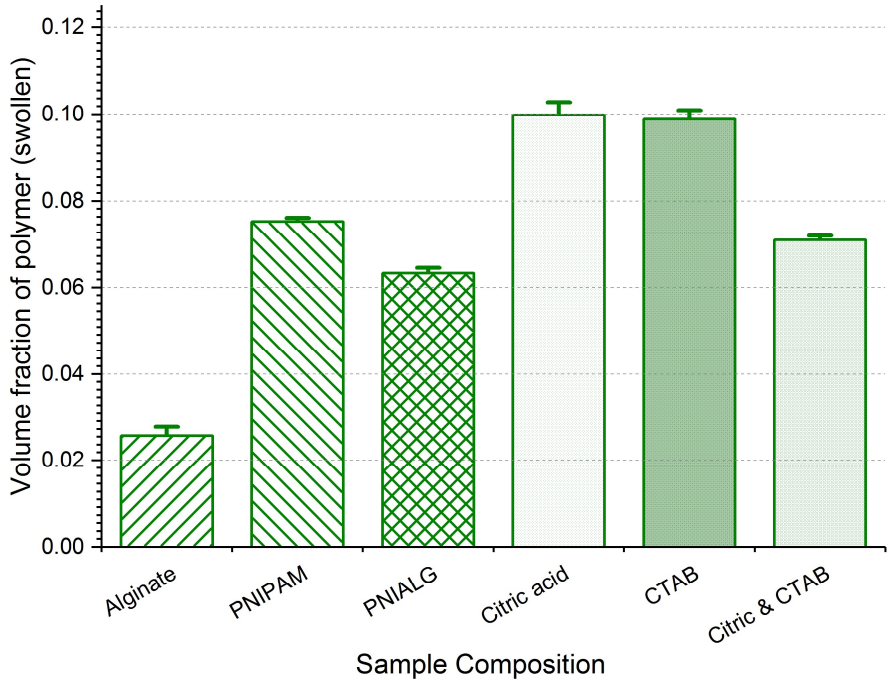

Figure 5.11. A comparison of the polymer volume fractions at equilibrium for different hydrogel compositions, including alginate and PNIPAM singly, in combination, and with the addition of 0.1%wt of citric acid, CTAB, or both to the combined gel. Error bars show standard error on mean of three samples.

The smallest polymer volume fraction seen for PNIPAM-alginate with nanorods is the unmodified concentration, corresponding to the largest water uptake. As can be seen from the equations presented in Chapter 1.4.1, this implies it has the lowest crosslink density and therefore the largest molecular weight between crosslinks.

It is energetically favourable for a charged network to expand, minimizing the electrostatic repulsion in the system, if this exceeds the entropic and enthalpic cost of stretching the polymers (described mathematically in section 1.4.1). This is seen when alginate is added to PNIPAM to make the base composite (see Figure 5.11 and also Petrusic).[42] It has been shown that ionised pure PNIPAM networks also exhibit increased swelling and transitions at a higher temperature compared to neutral PNIPAM.[43] The zeta potential measurements (Table 5.1) indicate that the addition of nanoparticles to alginate creates a complex with a reduced net negative charge, which would result in a lower repulsion and less expansion, as is seen in Figure 5.10.

The trend for PNIPAM-alginate volume fractions with the addition of nanoparticles is broadly linear, significantly different from zero (ANOVA) and shows a gradient of 0.00452 ml/μg, corresponding to an increase of about 0.005 of polymer volume fraction for each microgram of nanoparticle solution. The linear trend is broken by a local maximum at a concentration of 3 μg/ml, rising again to 5μg/ml before decreasing. Both binding with CTAB-stabilised gold nanorods and surfactants are recorded in the literature for alginate networks.[30] PNIPAM has also been observed to change in microscopic conformation in response to the addition of nanoparticles, namely graphene flakes, exhibiting smaller pore sizes. Since this latter correlates with less swelling, this is also as expected.[44]

This could be due to an anomaly in the samples, or a deeper matter arising from the interplay of the two components – this will be discussed in more detail in Section 5.4.6. It can be deduced that nanorods themselves are a significant contributor to the effects of the nanorod solution, since PNIPAM-alginate with 3 ml of nanorods has a polymer volume fraction of 0.11, almost twice the value of the unmodified gel, and that with just citric and CTAB 0.07. However, while both citric acid and CTAB cause an increase in polymer volume fraction relative to native gel, together they seem to counter each other, with the effect of each singly being more than that of both.

Citric acid dissociates in water into citrate and hydronium ions. The former is a chelating agent and could be expected to uptake some of the available calcium ions from solution, removing their availability to bind alginate

chains and thus encouraging greater swelling. However, the latter will enable the protonation of carboxyl groups in the alginate backbone, promoting hydrogen bonding between the strands. From the polymer volume increase observed it seems the latter effect dominates.

Aggregation of alginates by the cationic detergent dodecyltrimethyl ammonium bromide (DTAB) has been recorded, mediated by the hydrophobic interactions between the tail and the chain.[45] This resulted in a radius of hydration decreasing linearly with the concentration of DTAB. Interestingly, this binding is insensitive to the monomer species within the polysaccharide, participating equally with M and G residues. This chemical is related to CTAB, differing only in the length of the tail (12 carbons instead of 16). If CTAB were able to involve M residues in binding this would highly increase the number of crosslinks possible in alginate and compact the gel significantly.

In summary, the addition of the nanorod solution to PNIPAM-alginate double network gels causes a clear change in their swelling ratios. The polymer volume fraction increases with the fraction of nanorod added, roughly doubling with the addition of the maximum quantity used in this study (3ml of a 15ml batch). This increase is attributed to increased binding of alginates through electrostatic and hydrogen bonding interactions, and arises due to both the nanoparticles and the extra chemicals in the supernatant.

Difference in volume swelling ratio has been exploited as a source of responsive shape changing behaviour for prints (see Naficy *et al.*[10], Studart and Erb[46]) so this result is potentially of interest. The swelling ratio for 3.0 ml of NP is 50% of that for the unmodified gel. However, this is an expensive route to achieve the outcome - similar changes in volume swelling ratio can be obtained by the simple addition of citric acid (see

Figure 5.11 5.11 above), a different percentage of alginate (see Panhuis *et al*., de Moura *et al.* [42,47]) or the addition of aluminium ions.[48] Nonetheless the effect on volume swelling ratio is significant and would make predictions of the shape change of printed samples inaccurate were it neglected.

5.4.6 RHEOLOGY OF CURED GELS WITH NANOPARTICLES

Cured gel samples were prepared using the method described in Section 4.3.3.1 and tested with the methodology described in Chapter 2, Materials and Methods. Pure alginate gels were constrained between two plates during the calcium ion curing stage to ensure a flat surface on the final sample. As this increased the linear distance for ions to diffuse to reach the centre of the sample, the time in the ion bath was increased to 48h, with the bath being refreshed at 24h. Graphs are the average of at least three samples of each composition, with the error bars representing standard error on the mean.

5.4.6.1 PNIPAM-ALGINATE WITH VARYING NANOPARTICLE CONCENTRATIONS

Amplitude oscillation sweeps were performed at a frequency of 1Hz to determine the values of the elastic and viscous moduli in the linear viscoelastic region, and the crossover point, as a function of concentration of nanoparticles. To find these first values, a line parallel to the *x*-axis was fitted to the region below 1% strain using Origin to assign the stationary value in this region and the corresponding error. ANOVA methods confirmed that at a P(0.05) significance level the data were not significantly different to the assigned fit. The crossover point location and errors were assigned by locating the lowest and highest strain values for which the error bars on the data points intersected, assigning the centre as the mean and the half-width as the error. Averaged data are presented in Figure 5.12 and key features are plotted as a function of concentration in Figure 5.13.

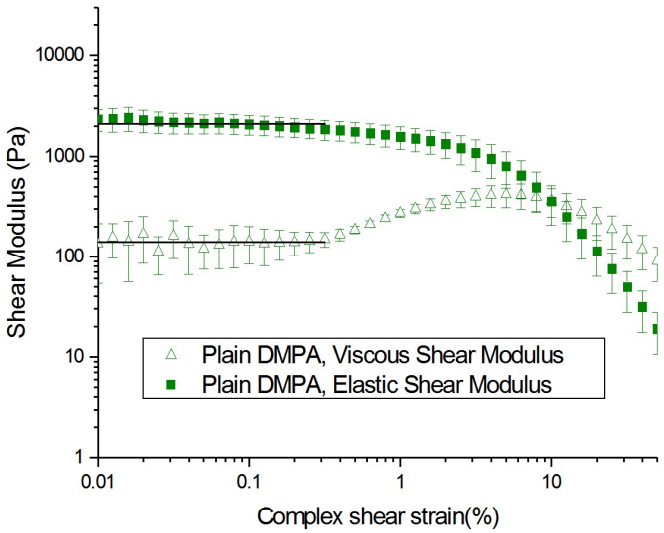

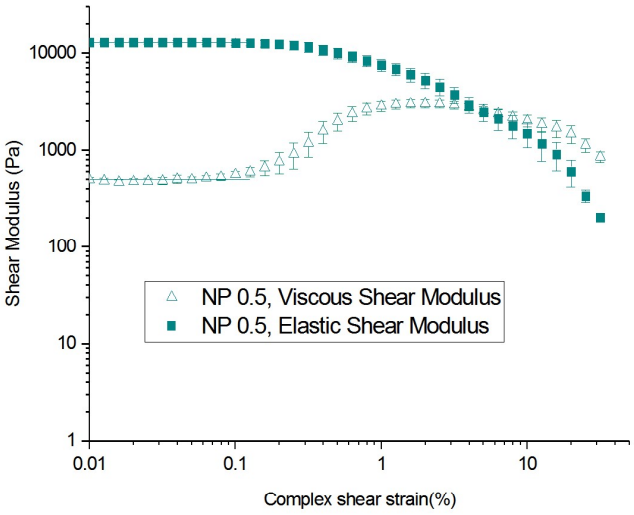

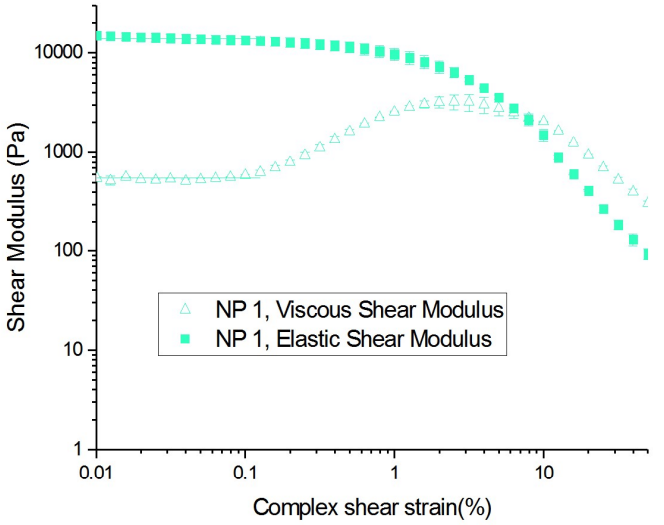

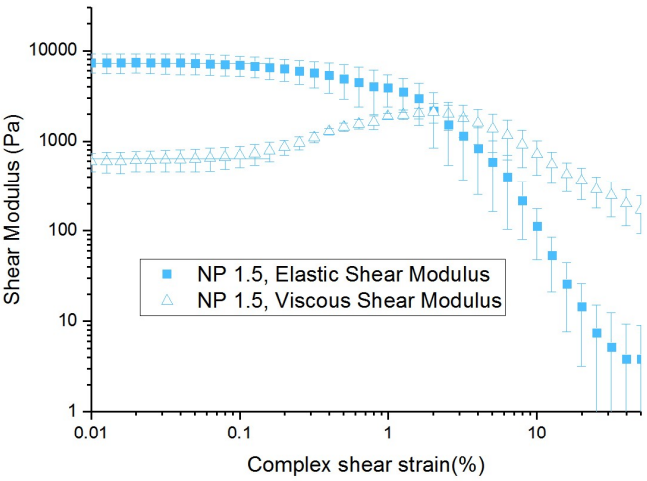

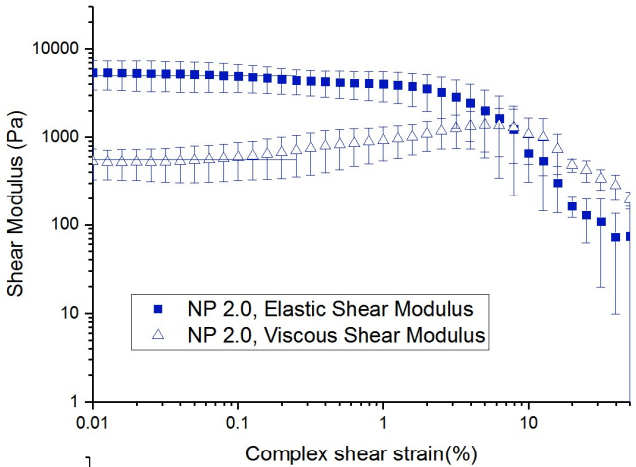

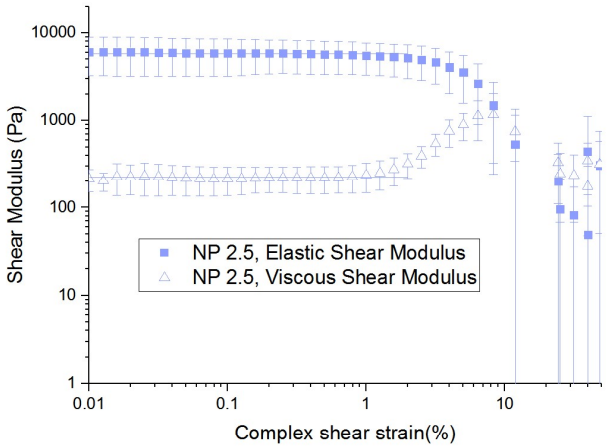

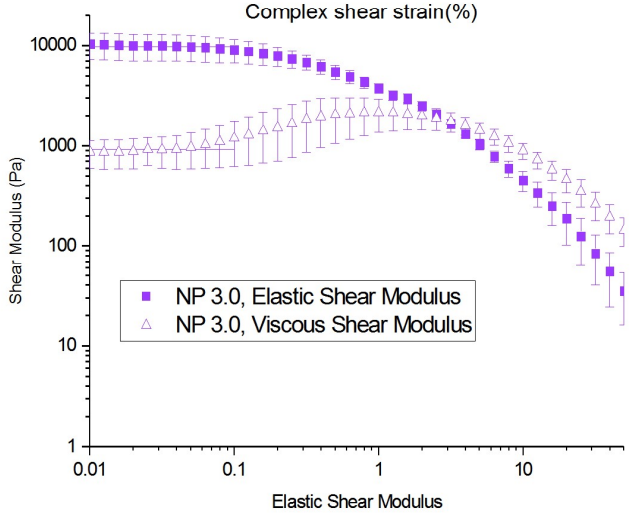

Figure 5.12. Viscoelastic behaviour as a function of strain amplitude, for gel samples with varying quantities of nanoparticles added to the double network PNIPAM-alginate gel. Samples are evaluated at a frequency of 1Hz and data shown are the average of at least three samples. Key values from these graphs are extracted and plotted as a function of concentration in Figure 5.13.

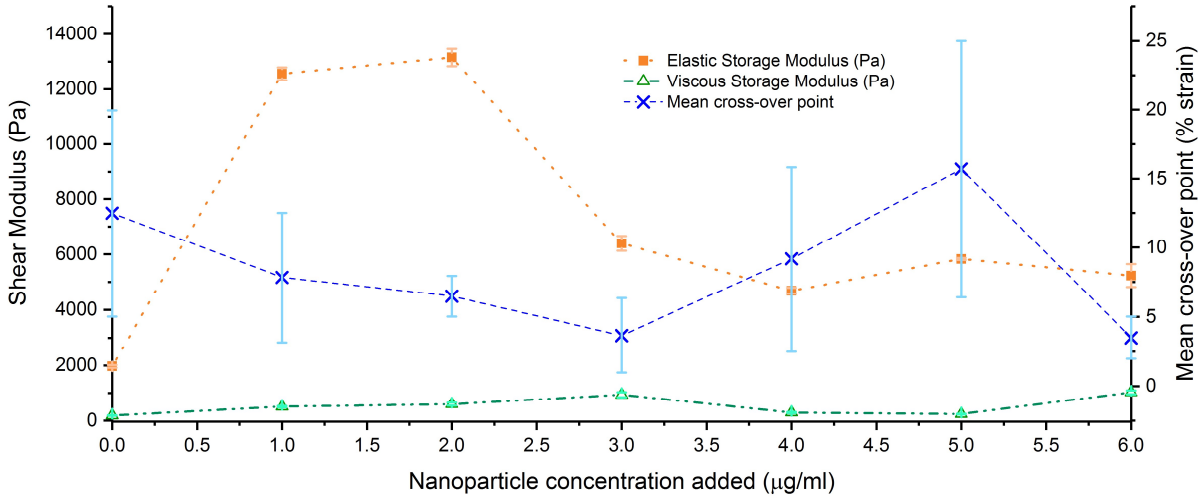

Figure 5-13 A summary of the differences in viscoelastic behaviour as a function of the concentration of gold nanorods added to PNIPAM-alginate gels. Both elastic (square) and viscous (triangle) shear moduli are plotted in the approximately linear region below 1% strain and plotted against the left-hand y-axis. The right-hand axis corresponds to the shear value at which the crossover between elastic and viscous behaviour occurs. These values are indicated with crosses. Values shown are derived from the graphs in Figure 5.12, and error bars, if not visible, are too small to be seen.

Examining the shear moduli as a function of nanoparticle concentration (Figure 5.13) the values of 1 and 2 μg/ml show an increase of at least a factor of two over the unmodified gel and increased concentrations. This non-monotonic response is surprising, as hydrogels are generally taken to exhibit mechanical properties which scale with their polymer volume fraction.[49,50] One expression of this was formulated by de Gennes:

$$E \cong Tc^{\frac{9}{4}}(v^{\frac{3}{4}}a^{\frac{3}{2}})$$

Equation 5.5.7

Here *E* is the elastic modulus (since only scaling laws are considered in the argument from which this is drawn, it applies equally to the shear and uniaxial elastic modulus), T is temperature, c concentration, v the excluded volume parameter (fixed for a given solvent and polymer combination) and a is the effective length per monomer unit. As can be seen by comparing Figure 5.10, we would thus expect an increase in shear modulus proportional to the polymer concentration to the power 9/4, which is not seen. The non-monotonic shape suggests there may be competing factors in play.

On the other hand, adding charged elements could change the alginate crosslink structure, which has its own effect upon gel performance for a fixed polymer volume fraction. Additional ions provide more sites for bonds to form around, theoretically distributing the load and making the gel stiffer. This would be expected to proceed until all available G blocks were saturated with ions. Beyond this point, further additions might reduce the Young's modulus, as has been observed by Donati *et al.* for intermediate G:M ratio alginates with increasing calcium concentrations.[51] They attributed this to the networking junction zones 'zipping' together, creating large aggregates rather than gel networks.

Varying nanoparticle concentration often results in a non-linear mechanical response, as reinforcement effects increase with weight until aggregation begins at a critical threshold. Beyond this, the elastic modulus decreases as the addition of more particles only increases the aggregate size and therefore the presence of failure initiation sites. Potentially the AuNR, being stiffer and at a larger length scale than other components, are reinforcing the system until a critical threshold. Beyond this threshold the network is disrupted rather than reinforced, as recorded by Bhattacharya *et al.*[52] However, this occurred at weight percentages of 1-5%, rather than 0.001%, the maximum recorded here.

There is also the possibility that the structure of one network directs the second, as (for example) an uncured alginate with larger aggregates could eliminate NIPAM monomers from the alginate-dense region. This would cause local phase separations and affect the degree of interpenetration between the two networks as the PNIPAM network is forming. In turn this would reduce the interfacial area between the networks and the efficacy of stress transfer between them. It has been observed for some double network hydrogels that an optimum crosslink density for one network exists, around which fracture stress declines in both directions.[53]

The crossover points have sufficiently large errors that no meaningful conclusions can be drawn. This arises from the imprecision of assigning these points, exacerbated by the large error size. One cause of the variation between samples, noticeably larger at higher strains, is slippage. While manufacturing, it was observed that the stickiness of the surfaces varied between compositions, resulting in some samples losing contact with the geometry during testing. While normal force monitoring from the instrument suggested that the results are reliable at least until 5% strain, the errors could be reduced by the use of a corrugated geometry or even sandpaper to increase grip.

5.4.6.2 PNIPAM-ALGINATE WITH CTAB AND SURFACTANTS

As mentioned in 5.3.1, the presence of citrate ions and CTAB surfactants in samples to which AuNR suspension was added may also have affected their shear response. This was tested by preparing samples with the addition of citric acid, CTAB, and both together, at the equivalent concentration which would have been incorporated by the addition of the greatest concentration AuNR used in this study. This corresponded to 0.02% wt of each (approx. 0.5mM).

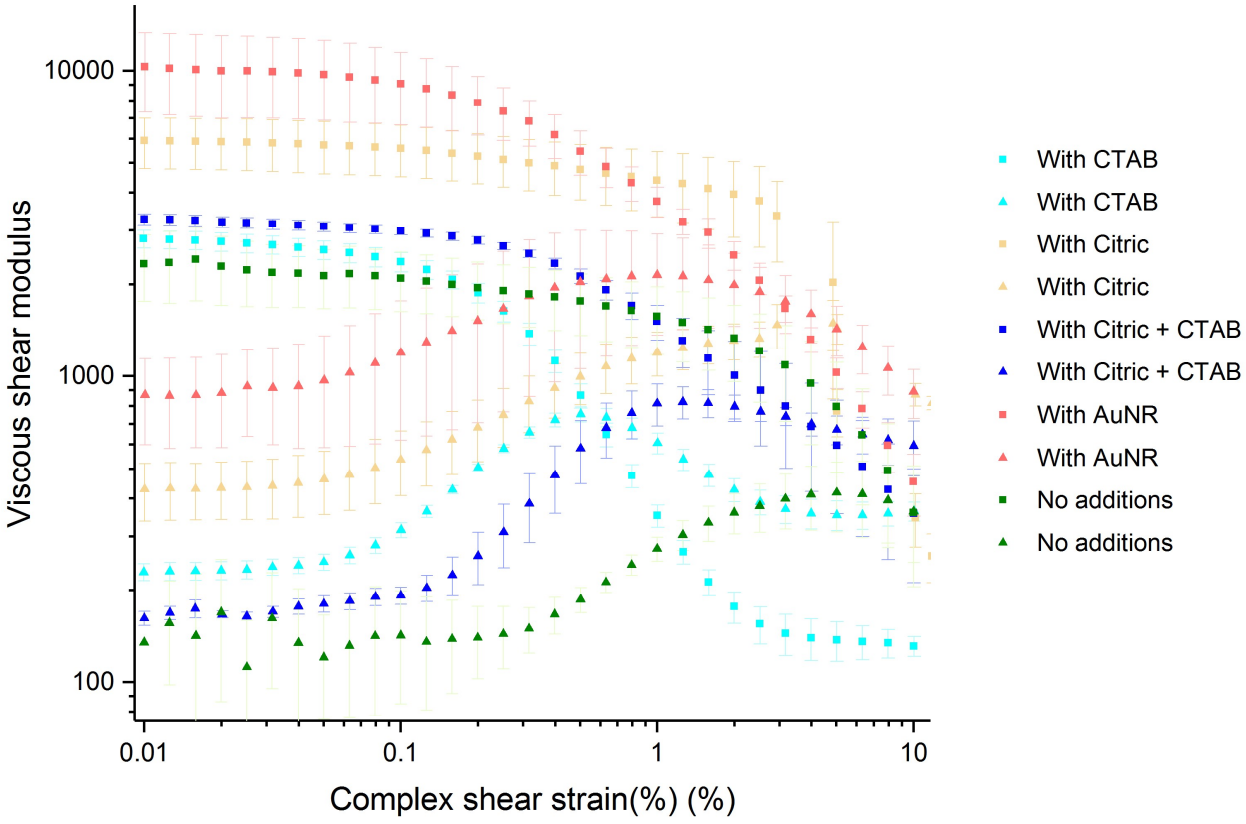

Figure 5.13. Viscoelastic behaviour as a function of strain amplitude - elastic shear modulus (squares) and viscous shear modulus (triangles) are shown. The nanoparticle solutions added (labelled with AuNR), also contains CTAB and citric acid, both of which will affect the gel. This was tested by preparing PNIPAM-alginate hydrogels with only citric acid, only CTAB, and with citric acid and CTAB added, in the absence of nanoparticles.

This graph elucidates somewhat the effects of each of the components of the nanoparticle solution. The addition of CTAB, a cationic detergent (coloured aqua on Figure 14), increases both viscous and shear moduli, and causes the crossover point where viscous effects dominate over elastic ones to shift to a lower strain. This would correspond to an increase both in the stiffness and/or number of bonds which deform elastically (represented by the elastic modulus), and in the energy required to deform the components inelastically. The fact that the

elastic contributions break down at a smaller strain than native gel suggests the bonds are less extensible. This is supported by the observations of Yang et al., who observe increases in viscosity of more dilute alginate solutions with the addition of equivalent concentrations of CTAB.[30] They attribute this to hydrogen bonding and hydrophobic interactions, whereby the CTAB molecules act as additional binding sites between the alginate polymers.

The addition of citric acid (yellow on Figure 5.13) again increases both the storage and loss moduli. Here the linear region continues to higher strains. This is likely to be due to an increase in the pH leading to protonation of carboxylate groups in the alginate backbone and increased hydrogen bonding.

However, the addition of citric acid and CTAB together (royal blue, Figure 5.13) have less effect on both shear moduli than either separately. This suggests they preferentially interact with each other rather than the polymers.

The addition of the full nanorod solution has an effect greater than either citric acid or CTAB separately, and therefore certainly more so than the combination. It can be concluded that while the changing behaviour of PNIPAM-alginate hydrogels is definitely affected by the presence of CTAB and citric acid at a 0.1% concentration in the nanoparticle solution, the presence of these elements is insufficient to explain all the effects seen.

5.4.6.3 ALGINATES WITH VARYING NANOPARTICLE CONCENTRATIONS

To clarify the effects of different system components, samples with only alginate and nanoparticles were prepared in an equivalent manner to PNIPAM-alginate samples and tested equivalently.

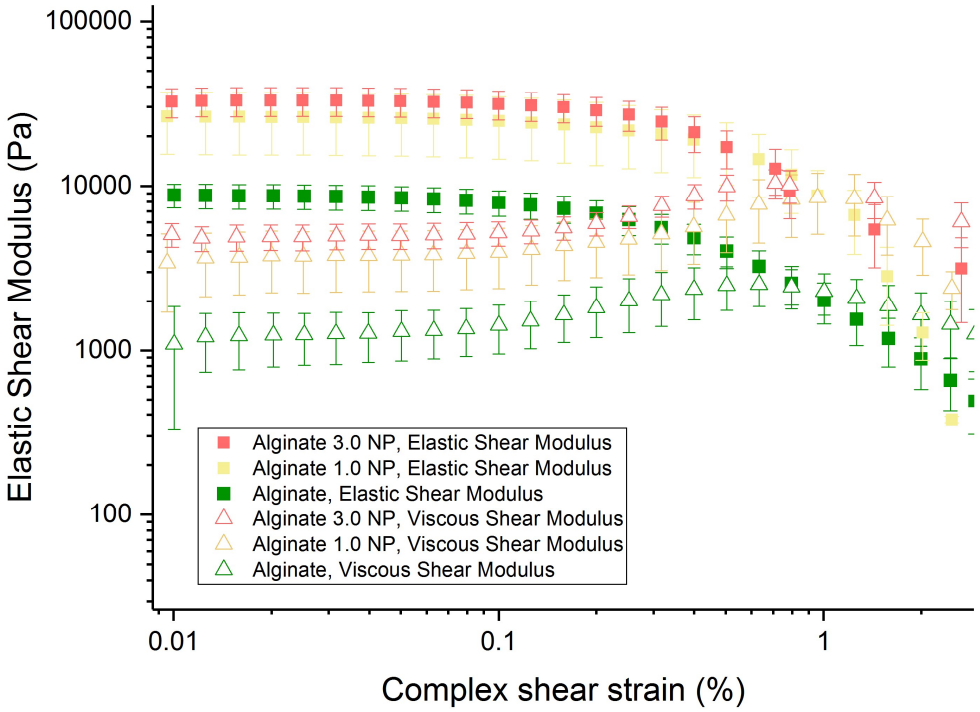

Figure 5.14. Viscoelastic response as a function of strain for alginate gels with the addition of 0, 1 or 3ml of gold nanorod suspension to the polymer blend before crosslinking – triangles are viscous, and squares, elastic, shear modulus. Overall polymer/solvent ratio was kept constant. Samples were tested at a frequency of 1Hz.

3% w/t alginate gels crosslinked with calcium chloride showed an increase in elastic shear modulus with the addition of nanoparticles. This is likely due to the positively-charged nanoparticles and CTAB in the suspension acting as additional electrostatic binding sites.

In contrast to the behaviour of PNIPAM-alginate gels of the last section, the response of pure alginate gels to nanoparticle addition did show a monotonic trend. A greater concentration of NR yielded higher elastic and viscous shear moduli in a roughly linear relationship, with the crossover points remaining fairly consistent. While it is important not to overclaim from the limited data points available, this suggests that the non-monotonic behaviour seen in the elastic shear moduli as a function of concentration is somehow related to the double network structure.

The moduli of the pure alginate samples are significantly greater – from 50% to 100% - than the equivalent PNIPAM-alginate hybrids. This could be attributed to the longer immersion time required to cure these gels (see Materials and Methods), resulting in a higher crosslink density. Alginate gels have approximately 2% higher swollen density than the PNIPAM-alginate gels, which would also be expected to increase their shear moduli.

5.4.7 COMPRESSION TESTS

The linear elastic modulus is relevant when considering the response of the material to axially applied stress. It is required to apply the Timoshenko model and to inform the development of more complex models of linear elasticity. While the Lamé equations relate elastic shear, here denoted as G, and the linear elastic modulus, E, this requires knowledge of one additional elastic constant – either the Poisson's ratio or the bulk compressibility – and additionally the assumption of isotropy. Since E is easier to measure for gels and will provide an indication of whether the material can be considered anisotropic, E was measured through compression testing.

5.4.7.1 PNIPAM-ALGINATE WITH VARYING NANOPARTICLE CONCENTRATIONS

Compression tests were performed on samples with 0, 0.5, 1, 1.5, 2, 2.5 and 3.0ml of AuNR suspension per 15ml batch. Samples were prepared as described in Materials and Methods. The force-extension data were transformed into engineering stress-strain graphs, for which examples are shown in Figure 5.15 and Figure 5.16. Complete data are provided in the appendix.

For soft materials such as hydrogels, plotting true stress and strain – which take into account the change in length and area throughout the experiment – is a more accurate representation of the forces experienced by the material during testing. This transformation was made according to the techniques described in Materials and Methods.

5.4.7.1.1 STRESS-STRAIN GRAPHS

The stress-strain curves yielded showed strain-hardening, an increase in the magnitude of stress response with increases in strain. Examples of results from a classic engineering stress-strain plot and a transformation into true strain are presented, showing the linearization effect of the latter. All strain values were negative under the true strain transformation, reflecting the compressive mode of testing. Gradient fits were performed in the region of strain magnitude less than 0.01 to obtain Young's moduli in the same strain region as rheological data.

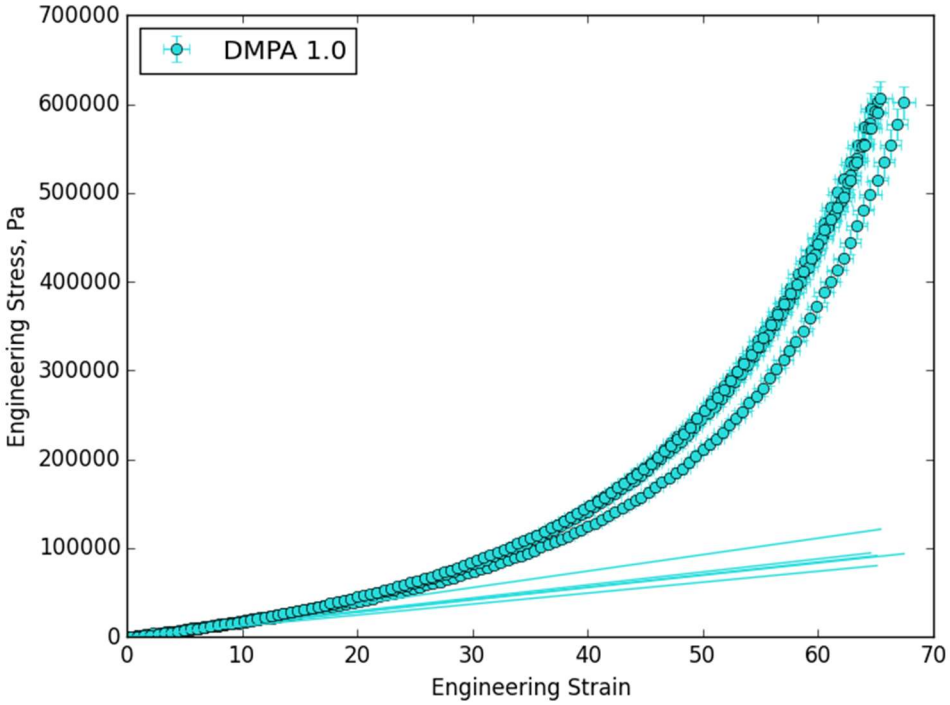

Figure 5.15. Engineering stress-strain data for PNIPAM-alginate gels with the addition of 1ml of nanoparticles, corresponding to a concentration of 2μg/ml of gold nanorods and 0.0067% by weight of CTAB and citric acid. Lines shown are linear fits to the strain region below 1%.

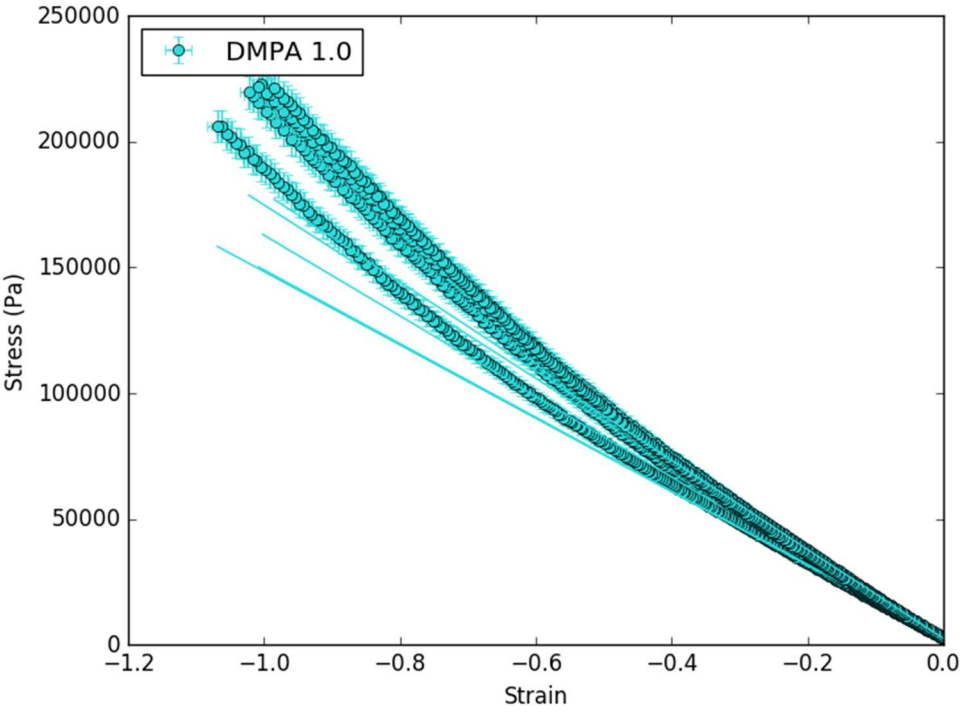

Figure 5.16. True stress-strain data for PNIPAM-alginate gels with the addition of 2.0ml of nanoparticles, corresponding to a concentration of 4μg/ml of gold nanorods and 0.02% by weight of CTAB and citric acid. Lines shown are linear fits to the strain region below 0.01.

5.4.7.1.2 LINEARIZATION OF GEL RESPONSE IN ELASTIC REGIME

Linear fitting on this region was performed as described in Materials and Methods for both engineering and true stress-strain plots.

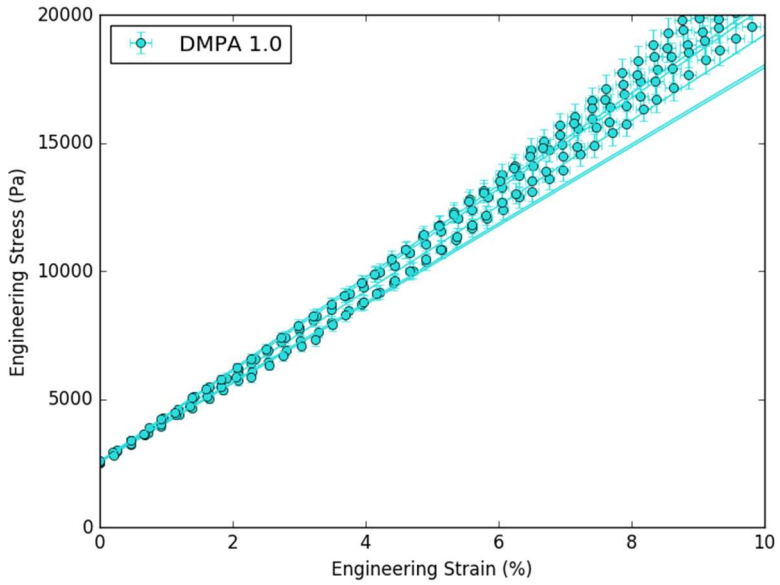

Figure 5.17. Stress-strain data below 10% strain for PNIPAM-alginate gels with the addition of 1ml of nanoparticles, corresponding to a concentration of 2μg/ml of gold nanorods and 0.0067% by weight of CTAB and citric acid. Lines shown are linear fits to the strain values below 1%, with a gradient corresponding to the Young's modulus in the elastic regime. For clarity, only alternate data points are shown.

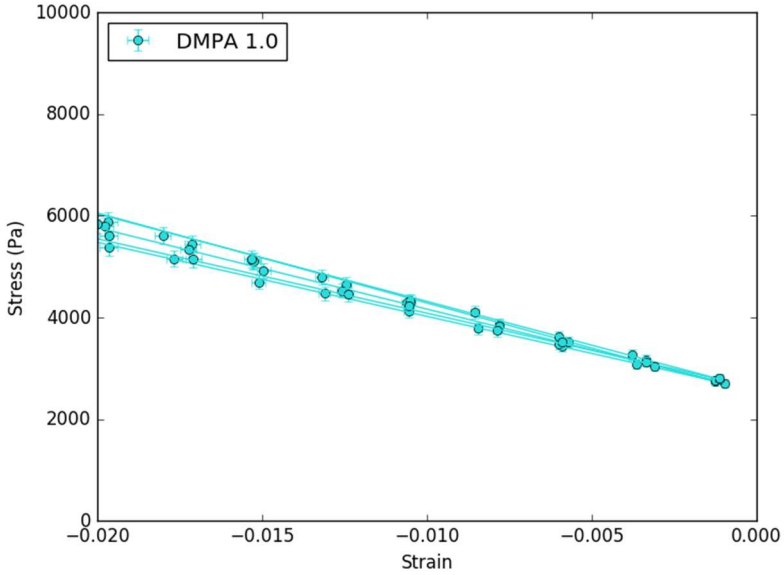

Figure 5.18. Stress-strain data below 10% strain for PNIPAM-alginate gels with the addition of 1.5ml of nanoparticles, corresponding to a concentration of 1μg/ml of gold nanorods and 0.0033% by weight of CTAB and citric acid. Lines shown are linear fits to the strain values below 1%, with a gradient corresponding to the Young's modulus in the elastic regime. For clarity, only alternate data points are shown.

The gradients extracted by this fitting, corresponding to the engineering and true Young's moduli,were plotted as a function of the volume of nanoparticle suspension added, shown in Figure 5.19. No obvious trend is seen.

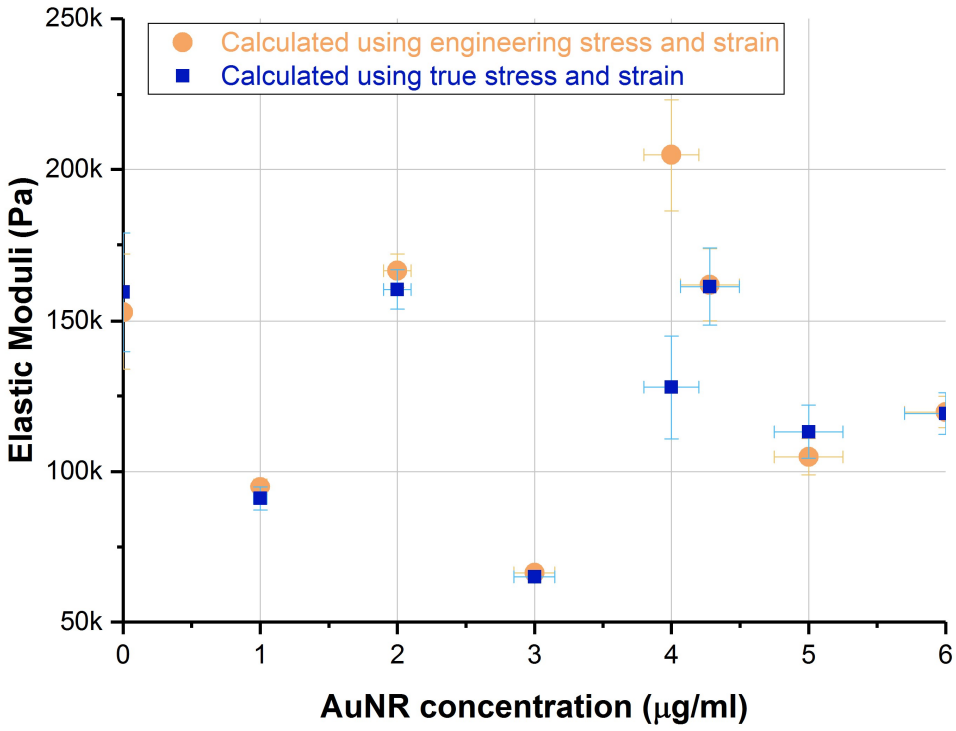

Figure 5.19. The elastic moduli extracted from the linear region below 0.01 strain during compression testing on PNIPAM-alginate gels, as a function of the concentration of gold nanorods incorporated in said gels.

However, when the variables were transformed according to the concentration scaling relationship of Equation 5.5.7 using the measured values for polymer volume fraction (proportional to concentration) from Figure 5.11, yielding Figure 5.20. For both true and engineering moduli, fitting shows a weak linear inverse correlation ($R^2 \approx 0.5$) between the adjusted elastic modulus, with a gradient of $-8 \pm 3 \times 10^6$ μg/ml·Pa.

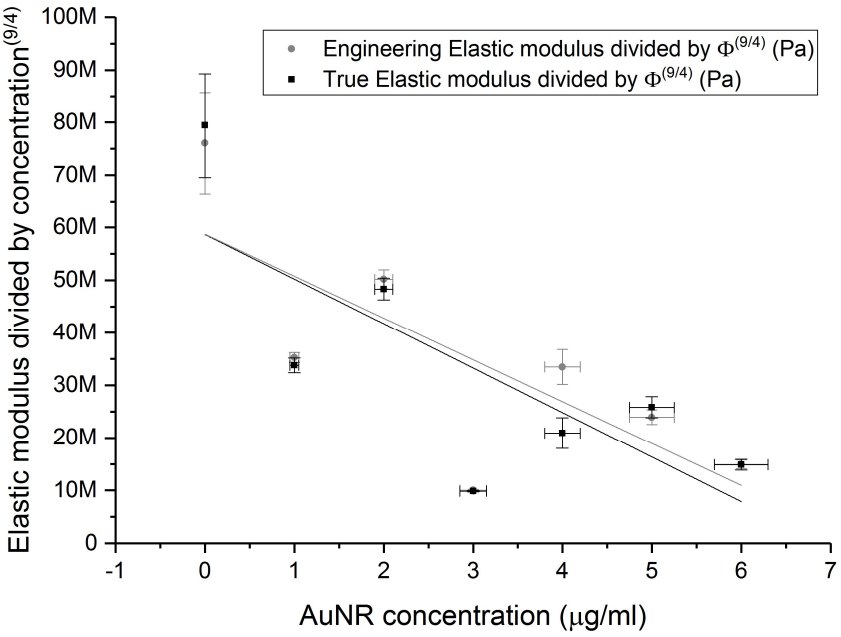

Figure 5.20. The effect of nanoparticle concentration on the uniaxial elastic modulus divided by the polymer volume fraction found previously to the power of (9/4), eliminating density effects.

While the fit is poor, it suggests there may be negative linear correlation between the concentration of nanoparticle suspension added and the elastic Young's modulus (E). This could be due to screening effects of charged species between the negative polyelectrolytes, reducing electrostatic repulsion and thus resistance to compression – a situation sketched in Figure 5.21. This would be expected to increase linearly with concentration. For both true and engineering calculations the Young's modulus is an order of magnitude larger than the elastic shear modulus, but does not reflect the characteristic hump shown by the shear modulus at concentrations of 1-2 μg/ml. Figure 5.22 shows a like-for-like comparison of the elastic moduli measured with each method, adjusted for polymer volume fraction.

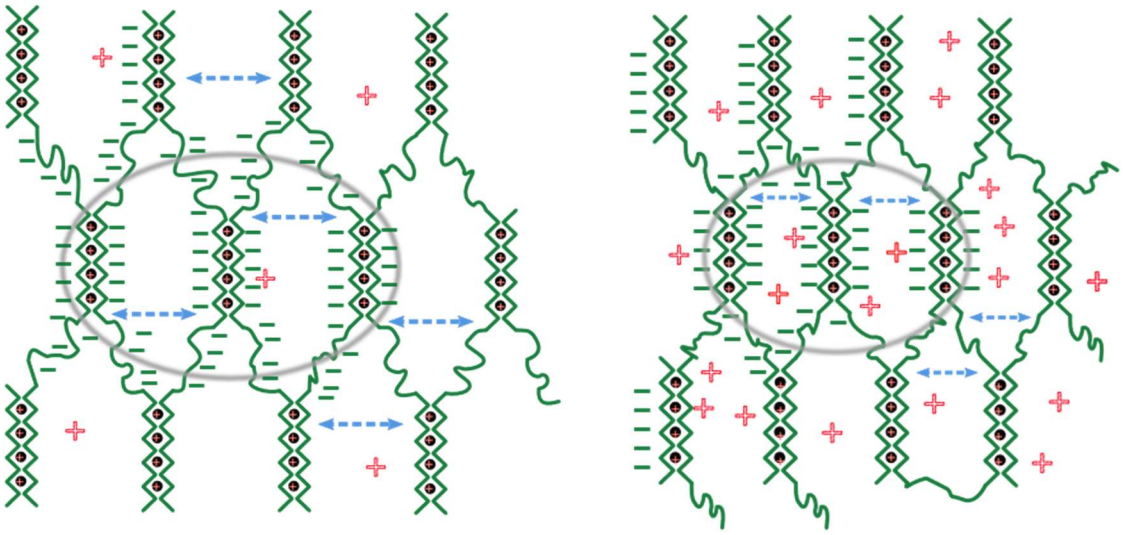

Figure 5.21. Schematic illustration of the effect of additional positive charges (red crosses) to the equilibrium spacing of an alginate network (green solid lines; straight lines represent guluronate units and bent mannuronate. Ca++ ions are black and red). In the right-hand case, the addition of more free positive charges reduces the effective negative charge experienced by the junction at the centre of the grey oval, and thus reduces the repulsion between negatively-charged polymers (represented here by blue dotted lines) relative to the left-hand case.

This contradicts both the scaling argument of equation 5.1, which should apply equally to both moduli, and the assumption that $E \approx 3G$ (shown as a dashed grey line in Figure 5.22), as discussed in section 4.4.3.5.2. All the considerations given there apply, including the possibility of the testing measuring the viscoelastic response in a different regime. Alternatively, there may be information contained about changes in material properties.

These data are intriguing, and there may be interesting results from investigating further how the direction of testing (normal or shear), the direction of strain (positive or negative) and the characteristic time of testing affect the performance of nanoparticle-laden double network hydrogel. A changing relationship between E and G suggests variation in the Poisson's ratio, which would imply a change in molecular packing.[54] Alternatively, the results may reflect some anisotropy in the material, perhaps arising from curing direction as seen in Chapter 4 or alginate junction zone compaction.

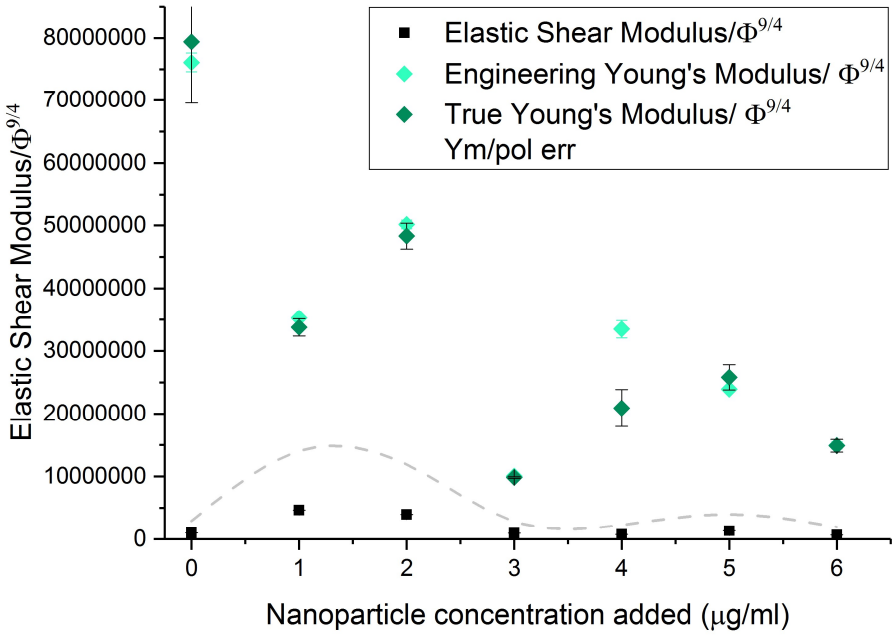

Figure 5.22. Summary of elastic shear (G) and Young's (E) modulus changes for PNIPAM-alginate gels with the addition of nanoparticles, divided by the polymer volume fraction of each gel to the power of 9/4 to adjust for polymer density.

Overall this highlights a salient point for the testing of gels – were only one testing modality, shear or compression, used, and a simple extrapolation made, this complex behaviour would not have been noted and inappropriate conclusions may have been drawn, potentially assigning a trend where none is shown, or even a trend in the opposite direction. This demonstrates the necessity of a careful consideration of testing modes, ideally matching the test method as closely as possible to the use-case to limit the extrapolation required. The use of multiple independent methods is also advantageous.

5.4.7.2 COMPARISON OF THE EFFECT OF SURFACTANT WITH THE ADDITION OF NANOPARTICLE SUSPENSION

As observed in 5.3.2, it is unclear whether the effects of the addition of nanoparticle suspension derive from the nanoparticles, the surfactant and citric acid used to passivate them and thus found in the solution, or some combination of the above. As a control, samples were generated using only the addition of surfactant, in equivalent quantities to a given nanoparticle concentration, and tested in the same manner. Results are shown in Figure 5.23. Only CTAB was included in this control, due to time limitations. Analysis of the average gradients for both sample sets in the below 1% strain region yielded values of 1200 ± 50 Pa for the compressive elastic

modulus of a 3.0ml nanoparticle/PNIPAM-alginate gel and 1050 ± 60 Pa for samples with equivalent concentration of CTAB in the gel.

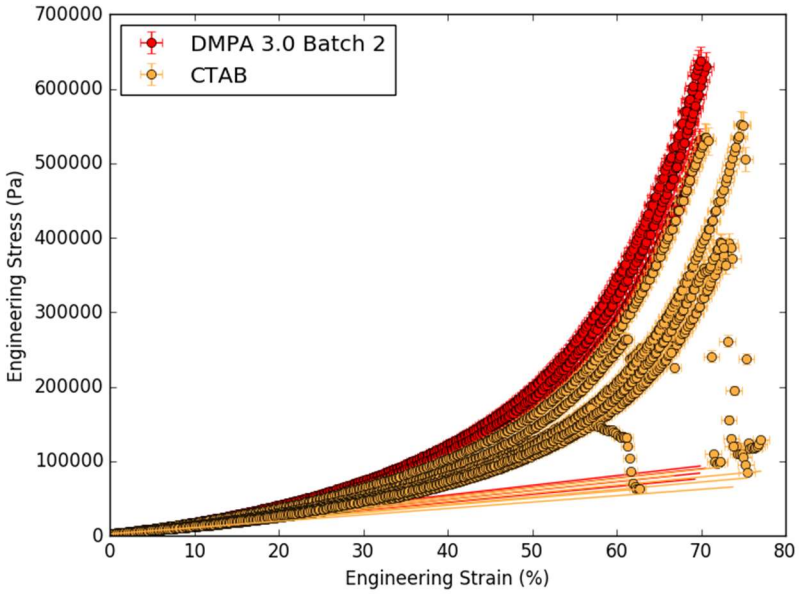

Figure 5.23. Engineering stress-strain graph for PNIPAM-alginate gels with the addition of 3.0ml of nanoparticles (red, top), corresponding to a concentration of 6μg/ml of gold nanorods and 0.02% by weight of CTAB and citric acid, and for PNIPAM-alginate gels with just 0.02% by weight of CTAB added.

This shows a decrease in Young's modulus with the addition of CTAB, corresponding to a less stiff gel. As mentioned above, this could be due to more rapid relaxation times in the AuNR gel, or a higher initial value. Comparing to Figure 5.13, the values for AuNR are a factor of 8 higher than CTAB gels, significantly larger. The data in Figure 14 also indicate a crossover point at lower strain for CTAB alone, suggesting that the component has more effect on the gels when there are no alternate components to interact with. Prior work has observed agglomeration between CTAB and alginate.[55]

This could create loops and agglomerations in the alginate around the additional netpoints introduced by CTAB, reducing the degree of interpenetration of the two networks and their ability to transmit stress.

In summation, the effect of gold nanorods and accompanying detergents and acids in solution on PNIPAM-alginate gel elastic behaviour is complex. The behaviour of hybrid gels in shear seems to have a peak elastic modulus at a concentration of 1-2μg/ml of AuNR, while compression elastic measurements showed a decrease with concentration. The lack of agreement between these measurements was perhaps due to different testing

regimes, a disparity between samples, or some changing property relating to the bulk compressibility. Discriminating between these possibilities would require further testing, potentially with a nanoindentation method.

From the variation in swelling ratio presented in 5.4.5, and the differences in shear modulus from 5.4.6, it seems possible that the addition of nanoparticle solution causes changes to the combined network structure of the two gels. This could manifest as the formation of aggregates or phase separation, a change in crosslink density or strength in either component, or a change in the geometric relationship or bonding between the networks.

The working hypothesis was that differences in the structure begin in the lightly cured blend, and then are locked in by photocrosslinking of the interpenetrating NIPAM monomer into a solid gel. Subsequent immersion in $CaCl_2$ then solidifies the remaining binding sites on the alginate strands. For insight into gel characteristics such as aggregration or network changes, small-angle X-ray scattering was used to examine the statistical distribution of junction zones, as in Stokke et al.[56]

5.4.8 SMALL ANGLE X-RAY SCATTERING

Small angle X-ray scattering (SAXS) can elucidate information about the structure of the sample at the nanometre length scale. Prior works have used SAXS to characterise the junction structure of alginates[56–58], and to explain the changes in gel structure underlying shifts in rheological behaviour.[59] Integrated data from small-angle neutron scattering and light scattering has revealed structural details in PNIPAM gels corresponding to regions of higher crosslink density, as well as the fundamental polymer parameters such as average molecular weight between crosslinks.[60]

SAXS was performed on calcium cross-linked alginate, PNIPAM, NIPAM monomer in alginate gels and fully cured PNIPAM-alginate to determine characteristic gel length scales at each stage in the gel preparation process, for comparison with those found by, for instance, swelling methods.

Double-network gels exhibit complex scattering patterns and so to provide a simpler window onto the structural changes single-network alginates with nanoparticles and surfactants added were also prepared. SAXS measurements were performed as stated in materials and methods, and data obtained were analysed and fitted with SASView.

5.4.8.1 ALGINATE GELS WITH NANOPARTICLE SOLUTION

One appropriate model for describing scattering from a gel is that of a mass fractal. This represents a structure which exhibits geometric self-similarity at different length scales. Intuitively, this matches the working picture of a gel: a sponge-like structure with pores of different sizes, or at a polymeric level, a branching tree-like structure. The extent of self-similarity is mathematically quantified by the fractal or Hausdorff dimension. This is a numerical measure of how the size of a space scales depending on the distance between points being considered: for example, for a volume with some voids, how the mass contained within measurement boxes of length r depends on the length r being considered. This relationship goes as $M(r) \propto r^{D}$, with D being the dimensionality.

Scattering from such self-similar structures is predicted to follow Porod-like behaviour.[61] This applies when the momentum transfer q (see definition in Materials and Methods) is such that correlations between surface segments and interfaces average, giving rise to an overall measure of surface roughness with a scattering intensity dependent on q^{-n}. Here n is the Porod exponent, characteristic of the scattering target and the q region. This can be generalised for structures whose character varies depending on the length scale. For length scales below l, the smallest feature size of the target, the surface appears even and classic Porod scattering is seen. Here $n = 4$. At length scales between l and the correlation length ξ, scattering detects surface structure, and $n = 6 - D$ (where D is the fractal dimension of the surface); and at length scales above ξ, the correlation length, the entire sample is probed. Here $n = -D$ for the same definition of D.[61]

The following formulation, developed by Mildner and Hall, calculates the intensity of mass fractal scattering as a function of q.[61] This is implemented in Sasview and was used to fit the alginate data shown in Figure 5.24 and Figure 5.25. Generally, scattering has the format shown in Equation 5.8:

$$I(q) = scale \times P(q)S(q) + background$$

Equation 5.8

Here, I(q) is the scattering intensity. Scale is a system dependent property which relates to sample volume, number of particles and scattering length density of particle and solvent. In this situation, it is approximately the same for all samples and is treated as a fitting parameter. P(q) is the form factor, a function of q which gives

information about the size and shape of particles. Correspondingly, S(q) is the structure factor, describing interactions between particles. In the absence of interactions, S(q) = 1. Background is the contribution from non-sample interactions: here set to a finite but small value (0.0001) as this correction is performed manually by subtracting the scattering from an empty cell before fitting data.

For this implementation of a mass fractal, the material has no well-defined shape and so the form factor is as for an ellipsoid with no preferred orientation (after Guinier)[62]:

$$P(q) = \left[\frac{3[sin(qR) - qR\,cos(qR)]}{q^3R^3}\right]^2$$

Equation 5.9

Here R is the radius of the ellipsoidal building block, corresponding to the smallest length scale of the system – below this there is no further structure.

The structure factor combines the mass fractal dimension, D_m, and the cut-off length ζ, beyond which no self-similarity is seen, in the following equation:

$$S(q) = \frac{\Gamma(D_m - 1)\zeta^{D_m-1}}{[1 + (q\zeta)^2]^{(D_m-1)/2}} \frac{\sin[(D_m - 1)\tan^{-1}(q\zeta)]}{q}$$

Equation 5.10

Here Γ is Euler's gamma function, analogous to a factorial function for non-integer values and defined for complex numbers z with a positive real as:

$$\Gamma(z) = \int_0^\infty x^{z-1}\mathrm{e}^{-x}\,\mathrm{d}x$$

Equation 5.11

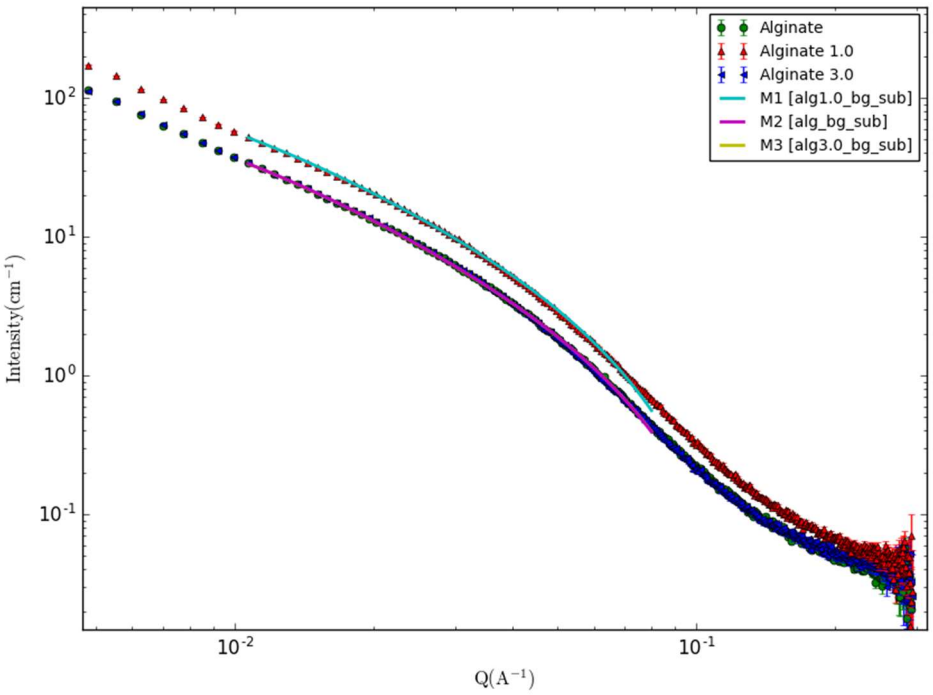

Figure 5.24. Guinier plot of scattering intensity as a function of momentum transfer for alginate gels. Shown for alginates with the addition of 1.0ml of nanoparticle solution (Alginate 1.0, red upward pointing triangles), with 3.0ml (Alginate 3.0, blue left-pointing triangles) and plain alginate (green circle. Fits describe a mass fractal model (Equation 5.8-Equation 5.11) for which parameters are given in Table 5.2

The overall shape of each scattering dataset is similar for alginates with all additives, suggesting the fractal gel structure of alginate is not significantly disrupted. Figure 5.24 suggests addition of 1.0ml of nanoparticle solution increases scattering intensity while the addition of 3.0ml has virtually no effect. This is unlikely to be due to the increased electron density due to the addition of gold, as that would cause both series to increase. It could be due to changes in the average junction size or another network parameter, which would match what is observed at a macroscale, with, for example 1.0ml having a higher shear modulus and 3.0ml having much the same as native gel.

Initial fitting of the mass fractal model to 0.01<q<0.08 for the data in Figure 5.24, presented in Table 5.2, showed fractal dimensions of 1.82±0.05 for the plain alginate network, 1.711± 0.03 for 1.0ml, 1.803±0.06 3.0ml of nanoparticle suspension, and 1.89±0.03 for the equivalent of CTAB. This value is compatible with literature values for SAXS on alginate gels which find dimensions of 1.8-2.05, attributing the higher numbers to an increase in junction zone functionality. However, the excessively small reduced χ^2 values indicated overfitting.

Composition	Scale	Error	Radius	Error	Fractal dimension	Error	Cutoff length (set)	Reduced χ^2
Alginate	0.0121	0.003	29.2	4.28	1.817	0.054	150	0.01246
Alginate 1.0	0.0224	0.003	30.9	2.59	1.711	0.03	150	0.01995
Alginate 3.0	0.0129	0.003	30.5	4.18	1.802	0.055	150	0.00703
Alginate with CTAB	0.0175	0.002	30.3	2.36	1.894	0.029	150	0.03288

Table 5.2. Mass fractal fits to SAXS data from alginate networks with added nanoparticles

Noting the similarity of the scale values and the radius, these values were fixed at 0.015 and 30 respectively, reducing the degrees of freedom. With these values fixed, and a cut-off length of 100 Å imposed, the fractal dimensions shown in Table 5.3 were obtained.

Composition	Fractal dimension	Error	Reduced χ^2
Alginate	1.81	0.003	0.46
Alginate 1.0	1.93	0.001	0.19
Alginate 3.0	1.81	0.003	0.43

Table 5.3. Mass fractal fits to SAXS data with fewer free parameters

This is compatible with the Porod models which have been fitted to alginate gels with fractal dimensions of 1.8-2.05 by Stokke et al.[56] With a reduced χ^2 of approximately order 1, this suggests this model is reasonable if coarse grained, and continues to return mass fractal values compatible with literature. The imposition of 30 Å as an approximate junction radius is plausible, corresponding to an average junction zone consisting of 7 ~4.3Å guluronate units.[63] However, the large error suggests a high degree of polydispersity, which is to be expected in this biopolymer.[63] More complex models, such as the 'broken rod' model of two unlike cylinders represented by weighted Bessel functions,[58,64] may better describe some of this variation but are beyond the scope of this work.

The values found are 1.81±0.003 for the plain alginate network and that with 3ml of nanoparticles added, increasing to 1.93±0.001 for 1.0ml of nanoparticle suspension added. The increase seen for 1.0ml is unlikely to be due to the increased electron density due to the addition of gold, because that would cause both series to

increase. The similarity between the values for alginate and alginate with 3ml of nanoparticle suspension, and dissimilarity with a 1ml addition, matches the non-monotonic trend observed in PNIPAM-alginate shear moduli and shown in Figure 5.12. While the shifts in fractal dimension are small, an increase would correspond to a higher degree of branching in the network. This would be expected if more junction zones were laterally associating, hypothesized to cause an increase in the resistance to shear by Donati.[51] With the addition of a greater amount of nanoparticles, the network is may then reach saturation and compact itself, partially losing its flexible polymeric nature.

However, this is not comparable with the shear data from alginates and nanoparticles alone (5.4.6.3), where a linear increase in elastic shear modulus accompanies an increase in nanoparticles. A potential explanation for this would be that the increase in association for PNIPAM-alginates causes larger junction zones which then have a decreased ability to transmit force between PNIPAM and alginate networks due to their relatively lower surface area. For pure alginate networks, there would be no penalty for a reduction in surface area if the strength of the single network remained consistent, and thus no decrease.

A higher degree of branching in alginates would correspond with a higher degree of porosity in the PNIPAM network, since the alginate defines the absence of PNIPAM. The addition of linear sodium alginates has been theorised to allow the more rapid transport of water from the bulk of PNIPAM hydrogels during contraction[65] – possibly the presence of a more or less branched network would have an effect on the rate of swelling and deswelling, which may explain the small enhanced thermal response seen for 1ml of AuNR in Figure 5.9.

5.4.8.2 ALGINATE GELS WITH CTAB AND SURFACTANTS

As referred to earlier, the additional chemicals present in the nanoparticle solutions could cause confounding effects. These were therefore tested separately and results are shown in Figure 5.25.

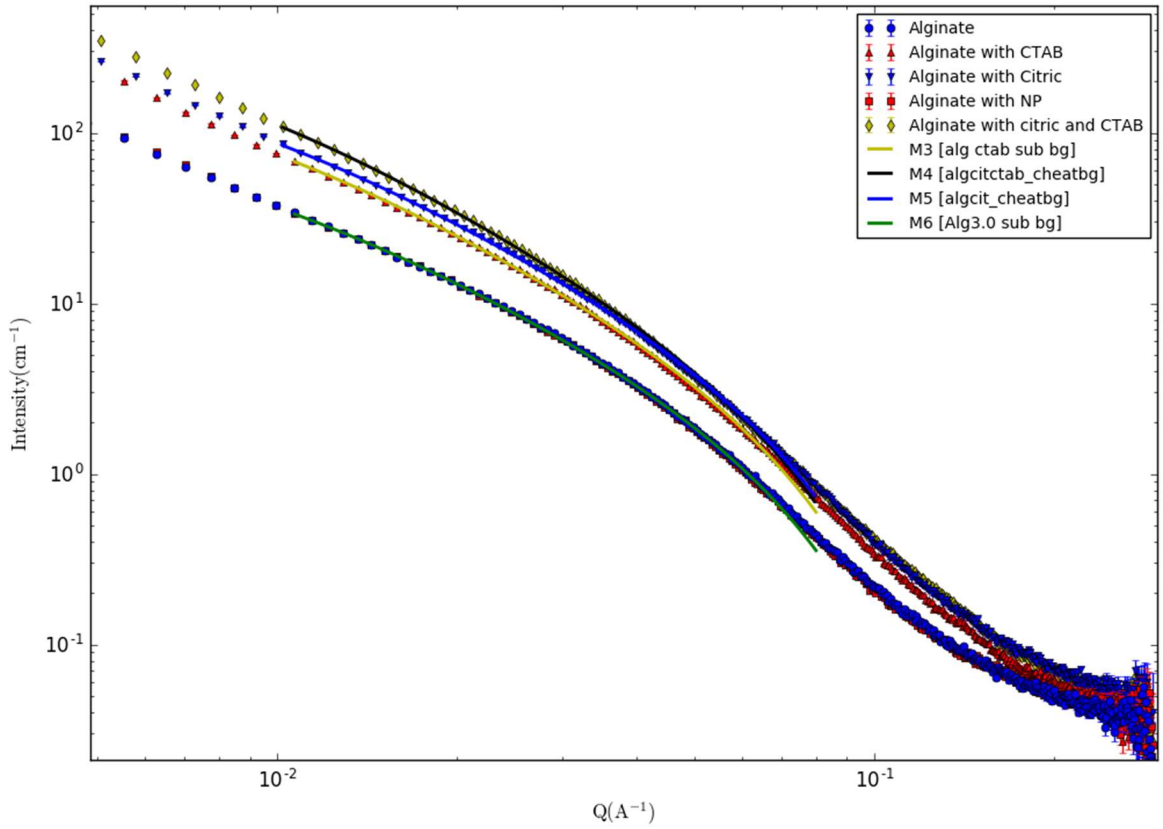

Figure 5.25. Guinier plot of scattering intensity as a function of momentum transfer for alginate gels. Shown for alginates with the addition of 0.02% wt CTAB, (Alginate with CTAB, red upward pointing triangles), 0.02%wt citric acid (Alginate with citric, blue downward-pointing triangles), 0.02% of citric and 0.02% of CTAB (yellow diamonds) and alginate with nanoparticle solution, containing both CTAB, citric and gold nanorods. (Alginate with NP, red squares). Series with NP, and plain alginate (blue circles) are virtually superimposed. Lines shown fit to a mass fractal model (equations 5.4-5.7) for which parameters are given in Table 5.4.

To control for the effect of other chemicals included in the nanoparticle suspension, the same approach was applied to scattering data of alginates with other chemicals. To enable comparison, the values for alginate and alginate with nanoparticles are reproduced here.

Composition	**Fractal dimension**	**Error**	**Reduced χ^2**
Alginate	1.81	0.003	0.46
Alginate with CTAB	1.98	0.001	0.74
Alginate with Citric	2.02	0.001	0.84

Alginate with Citric and CTAB	2.07	0.001	2.83
Alginate 3.0ml	1.81	0.003	0.43

Table 5.4. Mass fractal fits to Alginate with citric and CTAB

The fractal dimensions are again within the range observed by Stokke.[64] The addition of both citric acid and CTAB increases the fractal dimension, potentially by creating binding sites, and unlike that trend shown for swelling ratios (see Figure 5.10) the effect of both citric and CTAB seems greater than either singly. However, the fit quality is low. The higher increase in fractal dimensions could be due to the increase in hydrophobic self-interaction between alginates, and their tendency to form aggregates.[45]

Again, the result of citric and CTAB differs from that of the complete nanoparticle solution, demonstrating the role of AuNR in the observed affects.

5.4.8.3 APPROACHING PNIPAM-ALGINATE DOUBLE NETWORK GELS

PNIPAM gels measured using small angle neutron scattering (SANS) have previously been fitted with a sum of Ornestein-Zernicke functional forms.[60] This scattering function describes material-characteristic correlation lengths. Within a gel, this is related to the mass between crosslinks and the characteristic size of regions where the crosslink density is locally higher or lower. This is qualitatively different from the alginate forms shown above, and it was of interest to see the scattering characteristic of the double network gels.

Interpenetrated PNIPAM-alginate hybrid gels, crosslinked PNIPAM, alginate, and alginate interpenetrated with IPAM monomers were tested, and results shown below.

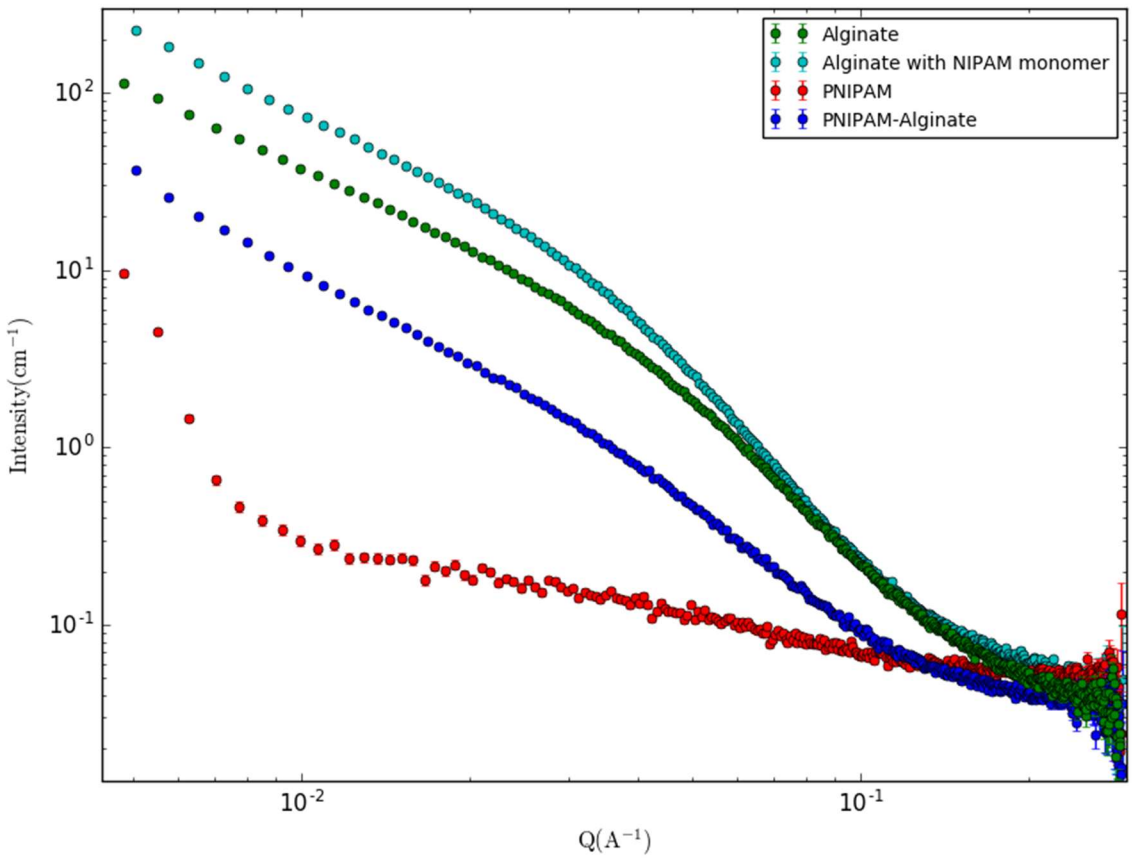

Figure 5.26. SAXS from gel samples of alginate, alginate with NIPAM monomer, PNIPAM and PNIPAM-alginate. Background scattering from the containing cell has been subtracted.

In Figure 5.26 we see that PNIPAM and alginate show wholly different and distinct scattering behaviour, corresponding to the higher 'roughness' of the alginate gel. When immersed in IPAM monomers, the alginate retains its characteristic mass-fractal structure, although there is an increase in scattering at low-q relative to alginate. This scattering region gives information about the size and shape of fundamental particles in the system and may indicate an increase in aggregation.

The NIALG model deviates from the fit generate at higher Q, and for PNIPAM-ALGINATE a mass-fractal fit is poor, suggesting that following photo-crosslinking of the second network the gel structure has fundamentally changed and is no longer adequately represented by a mass fractal description. The combined PNIPAM-alginate gel scattering data lies intermediate between PNIPAM and alginate gels. The shape of scattering data for PNIPAM is similar to previously published work reproduced in Figure 5.27.

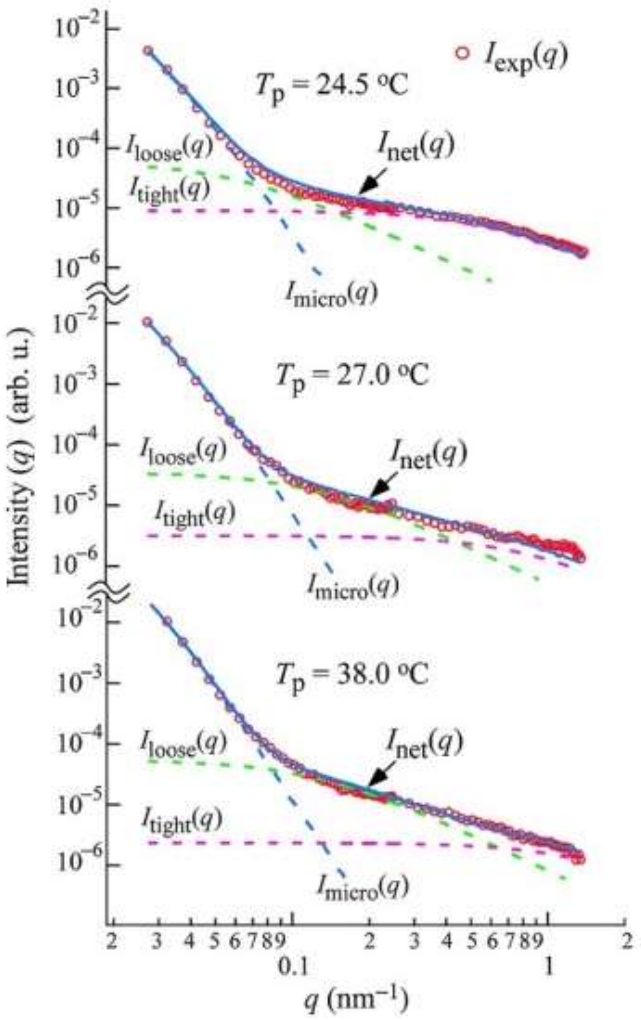

Figure 5.27. Fitting of small angle neutron scattering data from heterogenous PNIPAM gels, from Hirokawa et al. Dotted lines indicate Ornestein-Zernicke type fits, each corresponding to scattering from a different length scale in the material: the size of tightly bound regions $I_{tight}(q)$, the size of loosely bound regions $I_{loose}(q)$, the size of the constituent microgels, $I_{micro}(q)$

In summary, the scattering behaviour of PNIPAM and alginate gels are qualitatively different, and scattering from hybrid PNIPAM-alginates clearly shows a different form to alginates interpenetrated with IPAM. The addition of nanoparticles, CTAB or citric acid shows small shifts in the characteristic dimensions of a mass fractal fit to the scattering data in the Porod region, which may indicate a change in functionality of the alginate network. However, the shifts are very small and far from conclusive.

For future developments, it would be interesting to examine any potential templating effects which changes in the binding of alginate in the uncrosslinked network cause to the shape of PNIPAM gels formed. The masking effects of double network systems could be avoided by stripping the alginate from the double network gel

formed in situ with nanoparticles and comparing it to an unblended sample. This could be achieved by removing the calcium ions with a more strongly chelating agent such as ethylenediaminetetraacetic acid and soaking to remove free alginate polymers, leaving only the PNIPAM network, a suggestion made by Sarah Michel. SAXS or confocal comparisons between PNIPAM formed around alginate and PNIPAM formed around alginate with NPs would elucidate the method by which nanoparticle inclusions affect the double network gels.

5.4. CONCLUSION

In summation, the addition of gold nanorod solution at a concentration below 6 μg/ml to PNIPAM-alginate double network gels does not affect the thermal response significantly, but does cause large changes in the elastic shear modulus as measured by strain ramps at a 1Hz frequency. These changes are non-monotonic, show a peak value at a concentration of 1-2μg/ml, and are not matched by an increase in the uniaxial elastic modulus. These effects persist when adjusted for changes in the polymer volume fraction, which increases by almost a factor of two with the addition of the maximum concentration. While citric acid and cetyl trimethylammonium bromide, also present in the suspension, cause changes in the gels both in isolation and together, these are smaller than the effects of the complete solution with nanorods.

The lack of infra-red laser triggering and the small magnitude of thermal shifts, as established by DSC, are likely due to the low concentration of nanorods used. However, even for this low concentration, the effect on the mechanical properties of the gel is large, with a seven-fold increase in instantaneous elastic shear modulus. Observed decoupling between the behaviour of the elastic shear modulus and uniaxial elastic modulus demonstrates that the assumption of a linear relationship between them, common in materials analysis of hydrogels, is inappropriate in this case. The decrease in uniaxial modulus with concentration was attributed to the screening effects of charged species reducing the electrostatic repulsion between alginates.

Further investigations into the mechanism of the shear modulus increase and the swelling ratio changes were inconclusive. It is likely that competing effects are taking place in the gels. The charge on the AuNR, and the ions and surfactants in solution, will interfere with the charge-mediated formation of the alginate network which contributes much of the toughness of the hybrid gel through its energy-dissipating physical bonds. This is supported by SAXS data suggesting larger aggregates in alginate gels. This will in turn affect the porosity of the PNIPAM network, affecting diffusion rates and thermal response. The concentration of nanoparticles used in

this research is too low to have significant reinforcement effects, but could have templating effects on the formation of the gels.

Much of the complexity of this analysis arose from the poorly-characterised behaviour of alginates and the multi-component system of the nanoparticle solution. While polyelectrolytes are required for a classic double-network gel, and the low cost and abundance of alginate is appealing, using a less variable source with well-described behaviour as a composite with PNIPAM would enable separation of contributions from the double-network and the nanoparticle components. Another route to simplify the system, and separate charge contributions from those of reinforcement, examining nanoparticles with different functionalisations would be a promising direction.

While the lack of thermal response makes this method of modification unsuitable for hydrogel 4D printing, the accompanying changes in elastic properties would be important information for programming shape change in hydrogel systems or tissue engineering purposes. This suggests that, even at low concentrations, researchers should carefully assess the affect on the gel matrix of the addition of nanoparticles. Testing modalities that directly probe the mechanical characteristics needed for prediction, in the relevant time regime should be favoured, to minimize the assumptions required in obtaining the values of interest.

5.5. REFERENCES FOR THIS CHAPTER

(1) Erb, R. M.; Sander, J. S.; Grisch, R.; Studart, A. R. Self-Shaping Composites with Programmable Bioinspired Microstructures. *Nat. Commun.* **2013**, *4*, 1712. https://doi.org/10.1038/ncomms2666.

(2) DiOrio, A. M.; Luo, X.; Lee, K. M.; Mather, P. T. A Functionally Graded Shape Memory Polymer. *Soft Matter* **2011**, *7* (1), 68–74. https://doi.org/10.1039/C0SM00487A.

(3) Wu, Z. L.; Moshe, M.; Greener, J.; Therien-Aubin, H.; Nie, Z.; Sharon, E.; Kumacheva, E. Three-Dimensional Shape Transformations of Hydrogel Sheets Induced by Small-Scale Modulation of Internal Stresses. *Nat. Commun.* **2013**, *4*, 1586. https://doi.org/10.1038/ncomms2549.

(4) Shim, T. S.; Kim, S.-H.; Heo, C.-J.; Jeon, H. C.; Yang, S.-M. Controlled Origami Folding of Hydrogel Bilayers with Sustained Reversibility for Robust Microcarriers. *Angew. Chem. Int. Ed. Engl.* **2012**, *51* (6), 1420–1423. https://doi.org/10.1002/anie.201106723.

(5) Na, J.-H.; Evans, A. A.; Bae, J.; Chiappelli, M. C.; Santangelo, C. D.; Lang, R. J.; Hull, T. C.; Hayward, R. C. Programming Reversibly Self-Folding Origami with Micropatterned Photo-Crosslinkable Polymer Trilayers. *Adv. Mater.* **2015**, *27* (1), 79–85. https://doi.org/10.1002/adma.201403510.

(6) Song, K.; Lee, S. J. Pine Cone Scale-Inspired Motile Origami. *NPG Asia Mater.* **2017**, *9* (6), e389. https://doi.org/10.1038/am.2017.79.

(7) Breger, J. C.; Yoon, C.; Xiao, R.; Kwag, H. R.; Wang, M. O.; Fisher, J. P.; Nguyen, T. D.; Gracias, D. H. Self-Folding Thermo-Magnetically Responsive Soft Microgrippers. *ACS Appl. Mater. Interfaces* **2015**, *7* (5), 3398–3405. https://doi.org/10.1021/am508621s.

(8) Carias, V.; Nemati Porshokouh, Z.; Stojak Repa, K.; Alonso, J.; Srikanth, H.; Rühe, J.; Toomey, R.; Wang, J. Remotely Controlled Micromanipulation by Buckling Instabilities in Fe_3O_4 Nanoparticle Embedded Poly(*N*-Isopropylacrylamide) Surface Arrays. *ACS Appl. Mater. Interfaces* **2016**, *8* (41), 28012–28018.

https://doi.org/10.1021/acsami.6b05899.

(9) Zhang, X.; Pint, C. L.; Lee, M. H.; Schubert, B. E.; Jamshidi, A.; Takei, K.; Ko, H.; Gillies, A.; Bardhan, R.; Urban, J. J.; et al. Optically- and Thermally-Responsive Programmable Materials Based on Carbon Nanotube-Hydrogel Polymer Composites. *Nano Lett.* **2011**, *11* (8), 3239–3244. https://doi.org/10.1021/nl201503e.

(10) Naficy, S.; Gately, R.; Gorkin, R.; Xin, H.; Spinks, G. M. 4D Printing of Reversible Shape Morphing Hydrogel Structures. *Macromol. Mater. Eng.* **2017**, *302* (1), 1600212. https://doi.org/10.1002/mame.201600212.

(11) Baker, A. B.; Wass, D. F.; Trask, R. S. Thermally Induced Reversible and Reprogrammable Actuation of Tough Hydrogels Utilising Ionoprinting and Iron Coordination Chemistry. *Sensors Actuators B Chem.* **2018**, *254*, 519–525. https://doi.org/10.1016/j.snb.2017.07.095.

(12) Liu, Y.; Boyles, J. K.; Genzer, J.; Dickey, M. D. Self-Folding of Polymer Sheets Using Local Light Absorption. *Soft Matter* **2012**, *8* (6), 1764–1769. https://doi.org/10.1039/C1SM06564E.

(13) Sydney Gladman, A.; Matsumoto, E. A.; Nuzzo, R. G.; Mahadevan, L.; Lewis, J. A. Biomimetic 4D Printing. *Nat. Mater.* **2016**, *15* (4), 413–418. https://doi.org/10.1038/nmat4544.

(14) Liew, K. M.; Lei, Z. X.; Zhang, L. W. Mechanical Analysis of Functionally Graded Carbon Nanotube Reinforced Composites: A Review. *Compos. Struct.* **2015**, *120*, 90–97. https://doi.org/10.1016/J.COMPSTRUCT.2014.09.041.

(15) Ma, X.; Li, Y.; Wang, W.; Ji, Q.; Xia, Y. Temperature-Sensitive Poly(N-Isopropylacrylamide)/Graphene Oxide Nanocomposite Hydrogels by in Situ Polymerization with Improved Swelling Capability and Mechanical Behavior. *Eur. Polym. J.* **2013**, *49* (2), 389–396. https://doi.org/10.1016/j.eurpolymj.2012.10.034.

(16) Zhu, C. H.; Lu, Y.; Peng, J.; Chen, J. F.; Yu, S. H. Photothermally Sensitive Poly(N-Isopropylacrylamide)/Graphene Oxide Nanocomposite Hydrogels as Remote Light-Controlled Liquid Microvalves. *Adv. Funct. Mater.* **2012**, *22* (19).

https://doi.org/10.1002/adfm.201201020.

(17) Song, K.; Lee, S. J. Pine Cone Scale-Inspired Motile Origami. *NPG Asia Mater.* **2017**, *9* (6), e389. https://doi.org/10.1038/am.2017.79.

(18) Zeng, X.; Jiang, H. Tunable Liquid Microlens Actuated by Infrared Light-Responsive Hydrogel. *Appl. Phys. Lett.* **2008**, *93* (15), 151101. https://doi.org/10.1063/1.2996271.

(19) Pralle, A.; Prummer, M. Three-Dimensional High-Resolution Particle Tracking for Optical Tweezers by Forward Scattered Light. *Microsc. …* **1999**, *386* (November 1998), 378–386.

(20) Dong, L.; Agarwal, A. K.; Beebe, D. J.; Jiang, H. Adaptive Liquid Microlenses Activated by Stimuli-Responsive Hydrogels. *Nature* **2006**, *442* (7102), 551–554. https://doi.org/10.1038/nature05024.

(21) Xie, H.; Shao, J.; Ma, Y.; Wang, J.; Huang, H.; Yang, N.; Wang, H.; Ruan, C.; Luo, Y.; Wang, Q.-Q.; et al. Biodegradable Near-Infrared-Photoresponsive Shape Memory Implants Based on Black Phosphorus Nanofillers. *Biomaterials* **2018**, *164*, 11–21. https://doi.org/10.1016/J.BIOMATERIALS.2018.02.040.

(22) Dong, L.; Agarwal, A. K.; Beebe, D. J.; Jiang, H. Adaptive Liquid Microlenses Activated by Stimuli-Responsive Hydrogels. *Nature* **2006**, *442* (7102), 551–554. https://doi.org/10.1038/nature05024.

(23) Zhu, C.-H.; Lu, Y.; Peng, J.; Chen, J.-F.; Yu, S.-H. Photothermally Sensitive Poly(*N* -Isopropylacrylamide)/Graphene Oxide Nanocomposite Hydrogels as Remote Light-Controlled Liquid Microvalves. *Adv. Funct. Mater.* **2012**, *22* (19), 4017–4022. https://doi.org/10.1002/adfm.201201020.

(24) Nguyen, H. H.; Payré, B.; Fitremann, J.; Lauth-de Viguerie, N.; Marty, J.-D. Thermoresponsive Properties of PNIPAM-Based Hydrogels: Effect of Molecular Architecture and Embedded Gold Nanoparticles. *Langmuir* **2015**, *31* (16), 4761–4768. https://doi.org/10.1021/acs.langmuir.5b00008.

(25) Alkilany, A. M.; Nagaria, P. K.; Hexel, C. R.; Shaw, T. J.; Murphy, C. J.; Wyatt, M. D. Cellular Uptake and Cytotoxicity of Gold Nanorods: Molecular Origin of Cytotoxicity and

Surface Effects. *Small* **2009**, *5* (6), 701–708. https://doi.org/10.1002/smll.200801546.

(26) RAY, P. C.; YU, H.; FU, P. P. Toxicity and Environmental Risks of Nanomaterials: Challenges and Future Needs. *J. Environ. Sci. Heal. Part C* **2009**, *27* (1), 1–35. https://doi.org/10.1080/10590500802708267.

(27) Hribar, K. C.; Metter, R. B.; Ifkovits, J. L.; Troxler, T.; Burdick, J. A. Light-Induced Temperature Transitions in Biodegradable Polymer and Nanorod Composites. *Small* **2009**, *5* (16), 1830–1834. https://doi.org/10.1002/smll.200900395.

(28) Kokufuta, E.; Zhang, Y.-Q.; Tanaka, T.; Mamada, A. *Effects of Surfactants on the Phase Transition of Poly(JV-Isopropylacrylamide) Gel*; 1993; Vol. 26.

(29) Watson Loh, *; Luciana A. C. Teixeira, and; Lee†, L.-T. Isothermal Calorimetric Investigation of the Interaction of Poly(N-Isopropylacrylamide) and Ionic Surfactants. **2004**. https://doi.org/10.1021/JP037190V.

(30) Yang, J.; Chen, S.; Fang, Y. Viscosity Study of Interactions between Sodium Alginate and CTAB in Dilute Solutions at Different PH Values. *Carbohydr. Polym.* **2009**, *75* (2), 333–337. https://doi.org/10.1016/J.CARBPOL.2008.07.037.

(31) Scarabelli, L.; Sánchez-Iglesias, A.; Pérez-Juste, J.; Liz-Marzán, L. M. A “Tips and Tricks” Practical Guide to the Synthesis of Gold Nanorods. *J. Phys. Chem. Lett.* **2015**, *6* (21), 4270–4279. https://doi.org/10.1021/acs.jpclett.5b02123.

(32) Gómez-Graña, S.; Hubert, F.; Testard, F.; Guerrero-Martínez, A.; Grillo, I.; Liz-Marzán, L. M.; Spalla, O. Surfactant (Bi)Layers on Gold Nanorods. *Langmuir* **2012**, *28* (2), 1453–1459. https://doi.org/10.1021/la203451p.

(33) Ferhan, A. R.; Guo, L.; Kim, D.-H. Influence of Ionic Strength and Surfactant Concentration on Electrostatic Surfacial Assembly of Cetyltrimethylammonium Bromide-Capped Gold Nanorods on Fully Immersed Glass. *Langmuir* **2010**, *26* (14), 12433–12442. https://doi.org/10.1021/la101105t.

(34) and, T. K. S.; Murphy*, C. J. Self-Assembly Patterns Formed upon Solvent Evaporation of Aqueous Cetyltrimethylammonium Bromide-Coated Gold Nanoparticles of Various Shapes. **2005**. https://doi.org/10.1021/LA047488S.

(35) and, B. N.; El-Sayed*, M. A. Evidence for Bilayer Assembly of Cationic Surfactants on the Surface of Gold Nanorods. **2001**. https://doi.org/10.1021/LA010530O.

(36) Zhang, C.-L.; Cao, F.-H.; Wang, J.-L.; Yu, Z.-L.; Ge, J.; Lu, Y.; Wang, Z.-H.; Yu, S.-H. Highly Stimuli-Responsive Au Nanorods/Poly(*N* -Isopropylacrylamide) (PNIPAM) Composite Hydrogel for Smart Switch. *ACS Appl. Mater. Interfaces* **2017**, *9* (29), 24857–24863. https://doi.org/10.1021/acsami.7b05223.

(37) Ahmed, Z.; Gooding, E. A.; Pimenov, K. V.; Wang, L.; Asher, S. A. UV Resonance Raman Determination of Molecular Mechanism of Poly(*N* -Isopropylacrylamide) Volume Phase Transition. *J. Phys. Chem. B* **2009**, *113* (13), 4248–4256. https://doi.org/10.1021/jp810685g.

(38) Zhang, G. Q.; Zha, L. S.; Zhou, M. H.; Ma, J. H.; Liang, B. R. Preparation and Characterization of PH- and Temperature-Responsive Semi-Interpenetrating Polymer Network Hydrogels Based on Linear Sodium Alginate and Crosslinked Poly(N-Isopropylacrylamide). *J. Appl. Polym. Sci.* **2005**, *97* (5), 1931–1940. https://doi.org/10.1002/app.21957.

(39) Suzuki, A.; Sanda, K.; Omori, Y. Phase Transition in Strongly Stretched Polymer Gels. *J. Chem. Phys.* **1997**, *107* (13), 5179–5185. https://doi.org/10.1063/1.474880.

(40) Afroze, F.; Nies, E.; Berghmans, H. Phase Transitions in the System Poly(N-Isopropylacrylamide)/Water and Swelling Behaviour of the Corresponding Networks. *J. Mol. Struct.* **2000**, *554* (1), 55–68. https://doi.org/10.1016/S0022-2860(00)00559-7.

(41) Mao, Y.; Yu, K.; Isakov, M. S.; Wu, J.; Dunn, M. L.; Jerry Qi, H. Sequential Self-Folding Structures by 3D Printed Digital Shape Memory Polymers. *Sci. Rep.* **2015**, *5* (1), 13616. https://doi.org/10.1038/srep13616.

(42) de Moura, M. R.; Guilherme, M. R.; Campese, G. M.; Radovanovic, E.; Rubira, A. F.; Muniz, E. C. Porous Alginate-Ca2+ Hydrogels Interpenetrated with PNIPAAm Networks: Interrelationship between Compressive Stress and Pore Morphology. *Eur. Polym. J.* **2005**, *41* (12), 2845–2852. https://doi.org/10.1016/j.eurpolymj.2005.06.007.

(43) Suzuki, A.; Sanda, K.; Omori, Y. Phase Transition in Strongly Stretched Polymer Gels.

J. Chem. Phys. **1997**, *1071* (10), 1214–10003. https://doi.org/10.1063/1.474880.

(44) Fernandes, P. A. L.; Schmidt, S.; Zeiser, M.; Fery, A.; Hellweg, T.; Tanaka, T.; Fillmore, D. J.; Pelton, R. H.; Chibante, P.; Kumar, A.; et al. Swelling and Mechanical Properties of Polymer Gels with Cross-Linking Gradient. *Soft Matter* **2010**, *6* (15), 3455. https://doi.org/10.1039/c0sm00275e.

(45) Ren, B.; Gao, Y.; Lu, L.; Liu, X.; Tong, Z. Aggregates of Alginates Binding with Surfactants of Single and Twin Alkyl Chains in Aqueous Solutions: Fluorescence and Dynamic Light Scattering Studies. *Carbohydr. Polym.* **2006**, *66* (2), 266–273. https://doi.org/10.1016/J.CARBPOL.2006.03.012.

(46) Studart, A. R.; Erb, R. M. Bioinspired Materials That Self-Shape through Programmed Microstructures. *Soft Matter* **2014**, *10* (9), 1284–1294. https://doi.org/10.1039/c3sm51883c.

(47) Panhuis, M. in het; Bakarich, S.; Beirne, S. T.; Wallace, G. G.; Spinks, G. M. Extrusion Printing of Ionic-Covalent Entanglement Hydrogels with High Toughness.

(48) Zheng, W. J.; An, N.; Yang, J. H.; Zhou, J.; Chen, Y. M. Tough Al-Alginate/Poly(N-Isopropylacrylamide) Hydrogel with Tunable LCST for Soft Robotics. *ACS Appl. Mater. Interfaces* **2015**, *7* (3), 1758–1764. https://doi.org/10.1021/am507339r.

(49) de Gennes, P.-G. *Scaling Concepts in Polymer Physics*, 1st ed.; Cornell University Press: London, 1979.

(50) Doi, M. *Soft Matter Physics*; OUP Oxford, 2013.

(51) Ivan Donati, *,†; Synnøve Holtan, †; Yrr A. Mørch, †; Massimiliano Borgogna, ‡; Mariella Dentini, § and; Skjåk-Bræk†, G. New Hypothesis on the Role of Alternating Sequences in Calcium−Alginate Gels. **2005**. https://doi.org/10.1021/BM049306E.

(52) Bhattacharya, S.; Srivastava, A.; Pal, A. Modulation of Viscoelastic Properties of Physical Gels by Nanoparticle Doping: Influence of the Nanoparticle Capping Agent. *Angew. Chemie Int. Ed.* **2006**, *45* (18), 2934–2937. https://doi.org/10.1002/anie.200504461.

(53) Tanaka, Y.; Kuwabara, R.; Na, Y. H.; Kurokawa, T.; Gong, J. P.; Osada, Y.; Yoshimi

Tanaka, †; Rikimaru Kuwabara, ‡; Yang-Ho Na, ‡; Takayuki Kurokawa, ‡; et al. Determination of Fracture Energy of High Strength Double Network Hydrogels. *J. Phys. Chem. B* **2005**. https://doi.org/10.1021/jp0500790.

(54) Greaves, G. N.; Greer, A. L.; Lakes, R. S.; Rouxel, T. Poisson's Ratio and Modern Materials. *Nat. Mater.* **2011**, *10* (11), 823–837. https://doi.org/10.1038/nmat3134.

(55) Koji Mitamura, †; Toyoko Imae, *,‡; Nagahiro Saito, † and; Osamu Takai*, §. 'Fabrication and Structure of Alginate Gel Incorporating Gold Nanorods. **2007**. https://doi.org/10.1021/JP076755A.

(56) Draget, K. I.; Stokke, B. T.; Yuguchi, Y.; Urakawa, H.; Kajiwara, K. Small-Angle X-Ray Scattering and Rheological Characterization of Alginate Gels. 3. Alginic Acid Gels. *Biomacromolecules* **2003**, *4* (6), 1661–1668. https://doi.org/10.1021/bm034105g.

(57) Draget, K. I.; Stokke, B. T.; Yuguchi, Y.; Urakawa, H.; Kajiwara, K. Small-Angle X-Ray Scattering and Rheological Characterization of Alginate Gels. 3. Alginic Acid Gels. *Biomacromolecules* **2003**, *4* (6), 1661–1668. https://doi.org/10.1021/bm034105g.

(58) Yuguchi, Y.; Hasegawa, A.; Padoł, A. M.; Draget, K. I.; Stokke, B. T. Local Structure of Ca2+ Induced Hydrogels of Alginate–Oligoguluronate Blends Determined by Small-Angle-X-Ray Scattering. *Carbohydr. Polym.* **2016**, *152*, 532–540. https://doi.org/10.1016/J.CARBPOL.2016.07.020.

(59) Draper, E. R.; Su, H.; Brasnett, C.; Poole, R. J.; Rogers, S.; Cui, H.; Seddon, A.; Adams, D. J. Opening a Can of Worm(-like Micelle)s: The Effect of Temperature of Solutions of Functionalized Dipeptides. *Angew. Chemie Int. Ed.* **2017**, *56* (35), 10467–10470. https://doi.org/10.1002/anie.201705604.

(60) Hirokawa, Y.; Okamoto, T.; Kimishima, K.; Jinnai, H.; Koizumi, S.; Aizawa, K.; Hashimoto, T. Sponge-like Heterogeneous Gels: Hierarchical Structures in Poly(*N* -Isopropylacrylamide) Chemical Gels As Observed by Combined Scattering and Confocal Microscopy Method. *Macromolecules* **2008**, *41* (21), 8210–8219. https://doi.org/10.1021/ma800518t.

(61) Mildner, D. F. R.; Hall, P. L. Small-Angle Scattering from Porous Solids with Fractal

Geometry. *J. Phys. D. Appl. Phys.* **1986**, *19* (8), 1535–1545. https://doi.org/10.1088/0022-3727/19/8/021.

(62) Guinier, A. La Diffraction Des Rayons X Aux Très Petits Angles : Application à l'étude de Phénomènes Ultramicroscopiques. *Ann. Phys. (Paris).* **1939**. https://doi.org/10.1051/anphys/193911120161.

(63) Atkins, E. D. T.; Nieduszynski, I. A.; Mackie, W.; Parker, K. D.; Smolko, E. E. Structural Components of Alginic Acid. II. The Crystalline Structure of Poly-?-L-Guluronic Acid. Results of X-Ray Diffraction and Polarized Infrared Studies. *Biopolymers* **1973**, *12* (8), 1879–1887. https://doi.org/10.1002/bip.1973.360120814.

(64) Yuguchi, Y.; Urakawa, H.; Kajiwara, K.; Draget, K. I.; Stokke, B. T. Small-Angle X-Ray Scattering and Rheological Characterization of Alginate Gels. 2. Time-Resolved Studies on Ionotropic Gels. *J. Mol. Struct.* **2000**, *554* (1), 21–34. https://doi.org/10.1016/S0022-2860(00)00556-1.

(65) Zhang, G.-Q.; Zha, L.-S.; Zhou, M.-H.; Ma, J.-H.; Liang, B.-R. Rapid Deswelling of Sodium Alginate/Poly(N-Isopropylacrylamide) Semi-Interpenetrating Polymer Network Hydrogels in Response to Temperature and PH Changes. *Colloid Polym. Sci.* **2005**, *283* (4), 431–438. https://doi.org/10.1007/s00396-004-1172-6.

6. OVERALL CONCLUSIONS AND FURTHER WORK

This thesis sought to improve the accessibility of 3D printing materials that change their shape in response to temperature, with a view to increasing the speed of technological developments and the ability to replicate scientific findings. Challenges were identified as the use of proprietary, high-cost technologies and materials and a limited palette of ways to create the anisotropic properties required. The thermoresponsive double-network hydrogel PNIPAM-alginate was selected as a printable smart material, resilient to testing and with much potential for modification.

An open-source 3D printer with UV curing capacity and chilled operating temperatures was developed. While lower in resolution, it is significantly lower cost – by a factor of between 5 and 1000 – than commercial systems with equivalent capabilities. As a result of this and appropriate licencing and documentation, it can be readily accessed, customised and improved by any interested parties. In this way, accessibility and reproducibility are improved.1,2

The UV curing capability of this printer created gradations in ambient swelling and thermoresponse withi printed PNIPAM-alginate pieces, using a previously undocumented phenomenon. This manifests as a difference in contraction and swelling between the directly illuminated face of the printed piece and the unilluminated - but still cured – side. Pieces initially printed flat therefore take on curvature both at ambient equilibrium and at maximum thermal contraction. The direction of curvature in either condition varies depending on the thickness of the piece. This method of creating gradation and bending is easy, rapid, one-step with the printer developed in this work, and requires no preparation of masks or moulds, all of which are necessary for other documented methods of creating curved gels.[3,4] The cause of the effect remains unknown but an osmotic gradient towards the first areas to polymerise is suggested.

Finally, a second approach to varying the properties of PNIPAM-alginate gel, this time with the addition of gold nanorods, was attempted. It was found that the maximum concentration of nanorods added (6μg/ml) was insufficient to create laser-induced heating. However, this very low concentration did increase the thermal transition temperature somewhat and reduce the swelling ratio of the gel at ambient temperature. The shear elastic modulus increased for a dose of 1-2μg/ml, decreasing for higher concentrations, while the Young's modulus decreased linearly. While not a cost-effective method of generating anisotropy, this shows that as little

as one part per million of gold nanorods can significantly affect mechanical properties of the hydrogel matrix surrounding them. This fact could be relevant for future workers interested in nanoparticle/hydrogel composites, such as those developing nanoparticle-enhanced responsive actuators or reinforced hydrogels.[5–8] This could also be relevant when developing synthetic tissues or hydrogel drug delivery, where stiffness affects cell interactions.[9,10]

In the section following, the three topics of work will be addressed separately in terms of outstanding questions and high-priority next steps.

6.1. OUTSTANDING QUESTIONS AND RESEARCH PRIORITIES

6.1.1. AN OPEN-SOURCE UV-CURING EXTRUSION 3D PRINTER

The printer developed uses an open-source printer body design, hardware and firmware, with open source syringes, connectors, and custom LED illumination integrated with the 3D printer electronics. The printer is capable of processing PNIPAM-alginate with a resolution of ± 0.25mm and to a maximum print size of 40mm diameter and 5mm height. Details for the printer parts are available on GitHub (https://github.com/MxEntropic/protea-parts) . More detailed documentation to assist others in assembling the system would be desirable, potentially by uploading to the Instructables website (run by Autodesk) as practiced by Marzo et al. to accompany their paper.[11,12]

The priority for future development is improving sample reproducibility. For this, even, well-defined illumination is the first requirement. This could be achieved using a more complex focusing element and collimator for the UV source, possibly shifting the beam to be offset from the needle location on the print-head to remove obstruction. The intensity and size of the UV illumination should be characterised, and when the source is better-defined and even curing prints. This should allow better definition of the bending properties of printed objects and provide a more reliable data set to model the deformation behaviour of the gels. This will enable investigation of the next development.

6.1.2. LIGHT-INDUCED GRADIENTS IN PNIPAM-ALGINATE PRINTS

The source of the observed curvature in PNIPAM-alginate prints is currently unknown, although it clearly has a dependency on sample thickness and illumination direction. This shows promise due to the interest in gradated systems,[13–15] and the ease of the technique compared to templated approaches. [1–4] Further investigation requires both microscale materials testing to establish the basis of the phenomenon and more precise definition of macroscale bending behaviour to achieve desired shape-change.

Work must first focus on probing into the origin of the effect. Confocal microscopy showed promise as a technique. Comparison of horizontal sections from different layers of a thick sample coupled with automated image processing to process a large number of pores seems to be the most efficient way to test for differences in porosity. Atomic force microscopy imaging of the local Young's moduli throughout the sample could also prove informative.[16] The aim of this work would be to correlate the mechanical properties of the gels as produced with the print conditions used and the final equilibrium configuration.

At this stage it would also be interesting to explore the bimodal pore distribution observed: is this unique to PNIPAM-alginate, or present in all PNIPAM samples if examined appropriately? How is it affected by the conditions of fabrication and what effect do the pores have on the mechanical and chemical properties of the material? The answers could have implications for those working with PNIPAM.[5,6]

A microscopic understanding of gel properties would inform investigation into the mechanism by which the gradient is introduced, and therefore requirements for the improvement of print quality. As mentioned in Chapter 3, the theory about osmotic swelling could be tested using an osmometer. If this is the case, humidity control should improve reproducibility.

Once sample production processes are refined, generation of more beam samples and samples with off-perpendicular illumination to investigate helical curling could follow, hopefully with reduced errors. The data thus generated would clarify the behaviour to be matched by theory.

To be useful in printing shapes with desired equilibrium configurations, a model of the shape-changing behaviour is required. Some work based on the Föppl–von Kármán equations of continuum elasticity has been done with

the kind assistance of Joshua Robinson.[7] This suggests that the addition of an expression of a thermally sensitive gradient to the equations of elasticity for a thin plate should produce a modification to the curvature term within the total elastic energy – a promising start which matches observations so far. This makes predictions for both 1D and 2D cases and could be compared to the behaviour of beams and discs with varying aspect ratios. If further data suggests more complex behaviour than described by this formalism, finite element analysis such as that used by Zhang, Breger and co-workers [17,18] may be necessary to understand the behaviour.

If the osmotic gradient theory is correct, swelling rates could be adjusted independently of thickness by modulating the time allowed for diffusion to take place, improving the diversity of final shapes available. A lower intensity curing dose for a thicker layer would allow greater solvent transport time and permit independent choices of curvature and thickness. Varying only curing dose and time could potentially lead to results similar to those of Na *et al.*[4] The curved shapes thus generated are of interest not only to the engineer, but to the mathematician, to inform and test understanding of elastic and geometric theories.[19]

Long term, the use of curing as a variable in hydrogel printing could provide a route to tailoring not only the shape, but the physical properties within a volume. Perhaps a matrix defining the swelling ratio required for each voxel of a print could be included in the 3D model sent to a slicer, and the print produced could vary dynamically in properties the way current prints vary in shape. This could have applications for technologies such as 'morphological computation' in soft robots, where intelligent navigation of obstacles arises naturally due to the mechanical properties of the robot body.[20,21]

6.1.3. GOLD NANOPARTICLE ADDITIVES IN PNIPAM-ALGINATE GELS

The work done investigating the effect of low concentrations of nanoparticles on PNIPAM-alginate yields information on the subtle effects of even small amounts of additive on the double-network gels, which can be detrimental to the desired outcome. While a general trend of the addition of nanoparticles disrupting electrostatic interaction is shown, many outcomes are complex, potentially reflecting effects on the polymerisation and crosslinking of both networks.

Further insight into the interaction between gold nanorods and P/NIPAM-alginate at multiple stages during the formation of the gel would clarify the process. This could be enabled by staged examination of the gels

throughout the manufacturing process using a combination of rheological observations and confocal microscopy as demonstrated successfully in the earlier chapter.

Preliminary work on three-stage shear rebuilding protocols conducted on NIPAM-alginate blends with the addition of citric acid, CTAB and various concentrations of nanoparticles shows differences between the compositions. For all, rebuild rate shows the interesting two-stage phenomenon, but the rate of rebuilding – related to inter-molecular forces and structure – varies. Some preliminary analysis has been done on this data, using Python to find the amplitude decay envelope and detect the time values for each stage. These are well fitted by exponential curves and show differences between formulations.

However, relating this behaviour to physical interactions is challenging as there are many potential microscopic explanations for the behaviour. A simple first step would be to run the measurements on alginic acid with the sodium ions removed as much as possible and note if both stages still persist: if one disappears or decreases significantly, this lends weight to the theory that the stages represent chelation of ions and formation of hydrogen bonds respectively. Alternatively, the two stages could represent initial formation of small networks which then extend until they join, or an entirely different phenomenon could be at work. To assess the validity of these theories, measurements could be complemented by molecular dynamics, taking an approach similar to Bauer and Bauer[22] to examine the network development and to Hecht and Srebnik[23] to look into ionic and hydrogen bonding. Thanks are due to Professor Hamerton for this suggestion.

As in the previous section, some salient lessons were learnt about appropriate methods for hydrogel analysis, focusing on the importance of matching viscoelastic regime and hydration levels.

6.2. SUMMARY

In conclusion, this work completely documents a new, simple way of shaping PNIPAM-alginate. While many questions remain unanswered about the origin and variables affecting this phenomenon, the ease of inducing the effect coupled with the availability of the system for reproducing it place it as a useful tool for those working on responsive soft materials. Additional insights into the sensitivity of PNIPAM-alginate to mixing order and the addition of micrograms per millilitre of nanoparticles may prove useful to researchers working with these and

similar materials. The importance of methodological choice and parameters when working with such sensitive, variable materials is highlighted throughout.

The same sensitive nature which makes thermally responsive hydrogels appealing as a technology – they can be easily driven out of equilibrium, a requirement both for adaptive technology – makes them complicated to predict. However, engineering with soft, responsive materials has potential for making the synthetic world more compatible with the natural world. This is a small contribution to bringing a flexible, adaptable future a little closer.

6.3. REFERENCES

(1) Pearce, J. M. The Case for Open Source Appropriate Technology. *Environ. Dev. Sustain.* **2012**. https://doi.org/10.1007/s10668-012-9337-9.

(2) Stark, P. B. Before Reproducibility Must Come Preproducibility World-View. *Nature*. 2018. https://doi.org/10.1038/d41586-018-05256-0.

(3) Yoon, C.; Xiao, R.; Park, J.; Cha, J.; Nguyen, T. D.; Gracias, D. H. Functional Stimuli Responsive Hydrogel Devices by Self-Folding. *Smart Mater. Struct.* **2014**, *23* (9), 094008. https://doi.org/10.1088/0964-1726/23/9/094008.

(4) Na, J.-H.; Bende, N. P.; Bae, J.; Santangelo, C. D.; Hayward, R. C.; Ionov, L.; Kempaiah, R.; Nie, Z.; Studart, A. R.; Erb, R. M.; et al. Grayscale Gel Lithography for Programmed Buckling of Non-Euclidean Hydrogel Plates. *Soft Matter* **2016**, *12* (22), 4985–4990. https://doi.org/10.1039/C6SM00714G.

(5) Lee, W.-F.; Tsao, K.-T. Effect of Silver Nanoparticles Content on the Various Properties of Nanocomposite Hydrogels by in Situ Polymerization. *J. Mater. Sci.* **2009**, *45* (1), 89–97. https://doi.org/10.1007/s10853-009-3896-7.

(6) Gou, M.; Qu, X.; Zhu, W.; Xiang, M.; Yang, J.; Zhang, K.; Wei, Y.; Chen, S. Bio-Inspired Detoxification Using 3D-Printed Hydrogel Nanocomposites. *Nat. Commun.* **2014**, *5*, 3774. https://doi.org/10.1038/ncomms4774.

(7) Daniel-da-Silva, A. L.; Carvalho, R. S.; Trindade, T. Magnetic Hydrogel Nanocomposites and Composite Nanoparticles--a Review of Recent Patented Works. *Recent Pat. Nanotechnol.* **2013**, *7*, 153–166. https://doi.org/10.2174/18722105113079990008.

(8) Zhang, C.-L.; Cao, F.-H.; Wang, J.-L.; Yu, Z.-L.; Ge, J.; Lu, Y.; Wang, Z.-H.; Yu, S.-H. Highly Stimuli-Responsive Au Nanorods/Poly(*N* -Isopropylacrylamide) (PNIPAM) Composite Hydrogel for Smart Switch. *ACS Appl. Mater. Interfaces* **2017**, *9* (29), 24857–24863. https://doi.org/10.1021/acsami.7b05223.

(9) Even-Ram, S.; Artym, V.; Yamada, K. M. Matrix Control of Stem Cell Fate. *Cell*. 2006. https://doi.org/10.1016/j.cell.2006.08.008.

(10) Malda, J.; Visser, J.; Melchels, F. P.; Jüngst, T.; Hennink, W. E.; Dhert, W. J. A.; Groll, J.; Hutmacher, D. W. 25th Anniversary Article: Engineering Hydrogels for Biofabrication. *Adv. Mater.* **2013**, *25* (36), 5011–5028. https://doi.org/10.1002/adma.201302042.

(11) Marzo, A.; Ghobrial, A.; Cox, L.; Caleap, M.; Croxford, A.; Drinkwater, B. W. Realization of Compact Tractor Beams Using Acoustic Delay-Lines. *Appl. Phys. Lett.* **2017**, *110* (1), 014102. https://doi.org/10.1063/1.4972407.

(12) Marzo, A. Acoustic Tractor Beam https://www.instructables.com/id/Acoustic-Tractor-Beam/.

(13) DiOrio, A. M.; Luo, X.; Lee, K. M.; Mather, P. T. A Functionally Graded Shape Memory Polymer. *Soft Matter* **2011**, *7* (1), 68–74. https://doi.org/10.1039/C0SM00487A.

(14) Luo, R.; Wu, J.; Dinh, N.-D.; Chen, C.-H. Gradient Porous Elastic Hydrogels with Shape-Memory Property and Anisotropic Responses for Programmable Locomotion. *Adv. Funct. Mater.* **2015**, *25* (47), 7272–7279. https://doi.org/10.1002/adfm.201503434.

(15) Naficy, S.; Kawakami, S.; Sadeghovaad, S.; Wakisaka, M.; Spinks, G. M. Mechanical Properties of Interpenetrating Polymer Network Hydrogels Based on Hybrid Ionically and Covalently Crosslinked Networks. *J. Appl. Polym. Sci.* **2013**, *130* (4), 2504–2513.

(16) Fernandes, P. A. L.; Schmidt, S.; Zeiser, M.; Fery, A.; Hellweg, T.; Tanaka, T.; Fillmore, D. J.; Pelton, R. H.; Chibante, P.; Kumar, A.; et al. Swelling and Mechanical Properties of Polymer Gels with Cross-Linking Gradient. *Soft Matter* **2010**, *6* (15), 3455. https://doi.org/10.1039/c0sm00275e.

(17) Zheng, W. J.; An, N.; Yang, J. H.; Zhou, J.; Chen, Y. M. Tough Al-Alginate/Poly(N -Isopropylacrylamide) Hydrogel with Tunable LCST for Soft Robotics. *ACS Appl. Mater. Interfaces* **2015**, *7* (3), 1758–1764. https://doi.org/10.1021/am507339r.

(18) Breger, J. C.; Yoon, C.; Xiao, R.; Kwag, H. R.; Wang, M. O.; Fisher, J. P.; Nguyen, T. D.; Gracias, D. H. Self-Folding Thermo-Magnetically Responsive Soft Microgrippers. *ACS Appl. Mater. Interfaces* **2015**, *7* (5), 3398–3405. https://doi.org/10.1021/am508621s.

(19) Pezzulla, M.; Shillig, S. A.; Nardinocchi, P.; Holmes, D. P. Morphing of Geometric Composites via Residual Swelling. *Soft Matter* **2015**, *11* (29), 5783–5972.

(20) Pfeifer, R.; Bongard, J.; Grand, S. How the Body Shapes the Way We Think : A New View of Intelligence; MIT Press, 2007.

(21) Howard, D.; Eiben, A. E.; Kennedy, D. F.; Mouret, J.-B.; Valencia, P.; Winkler, D. Evolving Embodied Intelligence from Materials to Machines. *Nat. Mach. Intell.* **2019**, *1* (1), 12–19. https://doi.org/10.1038/s42256-018-0009-9.

(22) Bauer, M.; Bauer, J. Aspects of the Kinetics, Modelling and Simulation of Network Build-up during Cyanate Ester Cure. In *Chemistry and Technology of Cyanate Ester Resins*; Springer Netherlands: Dordrecht, 1994; pp 58–86. https://doi.org/10.1007/978-94-011-1326-7_3.

(23) Hecht, H.; Srebnik, S. Structural Characterization of Sodium Alginate and Calcium Alginate. *Biomacromolecules* **2016**, *17* (6), 2160–2167. https://doi.org/10.1021/acs.biomac.6b00378.

7. APPENDIX

7.1. MATHEMATICS OF SHAPE CHANGING GELS

7.1.1. JUSTIFICATION FOR ASSUMING INDEPENDENT BETWEEN MODULUS RATIO AND HEIGHT

Naficy *et al*. observe that for PNIPAM-polyurethane double network gels the relationship is such that Equation 7.1 holds, where -ν is a material specific parameter, predicted by theory to be 27/4 for fully swollen networks and 8 for more compact networks.[1]

$$E \approx \lambda^{-\nu}$$

Equation 7.1

This then means that for some hydrogels n can be re-expressed as the ratio of the linear expansion ratio of each hydrogel, $\lambda_{1,2}$:

$$n = \left(\frac{\lambda_2}{\lambda_1}\right)^{\alpha}$$

Equation 7.2

Where α = ν + 1. Naficy *et al*. find for PNIPAM-polyurethane α is 6.9.[2] The question arises whether PNIPAM-alginate, a double network material that has a more complex structure due to the variation in the alginic acid binding blocks and the rod-like nature of the junctions, also follows this relationship between E and λ.

Data from de Moura *et al.* on the swollen and dry weight and compressive Young's moduli of different PNIPAM-alginate sample compositions[3] was reprocessed to yield the linear expansion ratio (simply the cube root of the swelling ratio, assuming isotropic expansion) and plotted as $\ln E$ versus $\ln \lambda$ to yield, if the relationship holds, a linear distribution with gradient ν. Results are shown in Figure 7.1.

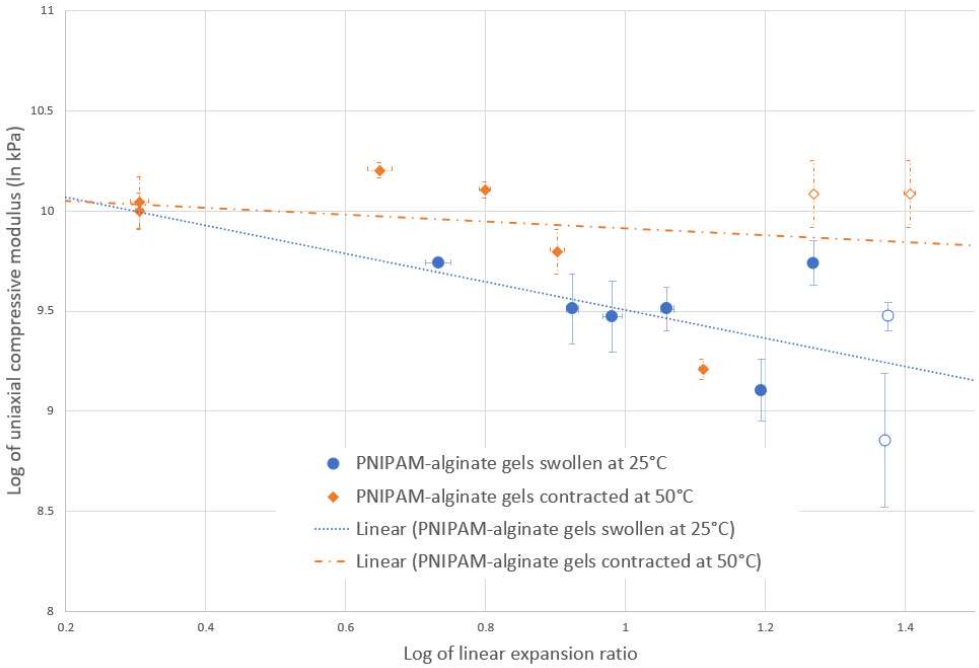

Figure 7.1. Swelling ratios versus Young's moduli for various PNIPAM_alginate compositions reprocessed from data by de Moura et al. Lines shown are fits to series representing ambient equilibrium swelling (blue circles) and contracted gels (orange diamonds). Both are poor fits, with gradients of -0.70481 and -0.1772 ln kPa for swollen and contracted conditions respectively. Two data points in each series represent compositions containing no PNIPAM at all, being pure alginate, and these are indicated by hollow markers.

The gradients found from compositional data indicate some sort of linear correlation between ln E and ln λ but the fit is poor (R^2<0.5) and the deviation from the trend greater for samples with a higher proportional of alginate. Since the highest ratio of alginate:PNIPAM in the data used for Figure 7.1 was 15.4:220.9 while the composition being considered here is 45:300, it seems likely that the PNIPAM-alginate composition in this study will deviate further from the trend. Therefore, n may be approximated as independent from λ. While there is a possibility that n may vary as a function of h, $f(m, n)$ is relatively insensitive to changes in n,[4] and as shown in figure 1.4 displays the same broad features regardless of its value: namely, a positive-valued function with a minimum at m≤1, followed by a linear increase in f(m,n) with m. Therefore, the dependency of n can be ignored for the purposes of this section and it will be set to 1.

7.1.2. RELATIONSHIP BETWEEN LINEAR EXPANSION AND SAMPLE HEIGHT

In section 4.4.7 the linear expansion ratio (LER) and sample height were stated to be variable in their relationship as a function of height. Figure 7.2 shows the percentage difference between the length of the illuminated and unilluminated beam surfaces plotted against the height of the beam. Since both surfaces are equal in length as printed the difference between them is indicative of a difference in LER. Lengths were measured using the segmented line tool in ImageJ and heights taken as the average of 10 measurements across the beam.

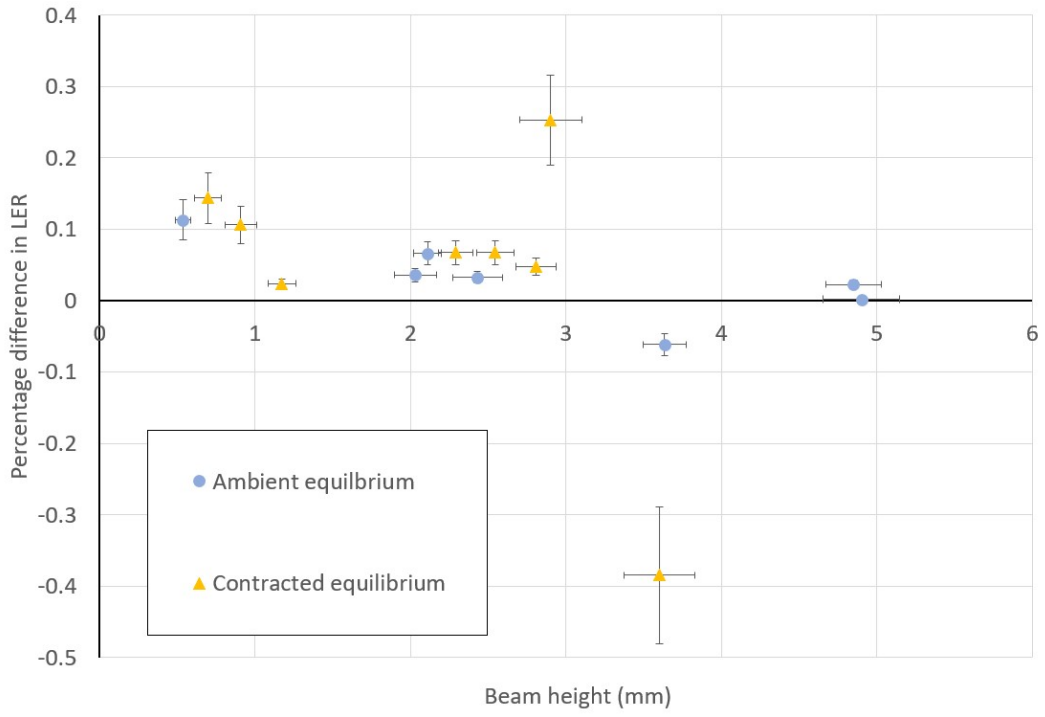

Figure 7.2 Relationship between the percentage difference in LER between top and bottom surfaces of illumination-gradated beams and the height of the beam. Errors in height are the standard deviation of 10 measurements of beam width and errors in percentage are fixed as 25% of the value.

7.2. STRESS-STRAIN GRAPHS FOR ALL PNIPAM-ALGINATE COMPOSITIONS

In Chapter 5, compression tests were used to generate the Young's modulus of PNIPAM-Alginate gels with varying concentrations of gold nanorods within the elastic limit. Example graphs were shown; full details of all concentrations are shown below.

7.2.1. FULL STRESS-STRAIN DATA

The following graphs show engineering stress plotted against strain for samples of the composition given in the legend. Tests were taken to rupture or a 50N force on the load cell, whichever was the lesser. Lines indicate fits to the values below |0.01| strain. Error bars are derived through standard error propagation and principally derive from errors in the measurement of initial sample dimensions, arising from measuring deformable materials with digital micrometer calipers.

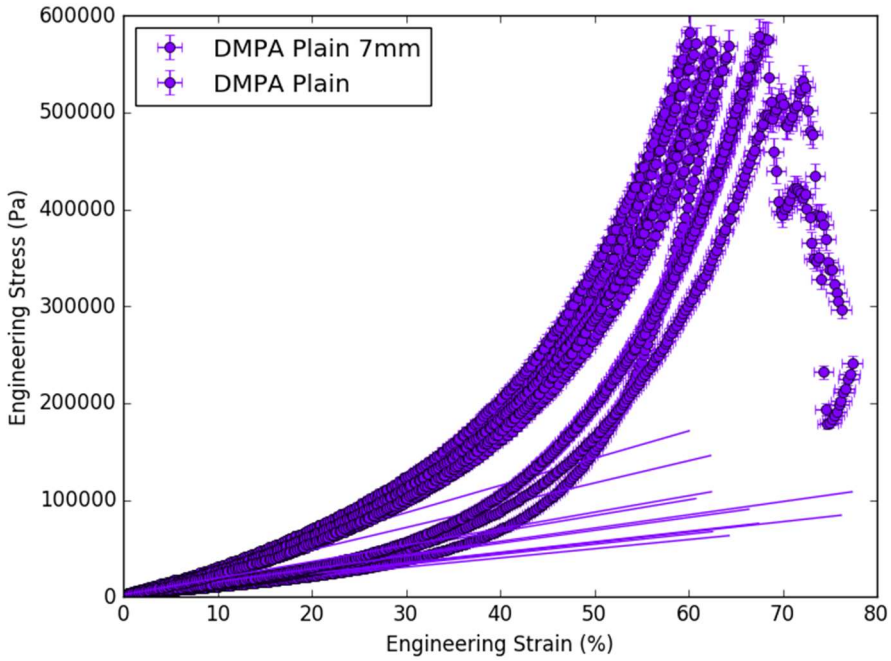

Figure 7.3 Native PNIPAM-alginate. The two groups visible reflect two different batches and show different behaviour. However the moduli fitted pass a test for normality and the values are within error of each other, so data were combined for a final value.

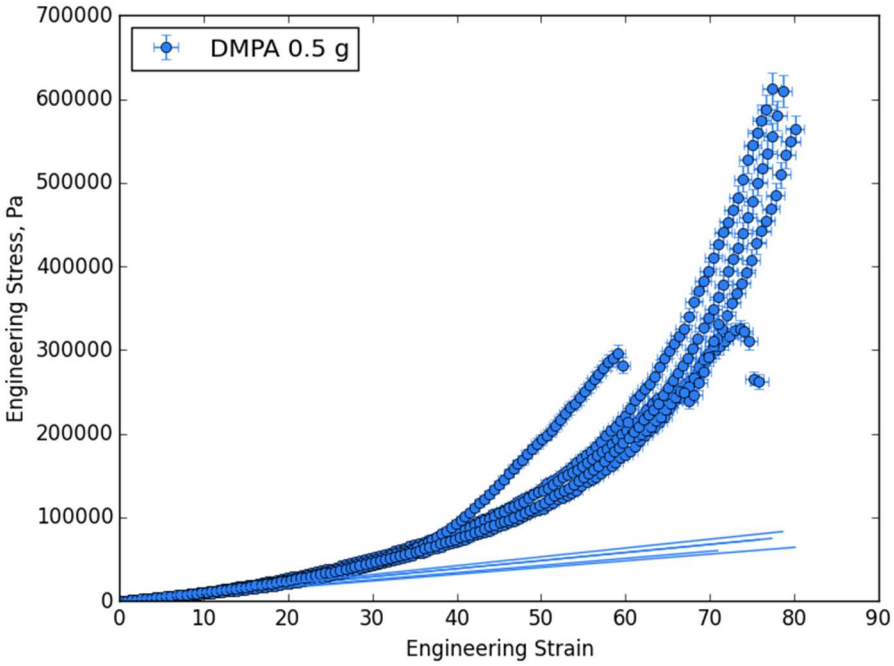

Figure 7.4. . PNIPAM-alginate with 1.0ml of gold nanoparticle solution in a 15ml batch.

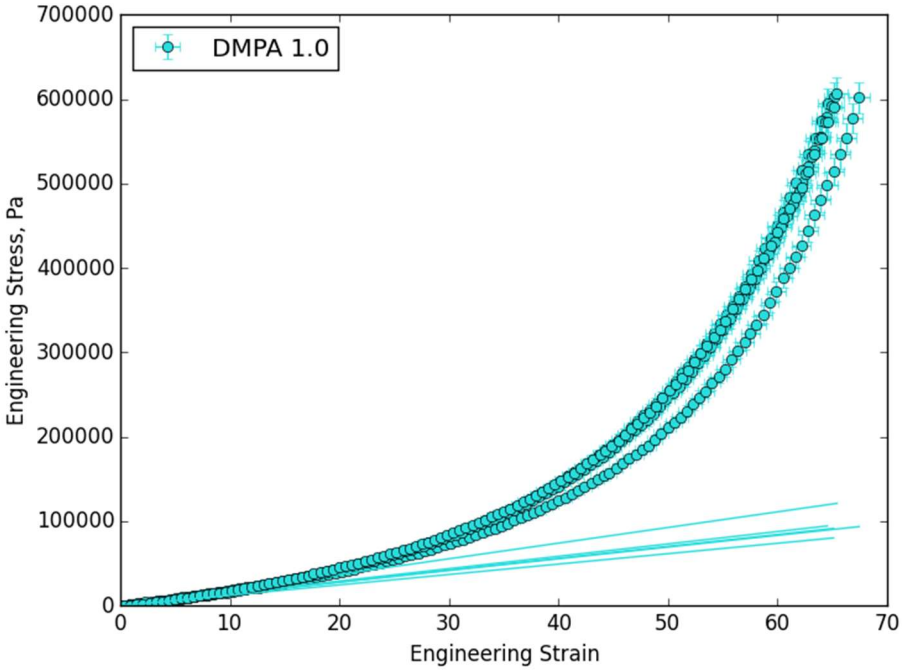

Figure 7.5. PNIPAM-alginate with 1.0ml of gold nanoparticle solution in a 15ml batch.

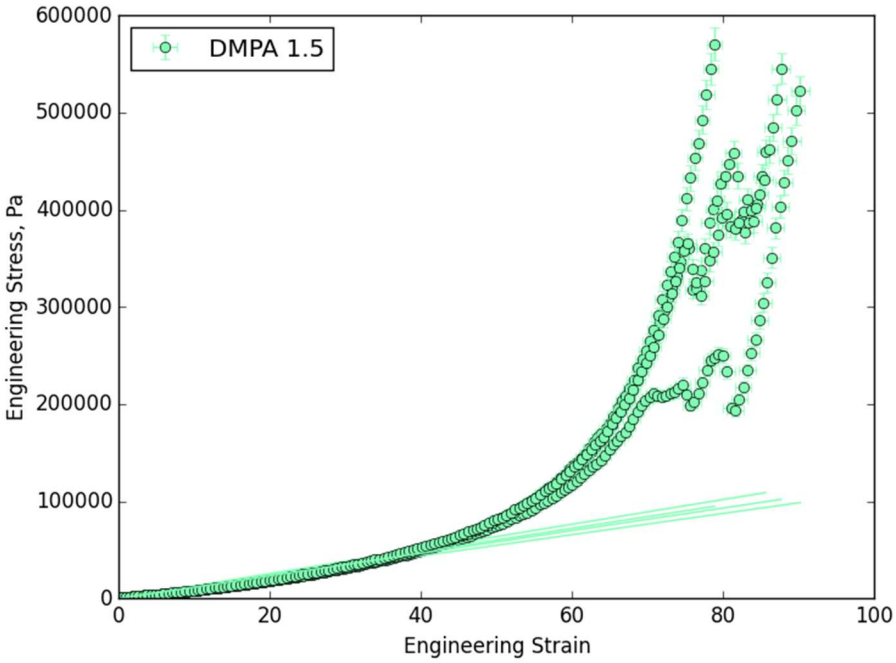

Figure 7.6 PNIPAM-alginate with 1.5ml of gold nanoparticle solution in a 15ml batch.

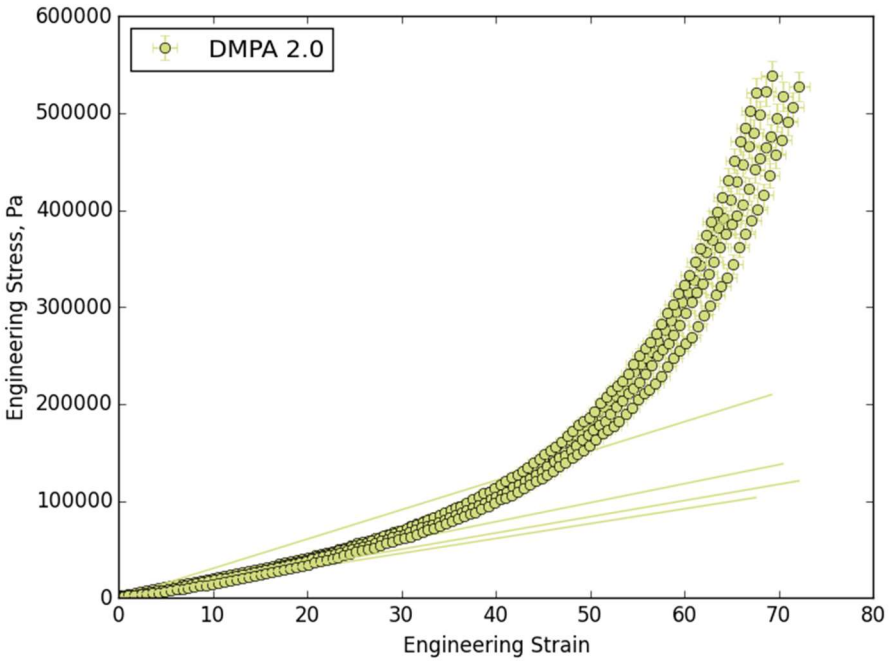

Figure 7.7 PNIPAM-alginate with 2.0ml of gold nanoparticle solution in a 15ml batch.

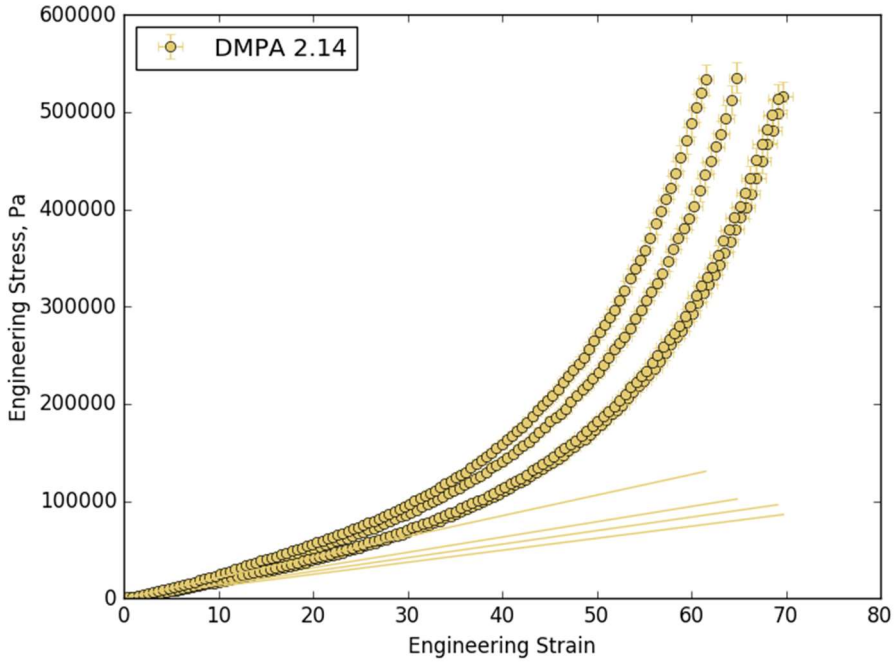

Figure 7.8 PNIPAM-alginate with 2.14ml of gold nanoparticle solution in a 15ml batch.

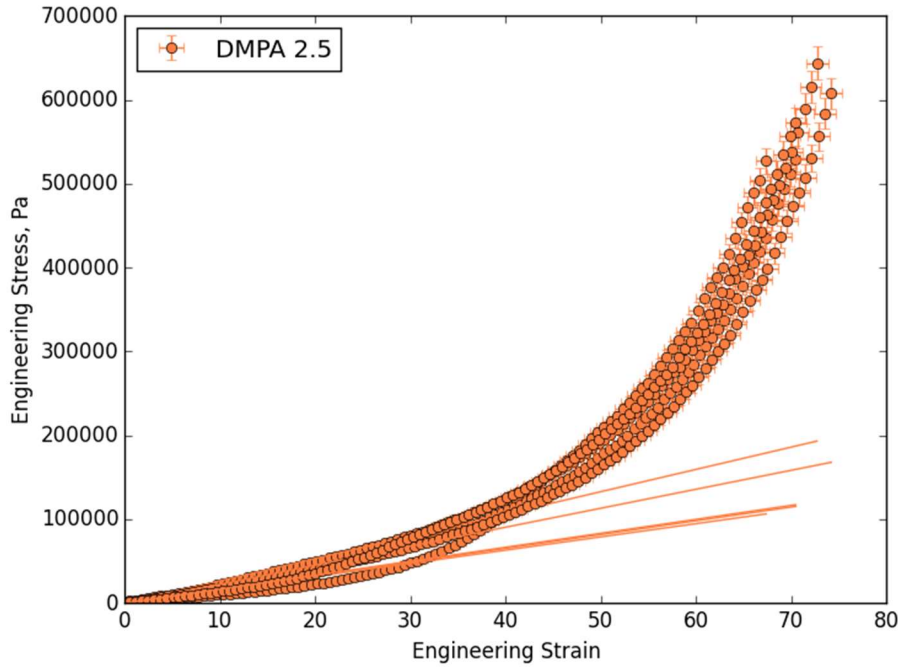

Figure 7.9 PNIPAM-alginate with 2.5ml of gold nanoparticle solution in a 15ml batch

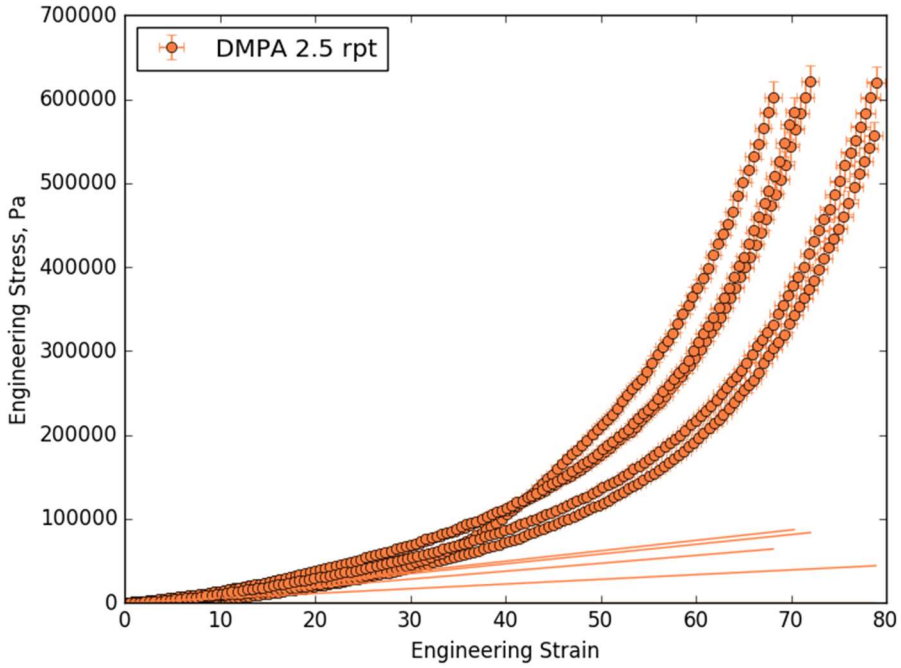

Figure 7.10 Repeated data for PNIPAM-alginate with 2.5ml of gold nanoparticle solution, due to anomalour value and interrupted sample manufacturing process

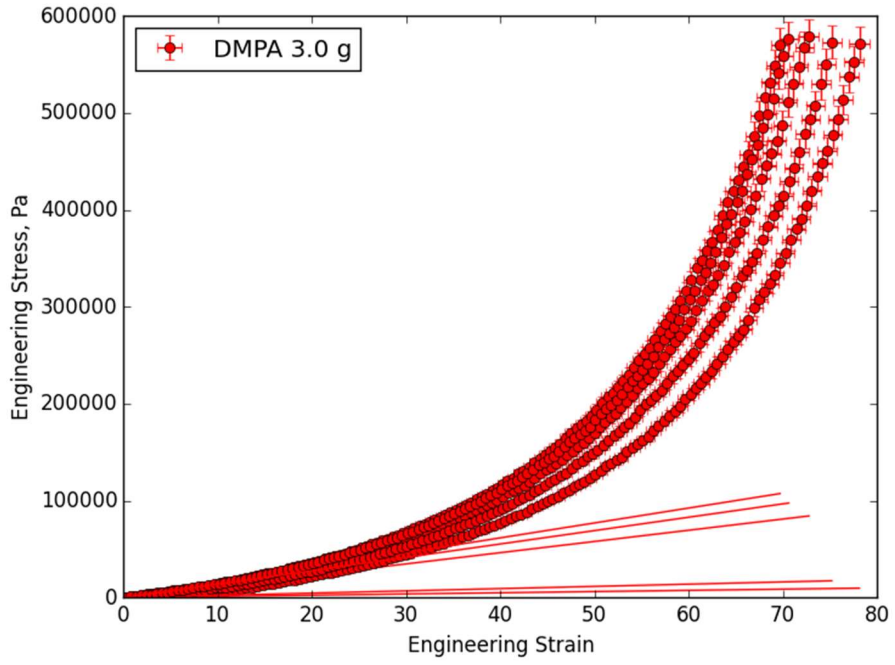

Figure 7.11 PNIPAM-alginate with 3.0ml of gold nanoparticle solution in a 15ml batch

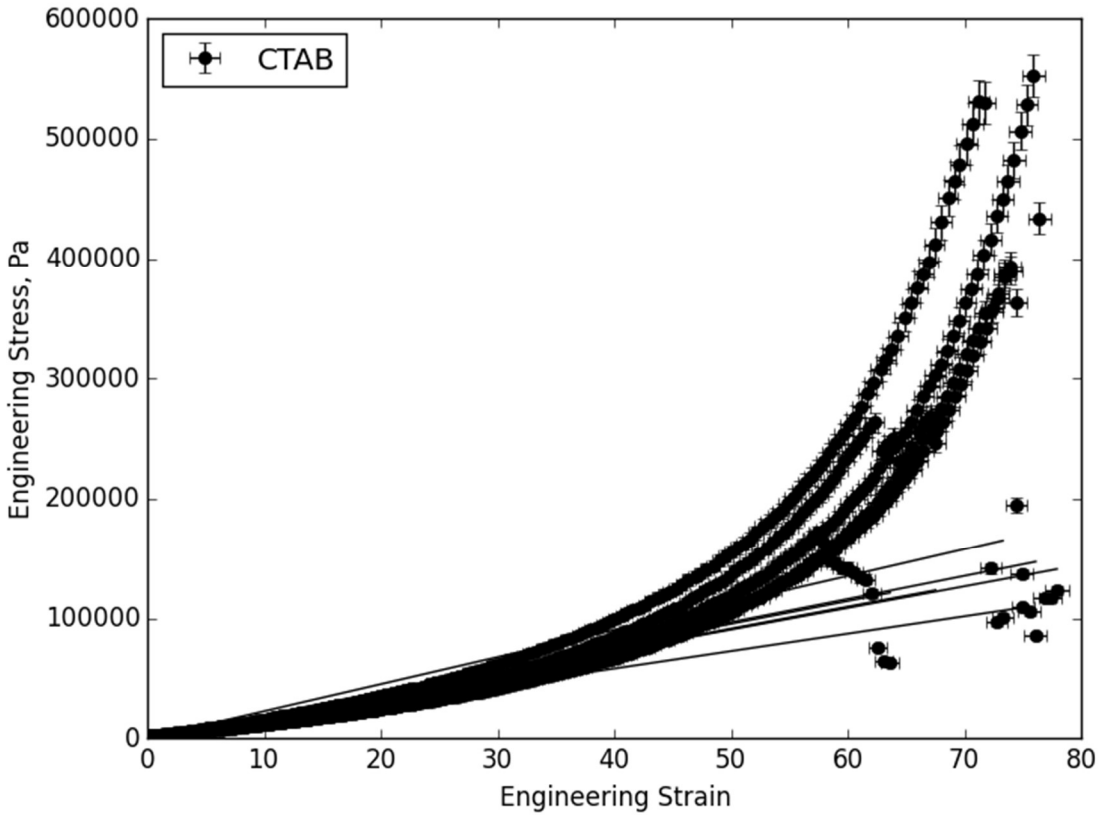

Figure 7.12 PNIPAM-alginate with the equivalent CTAB content of 3.0ml of gold nanoparticle solution in a 15ml batch

7.2.2. SMALL-STRAIN REGION

These graphs focus on the fitted region and permit inspection of the fit quality for the composition given in the caption. The gradients of these lines were used to determine the Young's moduli for these compositions.

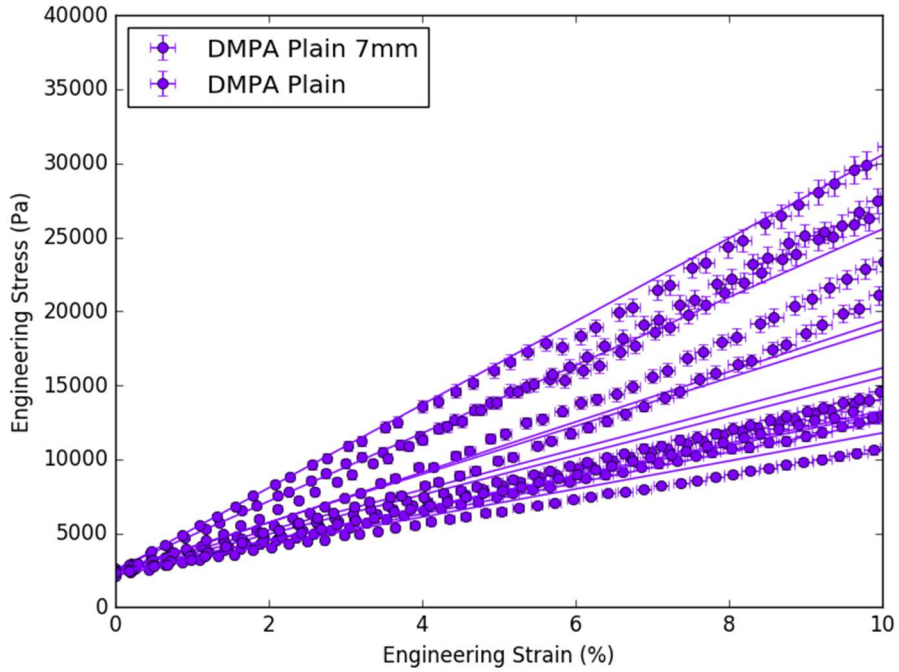

Figure 7.13 Native PNIPAM-alginate

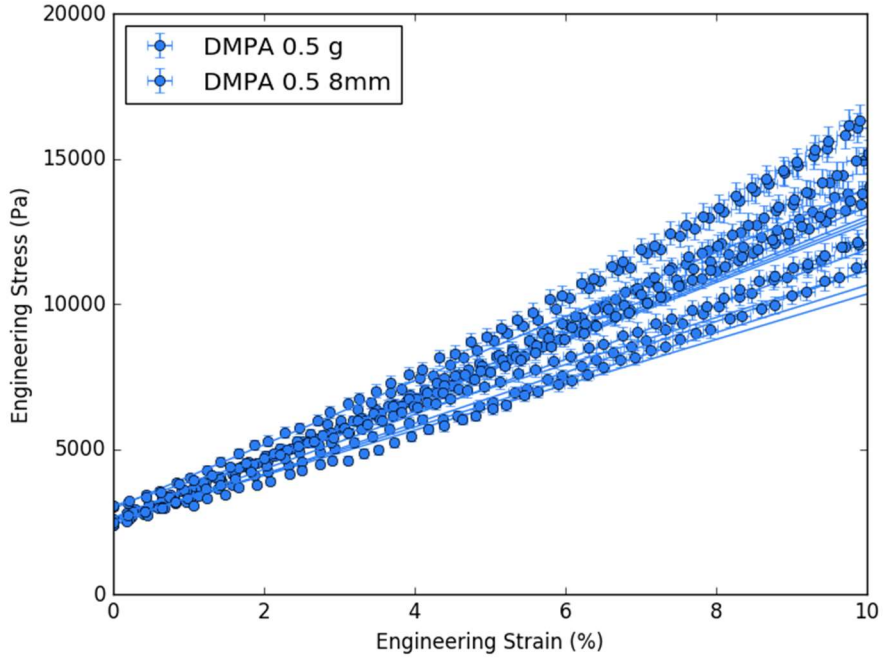

Figure 7.14 PNIPAM-alginate with 0.5ml of gold nanoparticle solution in a 15ml batch

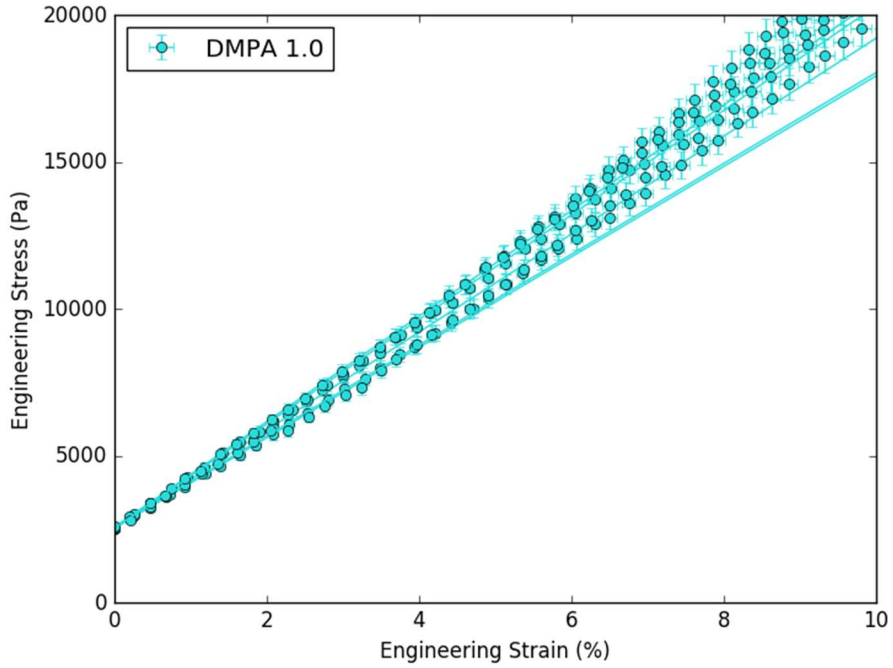

Figure 7.15 PNIPAM-alginate with 1.0ml of gold nanoparticle solution in a 15ml batch

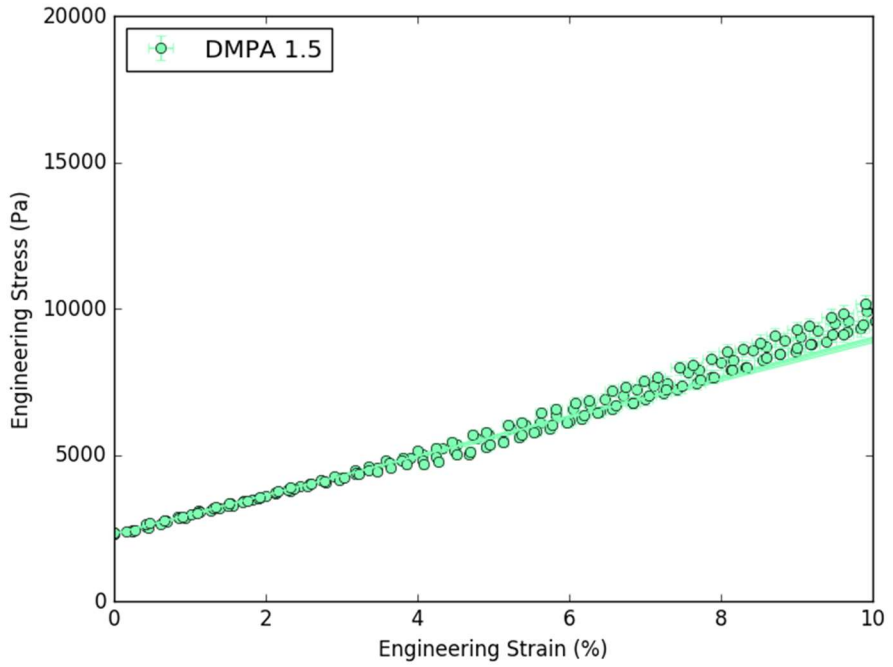

Figure 7.16 PNIPAM-alginate with 1.5ml of gold nanoparticle solution in a 15ml batch

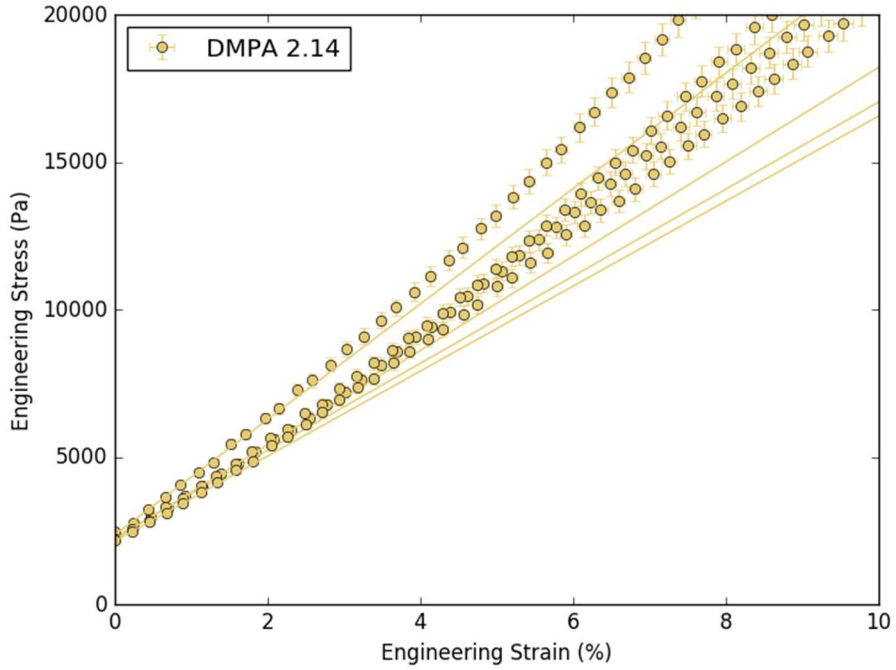

Figure 7.17 PNIPAM-alginate with 2.14ml of gold nanoparticle solution in a 15ml batch

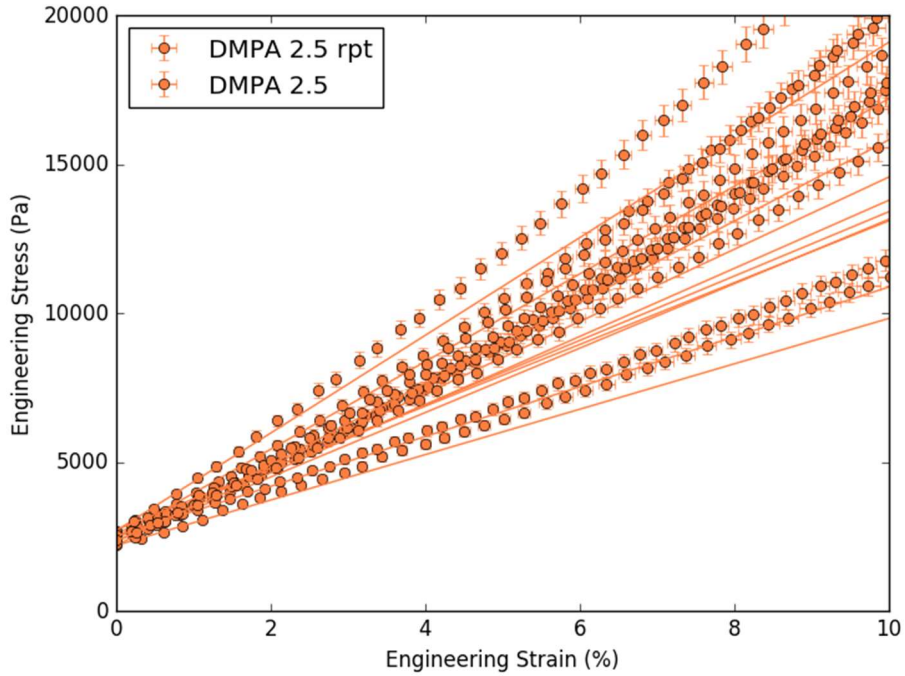

Figure 7.18 All data from both batches of PNIPAM-alginate with 2.5ml of gold nanoparticle solution per 15ml batch

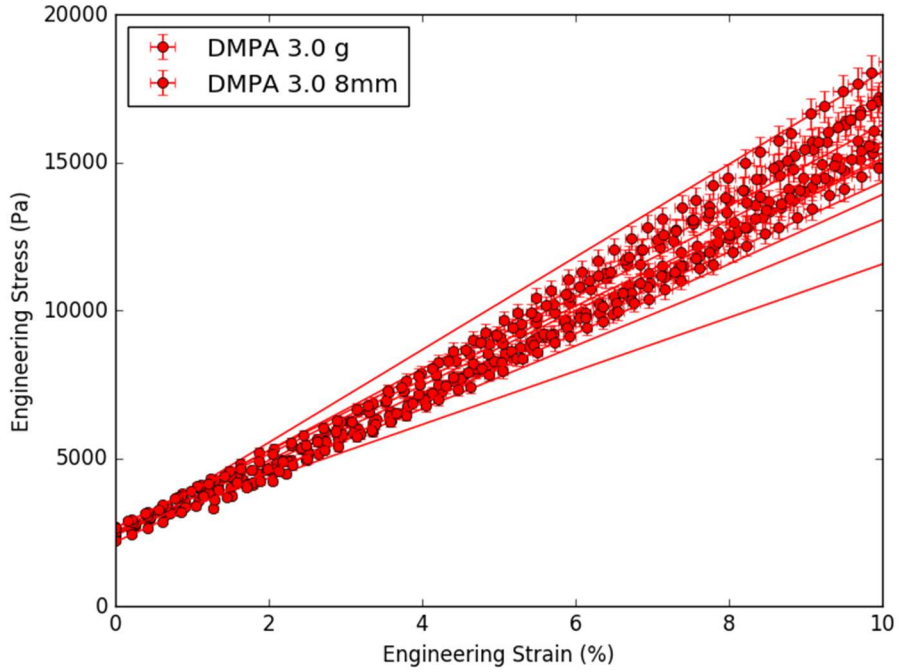

Figure 7.19 PNIPAM-alginate with 3.0ml of gold nanoparticle solution in a 15ml batch

7.3. THREE-STAGE SHEAR REBUILD PROTOCOL AS A PROBE OF MOLECULAR INTERACTION

As mentioned in Sections 4.4.3.3. and 6.3, three-stage shear rebuild measurements showed an intriguing two-phase rebuild process. This differs between samples with different compositions (see Section 4.4.3.3.). Work has been done to fit exponential functions to the envelope of this displacement oscillation; this may yield information about the interactions of molecules during structural rebuilding.

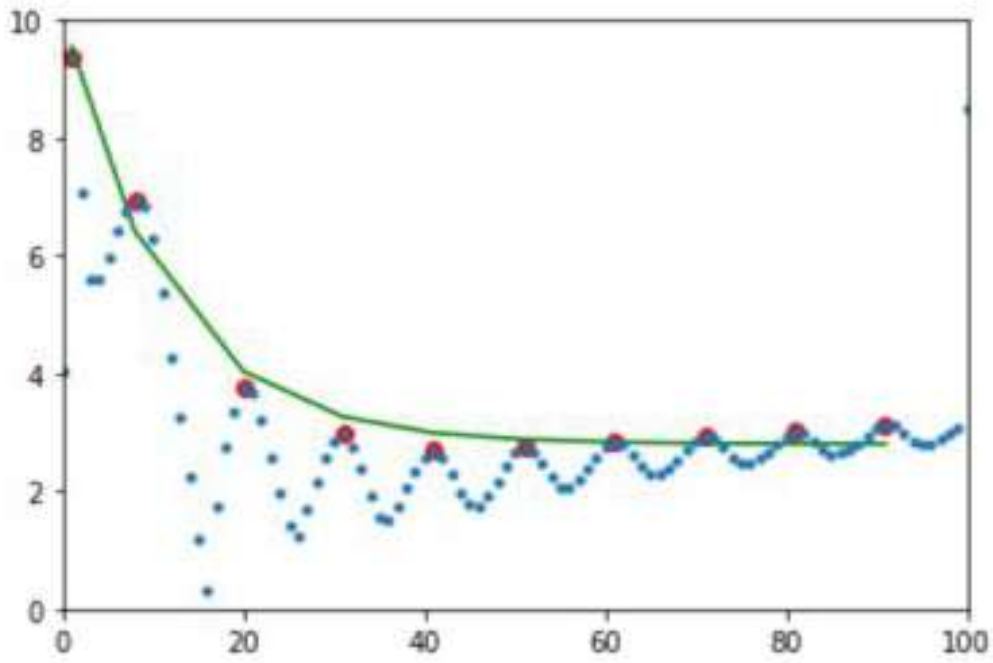

Figure 7.20 Following segmentation of modulus versus time data into separate decay stages, peaks are identified (red dots) and a fit to a function of form a·exp (bx) + c performed (green line).

7.4. REFERENCES FOR APPENDIX

(1) Naficy, S.; Gately, R.; Gorkin, R.; Xin, H.; Spinks, G. M. 4D Printing of Reversible Shape Morphing Hydrogel Structures. *Macromol. Mater. Eng.* **2017**, *302* (1), 1600212. https://doi.org/10.1002/mame.201600212.

(2) Naficy, S.; Gately, R.; Gorkin, R.; Xin, H.; Spinks, G. M. 4D Printing of Reversible Shape Morphing Hydrogel Structures. *Macromol. Mater. Eng.* **2017**, *302* (1), 1600212. https://doi.org/10.1002/mame.201600212.

(3) de Moura, M. R.; Guilherme, M. R.; Campese, G. M.; Radovanovic, E.; Rubira, A. F.; Muniz, E. C. Porous Alginate-Ca2+ Hydrogels Interpenetrated with PNIPAAm Networks: Interrelationship between Compressive Stress and Pore Morphology. *Eur. Polym. J.* **2005**, *41* (12), 2845–2852. https://doi.org/10.1016/j.eurpolymj.2005.06.007.

(4) Reyssat, E.; Mahadevan, L. Hygromorphs: From Pine Cones to Biomimetic Bilayers. *J. R. Soc. Interface* **2009**, *6* (39), 951–957. https://doi.org/10.1098/rsif.2009.0184.